Single Molecule Studies of Seven Transmembrane Domain Proteins

Thesis submitted to the Board of the Medical Sciences Division
in partial fulfilment of the requirements for the Degree of
Doctor of Philosophy at the University of Oxford

Olivia Berthoumieu

St Hugh's College
University of Oxford

Trinity Term 2011

Abstract

This work aimed at studying biophysical properties of two membrane proteins, one of potential nanotechnological use, bacteriorhodopsin, and one potential drug target, the NTS1 neurotensin receptor, at the single molecule scale.

Bacteriorhodopsin (BR) is the only protein in the purple membrane (PM) of the halophilic organism *Halobacterium salinarium*. It is a light-driven proton pump converting light into a transmembrane proton gradient through isomerization of its retinal chromophore. Its stability, as well as its photoactivity remaining in dry protein layers, has made BR an attractive material for biomolecular devices. Indeed, the increasing need for miniaturisation of electronic devices will soon reach the limit of lithographic techniques and molecular electronics, including BR-based bioelectronics approaches, looks like a promising alternative. Numerous studies have been published on this topic; however, they have all used BR within the PM, on relatively large (µm-wide) surfaces.

Here, conducting-probe atomic force microscopy (C-AFM) analysis was performed after removing most of the membrane lipids. For the first time, it was shown that the molecular conductance of BR can be reversibly photoswitched with predictable wavelength sensitivity. Intimate and robust coupling to gold electrodes was achieved by using a strategically engineered cysteine mutant located on the intracellular side of the protein which, combined with partial delipidation, generated protein trimers homogenously orientated on the surface. C-AFM proximal probe analysis showed a reproducible 3 fold drop of BR mean resistance over ~5 cycles of interspersed illuminations for single gold-BR-gold junctions when $\lambda > 495$ nm, while no shift was observed with other wavelengths. Numerous controls using biophysical (SPR, ellipsometry, Kelvin-probe AFM) and chemical (electrochemistry) techniques were performed in order to confirm the wavelength specificity of the photoswitch, the anchoring role of the mutation and the homogenous orientation of the protein on the gold surface.

Neurotensin is a brain and gastrointestinal 13 amino acid peptide acting as a neuromodulator in the central nervous system and as a hormone in the periphery. Its wide range of biological activities is primarily mediated through its binding to the neurotensin type 1 receptor (NTS1). NTS1 expressed in *E.coli* was purified and inserted into 100 nm brain polar lipid liposomes in a conformation which retained its ligand-binding capabilities. Initial AFM characterisation was performed as a prelude for ligand-receptor interaction studies, including high resolution imaging, force spectroscopy and solid state NMR approaches.

List of publications

Berthoumieu O., Patil A., Xi W., Aslimovska L., Davis J.J. and Watts A., *Molecular scale conductance photoswitching in engineered bacteriorhodopsin*, Nano Lett. 2012 Feb 8;12(2):899-903. Epub 2012 Jan 10.

Patil A., Premaruban T., **Berthoumieu O**., Watts A and Davis J. J., *Enhanced photocurrent in engineered bacteriorhodopsin monolayers,* J Phys Chem B. 2012 Jan 12;116(1):683-9. Epub 2011 Dec 21.

Patil A., Premaruban T., Berthoumieu O., Watts A and Davis J. J., *Engineered bacteriorhodopsin: a molecular scale potential switch* (accepted for publication in Chem. Eur. J.).

Prior to DPhil:

Milhiet P-E., Yamamoto D., **Berthoumieu O.**, Dosset P., Le Grimellec C., *et al. Deciphering the Structure, Growth and Assembly of Amyloid-Like Fibrils Using High-Speed Atomic Force Microscopy.* PLoS One. 2010 Oct 8;5(10):e13240.

Odorico M., Teulon J-M., **Berthoumieu O.**, Chen S-W., Parot P., and Pellequer J-L.: *An integrated methodology for data processing in Dynamic Force Spectroscopy of ligand-receptor binding,* Ultramiscropy. 2007 Oct; 107 (10): p.887-894.

Oral presentations

Towards single molecule studies of 7 TM domain receptors, **4th UK-Japan Bionanotechnology workshop, Kobe**, Sept.2008; funded by Bionanotechnology IRC.

Purification and reconstitution of the NTS1 receptor into liposomes for single molecule studies of ligand-receptor interactions, **7th NCCR Workshop (protein crystallization), Basel**, Switzerland, Oct. 2008; funded by the EU Marie Curie Training Course Fellowship.

Switching of the electrical conductance of bacteriorhodopsin on illumination, **22nd French Biophysical Society Meeting, Nice**, Sept. 2010; funded by EPSRC.

Engineered bacteriorhodopsin: a novel molecular scale conductance photoswitch, **8th European Biophysics Congress (EBSA), Budapest,** Hungary, August 2011; funded by the Postgraduate Travel Fund, Department of Biochemistry, University of Oxford.

Poster presentations

Studying neurotensin receptor type I interactions in a lipid model membrane system, **7th European Biophysics Congress (EBSA), Genoa**, July 2009; funded by EPSRC.

AFM-based single molecule studies of 7TM domain receptors, **1st Nano Measure Meeting, Krakow**, June 2010; funded by the Barbinder Watson Trust award, St Hugh's College, Oxford.

"Single Molecule Studies of 7 TM domain receptors", **4th Midlands Biophysics Symposium**, Warwick, UK – Best Poster Presentation Prize laureate

"Engineered bacteriorhodopsin: a novel molecular scale conductance photoswitch", **8th European Biophysics Congress (EBSA), Budapest,** Hungary, August 2011; funded by the Postgraduate Travel Fund, Department of Biochemistry, University of Oxford.

Abbreviations

- AFM: atomic force microscopy
- Å: Ångström
- ATP: adenosine triphosphate
- BPL: brain polar lipids (porcine)
- BSA: bovine serum albumin
- BR: bacteriorhodopsin
- BR_{cys}: bacteriorhodopsin M163C cysteine mutant
- C-AFM or CP-AFM: conducting probe-AFM
- CHAPS: 3-[(3-cholamidopropyl) dimethylammonio]-1-propanesulfonate
- CHS: cholesteryl hemisuccinate
- CMC: critical micellar concentration
- CP: cytoplasmic side
- CV: column volume
- CV: cyclic voltammetry / voltammogram
- DCM: dichloromethane
- DMF: dimethyl formamide
- DDM: n-dodecyl-ß-D-maltoside
- DIPEA: *N*, *N*'-diisopropylcarbodiimide
- DMF: dimethylformamide
- dH_2O: deionised water
- DTT: dithiothreitol
- *E. coli*: *Escherichia coli*
- EC: extracellular side
- EDTA: ethylene-diamine-tetraacetic acid
- Fmoc: 9-fluoenylmethoxycarbonyl

- FRET: fluorescence resonance energy transfer
- GDP: guanosine diphosphate
- GPCR: GTP-binding protein-coupled receptor
- HBTU: 2-(H-Benzotriazole-1-yl)-1,1,3,3-tetramethyluronium hexafluorophosphate
- HEPES: 4-(2-hydroxyethyl)-1-piperazineethanesulfonic acid
- HOBt: N-Hydroxybenzotriazole
- HOPG: highly orientated pyrolitic graphite
- HPLC: high performance liquid chromatography
- *IE:* current-potential
- *I-V*: current-voltage
- IMAC: immobilised metal ion affinity chromatography
- ITO: indium tin oxide
- KFM: Kelvin-probe AFM
- MBP: *E. coli* maltose binding protein
- MWCO: molecular weight cut-off
- NMR: nuclear magnetic resonance
- NT: neurotensin
- NT_{8-13}: six C-terminus residues of NT
- NTS / NTR: neurotensin receptor
- NTS1A: MBP-T43NTS1-TrxA-H10
- NTS1B: MBP-TeV-T43NTS1-TeV-TrxA-H10
- OD : optical density
- PBS phosphate-buffered saline
- PC : phosphatidyl choline
- PDB protein data bank
- PE : phosphatidylethanolamine
- PG: phosphatidylglycerol

- PI: phosphatidylinositol
- PM: purple membrane
- POPC: 1-palmitoyl 2-Oleoyl-*sn* glycero 3-phosphocholine
- POPE: 1-palmitoyl 2-Oleoyl-*sn* glycero 3-phosphoethanolamine
- POPG: 1-palmitoyl 2-Oleoyl-*sn* glycero 3 [phospho-*rac*-(1 glycerol)]
- ppm: parts per million
- PS: phosphatidyl serine
- PyBOP: benzotriazol-1-yl-oxytripyrrolidinophosphonium hexafluorophosphate
- R_{eff}: effective detergent : lipid ratio
- RT: room temperature
- SAM: self assembled monolayer
- SDS-PAGE: sodium dodecyl sulphate polyacrylamide gel electrophoresis
- SPM: Scanning probe microscopy
- SPPS: solid-phase peptide synthesis
- SPR: Surface plasmon resonance
- ssNMR: solid state NMR
- STM: Scanning Tunneling Microscopy
- T43NTS1: N-terminally truncated NTS1
- *t*-Boc: *tert*-butoxycarbonyl
- TCEP: Tris (2-carboxyethyl) phosphine hydrochloride
- TEM: transmission electron microscopy
- TeV: tobacco etch virus
- TFA: trifluoroacetic acid
- TM: transmembrane
- Tris: 2-amino-2-hydroxymethyl-1,3-propanediol
- TrxA: *E. coli* thioredoxin
- WT: wild-type

Contents

Chapter IV – Molecular scale conductance photoswitching in engineered bacteriorhodopsin ____ 103

Chapter I - Introduction

1.1 Biological membranes

All living organisms are constituted of one or more cell(s) surrounded by a membrane separating an intracellular space from an extracellular space, and acting as a highly selective barrier: some 85% of all the information coming from or towards the intracellular compartment must go through the membrane.

Cell membranes are highly complex dynamic structures involved in numerous functions that are essential for the organism, such as cellular recognition, biosynthesis, transports, ion channels, hormonal receptors, or energy transduction. They are constituted predominantly of lipids forming a bilayer structure, proteins and carbohydrates (Figure 1.1). Different types of lipids and proteins can be found in various ratios according to the cell type and the biological function. Membrane proteins typically constitute 50 % of the dry mass of biological membranes although, depending on the particular location and function, a biological membrane may be composed of between 20 and 80 % protein[1]. Moreover, the membrane lipids and proteins are in dynamic equilibrium within the membrane, adding to the complexity of the structure. In order to understand the general organisation of biological membranes, a model simplifying their structure while including the general features found in all membranes has been adopted and was named: the fluid mosaic model[2, 3] (Figure 1.1).

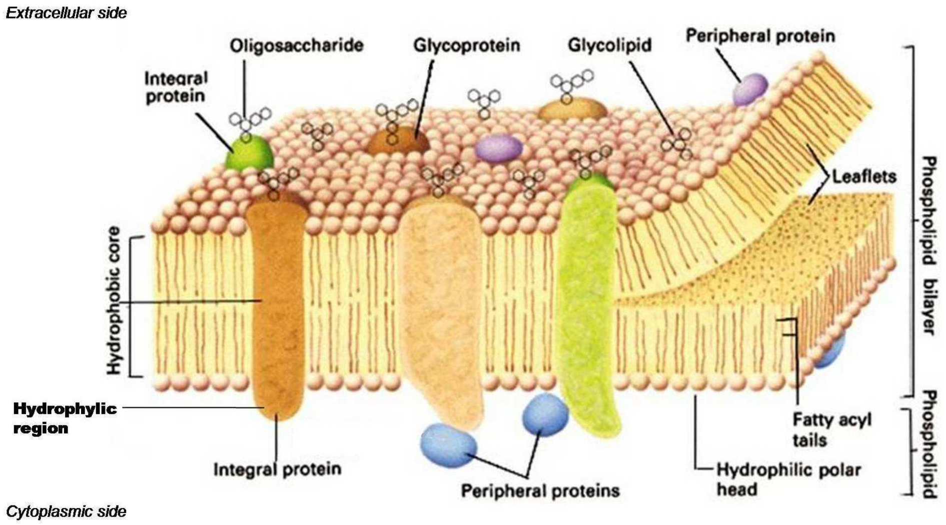

Figure 1.1: **Typical cell surface plasma membrane.** Phospholipids are organised into lamellar asymmetric bilayers in which proteins are embedded. Adapted from[4].

1.1.1 Membrane lipids

Membrane lipids are amphipathic molecules that self-assemble into a bilayer, forming a semi-permeable barrier in aqueous environments and giving the membrane its flexibiltiy. Indeed, the cell membrane is freely permeable to water molecules, but its hydrophobic component makes it relatively impermeable to ions and polar molecules[5]. Phospholipids (Figure 1.2.a) are the most abundant lipid molecules found in eukaryotic cells. They consist of a polar head exposed to water molecules and hydrophobic chains oriented towards the centre of the membrane. The chemical structure of the polar headgroup determines the overall charge and, therefore, the physical characteristics of the phospholipid. For example, if the phosphate is esterified to positively-charged alcohols such as choline (phosphatidylcholine, PC) and ethanolamine (phosphatidylethanolamine, PE), the phospholipid will be zwitterionic and will have an overall neutral charge.

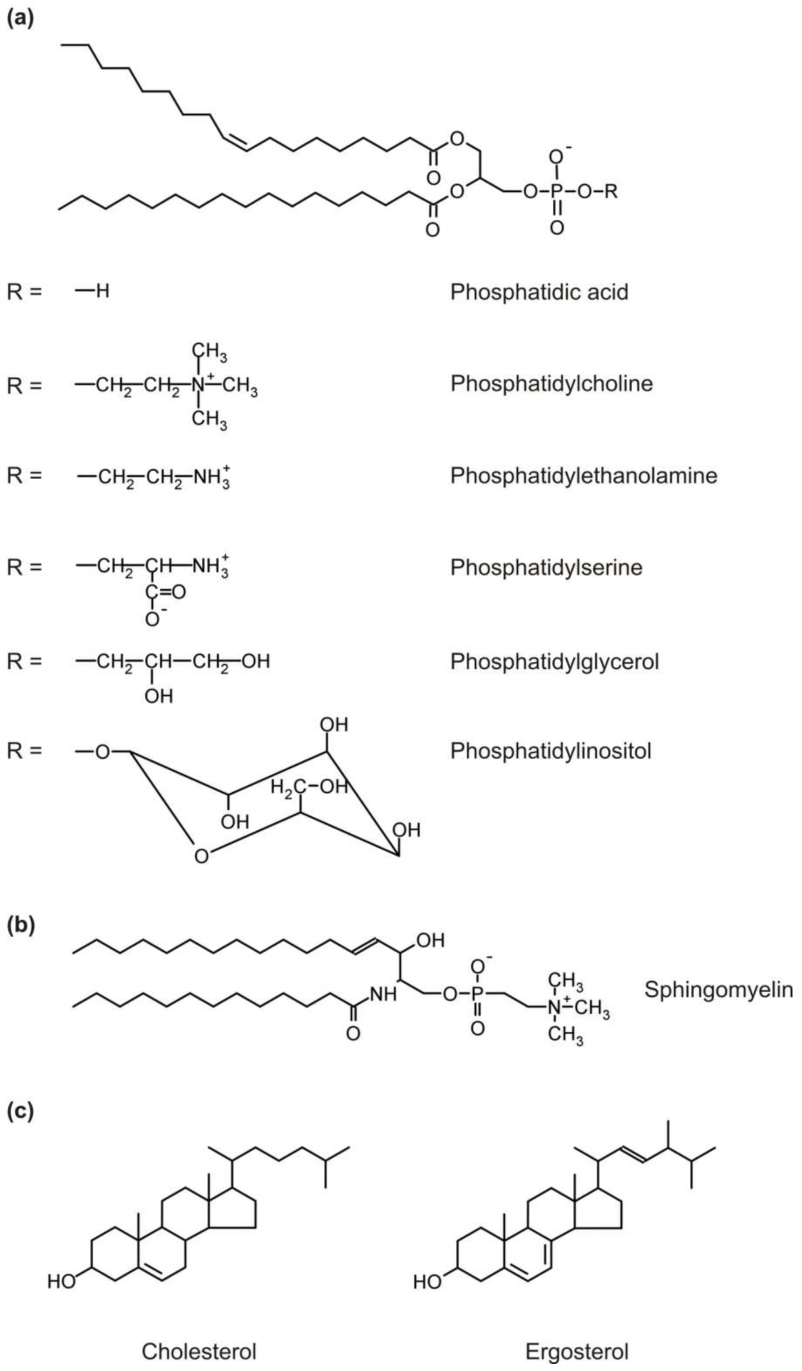

Figure 1.2: The major lipid components of most biological membranes (a) The general structure of a phospholipid. Glycerol is esterified to two fatty acid chains and a phosphate head group. The phosphate is esterified to an alcohol (R). Some common alcohols are shown with the name of the resulting phospholipid. (b) Sphingomyelin, present in eukaryotic membranes (c) Sterols of eukaryotic membranes: cholesterol is the most common sterol in higher eukaryotes, while ergosterol is the major sterol in yeasts.

However, if the phosphate is esterified to alcohols with an overall neutral charge, such as serine (phosphatidylserine, PS), glycerol (phosphatidylglycerol, PG), and inositol (phosphatidylinositol, PI), the phospholipid will have an overall negative charge. Phospholipids head groups thus create diversity within cell membrane compositions, with an even greater level of complexity achieved by the phospholipid hydrocarbon chain structure. Indeed, the carbon chain can vary in length from 12 to 26 carbon atoms and can have different degrees of saturation, the number of double bonds per fatty acid chain commonly ranging from zero to six[6]; some chains can also be highly branched, like in archae. A high level of complexity of cell membrane compositions is therefore achievable, through the possible combinations of head groups and hydrocarbon chains. This diversity is responsible for the different cell membrane compositions observed between different classes of organisms, some of which are characteristic of the organelle, as well as between different tissue types within a single organism.

Biological membranes also contain carbohydrates, which are found as components of glylipids and glyproteins. The oligosaccharidic part of glycoproteins and glycolipids is generally exposed on the extracellular side. The oligosaccharide component of glycoproteins is covalently attached to its protein through a glycosidic link to the hydroxyl group of a Ser or Thr residue (*O*-linked), or through an *N*-glycosyl link to the amide nitrogen of an Asn residue (*N*-linked). The oligosaccharide portions of glycoproteins are often branched, forming highly specific sites for recognition and high-affinity binding by other proteins. A number of proteins, such as the human protein interferon IFN-β1, produced in two types of tissues, have different glycosylation patterns according to their location: oligosaccharidic chains may thus be considered as tissue-specific markers[5]. Glycolipids also serve as markers for cellular recognition by carbohydrate-binding proteins. These components of the membrane may be protective, insulators, or sites of receptor binding[5]. A change in glycosylation patterns has been proposed to be a potential biomarker for cancer diagnostic[7].

1.1.2 Membrane proteins

Membrane proteins typically constitute 50 % of the dry mass of biological membranes although, depending on the location and function, a biological membrane may be composed of between 20 and 80 % protein[1]. They are divided into two categories: integral proteins, which are embedded within the membrane, and peripheral proteins, which are attached to the membrane surface.

Membrane proteins are insoluble in aqueous solution. Indeed, the large hydrophobic regions present on their surface enable them to sit within the hydrophobic region of the membrane lipid bilayer. Detergents are usually required to stabilise membrane proteins in aqueous environments, which makes it difficult to crystallize them afterwards, due to the molecular disorder. The first successfully determined membrane protein structure was obtained for bacteriorhodopsin (BR)[8]. This protein, found within the purple membrane of *Halobacterium salinarium*, is naturally organised in 2D-crystals which are suitable for electron diffraction analysis. Higher resolution structural information has subsequently been obtained by 3D X-ray crystallography for BR and for the other ~120 membrane proteins that can be crystallised (< 1% of all PDB entries). Structure determination using solution state nuclear magnetic resonance (NMR), the other direct means of protein structure determination, is hampered by the size of micelles made of a membrane protein-detergent mixtures, which decreases the efficiency of NMR analysis through line broadening. Membrane proteins are responsible for the wide range of major biological activities occurring at the membrane level. Such functions include cell-cell communication, sensory transduction, neuronal transmission and hormonal signalling, involving transport proteins that build electrical and chemical gradients across the cell through the plasma membrane, channel proteins, receptors regulating extracellular signal transduction, and proteins responsible for cell-cell recognition. It has been estimated that 30-40% of all genes in the human genome encode membrane proteins[9].

The critical biological importance of membrane proteins is of major interest for the pharmaceutical industry: they account for 70% of known drug targets[10] (Figure 1.3). Drug design techniques have evolved in the past decades from the general screening of chemical compounds for identifying novel drug molecules, to a structure-based drug design at the nanoscale, providing a targeted approach.

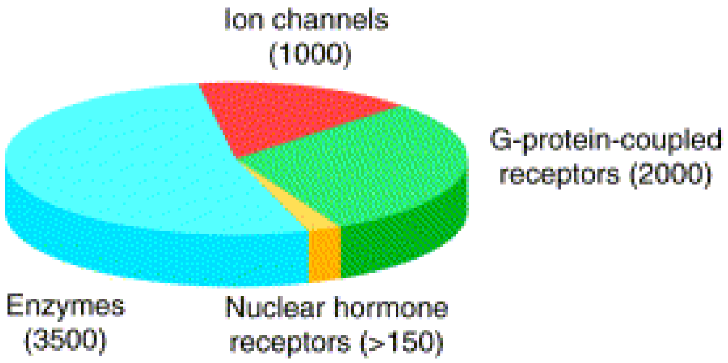

Figure 1.3: Pharmaceutical importance of membrane proteins: predicted numbers of potential drug targets belonging to different classes of membrane protein. Membrane proteins are responsible for key biological function occurring at the membrane level, such as cell-cell recognition or hormonal signalling, and is assumed that they will represent up to two third of drug targets[11].

Resolving the structures of membrane proteins is thus of critical importance for the elaboration of new drugs. Despite this, while the total number of protein structures deposited in the protein data bank (PDB[12]) is over 76,000 only 1100 structures of membrane proteins have been published to date[12]. This is largely due to the problems encountered with overexpression, purification and 3D crystallisation of membrane proteins.

1.1.3 Seven transmembrane domain receptors (7 TMRs)

Most vital physiologic functions of higher-order animals are critically regulated by signal transduction of extracellular signal through 7 transmembrane receptors (7TMRs), which has traditionally been understood to be mediated via coupling to heterotrimeric G proteins and downstream second-messenger molecules[13, 14].

1.1.3. a GPCRs

G protein-coupled receptors (GPCRs), the largest group of membrane receptors (~800 in human), are encoded for by 1% of the genome of higher life forms. GPCRs are seven transmembrane helix proteins, connected by three intracellular and three extracellular loops. They are activated by a wide range of stimuli, including hormones, neurotransmitters, ions, odorants, and photons of light[10]. The GPCR superfamily is involved in a variety of biological and pathological processes such as cell growth and proliferation[15], neurological disorders[16], angiogenesis[17], metabolic disorders[18], and immune system and inflammation[19]. Consequently, they are one of the largest classes of drug targets to which agonists and antagonists are currently focused. Although approximately 50% of pharmaceutical products target GPCRs, only 10% of the GPCRs excluding olfactory receptors are targeted by marketed drugs, indicating the possibility of the remaining 90% of the GPCRs for the treatment of human diseases[20].

When bound to their ligands, GPCRs are stabilized in an active conformation and stimulate heterotrimeric guanine-nucleotide-binding regulatory proteins (G proteins) through their intracellular domains. GPCRs lack catalytic activity, but interaction of the receptor with an agonist promotes the dissociation of G proteins into G_α and $G_{\beta\gamma}$ subunits. The G protein subunits (both G_α and $G_{\beta\gamma}$) then amplify and propagate signals inside the cell by modulating the activity of one or more effector molecules, including adenylyl cyclases, phospholipases and ion channels[20, 21]. In turn, the activity of these effector enzymes and ion channels regulates the production of second messenger molecules, which elicit cellular responses by activating different signalling pathways (Figure 1.4). Examples of second messengers include cyclic AMP and inositol-1,4,5-trisphosphate ($InsP_3$).

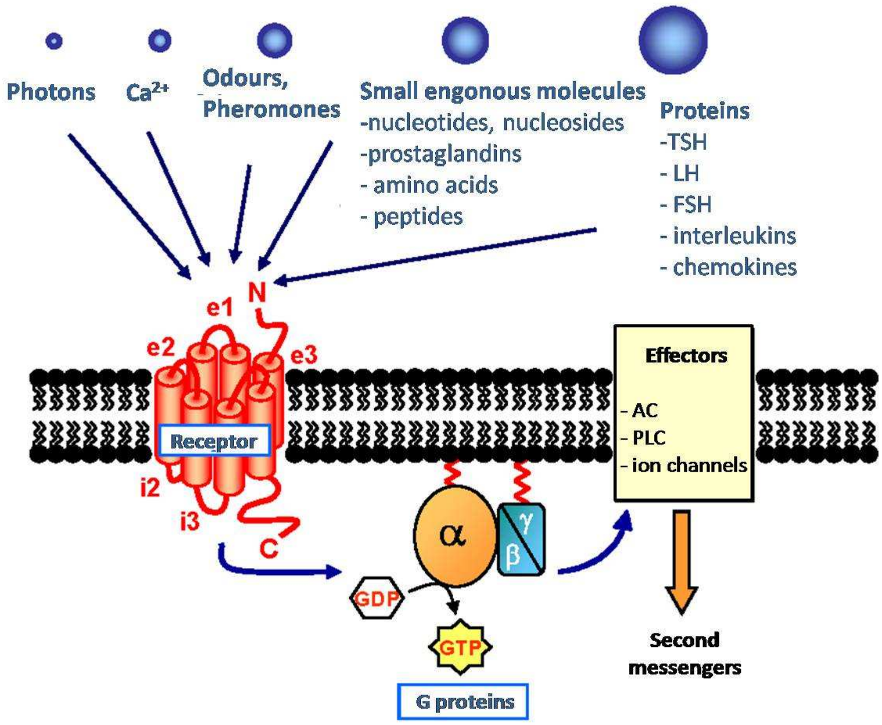

Figure 1.4: Schematic of the GPCRs signaling pathway. The basic unit of G-protein-coupled receptor signalling comprises three parts: a seven-transmembrane-spanning receptor; a heterotrimeric G protein and an effector (adapted from [22]).

The work presented in Chapter V of this thesis consisted in preparing a GPCR, the neurotensin receptor type 1 (NTS1), for future ligand-receptor interaction measurements using single molecule approaches, with the aim to add to the knowledge base of structural and functional properties of this membrane receptor.

1.1.3.b Other 7 TM domain proteins

Over the past several years, evidence has emerged from biochemical and cellular studies that heptahelical receptors can signal through associations with intracellular partners other than G proteins[13, 21]. In some cases, these partners are known receptor-interacting proteins, such as arrestins and G protein-coupled receptor kinases (GRKs), which were thought previously to be involved only in receptor desensitization. In other cases, they are novel partners, such as Na^+/H^+ exchanger regulatory factor (NHERF) or the Homer neuronal protein, which were not known previously to interact with heptahelical receptors.

The work presented in Chapters III and IV studied the electrical properties of a 7 TM domain protein, the light-sensitive archea proton pump bacteriorhodopsin (BR). Although BR is not a GPCR and does not interact with a ligand (its action is mediated by the isomerization of its chromophore), it is closely related to visual rhodopsins, which are GPCRs, and is used as a paradigm for this superfamily of membrane receptors.

1.2 Introduction to molecular and bio-electronics

In the past 50 years, silicon devices such as transistors have been developed, miniaturised and increasingly integrated into numerous items used on a daily basis, from cars to cameras or mobile phones. Miniaturisation occurs at the insulator level, which is a gate oxide made of silicon atoms (Figure 1.5), and has become the critical step when developing new devices[23]. Reducing the gate oxide thickness is possible until the layer becomes so thin that it does not function as an insulator anymore. It is predicted that the semiconductors feature sizes will approach the molecular domain around 2030[24, 25]. It is thus necessary to find alternatives, and using functional biomolecules as a replacement of silicon, “molecular electronics”, constitutes one of the most promising options[26].

Molecular electronics consists in the encoding, manipulation and retrieval of information at a molecular or macromolecular level. This approach contrasts with current techniques, in which these functions are accomplished via lithographic manipulation of bulk material to generate integrated circuits. One of the key advantages of this method is the possibility to design devices on a residue-by-residue, if not atom-by-atom, basis while it is quite unlikely that the lithographic approach can ever reach the level of control achieved through organic synthesis or genetic manipulation.

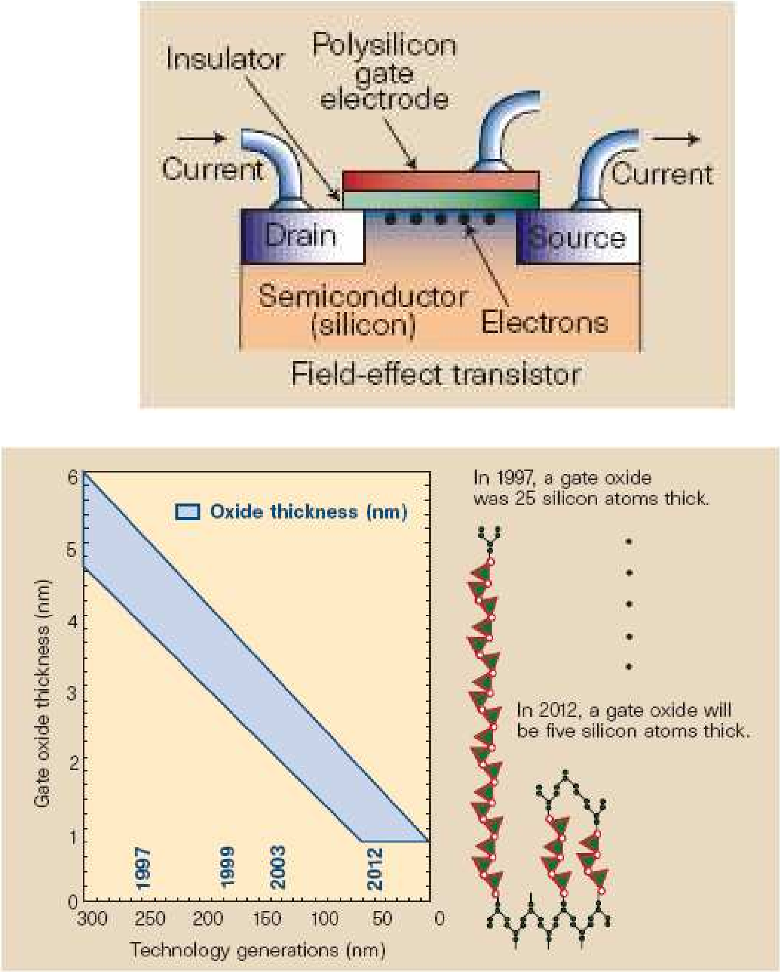

Figure 1.5: Schematic representation of a silicon-based device, and of the evolution of the miniaturisation of silicon-based devices. a. Representation of a field-effect transistor, where applying a bias on the gate electrode results in an accumulation of electrons on the opposite side. The semiconductor part then become conducting and current flows from the drain to source. **b.** Representation of the miniaturisation of silicon-base oxide gate over the past two decades. Adapted from[23].

Liquid crystal displays (LCDs) represents one well-known commercial success of biomolecular electronics, demonstrating the potential of this new, hybrid molecular and semiconductor technology[27]. Bioelectronics is a subfield of molecular electronics that investigates the use of native as well as modified biological molecules (proteins, chromophores, etc) in electronic or photonic devices. Genetic engineering provides a high level of control and manipulation of molecules, making bioelectronics a promising alternative to current techniques. Much of the current research in the field is focused on self-assembled monolayers and thin films, biosensors and protein-based photonic devices.

One of the fundamental goals of molecular electronics and bioelectronics, is the realization of nanoscale devices in which very few, or even better, a single molecule can be used to transfer and process an electronic signal.

The main challenge of this area is the assembly of the molecules into a transducer, such as an electrode surface in a robust, controllable and electrochemically addressable manner. Indeed, the small size (~1-6 nm) of proteins, and their labile nature, constitute some of the main challenges in molecular devices design.

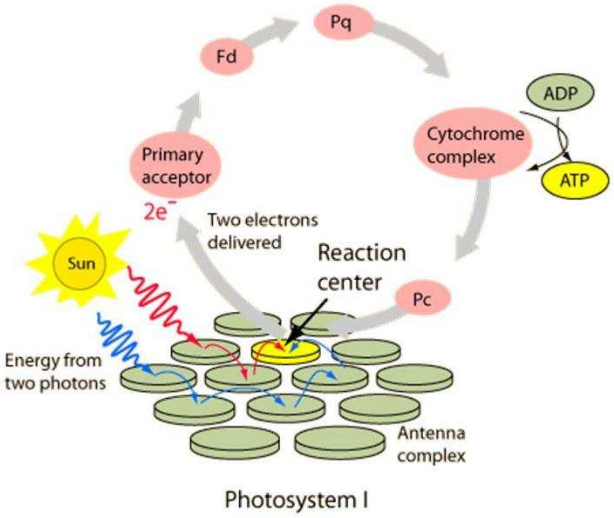

Figure 1.6: Electron transfer process during photosynthesis. Photon absorption by the antenna generates an electron transport that energizes the two photosystems embedded in the thylakoid membranes of chloroplasts. This results in the production of ATP and NADPH which provide chemical and reducing power to the sugar-making reactions of the Calvin cycle (adapted from[28]).

Redox-active proteins are a group of nm-sized electron shuttles involved in numerous fundamental biological processes, notably in photosynthesis (Figure 1.6). Understanding the electron transfer mechanisms occurring within these proteins has become a major research subject for the past two decades. These studies have been performed on a variety of proteins, such as cytochrome c and azurin, for example[29].

Cytochrome *c* and azurin are single electron shuttles found in eukaryotic and prokaryotic electron transport chains, respectively. Cytochrome *c* contains an iron redox centre while azurin contains a copper redox centre. One important point about these two proteins is that they both naturally contain surface cysteine residues, which allow their surface confinement on gold electrodes by forming self-assembled monolayers. The cysteine residues also ensure a homogeneous and functional orientation of the protein layer. However, although redox-active proteins present the advantage of performing efficient electron transfer at the nm scale, they also involve oxidative phosphorylation, bacterial electron transport chains and mitochondria. Another issue that needs addressing is the stability of the proteins out of their native environment, and their capacity to maintain an effective electron transfer once fixed between electrodes. One alternative system, involving no other biological component but the protein itself, is a proton-pump found in the membrane of the extremophilic archea *Halobacterium salinarium*, bacteriorhodopsin. Bacteriorhodopsin represents the simplest naturally existing photosynthetic system. It mediates a proton transport, not an electron transfer as seen previously, and is stable over a wide range of environmental conditions. This protein is the main subject of this thesis and the details of its study can be found in Chapters III and IV.

1.3 Metal-molecule-metal (mMm) junction construction

The central step towards a configuration capable of assaying the current passing through a molecule is the immobilisation of the species between electrodes, *i.e.* the construction of a metal-molecule-metal (mMm) junction or, more generally, conductor-insulator-conductor.

1.3.1 Physisorption and chemisorption

Sample immobilization on the electrode may be performed through physical (electrostatic, hydrophobic) or chemical interaction (Figure 1.7).

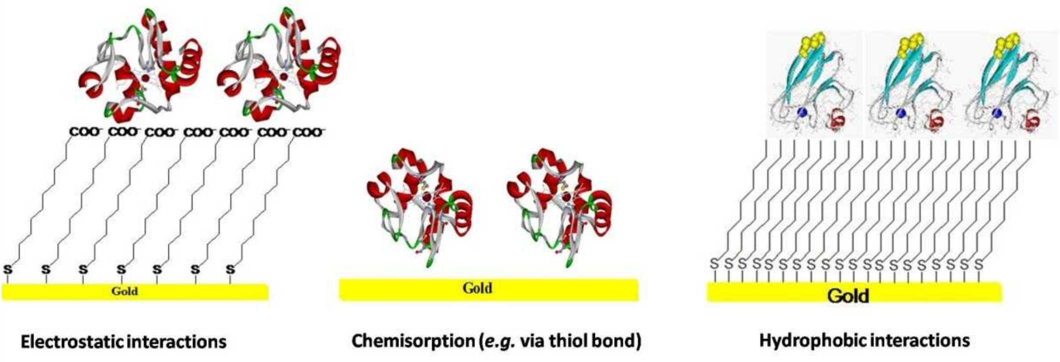

Figure 1.7: Schematic representation of different possibilities for sample adsorption onto a gold electrode. Fixing the molecule of interest between electrodes (metal-molecule-metal junction construction) constitutes a critical step in molecular electronics. Common means of sample immobilisation are based on physical (electrostatic, hydrophobic) interactions with the gold substrate, or chemisorption.

Covalent chemical bonds are strong, with, for example, a chemisorption enthalpy for Au-S bonds in an alkanethiolate monolayer on gold of 126kJ/mol[30], and provide a well-defined anchor point, orienting the molecule homogeneously on the electrode[31]. Gold is chemically inert, conducive to surface assembly, and sulphurs can be engineered into organic or biological molecules with relative synthetic ease: gold-sulphur bonds are thus widely used for mMm junction construction.

1.3.2 Self Assembled Monolayers

Gold electrodes can easily be coated with thiolated monolayers that present a functionalised end, making these an attractive option for engineering molecular junctions when the molecule of interest is lacking thiol groups.

In 1983, Nuzzo and Allara[32] reported for the first time the formation of self-assembled monolayers (SAMs) of thiols and disulfides on gold 111. SAMs are ordered and chemically stable two-dimensional assemblies formed by the spontaneous absorption of surface-active molecules onto a solid. A typical surface-active molecule consists of a head group, involved in strong interactions with the surface, a molecular backbone responsible for the 2D organisation of the SAM by facilitating lateral interactions with the backbone of contiguous molecules, and a tail group, determining the chemical properties of the assembly. The tail group is involved in the functionalisation with molecules of interest. Inter- and intramolecular interactions within the assembly determine the stability of the SAM. SAMs presents the advantage of forming a homogenous coverage on gold, and more particularly, they can be easily functionalised with molecules of interest through chemical reactions. One drawback in using SAMs for mMm junction construction lies in the fact that they insulate the molecule of choice from the electrode by introducing an additional tunnelling barrier, meaning that they must be of suitable length and of high conductivity in order to allow significant tunnelling currents to flow. Large molecules, particularly proteins, can be oriented by the interactions of their hydrophilic/hydrophobic or charged components with the monolayer end groups[33], a factor that can, as with orientation through chemisorption, greatly affect the electron transfer efficiency between molecule and electrode. SAMs have been studied for their potential molecular electronics applications, such as chemical sensors, non linear optical material[34], microelectronics and computer technology[35-38]. The most popular SAMs-forming molecules are alkanethiols, which absorb spontaneously on the metal surface and form highly ordered arrays[39-42], and are commercially available. Coating a gold surface is easily performed by immersing the substrate into a dilute solution of thiol or disulfide[43]. SAMs are formed by the oxidative addition of the S-H bond onto gold, followed by a reductive elimination of hydrogen and resulting in the creation of the gold-thiolate species[44]:

$$\text{R-SH} + \text{Au}_n^0 \Rightarrow \text{R-S}^- - \text{Au}^+ + \tfrac{1}{2}\,\text{H}_2 + \text{Au}_{n-1}^0$$

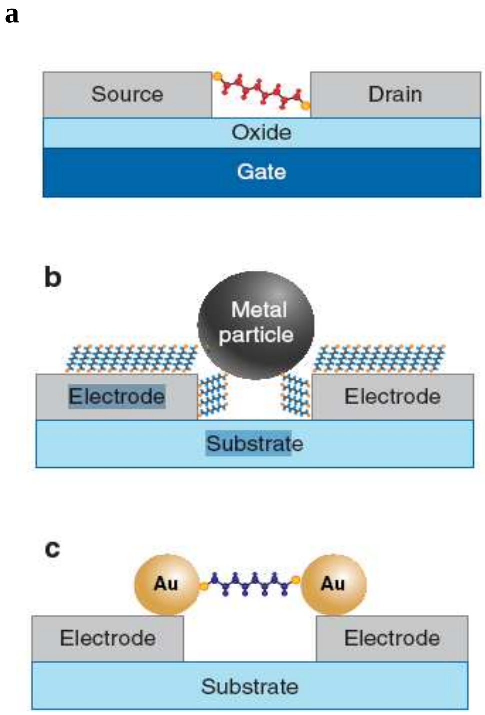

Figure 1.8: Example of alternative configurations used for metal-molecule-metal junction construction. a. the molecule of interest is trapped between electrodes separated by a molecule-wide gap; b. a metal particule is used for bridging both electrodes; c. the molecule of interest is bridged between two gold particles (adapted from[45]).

1.3.3 Alternative means of mMm junction construction

Some successful alternative configurations used in molecular electronics are presented in Figure 1.8. These include a single molecule bridged between two electrodes with a molecule-sized separation (Figure 1.8 a), using a metal particle for bridging a relatively large gap between two electrodes (Figure 1.8 b), or the formation of a dimeric structure, consisting of two gold particles bridged with one molecule. The common issue with all these method is that it is impossible to ensure only one single molecule will be trapped in the system.

In this thesis, metal-molecule-metal junctions construction is achieved by both chemisorption of the molecule of interest onto a gold substrate through a thiol bond, and by using the gold-coated probe of a conducting-probe atomic force microscope (C-AFM). Scanning probe microscopy techniques (SPMs), described in details in Chapter II, are used here both to create the molecular junction and to probe its electrical characteristics.

1.4 Electron transport in metal-molecule-metal junctions

The majority of the results presented in this thesis were obtained from the study of the electronic conductance behaviour upon illumination of a photochromic membrane protein, bacteriorhodopsin, at the single molecule scale after partial delipidation (Chapters III and IV). Gold-molecule-gold junctions were assembled and studied by current-voltage spectroscopy: these processes will be described in the following chapters. Beforehand, it is important to understand what data were acquired.

There are two types of electron transfer, although both types present common grounds: one consists in the electron tunnelling to an active centre and remaining there (electrochemistry), and one where the electron is tunnelling through an active centre while passing between electrodes (mMm junctions).

Electrochemical techniques (cyclic voltammetry and photocurrent measurements) are used here for the qualitative determination of current-voltage behaviour upon illumination in a resonant mMm system (bacteriorhodopsin), and, to a slighter level, for determining the photocurrent characteristics of this system.

1.4.1 Direct electron transport through molecules in mMm junctions

The invention of scanning probe microscopy (SPMs techniques enabled direct atomic-scale measurements to be made, such as of tunnelling electron transfer within an mMm junctions. There are two categories of electron transfer occurring at the junction level: non-resonant - or direct - tunnelling, characterised by a straight flow of electrons from one electrode to the other through a dielectric, and resonant tunnelling, in which a potential well located within the dielectric enhances the electron transfer.

In classical physics, at the macroscopic scale, a particle such as an electron with a low energy cannot traverse a potential energy barrier of higher energy (Figure 1.9a). However, at the nanometric scale, the wave-particle dualism may allow this electron to traverse the barrier by tunnelling effect: if the particle is given enough energy, part of it cannot get through the barrier, but a small part of it will be transmitted across the barrier (Figure 1.9 b). In STM, a voltage is applied in order to provide the electrons with the energy required to traverse the barrier, resulting in a tunnelling current being detected. The height of the barrier can be averaged as the work function of the sample and tip:

$$\phi = ½ (\phi_{\text{sample}} + \phi_{\text{tip}})$$

The relation between the tunnelling current and the gap distance between the tip and the sample in STM can be obtained from the following equation:

$$I = \kappa \rho_t \rho_s \exp (-k^0 d \phi^{½})$$

where ϕ is the average work function of the probe and sample, d is the distance between the probe and the sample, ρ_t et ρ_s are the respective densities of states of the probe and sample, and κ and k are constants.

Whether looking at resonant or non-resonant electron tunnelling, the current-voltage spectrum gives crucial information about the junction electronic behaviour. The following section will describe the Simmons model, used for analysing elementary tunnelling current between two electrodes.

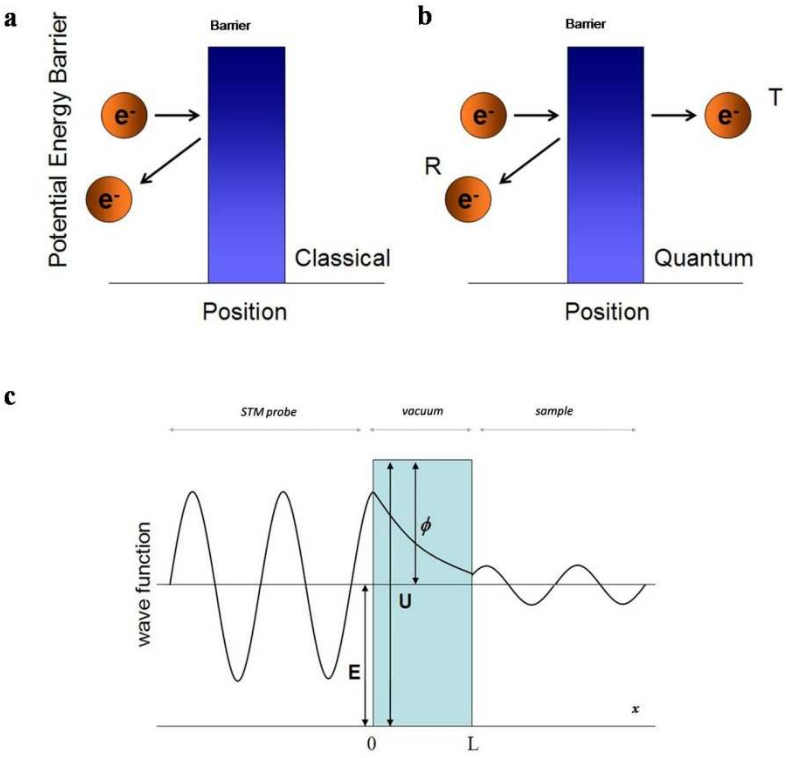

Figure 1.9: the concept of tunnelling in STM a. In classical physics, a particle with low energy cannot traverse a potential energy barrier of higher energy. **b.** In quantum physics, if the particle is given enough energy, part of it will be transmitted across the potential energy barrier, while the other part is reflected. **c.** Schematic of the potential energy of an electron incident from the STM probe. In the barrier region (green), the wave function is exponentially decaying. In STM, an applied voltage provides the electrons with the energy required to traverse the barrier.

1.4.1.a Current-voltage (I-V) spectroscopy

In C-AFM, the voltage bias applied between the tip and substrate when performing *I-V* spectroscopy may be either kept constant or altered. Applying a voltage bias results in moving the positively biased electrode’s Fermi energy down by the amount of applied bias relative to that of the negatively biased electrode (Figure 1.10). If the molecular medium between both electrodes allows it, electrons can then flow from the full states in the negatively biased electrode to the empty states in the positively biased electrode. When recording *I-V* spectroscopy scans, an increase in the applied bias will result in more states being overlapped between the Fermi energies of the electrodes, and thus, in a larger current being detected. This is then shown on the recorded *I-V* spectrum.

I-V spectroscopy has been used extensively in this thesis to investigate the electronic behaviour upon illumination of the photo-sensitive proton pump bacteriorhodopsin at the single molecule scale. *I-V* spectroscopy usually consists in sweeping the bias voltage linearly between two values over a short period of time. This can induce a charge build-up or other unwanted effects, but if these are controlled, the *I-V* spectra obtained are of great use in the characterization of the electronic properties of molecular species.

1.4.1.b Direct electron tunneling through an insulator: the Simmons Model

The phenomenon of quantum mechanical tunnelling arises from the solution to the Schrödinger equation for particles incident on a potential barrier; there is a non-zero probability that a particle with less energy than an energy barrier height penetrates through to the other side. In 1963, John G. Simmons published a formulation describing the current between two conductors separated by a thin dielectric insulator[46].

Conditions of the Simmons formulation include a temperature low enough to ignore thermal excitation across the barrier[46, 47]. Figure 1.10 is a representation of the Simmons model, and shows the electrode and barrier energies at equilibrium, as well as when a voltage bias is applied. Prediction of the *I-V* behaviour in the Simmons model approximates the complex energy barrier by a rectangular potential spanning the insulated gap between both electrodes.

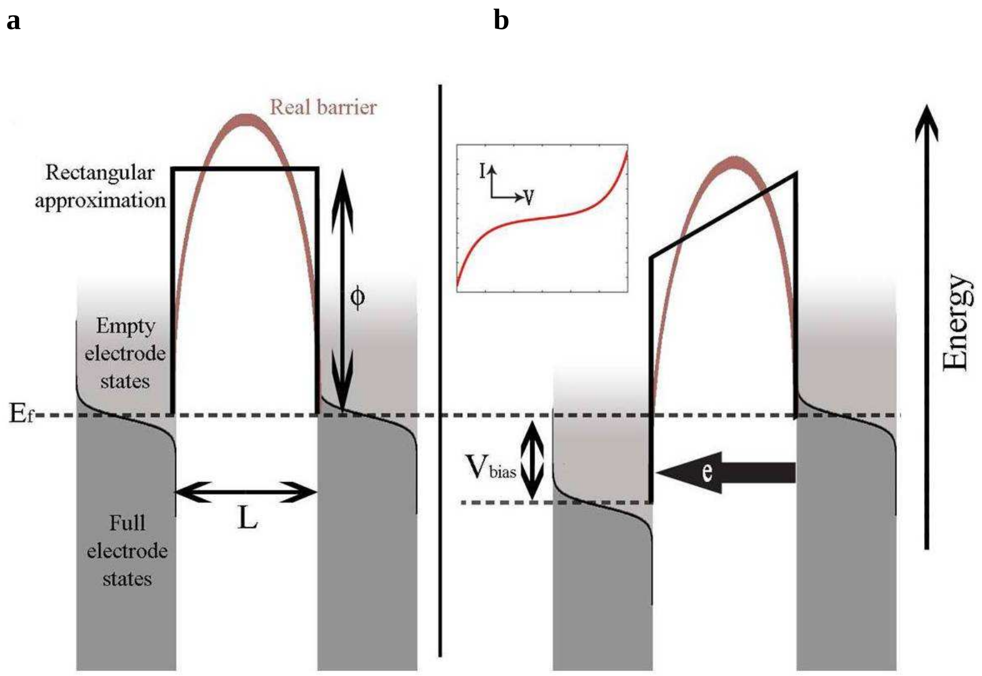

Figure 1.10: Schematic representation of tunnelling between two electrodes according to the Simmons model. The complex energy barrier is approximated here by a rectangular potential spanning the insulated gap between the electrodes (Thanks to Ben Peters for this representation). **a.**When no bias is applied: the Fermi levels of both electrodes have the same energy. **b.** When a voltage bias is applied: the Fermi energy of the positively biased electrode is shifted downwards. The electric field is assumed to drop linearly across the dielectric. Inset: Predicted sigmoidal dependence of current towards the applied voltage according to the Simmons model.

The theory assumes that electrons tunnelling through an insulator are confronted to three parameters: the energy barrier height ϕ (in volts), its length *L*, and an asymmetry factor α, which measures the different drops of potential occurring at tip and substrate levels. Depending on the voltage bias *V* applied across the electrodes, the formulation takes one of its possible forms:

- First, in the ‘low bias’ region near *V* = 0 the current density *i* is related to *V* by:

$$i = \frac{3e^2\sqrt{2m\phi}}{2h^2L} \mathrm{V} \exp[- (4\pi\sqrt{2m\phi} /\mathrm{h})\mathrm{L}]$$

where m is the electronic effective mass. This simplifies to $i = KV \exp(-\beta L)$, where K is a constant and β is the tunnelling decay constant, a measure of the penetrability of the barrier ($\beta \propto \sqrt{\phi}$). It can also be noted that near $V = 0$ the tunnelling current is linear with respect to V.

- Then, at 'medium voltages', defined as $V < \phi$, the current depends on the applied bias as:

$$i = \frac{e^2}{2\pi h L^2} \{(\phi - \alpha V) \exp[-K(\phi - \alpha V)^{1/2}] - (\phi + (1 - \alpha)V)^{1/2}]\}$$

where $$K = \frac{4\pi L}{h}(2me)^{1/2}$$

In the medium voltage regime the tunnelling current has a sigmoidal dependence on bias (Figure 10). This form of the model is often used to estimate ϕ, L and α in metal-molecule-metal junctions by fitting to the measured current-voltage curves.

1.4.2 Resonant tunnelling in mMm junctions

The Simmons model described above is used when the metal-insulator-metal system can be approximated by a featureless barrier between both electrodes. However, in practical (molecular) electronic, configurations of the electrons are affected in a more complex way than for direct tunnelling. For example, if a narrow potential well exists between the electrodes, electrons may tunnel in to it, reside for a finite amount of time in one of the allowed states, and subsequently tunnel out again. Switching and negative differential resistance (NDR) are the two most commonly observed phenomena in *I-V* spectroscopy. In switching, *I-V* spectra are characterized by a rapid increase in current at a certain applied bias before levelling out, while an NDR consists in an increase in current followed by a subsequent decrease in current while the applied bias is increasing.

Modulation of these phenomena is the centre of transistor-like configurations (resonant tunnelling devices – RTD), and also provides information regarding the tunnelling mechanism that is taking place.

1.4.2.a Resonance in molecular configurations

The main characteristic of semiconductor RTDs is the presence of an electronic state within the insulating dielectric barrier through which the electronic charge tunnels. RTDs are fabricated with very thin barrier layers, in order to provide an efficient tunnuelling into the well. Single redox molecules trapped in a metal-molecule-metal junction offer an analogue to semiconductor devices in that the redox centre is able to accept electrons of a certain energy. The electrons must tunnel distances of nanometres in length from an electrode, through the intervening insulating molecular matrix to the active centre, and out again. A significant number of molecular scale studies have now been made which demonstrate characteristics associated with resonant tunnelling. The exact nature of electronic behaviour on its course between the electrodes is the subject of some debate, and one of the key issues is that of residence on the molecular orbital, as to whether the molecule does get reduced. Electronic transport in mMm junctions can be divided into two categories. If the electron does not reduce the molecule and simply uses the molecular states as a pathway for efficient tunnelling, the transport is called ‘one-step’. Alternatively, if the molecular redox state becomes reduced, and is subsequently oxidized so that the complete transport between electrodes occurs, the situation is then labelled ‘two step’.

1.4.2.b Current-voltage (I-V) spectroscopy in resonant SPM configurations

As mentioned previously, the presence of a structure between the electrodes can lead to an electronic behaviour above the monotonic increase in the *I-V* spectra obtained for a featureless barrier. Regarding *I-V* spectroscopy performed on mMm junctions using C-AFM, the bias at which one expects to see spectroscopic features depends on two things, the energy of the molecular states relative to the Fermi levels of the electrodes, and the energy of any peaks in the electrode density of states. Since there is no absolute potential control in the C-AFM setup, the energy of the molecular states is fixed relative to the tip and substrate and the bias position of spectroscopic features is also expected to be fixed.

1.5 Aims of the thesis

The work presented in this thesis investigates the use of scanning probe microscopy techniques (SPMs, described in Chapter II), together with numerous biophysical and electrochemical methods, to study two 7 TM domain proteins at the single molecule scale. Scanning probe microscopes use a sharp probe that is raster-scanned over the sample under constant feedback and, depending on the microscope, provide information on the topography, surface potential, current or magnetic field of the sample. Atomic resolution can be obtained on solid surfaces, making SPM techniques valuable tools in material sciences. SPM experiments can be performed in air or liquid environment and do not require any prior treatment of the sample, such as coating or staining and are thus of big interest for studying biological samples.

SPMs have first been used here for studying the electronic properties of the light-sensitive retinal-bond archae proton pump bacteriorhodopsin (BR). The protein, described in Chapter III, has unique physical and chemical properties that make it an attractive material for developing molecular devices. All previous studies, to the best of our knowledge, have only been performed on the protein embedded within the membrane. Here, partial delipidation of BR coupled to a unique and strategically located mutation (“BR_{cys}”) are expected to provide a facile, robust and oriented adsorption of the protein on gold electrodes. The work presented in chapter III focuses on surface characterisation and has for objectives to:

- ascertain the best protein deposition technique on gold so as to maximise surface coverage (AFM and KFM imaging)
- determine the anchoring role of the mutation, compared to wild-type BR (SPR, electrochemistry: reductive stripping voltammetry)
- confirm the homogenous orientation of isolated trimers of BR_{cys} on the gold electrode (photocurrent)

The next step consists in measuring the electronic properties of the protein, and in particular, in attempting to detect for isolated trimers of BR_{cys}, the shift of conductance upon illumination that has been previously reported for BR embedded within the membrane. The work presented in chapter IV thus had for objectives to:

- measure the current detected for gold-BR_{cys}-gold molecular junctions upon successive illuminations, towards an applied bias (C-AFM)
- assess the wavelength-specificity of the phenomenon (C-AFM, KFM surface potential measurements, photocurrent)
- ascertain the crucial role of the retinal chromophore in the photon-induced response of BR.

Scanning probe microscopy techniques also offer the possibility to make force measurements. This function can be used, for example in the case of biological samples for protein unfolding or measuring protein-ligand interactions. Chapter V presents another 7 TM domain protein, the neurotensin receptor type 1 (NTS1). The peptide-ligand of NTS1, neurotensin, is a brain and gastrointestinal peptide acting as a neurotransmitter in the central nervous system and a hormone in the periphery, and involved in a wide range of diseases such as colon cancer or Alzheimer’s disease. The aim of this project was to prepare NTS1 samples for future ligand-receptor interaction measurements, and consisted in the purification of NTS1 expressed in *E.coli* and its reconstitution into 100 nm brain polar lipid (BPL) liposomes. Initial AFM imaging characterisation of the liposomes prior and following NTS1 reconstitution was performed as a prelude for ligand-receptor interaction studies, including high resolution imaging, force spectroscopy and solid state NMR approaches, with the ultimate goal of new ligand design.

Chapter II – Experimental details

2.1 Introduction

In this chapter the various instruments, methods and techniques used to acquire the data presented in Chapters III to V will be outlined. The most fundamental techniques to this thesis are the scanning probe microscopes (SPM)-based methods, and relevant sample and probe preparation methods will be detailed. Additional surface characterization techniques such as SPR, ellipsometry and cyclic voltammetry will also be described. The final section of the chapter will give an outline of the programming that was used to analyze data.

2.2 Scanning probe microscopes

Scanning probe microscopes were first developed in 1981 at the IBM laboratories in Switzerland by G.Binning and W. Rohrer, who were awarded the Nobel Prize in 1986. The basic principle consists in obtaining topographical, electronical or potential information about a sample by scanning a sharp tip over the specimen surface under a piezoelectrical feedback loop (Figures 2.1 and 2.3). SPM techniques have become invaluable tools for surfaces characterisation due to their very high resolving power (Angström resolution in the lateral and vertical directions is achievable for solid surfaces), and to the possibility to image the sample surface while measuring its physical properties. Indeed, one can measure parameters such as the surface conductivity, static charges distribution, local interactions, elastic moduli or magnetic fields, at the same time as topography images are acquired. SPM techniques are thus used extensively in engineering as well as for physical, chemical and biological studies, and played a significant role in the recent rise of nanotechnology. They are of particular interest for studying biological samples, indeed, as studies can be carried out in solution, under physiological conditions, under flexible, controllable conditions and do not require any prior treatment of the sample such as coating or staining. Among numerous applications, SPM has been extensively used for the characterisation of bioelectronic interfaces[48-50], the study of membrane proteins[51-56] and protein-protein interactions[55, 57-61]. Since the first SPM developed by Binning and Rohrer, several variants of the technique have since been developed and now allow the characterisation of numerous physical and electrical properties of the sample (Table 2.1).

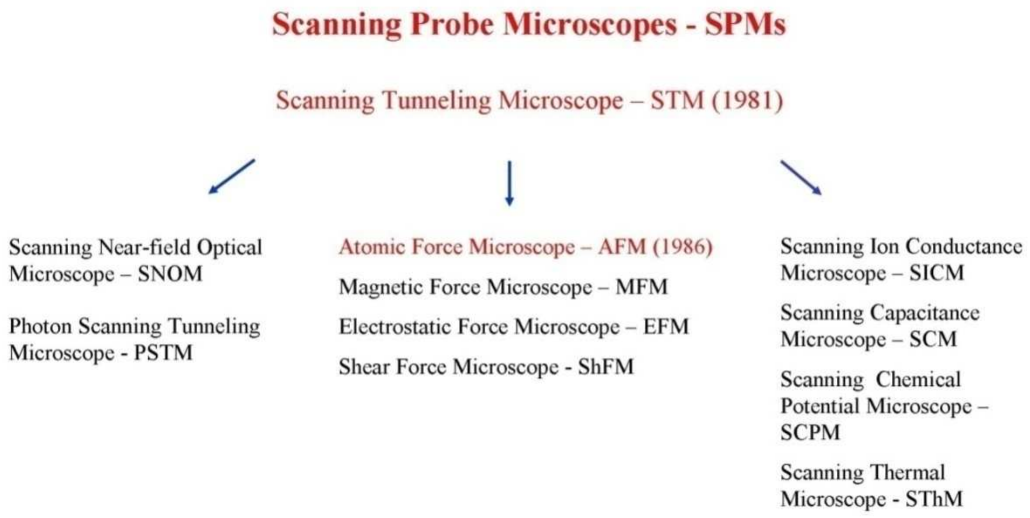

Scanning Probe Microscopes - SPMs

Scanning Tunneling Microscope – STM (1981)

Scanning Near-field Optical Microscope – SNOM

Photon Scanning Tunneling Microscope - PSTM

Atomic Force Microscope – AFM (1986)

Magnetic Force Microscope – MFM

Electrostatic Force Microscope – EFM

Shear Force Microscope - ShFM

Scanning Ion Conductance Microscope – SICM

Scanning Capacitance Microscope – SCM

Scanning Chemical Potential Microscope – SCPM

Scanning Thermal Microscope - SThM

Table 2.1: The scanning probe microscopes family.

2.2.1 STM

Scanning tunnelling microscopy (STM) was the first technology commercially available amongst all scanning probe techniques, in 1984. For the first time, it was possible to image individual atoms of a surface; indeed, a lateral resolution of about 1Å and a vertical resolution of up to 0.01nm can be achieved. The basic principle consists in bringing a sharp metallic tip (Figure 2.1) in close proximity (a few Å) to a conductive sample, and measuring the electric current (0.01nA-100nA) flowing between the tip and the substrate when a voltage bias is applied. Current can flow from the STM probe to the sample although the probe is not in physical contact with the specimen: this phenomenon is called electron tunneling**.** The tunneling current observed is exponentially dependent on the tip-to-sample distance, providing a high vertical resolution. By scanning the probe across the surface, a map of the sample current can be generated with a resolution in the order of atomic distances.

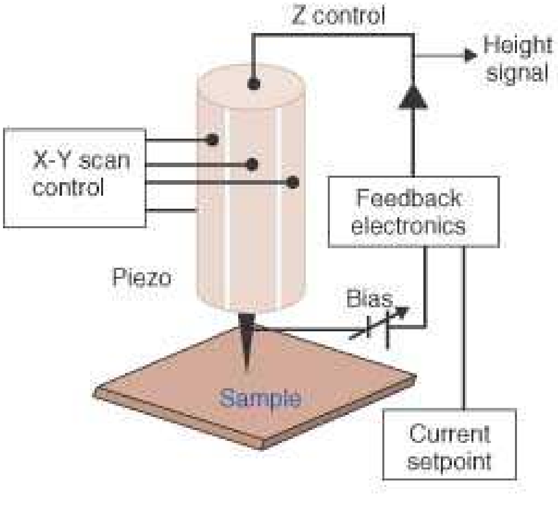

Figure 2.1: Schematic representation of the principle of an STM. A sharp metallic probe is brought in close proximity (a few Å) of a sample and detects the topographical and/or electronic properties of the sample. Unlike some other SPMs, the STM probe never gets in contact with the sample (adapted from[62]).

An STM image cannot be interpreted as a topographic map of the sample since the tunneling current is influenced by the lateral and vertical variation of the electronic state density of the surface: an STM image is an image of the sample's charge density. STM can be used in ultra high vacuum, air or liquid environments. The technique was briefly used in this thesis for imaging the photosensitive protein bacteriorhodopsin adsorbed on gold (Chapter III) prior measurement of its electronic characteristics (Chapter IV).

While STM has the advantage of providing extremely high resolution data, it is restricted to conductive samples and is, therefore, not applicable to insulating surfaces such as biological specimen. Following the invention of STM, Binnig and Quate, joined by Gerber[63], developed a related system, the atomic force microscope (AFM), in order to overcome this issue. Instead of monitoring a tunnelling current, AFM works by detecting the z-motion of a microfabricated cantilever-mounted stylus brought in contact with the sample, as described in details below. Other scanning probe microscopes variants include the Kelvin-probe AFM (KFM), for measuring surface potentials, and scanning electrochemical microscopy (SEM), for mapping a surface electrochemical activity. In addition to these variants, SPMs can be coupled to other analysis tools, such as fluorescent microscopy, electrochemistry or surface plasmon resonance[64, 65]. In this thesis, scanning probes techniques are used as surface analysis tools, but predominantly as an integral part of molecular junctions construction, where both the probe and the gold substrate act as electrodes sensing the molecular species trapped in between. Such metal-molecule-metal (mMm) junctions present the advantage of being well defined, with a high level of external control achievable over them through the feedback loop of the microscope. These specificities make them invaluable tools for the reliable characterisation of molecular properties, and demonstrate that molecular devices are practically feasible. Chapters III and IV of this thesis focus on the creation and the characterisation of mMm junctions between the light-sensitive archae proton pump bacteriorhodopsin, and the gold probe and substrate of a conducting-probe atomic force microscope (C-AFM).

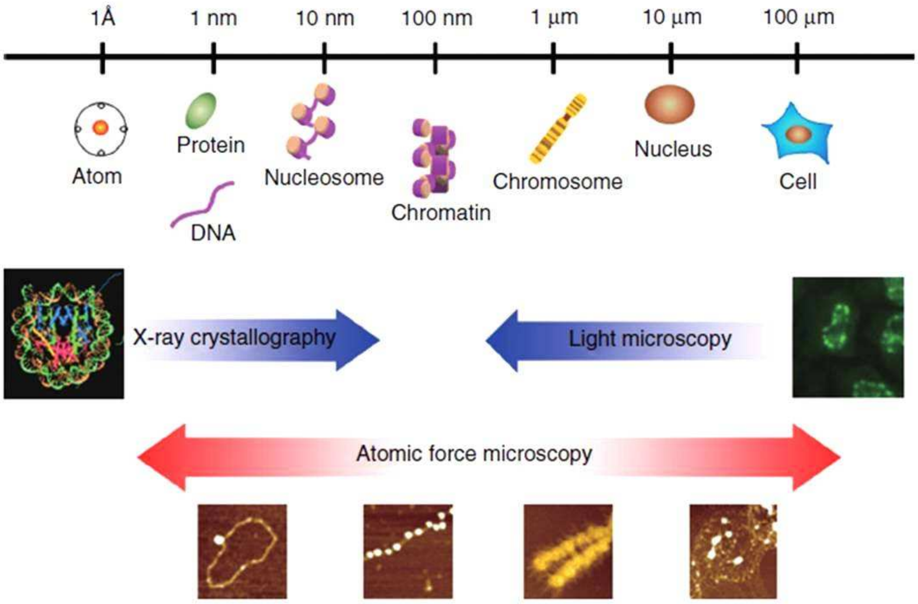

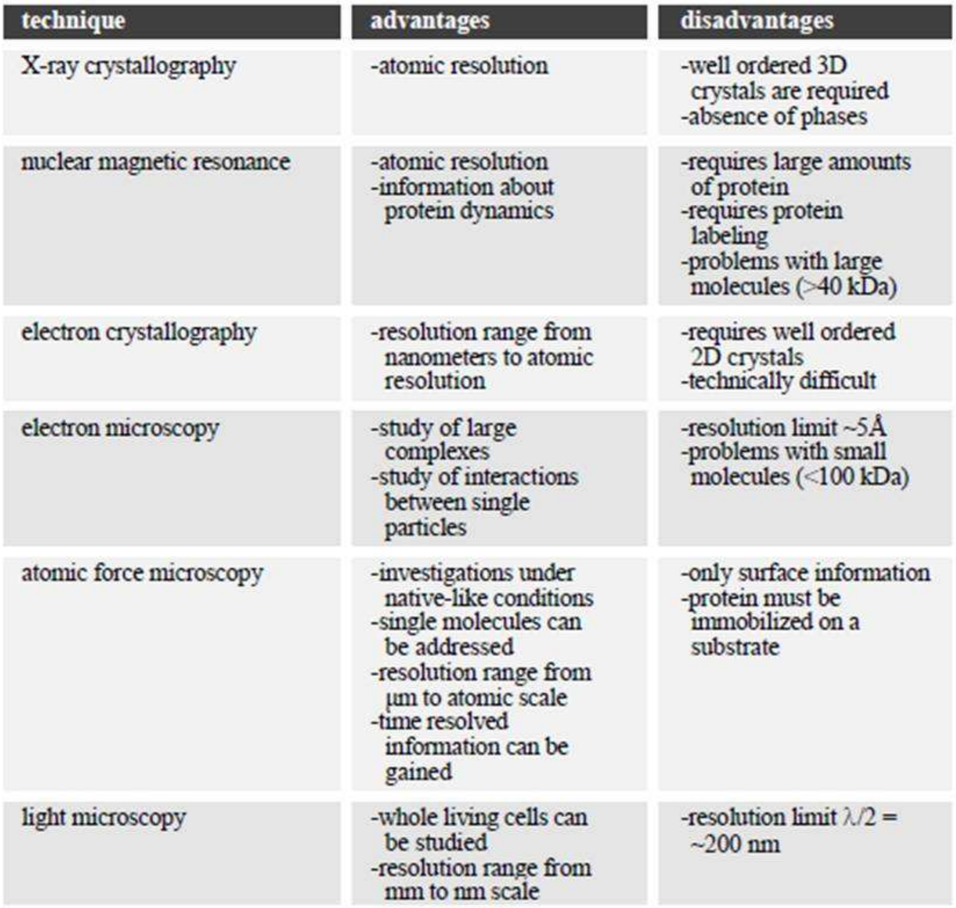

technique	advantages	disadvantages
X-ray crystallography	-atomic resolution	-well ordered 3D crystals are required -absence of phases
nuclear magnetic resonance	-atomic resolution -information about protein dynamics	-requires large amounts of protein -requires protein labeling -problems with large molecules (>40 kDa)
electron crystallography	-resolution range from nanometers to atomic resolution	-requires well ordered 2D crystals -technically difficult
electron microscopy	-study of large complexes -study of interactions between single particles	-resolution limit ~5Å -problems with small molecules (<100 kDa)
atomic force microscopy	-investigations under native-like conditions -single molecules can be addressed -resolution range from µm to atomic scale -time resolved information can be gained	-only surface information -protein must be immobilized on a substrate
light microscopy	-whole living cells can be studied -resolution range from mm to nm scale	-resolution limit $\lambda/2$ = ~200 nm

Figure 2.2: **Comparison of the AFM properties with those of other major techniques** (adapted from[66, 67]).

2.2.2 Atomic force microscope

As mentioned above, AFM has been developed in order to overcome the main issue of the scanning tunnelling microscope, which can only be used on conducting specimen. Though both techniques are very similar, their major differences will be highlighted here. In AFM, the probe is located at the end of a flexible cantilever. The basic principle is that the local attractive or repulsive forces established between the tip and the sample result in the bending (deflection) of the cantilever towards or away from the surface (Figure 2.3). A laser beam is focused on the back of the cantilever and is reflected on a mirror and then onto a photodiode detector. When scanning the sample surface, any small bending of the cantilever results in a different reflected angle of the laser beam, which is thus reflected on a different part of the detector.

The photodiode is made of four quadrants (Figure 2.3), allowing the position of the laser to be determined in two directions. Comparison of the signals obtained from the top and bottom halves of the photodiode provides data about the vertical deflection of the cantilever, which corresponds to the interaction forces. Lateral displacements of the cantilever are analysed by comparing the left and right halves of the photodiode. The laser alignment at the centre of the detector (“0” position) before starting an SPM experiment is a crucial step in order to obtain reliable results. Indeed, the laser position on the photodiode before starting an SPM scan is used as the position of reference by the microscope controller to process all laser deviations occurring during a scan; a misaligned laser would result in blur images or noisy spectra.

During operation, the sharp tip is brought in contact with the substrate and raster-scanned over a small area of the surface in the “x-y” plane by a scanner made of piezoelectric ceramic. The piezo material changes its geometry when a voltage is applied: it can expand or retract, in a controlled manner, depending on the polarity of the applied bias.

The maximum scan size varies according to the model of piezo but is generally about 100 µm (1024 data points per line, +220 V to -220 V).

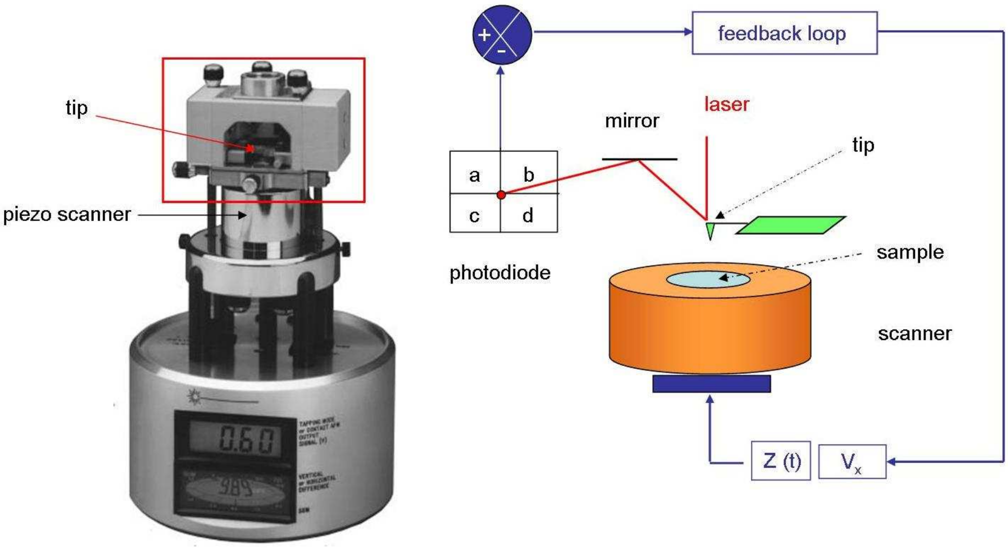

Figure 2.3: Principle of an atomic force microscope (AFM). The sample is scanned by a tip located on a flexible cantilever on which a laser beam is directed. Every feature of the specimen detected by the tip results in a deviation of the laser beam reflected by a mirror onto a photoreceptor, and is recorded and processed to provide images of the sample surface. During an experiment, the tip-to-sample distance is adjusted by a feedback loop that prevents from damaging the sample and the tip. The picture shows a Multimode AFM by Veeco (Bruker).

Additional piezoelectric crystals in the "z" direction, known as the z-piezo, controls the tip-to-sample distance and is connected to a feedback loop (the precise control of the probe position in the x, y, z directions make 3D imaging possible). This feedback loop attempts to maintain a constant interaction force between the probe and the substrate, called the "setpoint". If the tip-sample interactions become lower than the setpoint, the system will act to adjust the tip position closer to the surface, and vice-versa for tip-sample interactions that become higher than the setpoint.

Cantilevers with spring constants ranging from 0.005 to 40 N/m are commercially available, allowing most samples, stiff and smooth, to be imaged. In AFM, like in all scanning probe techniques, samples can be studied in solution, under native conditions, and over a wide range of temperature. Its particularly high signal to noise ratio and nanometre scale control, coupled with its ability to image, measure and manipulate samples to provide 3D representations of surfaces, make it an ideal tool for probing biological structures.

High resolution imaging can thus be obtained for living cells[64] or plasma membrane[68, 69], as well as for single molecules such as proteins[70-74] or DNA[75]. The microscope's detection sensitivity of forces in the pN range makes it a reliable tool for measuring mechanical properties such as molecular interactions via dynamic force spectroscopy[76].

2.2.2.a AFM imaging modes

AFM imaging can be performed in three major modes, each varying by the type and duration of the probe-sample contact (contact, intermittent contact, non-contact). Many secondary modes have been derived from the major ones (conducting AFM, force modulation imaging, scanning thermal microscopy, etc…) but only contact and intermittent contact imaging modes, as well as conducting AFM, which have been used here, are presented below.

2.2.2.a.i Contact mode imaging

In contact mode AFM imaging, the probe is constantly in contact with the sample while scanning its surface, which provides data with the highest resolution. This is the typical mode where the piezo determines the nanopositioning of the probe according to the deflection of the cantilever. Cantilever used in contact mode are usually soft cantilever, with spring constants inferior to 0.5 N/m and resonant frequency values of about 8-12 kHz. Vertical deflection of the cantilever is monitored, so the compression of the sample is limited. However, although a feedback is constantly applied, this mode increases the risk of damaging the sample and/or contaminating the tip apex due to the lateral forces applied as the tip moves across the surface.

2.2.2.a.ii Intermittent-contact (“tapping-modeTM”) imaging

Another way of imaging soft and fragile samples while reducing the risk of damaging both the specimen and the probe, is to scan the surface intermittently, with an oscillating tip. The lateral forces are then much lower and enable AFM imaging to be performed on samples that are not tightly adsorbed on the substrate, without displacing them during the scan. This mode is called “intermittent contact”, also known as “tapping mode^{TM}”, a trademark of Veeco. In intermittent mode, the tip is not in contact with the surface for most of the oscillation cycle.

It is possible, by applying an alternating voltage to the piezo, to drive the cantilever frequency close to its resonant frequency, and to engage the surface with the vibrating tip. Here, instead of measuring the tip-surface interactions by the tip offset (which is now impossible as the tip is vibrating), motion in the z direction is regulated from the amplitude oscillation of the probe. When approaching the sample, at the beginning of an experiment, the tip is allowed to vibrate freely until it interacts with the surface. Then, the amplitude is reduced by a combination of energy dissipation and a shift in the cantilever power spectrum[77] (the need to detect this shift is the reason for driving *near* and not *at* the cantilever resonant frequency, so that any significant change in the amplitude can be observed). An amplitude setpoint is thus set and kept constant by the z feedback loop. Stiffer cantilevers are generally used for intermittent mode imaging, especially in air and usually have spring constants higher than 10N/m and resonant frequencies ranging from 200 to 400 kHz.

During an AFM experiment in intermittent contact mode, the cantilever is driven at a specific resonance frequency: depending on the imaging conditions, there will be some phase shift between the drive amplitude (applied to the piezos) and the lock-in amplitude (measured from the detector). Most contributions to this phase shift are independent of the sample position and will not change over a scanned image.

The part of the phase shift that is due to the tip-sample interaction can show contrast between parts of the sample. This phase shift can be measured and displayed in a "phase image"; the height and phase images are collected simultaneously In some cases, and in particular for flat samples, the phase acquisition provides details about the sample that were not detected in the height image (Figure 2.4).

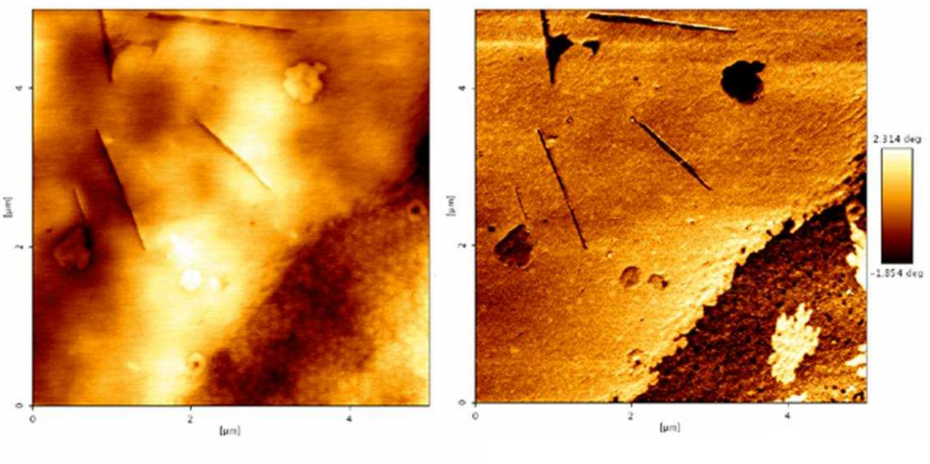

height image

phase image

Figure 2.4: AFM height and phase images of a same sample obtained in tapping mode; during a same scan, different features of the sample can be highlighted by different types of imaging (adapted from JPK Nanowizard handbook v.2.2).

2.2.2.b AFM imaging constraints

The major factor determining AFM imaging resolution is the size and shape of the tip. AFM probes are usually made from silicon or silicon nitride, using a batch etching process. The radius of curvature of the end of the tip will determine the highest lateral resolution obtainable with a specific tip. If the tip dimensions are close to or larger than the sample features being imaged, then the topography image obtained will be highly influenced by the tip geometry. In such cases, the features will appear larger than their real physical size, a phenomenon called “probe broadening” (Figure 15). When imaging large samples such as live cells, probe broadening is generally not an issue since a typical tip radius of curvature lies between 10-20 nm, or higher when a coating is applied to the tip. The tip geometry becomes a limiting factor when attempting to image individual organic or bio-molecules, or atomic structures in very high resolution studies.

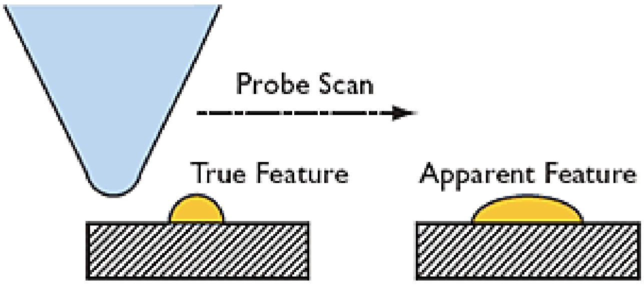

Figure 2.5: schematic illustration of the probe broadening phenomenon. The typical radius of curvature of an AFM probe lies between 10-20 nm, decreased down to 2 nm for high resolution probes. If the tip is wider than the sample features being imaged, these will appear larger than their real physical size, a phenomenon called “probe broadening”.

SPM probes are, by nature, dynamic systems. In addition to any deliberate scanning by the x-y piezo, there will be a mechanical drift as the system relaxes into equilibrium, a phenomenon that can be directly observed as lateral “streaking” in images acquired shortly after experimental set up. Leaving the system for some time, so it reaches equilibrium, greatly improves the results although drift can rarely be totally cancelled, particularly when working at room temperature.

The ideal AFM probe would be long, in order to enable measurements of high features, and of close-to-zero radius of curvature (i.e. have a quasi-infinite aspect ratio). Silicon, “super sharp” tips having a typical radius decreased down to < 2 nm (5 nm guaranteed) are commercially available and allow high resolution imaging to be performed. However, such probes are fragile and the process of scanning the surface while imaging will lead to blunting and/or fouling of the apex happening quicker than for casual probes. The effective radius of curvature will thus progressively increase over the experiment, limiting the imaging time performed at the highest resolution. Sharper tips can also be obtained by modifying the probes with carbon nanotubes[78, 79].

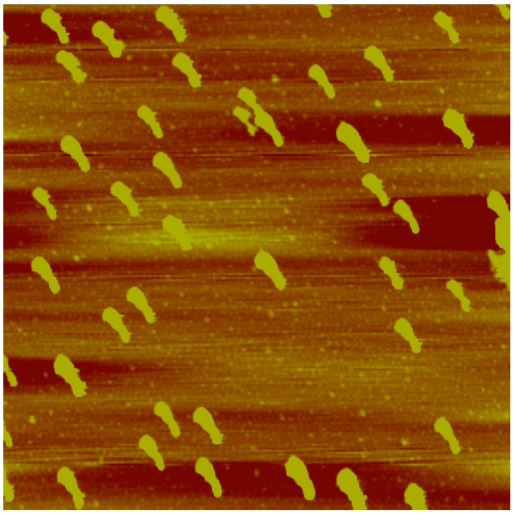

Figure 2.6: **Example of AFM imaging constraints, showing probe contamination**. When the tip has caught a contaminant, either from the ambient air or a (nm-wide) piece of sample, a same feature can be typically observed all over the image. When the imaging environment has high level of ambient vibrations, blur parts appear on the image, just a the sample location that the probe was scanning when the noise occurred. Stopping the source of vibrations (people stopping talking for example) results in an immediate return to good quality imaging.

Another major constraint when using AFM, and all scanning probe techniques in general, is the equipment environment: good vibration isolation is always required for SPM experiments. Any loud noise or moving air will cause vibration, so the equipment should be placed in a quiet room with few passing people, and away from doors and windows.

2.2.2.c AFM Force spectroscopy

AFM can be used in imaging mode and provide topographical, electrical or potential information about the surface, but it can also be used for force measurements (AFM force spectroscopy), with a detection sensitivity lying within the pN range of interactions.

In this work, AFM force spectroscopy is used to determine the load applied to the sample during contact mode investigations (Chapters III and IV), but in advanced applications, the technique is used to detect and characterize biological events such as protein folding[80-82] or molecular recognition[55, 83-87]. Chapter V presents the reconstitution into liposomes of a membrane protein, the neurotensin receptor 1, whose interactions with the neurotensin peptide are planned to be ultimately studied using AFM force spectroscopy.

Unlike AFM imaging, which consists in scanning the surface to collect information about the sample, AFM force spectroscopy is performed locally. Here, the probe is gradually moved towards the sample by the z piezo until it contacts the surface, and is then vertically pulled back until there is no tip-sample interaction anymore. The tip approach and withdrawal are major steps in the process and can have a great impact on the results, they are thus precisely monitored. The speed and applied load at which the probe enters in contact with the sample is called the « loading rate » and is one of the most important parameters in force spectroscopy.

Force measurements in AFM are obtained as force plots, or force spectra. An AFM force spectrum is a plot of the deflection of the cantilever against z distance (Figure 2.7). It should be read from left (tip approaching the surface) to right (retracting stage):

- during the approach process, the probe is far from the surface and does not interact with it: there is no deflection of the cantilever and the force spectrum is thus flat (point 1 on Figure 2.7).
- when the probe is close enough from the sample, attractive Van der Waals interactions occur: probe-sample contact is established (2).
- probe-sample contact results in the tip exerting a pressure on the surface, and thus in the deflection of the tip cantilever. This is shown in the force spectrum as a linear increase in tip z position until it reaches a preliminarily determined deflection threshold, or setpoint (3).

- the tip is then progressively retracted, resulting in a decrease of the cantilever deflection, which comes back to an horizontal position (4).

- If no other interactions occurred, the probe is fully retracted and the cantilever comes back to its initial position (Figure 2.7.1 and 2.8. a.).

- However, when retracting the tip under ambient conditions, a water meniscus is commonly formed between the probe and the surface[88]. The meniscus exerts attractive forces on the probe while it is being retracted: negative values of the deflection are observed, showing the cantilever bends (4 to 5) until the probe withdrawal pulling forces overcome the interactions, resulting in sudden loss of contact (5) and a return of the cantilever to its initial position (1).

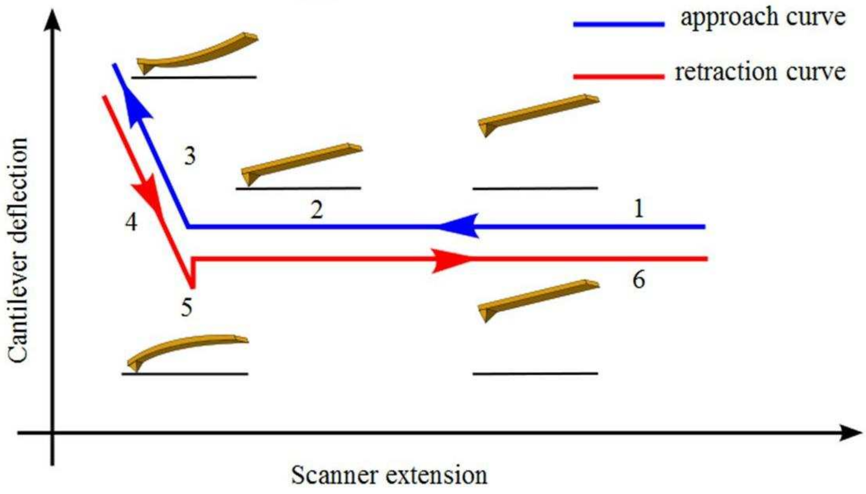

Figure 2.7: Schematic representation of an AFM force spectrum. The spectrum plots the cantilever deflection against z distance upon probe approach towards the surface, probe-sample interaction and probe retraction, and should be read from left to right. The different steps are detailed in the main text. This figure is freely available at http://www.freesbi.ch/en/illustration/.

Similar force spectra are observed when measuring protein unfolding or intermolecular interactions. In the case of ligand-receptor interactions, for example, the receptor is adsorbed on the surface while the ligand is bound to the tip, or vice versa. When the tip-substrate contact occurs, it is likely that one, if not several, ligand-receptor bond is created. Force spectra resulting from the breaking of one single interaction will show one negative deflection peak, as described earlier (Figure 2.7). When several ligand-receptor bonds are formed and then broken, successive rupture events are detected as successive negative peaks on the force spectra (Fig 2.8.b.).

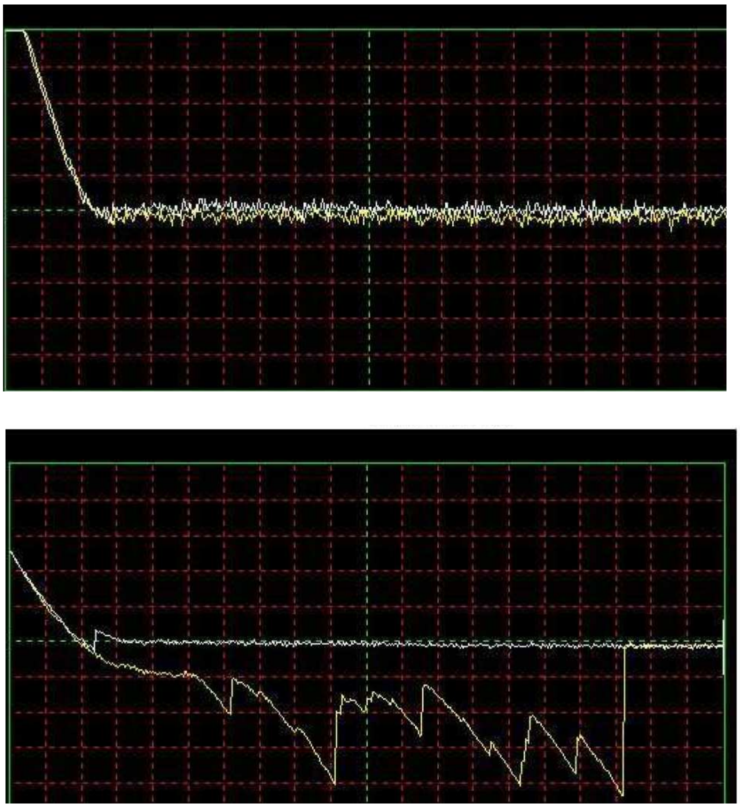

Figure 2.8. Example of AFM force spectra obtained for antibody-antigen interaction measurements when no interaction (top) or multiple interactions (left) are detected between the antibody-coated probe and antigen-coated sample[89].

Regarding the meniscus force, it can be reduced by drying the atmosphere with an inert gas and/or dessicant, or by performing AFM under fluidic conditions that completely eliminate the meniscus effect with the added benefit of providing a more physiological environment for biological specimens.

AFM force spectroscopy will be used for studying the ligand-receptor interactions of the neurotensin receptor 1 (NTS1) with the neurotensin peptide (Chapter V).

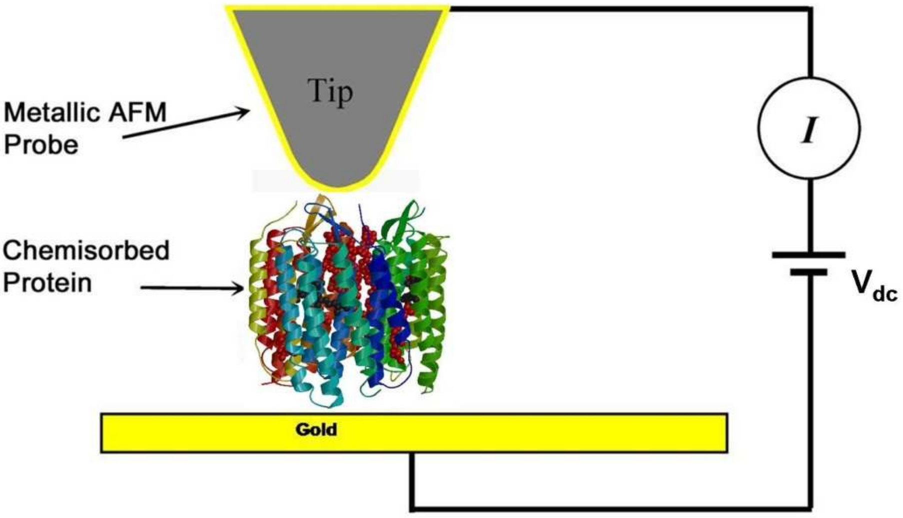

Figure 2.9: Principle of the conducting-probe AFM (C-AFM) The sample is adsorbed on a gold substrate; the tip is conductive (gold-coated)**.** A bias is applied to the tip, and the substrate is held at ground potential. Current passing between the tip and sample is measured.

2.2.3 Conducting-probe atomic force microscopy

Conductive atomic force microscopy (C-AFM or CP-AFM) is a secondary mode derived from contact AFM that characterizes conductivity variations across medium- to low-conducting and semiconducting materials[90]. C-AFM employs a conductive probe tip and has a current range of pA to μA. During operation, a DC bias is applied to the tip and the sample is held at ground potential (Figure 2.9). While the Z feedback signal is used to generate a traditional contact AFM topography image, the current passing between the tip and sample is measured. C-AFM is also used to characterise molecular electrical properties through its current-voltage (*I-V*) spectroscopy function. In this thesis, the technique has been mainly for detecting the current running through gold-bacteriorhodopsin-gold junctions as a function of illumination, under an applied bias.

2.2.4 Kelvin Probe Force Microscope (KFM)

Kelvin probe force microscopy (KPFM or KFM) is a minimally invasive SPM variant that is used to map dynamically a sample's topography and its electric potential with high spatial (nm) and electric (few mV) resolution[91, 92]. KFM has been used on a variety of interfaces, such as semiconductor surfaces[93, 94], solid state transistors[95, 96], redox active monolayers[92], immobilised DNA strands[97, 98] and photoactive membranes[99], although little has been reported regarding spatial resolution at the molecular scale.

After the invention of the atomic force microscope by Binnig and Quate in 1986[63], Nonnenmacher *et al.* applied the Kelvin method using an AFM to detect surface potentials in 1991[100]. The general principle of KPFM imaging is very similar to that of AFM in non-contact mode, the main difference being that probe is coated in a layer of thin conductive metal, in this case gold, and the tip holder is modified so that it is electrically grounded. During operation, the probe is excited by an electrical AC voltage at the cantilever resonnance and a DC offset, in addition of being excited at its resonnant frequency. The surface is then analysed using a two-pass technique, known as Lift Mode, in which each line of the sample is scanned twice: the first time for measuring the topographical data, the second time to measure the surface potential. Before the second scan the tip is lifted a predefined distance above the surface, so that the topographic features of the sample do not affect the potential measurements. As the tip travels over the surface for the second scan, it experiences a force wherever its potential is different to that of the sample. A feedback then adjusts the DC offset applied to the tip until the potential difference between it and the sample is nullified.

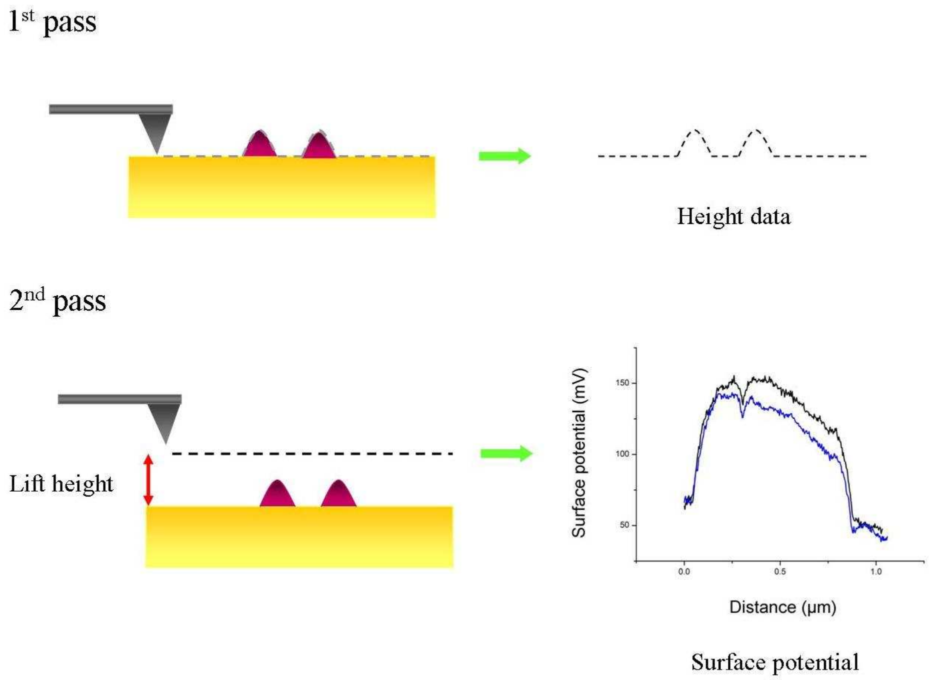

Figure 2.10: Schematic representation of the KFM-Lift Mode technique used to image the potential surface of a sample. The KFM probe is conducting, the substrate is gold substrate on mica. The first pass, in intermittent contact mode, provides topographical data of the surface. The tip is then lifted a predetermined height before performing a second pass to map the surface potential.

A potential map of the surface can then be obtained by plotting the offset value at each (x,y) point. Previous applications of KPFM have involved the study of surface potentials of various samples including inorganic[101] and organic thin films[102] as well as protein layers[98, 103]. It has also been reported that the KPFM is a viable technique for mapping photocharge density variations in donor-acceptor blends at surfaces[104, 105], as well as providing direct measurements of potential drops for different source and gate voltages[95, 106]. In this thesis, KFM was used for bacteriorhodopsin studies (Chapter IV),

2.2.5 Investigating mMm junctions by SPM

2.2.5.a Methods of contact

Whether scanning probe techniques are used for imaging or for spectroscopy there will be some junctions formed between the probe and the substrate. The tip and substrate provide two electrodes, and the question remains on the nature of the contact established when approaching the molecules adsorbed on the surface.

Spectroscopic studies where the probe is required to remain static, like in C-AFM for example, are best performed on target molecules densely packed on the surface. Indeed, if the tip drifts during the experiment, it will then move to another molecule of interest, continuing to record data of interest, rather than to bare substrate. A further consideration with direct probe-sample contact is that there can be variation in electronic behaviour between tips. Such variations can be detected by performing simple controls after experimental set up, allowing any bad probe to be discarded. Direct measurement of molecular electronics has been successfully applied to numerous organic[107] and biomolecular systems[108].

Another method for studying a mMm junction by SPM is to covalently couple the target molecule to a conductive intermediate, such as gold nanoparticles, and to probe this with the tip. This is supposed to abolish the tip variability and allows an easy visualisation of the sample repartition on the surface. However, non-specific adsorption of the nanoparticles may occur, and the protective monolayer usually coating the nanoparticles become part of the junction and add to the junction resistance.

A last alternative for contact consists in modifying the probe with the molecule of interest, and in engaging the ensemble on a bare conducting substrate. Although meaningful results can be obtained, the method relies on the target molecule adsorption on the very apex of the probe, which is a stochastic and poorly controlled process.

Moreover, characterisation of the tip-sample coupling is far more complex than imaging the coverage of the substrate. The use of this technique has been reported in the literature, and successful applications include, for example, the electronic examination of the blue copper protein azurin[109]. It has been briefly used in this thesis in *I-V* spectroscopy of isolated trimers of bacteriorhodopsin (Chapter IV), but the direct measurement of molecular electronic characteristics was preferably performed using a direct contact between the probe and the protein adsorbed on the substrate.

Once the mMm junction has been formed, the next factor to consider is how the junction electronics will be characterized. SPM comprise three main techniques for determining current switching or modulation in junction characteristics: STM apparent height modulation and *I-V* spectroscopy, which can be applied to any molecular specimen, and IE spectroscopy, which is related to *I-V* spectroscopy and is used for characterising redox-active systems. *I-V* spectroscopy will be briefly outlined here and will be developed in details in chapter IV.

2.2.5.b STM apparent height modulation

Alteration of the sample conductance due to variation in its local environment will be detected as a change in the specimen measured height by STM imaging. Indeed, a change in topographic height or a change in the tunnelling efficiency across the tip-substrate gap will lead to a variation in STM tunnelling current. Therefore, an increase in the sample molecular conductance will result in a larger measured height, and reciprocally when a decrease of conductance is observed. STM apparent height modulation has been used, amongst other work, to show the conductance modulation under applied voltage of a redox-active molecular hot wire. In this thesis, STM imaging only has been used to image the adsorption of isolated trimers of bacteriorhodopsin on gold prior measuring their conductance behaviour by *I-V* spectroscopy upon illumination (Chapter IV).

2.2.5. c *I-V* spectroscopy

I-V spectroscopy consists in measuring the current resulting from the sweep of a voltage bias between the probe and the substrate. It takes into account the effects of high and low inter-electrode fields, pointing in opposite directions across the gap at positive and negative biases, and thus gives a global view of the behaviour of the junction. However, sweeping the bias can lead to unwanted charge build-up, particularly if the electron transfer probability is low or if experiments are performed in an ionic environment (such as buffer). In some cases, it may thus be necessary to apply high voltages in order to observe events of interest, and this could alter the structure of the molecule or the nature of the probe-sample contact (reduction of the Au-S bond linking the sample to the substrate, for example). In this thesis *I-V* spectroscopy, performed via C-AFM, has been successfully used to demonstrate the reversible switching of the electronic conductance of bacteriorhodopsin upon illumination (Chapter IV).

2.3 Non-SPM characterisation techniques

2.3.1 UV-vis absorption spectroscopy

UV-vis spectroscopy consists in measuring the intensity of absorbance of a sample as a function of a wavelength comprised in the near-ultraviolet to visible light ($200 < \lambda < 800$ nm) spectrum. The technique is used for the quantitative determination of analytes such as biological macromolecules, for example, and has a wide range of applications. It used in used here for following the growth of cell cultures by measuring the variation of absorbance of the culture medium, and for during the delipidation process of a membrane protein (Chapters III and IV) . The technique is generally performed for samples in solution, but can be adapted to transparent substrates, as presented in Chapter III.

2.3.2 Ellipsometry

Ellipsometry is an optical technique that is used to measure the thicknesses of thin films. Plane-polarized light is reflected non-normally from a surface covered with a thin film (Figure 2.11). The reflected light is elliptically polarized, and the difference between the elliptical polarization parameters of a blank and a film-coated substrate can be used to calculate film thickness from the Fresnel equations, providing a film dielectric constant can be assumed[110].

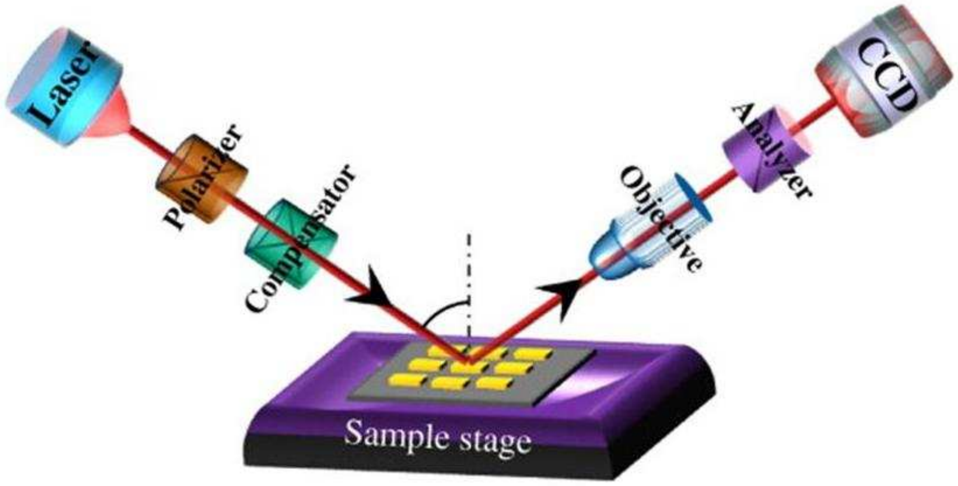

Figure 2.11: Principle of ellipsometry. The technique consists in analysing the change of polarization of light, which is reflected off a sample. Ellipsometry can yield information about layers that are thinner than the wavelength of the probing light itself, even down to a single atomic layer (adapted from[111]).

Ellipsometry is used here to determine the thicknesses of bacteriorhodopsin samples adsorbed onto gold and support SPR and imaging-derived coverage estimations (Chapter III).

2.2.3 Surface plasmon resonance

Surface plasmon resonance (SPR) is an optical technique used to measure the adsorption of molecules onto a metallic surface. SPR system detects changes in the refractive index of the surface layer of a sample solution in contact with the sensor chip. At the interface between two transparent media of different refractive index (e.g. glass and water), part of the light coming from the side of higher refractive index is reflected, while the other part is refracted (Figure 2.12). Above a certain critical angle of incidence, no light is refracted across the interface and total internal reflection is observed. Although the incident light is then totally reflected, an electromagnetic field component called the evanescent wave penetrates a short distance (in the order of one wavelength) into the medium of lower refractive index. If the interface between both media is created with a thin layer of metal (usually gold or silver) and the light is monochromatic and polarized, then the intensity of the reflected light is markedly reduced at a specific incident angle, producing a sharp decrease of intensity. This phenomenon is called surface plasmon resonanc*e* (SPR), and the incident light angle at which the decrease of intensity is observed is called SPR angle. It depends on several factors, the most important is the refractive index of the medium into which the evanescent wave propagates.

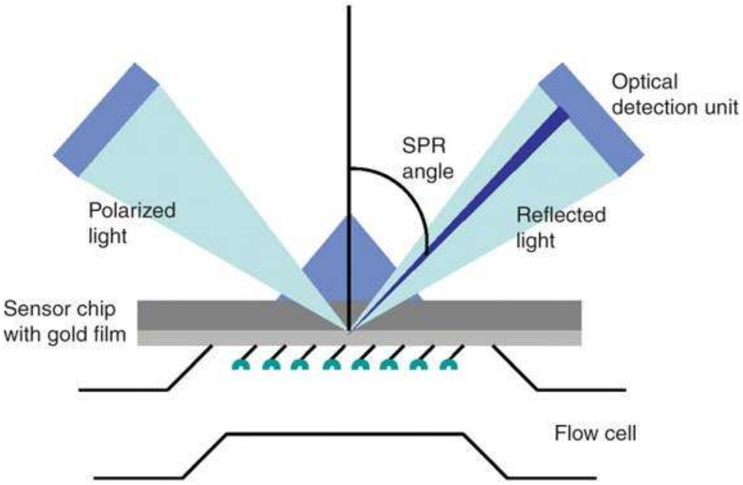

Figure 2.12 Schematic of an SPR detector. The light source is shone through the prism on to the back side of a thin metallic (usually gold) coating, and the critical angle is monitored. Changes in the refractive index of the analyte, through adsorption for example, lead to a change in the critical angle which can be monitored and used to infer adsorption kinetics and/or surface coverage (adapted from[112]).

The refractive index of the medium is affected by the surface concentration of molecules: monitoring the SPR angle thus provides a real-time measure of changes in the sample concentration on the sensor chip. The angle shifts when biomolecules bind to the surface, changing the refractive index of the surface layer. The sensorgram is a plot of the SPR angle against time, and displays the real-time progress of the interaction at the sensor surface[113].

The technique has a variety of uses including detection of surface binding events, assessing stability of adsorbate layers to washing or the local potential environment (when combined with electrochemical apparatus), and determination of surface coverage[114]. Here it is used to demonstrate chemical bonding of target molecules to gold surfaces and to calculate surface coverage (Chapter III).

2.3.4 Electrochemistry

Alternative characterisation methods of metal-molecule junctions consist in assaying the electroactive elements of the surface adsorbates. In this thesis, two electrochemical techniques, cyclic voltammetry and photocurrent measurements, are used as controls for surface characterization (Chapter III) and electronic properties measurements of mMm junctionns (Chap IV), respectively.

2.3.4.a Cyclic voltammetry

Cyclic voltammetry (CV) is used here as a reductive stripping method for assessing the role of a cysteine residue in the stronger adsorption of mutant bacteriorhodopsin protein compared to wild-type.

A typical electrochemical cell consists of three electrodes: working, counter and reference electrodes connected by an electrolyte which permits ionic current flow to complete the circuit. The reaction of interest is set on the working electrode, while a balancing reaction is set on the counter electrode (also called the auxiliary electrode): a current is thus passed between the working and counter electrodes. The potential of the working electrode is monitored according to that of the reference electrode which is set at a standard potential.

In CV the working electrode potential is swept between two defined values back and forth, while the current passing through the electrode is recorded. When the working electrode potential is swept towards the set value, an electron transfer reaction is detected when the potential crosses the standard potential (oxidation for example in the case of a redox centre), indicating that the reaction has taken place.

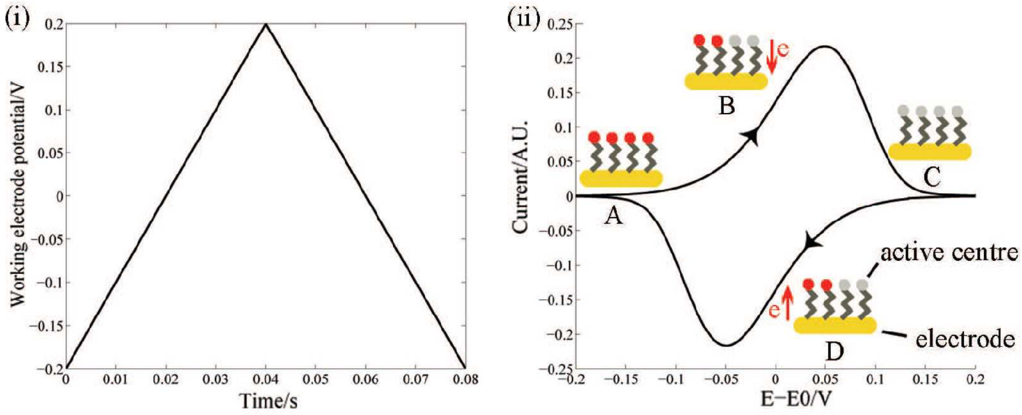

Figure 2.13. **Evolution of potential with time (i) for a typical cyclic voltammogram (ii). i**. The potential is swept towards the initially set value, and its direction is switch back to the initial value depending on the limits of potential and the sweep rate. (ii) Resulting cyclic voltammogram of a redox centre obtained at a sweep rate of 10Vs^{-1} with rate constant 100^{s-1}. Thanks to Ben Peters. Points A to D are described in the main text.

When the potential is swept back to its starting value, the opposite electron transfer reaction will occur (reduction, for example) and a current flow will be observed in the opposite direction (Figure 2.13).On the cyclic voltammogram (Figure 2.13 ii), the separation between both current peaks depends on the potential sweep rate and the mid-point between the peaks provides an estimate of the standard potential of the electron transfer reaction; from this, parameters such as the electron transfer constant rate and the nuclear reorganization energy can be estimated. The different reactions occurring during CV performed on a redox centre can be described as follow: A: At the initial potential value, set below the reduction potential of the surface specie, the redox centre is reduced (red circle). B: As the potential increases towards positive values the empty electrode energy levels draw level with the molecular level, and the active centres begin to be oxidized. C: at high enough positive potentials, and sufficient time for electron transfer to occur, the majority of surface species are oxidized. D: as the potential is swept back to its initial value, i.e. towards negative values, the active centres are reduced, until the original situation at A of a fully reduced monolayer is regained.

In this thesis, cyclic voltammetry is used for testing thiol bond between a protein and a gold surface. To do so, the technique is used in chronoamperometry mode.

2.3.4.b Chronoamperometry

The main difference between CV and chronamperometric measurement lies on the fact that, instead of being linearly swept as in CV, the potential is here stepped suddenly from one value to another.

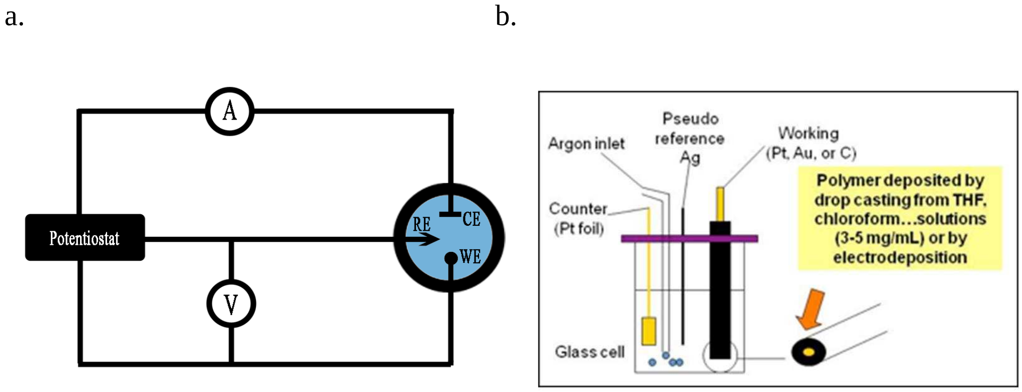

Figure 2.14. a. Schematic representation of a potentiostatic electrochemical configuration[115]. The reactions at the working and counter electrodes produce a current flow which is monitored, while the potential of the working electrode is fixed relative to a reference electrode. The electrochemical cell consists of the three electrodes connected by an intervening electrolyte, in one or two compartments. **b.** Schematic representation of the experimental set up.

If the step is across the mid-point of the electron transfer reaction then a Faradaic current will flow upon oxidization (upwards step) or reduction (downwards step) of the active centre. The current is transient: once all electron transfer processes have been completed, no further electrons may flow. There is thus an initial current spike, followed by exponential decay. For very fast electron transfer processes the initial spike may be very large and the decay rapid, meaning that a high current sampling rate is required[116, 117].

2.3.4.c Photocurrent measurements

An alternative way to measure the electrical properties of the protein of interest was to use the chronoamperometric method described above to measure the photon-generated current of bacteriorhodopsin. Here, the working electrode is a transparent gold on chromium electrode onto which is adsorbed the sample. A photocell is then constituted by the working electrode, sample and an electrolyte solution, and is tightly closed by silicon spacers on the sides, and a gold or ITO on glass counter electrode on top (Figure 2.15).

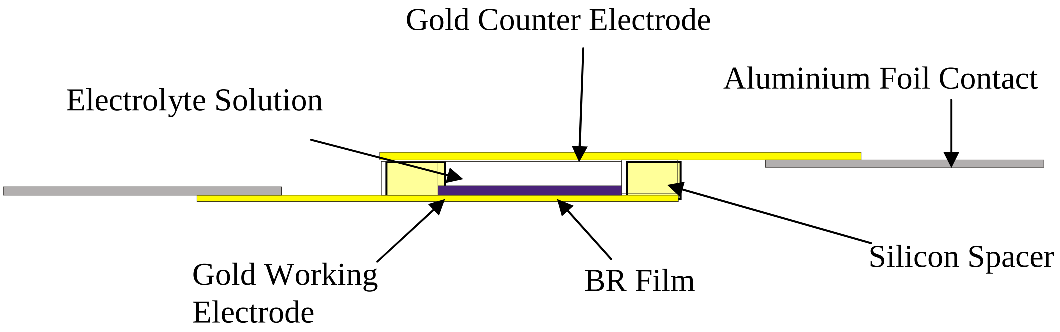

Figure 2.15: Schematic representation of the gold photocell used for photocurrent measurements. The BR film and supporting electrolyte are sandwiched between two optically transparent gold slides, acting as electrodes.

The principle consists in applying a voltage to the cell and measure the resulting current depending on the illumination conditions of the sample. In these experiments, performed on bacteriorhodopsin, current will result from the photoactivation of the protein photocycle that will generate the release of protons in the photocell, and thus cause local pH variations on the working electrode.

2.4 Instrumentation - Scanning probe microscopes

2.4.1 PicoSPM (Agilent)

The PicoSPM was used for imaging the gold-bacteriorhodopsin-gold junctions in STM mode, and measure the molecular electronic properties of these junctions by *I-V* spectroscopy in CP-AFM mode. It is an ‘open loop’ system, meaning there is no feedback in the x-y plane and uses tube piezos for x-y scanning in both AFM and STM modes. Figure 2.16 shows the PicoSPM with 1196AFMS AFM scanner and associated apparatus for CP-AFM expeirments. This scanner has a range of 5µm in either lateral or dimension and a z-range of 1.1 microns. The current sensing preamplifier has a limit of 10 nA, large enough to detect molecular tunnelling currents. The substrate is connected to the current sensing circuit by a small wire (Ag). When prepared for operation the head sits on a perspex environmental chamber which can be filled with inert gas to reduce the atmospheric humidity down to 20%. The ambient STM configuration for imaging was prepared in a similar fashion to CP-AFM with the scanner replaced with either an STM ‘A’-scanner (1µm lateral range) or ‘S’-scanner (10µm). *IV* spectroscopy was carried out with a constant sweep duration of 0.5s for CP-AFM measurements. The PicoSPM system provided valuable data regarding surface characterisation and *I-V* spectroscopy results by detecting, for the first time, photoswitching of the electrical conductance of gold-bacteriorhodopsin-gold junctions. However, technical issues and the age of the microscope lead without sufficient data to support the first encouraging observations.

Another SPM equipment, Nanowizard system by JPK, was thus used for the rest of the work presented in Chapter IV.

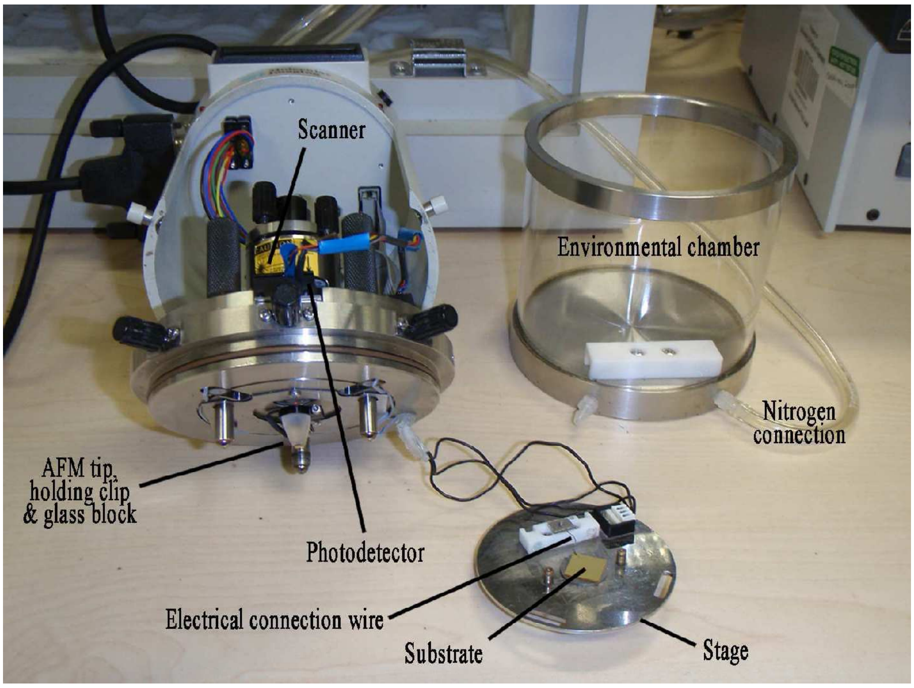

Figure 2.16: The Molecular Imaging PicoSPM system, showing the scanner head. The head comprises the scanner controlling the tip-to-sample distance and current-voltage parameters (here a 1196AFMS scanner), and a glass block holding the tip (photograph by Ben Peters).

2.4.3 Nanowizard (JPK)

The Nanowizard AFM by JPK provided most of the data related to the molecular conductance behaviour of bacteriorhodopsin presented in Chapter IV. The basic principle of the JPK is identical to all AFMs. One particularly convenient functionality of JPK microscopes, compared to the other systems used in this study, is the possibility, from a AFM image, to choose one specific point of the surface (such as one adsorbed protein) and to locate the probe on that specific point, with high precision. Other microscopes offer the possibility to zoom within a user-defined zone of the sample to be re-scanned, but with less accuracy.

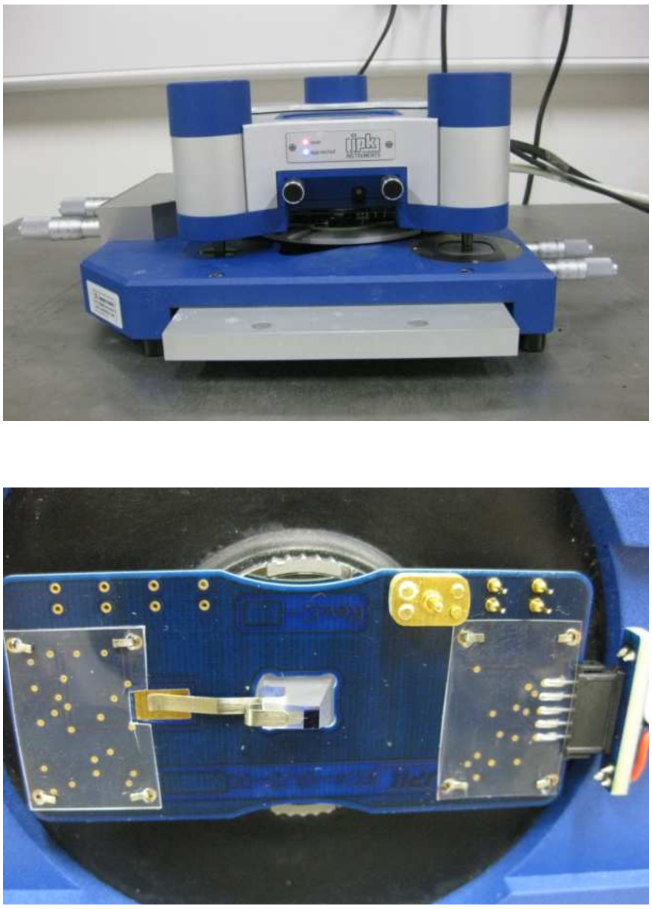

Figure 2.17: The JPK Nanowizard AFM (top) and a magnification of its conducting module (bottom).

2.4.3 Multimode AFM (Veeco)

The multimode AFM by Veeco was used in Chapter III to image purple membrane patches of the wild-type light-sensitive proton pump bacteriorhodopsin, in Chapter IV for measuring the surface potential of bacteriorhodopsin adsorbed on gold, and in Chapter V for high resolution imaging of liposomes before and after reconstitution of the neurotensin receptor type 1. The Multimode microscope is pictured on Figure 2.3 showing the general principle of AFM.

2.5 Materials

2.5.1 Substrates

2.5.1. a Mica

Most AFM imaging experiments (except in conducting mode) are performed on mica, a lamellar, atomically flat mineral. Mica represents a much faster (a few minutes incubation time, *vs* overnight incubation on gold) and affordable way to visualize samples. It is a dielectric material and therefore, on its own, cannot hold a charge. It thus cannot be used for *I-V*spectroscopy where the substrate needs to be conductive - transparent gold on mica is an alternative.

2.5.1.b Gold on glass

Gold substrates present the advantages over other surfaces (such as silver or copper) of being inert to oxidation upon air exposure, and are thus the substrates of choice for the work presented here. However, gold gets quickly contaminated and specific procedure must be followed prior use with the molecule of interest in order to avoid surface contaminants to interfere with the measures.

Gold on glass was obtained pre-fabricated in 11×11mm2 squares from Arrandee, Germany, with a coating thickness of 300nm. Prior to use for SPM these were washed in absolute ethanol and sonicated in water for 30s to remove physical surface adsorbates. There occasionally remained some glue (used to hold the substrates in place on a support during transit) on the underside of the glass that needed removing with a scalpel before washing again with ethanol and drying; removal is important this could contaminate the surface on annealing and/or cause uneven annealing on the gold-coated side. Once clean and dry the substrates were held with clean tweezers (kept specifically for the purpose of annealing, to prevent cross-contamination between fabrication processes) and annealed in a butane flame for approximately 5 minutes.

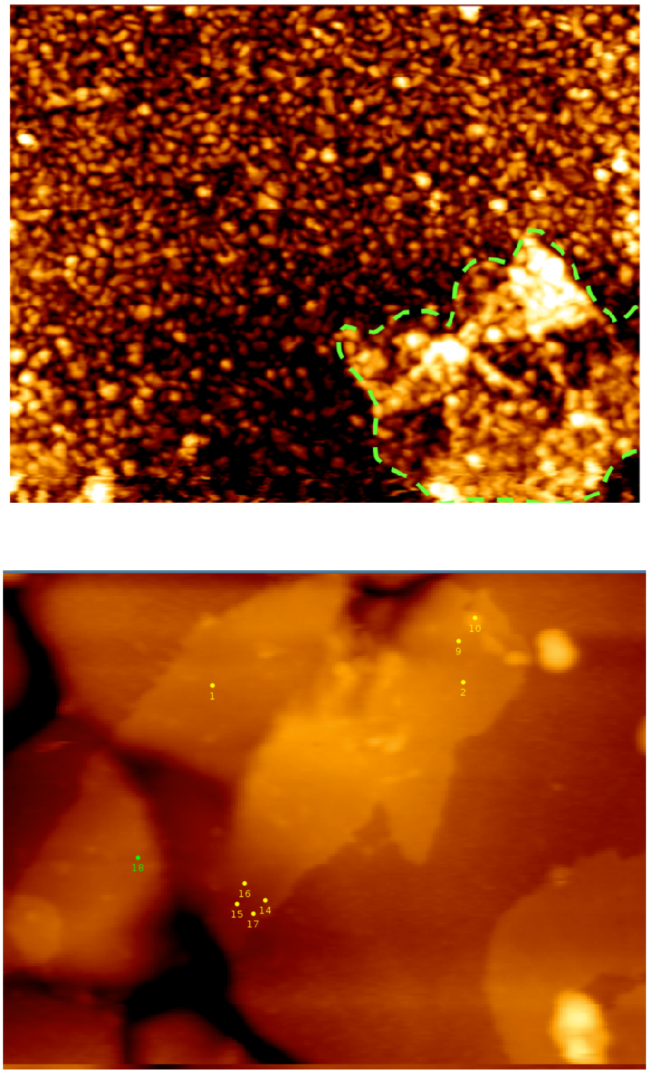

Figure 2.18: AFM images of a gold substrate adsorbed with a cysteine mutant of *Halobacterium salinarum* purple membrane without prior annealing (top) and after annealing (bottom picture). The granular aspect of bare gold was flattened upon annealing. Sample features, here the superimposition of bacteriorhodopsin membrane patches, are better resolved on a flat, homogenous substrate obtained after annealing. Highlighted points on the second picture are points where the microscope made current measurements (cf Chapter IV). Contact mode AFM images, Nanowizard AFM mounted with its conducting module, JPK (1µm x 750 nm).

The annealing process was performed in the dark so that the temperature of the surface could be gauged; the surface was held at a constant dim red glow for 20-60 seconds at a time before being allowed to cool and the process repeated. Once annealed, a visual aid to the quality of annealing is the formation of a dull white sheen on the Au surface, usually towards the centre of the substrate where the heating is concentrated. If this sheen was not observed the substrate was annealed further until it became apparent. Care must be taken when annealing not to heat the glass to too high a temperature in one place as this will cause the support to warp, making it difficult to use for SPM purposes, particularly fluid STM where a liquid-tight seal between surface and fluid cell is required. Once the surface was annealed it was allowed to cool in air before being washed again with ethanol and dried under a nitrogen stream. It was then introduced directly to the incubating solution as quickly as possible (within one minute of cooling) to ensure that airbourne contaminants did not adhere to the surface.

2.5.2 SPM probes

The choice of SPM probe depends on the application. For C-AFM *I-V* investigations it is necessary to combine a conductive coating with a low force constant cantilever so that low applied loads may be achieved. Due to the possibility of tip contamination during transport and storage, C-AFM tips were cleaned for at least 20mins in a UV/ozone cleaning box (Bioforce Laboratories, USA). The Pt-coated NSC35 series cantilevers have the desired characteristics for KFM of medium spring constant to ensure stable tappingmode operation, but sufficient flexibility for the sensitive potential detection scans BudgetSensors (Bulgaria) gold coated contact probes, the contGB-G range [170], have a low spring constant of $0.2 Nm^{-1}$ that enables precision forcecontrol and were found to exhibit good conductance characteristics on direct contact with Au and HOPG.

2.5.3 Piranha solution

Piranha is a 3:1 mixture of H_2SO_4 and H_2O_2 commonly used to clean surfaces, equipment and glassware where a very clean environment is desired. Here, it is used in Chapters III and IV during photocurrent measurements preparation. As a strong oxidizing agent it is known to dissolve most organic impurities, and hydroxylates surfaces to form a hydrophilic region. Piranha needs to be handled with extreme caution as it is highly corrosive and volatile in contact with organic materials, particularly organic solvents. Only small amounts should be formed at any time and the solution should never be stored in a closed container or for any longer than is absolutely necessary. Protective clothing should be used when handling piranha.

2.6 Methods

2.6.1 Sample preparation and surface immobilisation

All containers were washed thoroughly with deionized water and ethanol before use. Following incubation, the surface is washed thoroughly with water or phosphate buffer (60mM PB, 150mM NaCl, pH 7.0), and dried under a nitrogen flow.

2.6.2 AFM Imaging and *I-V* spectroscopy

Although experimental parameters vary according to the sample studied and the imaging mode, which will then be detailed in the corresponding sections, some general principles are described below.

2.6.2.a Assessing the force applied by the probe to the sample

Although it is possible to choose what force to apply to the sample from the microscope control panel, each AFM probe has its specific properties and for a same applied force chosen in the microscope settings, there can be a big variability in the actual force applied to the sample. AFM experiments thus start by calibrating the probe. Once the probe is in contact with the sample (the approach is performed at minimum load), the microscope is switched to force modulation mode and a force curve is acquired. This force curve will allow determining the sensitivity of the system, given by the gradient of the contact slope. The sensitivity is then used to convert the deflection into a cantilever bending distance. Since the feedback loop stops the approach when a 'zero' deflection is reached (at the set-point), the offset of deflection from zero gives the bending distance necessary for the force calculation according to Hooke's law, $F = kx$. This process is performed through the microscope software allow to precisely adjust the force applied to the sample during the experiment[118].

2.6.2.b I-V spectroscopy

I-V spectroscopy was performed on trimers of bacteriorhodopsin adsorbed on gold (Chapter IV). C-AFM *I-V* spectra were collected in batches of 30-50 at each applied force. After initially engaging at a given set-point the tip remained in contact with the surface and the force increased stepwise The sweep duration of the voltage bias was 0.5s. Fast sweep rates could lead to charge build-up affecting the measured *I-V* characteristics. Although being the best way to locate sample on the surface for current measurements, in particular for low sample concentration, imaging was avoided before C-AFM *I-V* spectroscopy due to the risk of tip contamination or degradation of the probe conducting coating. The protein is easily expressed in large amounts; in order to obtain a high coverage of discrete features on the gold surface, high concentrations (25 µM) were used in this work compared to traditional, non-conducting, imaging AFM (5µM and below).

2.6.2.c Data analysis

Over the course of the research described in this thesis, many thousands of *I-V* spectra have been collected , making highly desirable the creation of automated data analysis process that have the ability to apply certain pre-determined detection rules and make rigourous comparison and measurement of spectroscopic features in *I-V* curves facile. Here, all data analysis was performed in the Matlab programming environment, with the automated accomplishment of spectroscopic feature detection and junction resistance calculation for each *I-V* curve.

2.6.2.d Reductive stripping/ cyclic voltammetry: electrode preparation

Gold disc electrodes of 2mm diameter (CH Instruments Inc.) were cleaned prior utilisation. First, reductive desorption of contaminants was performed by cyclically sweeping the electrode from -0.5V to -1.5V Vs SCE at $1Vs^{-1}$ in 0.1M NaOH for 200 scans. The electrode was then polished mechanically with 0.05µm alumina slurry on a Buehler polishing cloth for several minutes, then sonically cleaned in deionized water for 1min before being immersed in hot piranha solution for 15-20mins.

After rinsing with deionized water and further sonication for 1min the electrodes were electrochemically polished by cyclic voltammetry in 0.1M H_2SO_4, -0.2V to 1.5V Vs SCE at $0.1Vs^{-1}$ for 25 scans. Electrochemical gold oxide reduction was then carried out by cycling from 0.75V to 0.2V in 0.1M H_2SO_4 for 10 scans, followed by a final step of chemical gold oxide reduction by soaking in ethanol for 15-20mins. The electrodes were then ready for sample incubation.

Chapter III: Engineering bacteriorhodopsin for probing its molecular electrical properties

3.1 Introduction

3.1.1 Halobacterium salinarium

Membrane proteins play a key role in a wide range of biological activities in living organisms, and vectorial ion transport across the cell membrane is one example of such ubiquitous function mediated by membrane proteins. Proton pumping results from the initial conversion of electrochemical or light energy into a proton-motive potential generated by integral membrane proton pumps. The energy stored within this potential is then harvested by an ATP synthase in order to regenerate ATP from ADP and P_i. Extremophilic organisms are amongst the simplest organisms using proton transport across their membrane in order to generate the energy required for their metabolism. The halophilic archea *Halobacterium salinarium* can be found in high salt (typically 4 to 5M NaCl) environments, including salt seas, salt lakes, rock salt and saline soils, and cannot survive in more dilute media such as sea water. *Halobacterium salinarium* is responsible for the typical red (aerobic conditions) or light-pink-to-dark-purple coloration (anaerobic conditions) of its environment (Figure 3.1a). Its cell membrane contains, on a permanent basis, an ATPase and two sensory rhodopsins, SRI and SRII, which act as light sensors and mediate positive or negative phototaxis in response to changing environmental conditions[119, 120]. SRI and SRII transmit light signal to their transducer proteins (HtrI and HtrII), which in turn initiate a phosphorylation cascade that regulates the cell's flagellar motors[121]. SRI is activated when the bacterium needs energy, and mediates migration to illuminated regions where the production of ATP can take place.

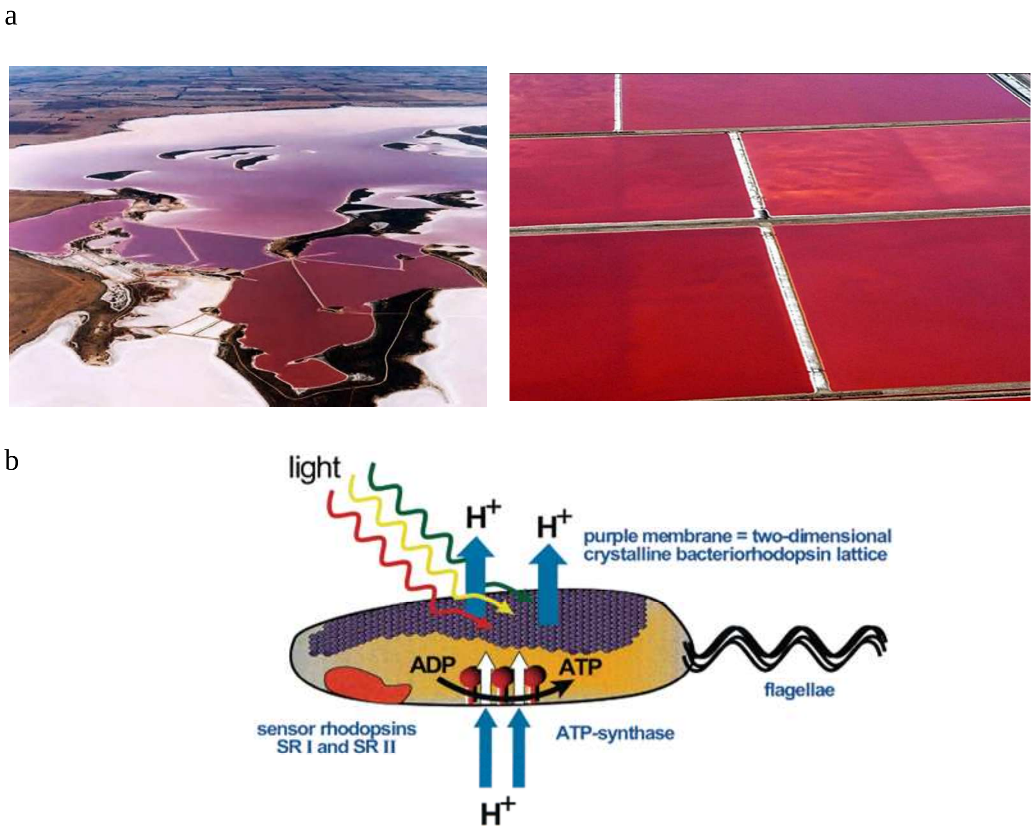

Figure 3.1: *Halobacterium salinarium* and bacteriorhodopsin. a. Saline in Australia showing the typical purple colour due to the presence of *Halobacterium salinarium*, and more precisely, due to the bacteriorhodopsin protein embedded within the purple membrane of the archea (pictures credits from Cheetham Salt Limited and M.Christian). **b.** Schematic representation of one *Halobacterium salinarium* cell. The purple membrane, synthesised under anaerobic condtions, is mainly composed of bacteriorhodopsin, which is the “solar cell” of the archea: it is the sole protein in charge of the conversion of light energy into chemical energy, as a proton gradient, which is then used for ATP synthesis (adapted from[121]).

When sufficient amounts of ATP have been synthesised, SRII is activated and mediates is aerobic, repellent phototaxis to darker areas. In halobacterial metabolism, oxygen is the primary electron receptor. However, when the oxygen concentration of the saline environment drops below a level necessary to maintain oxidative phosphorylation, the archea synthesise a purple membrane as part of their outer membrane (Figure 3.1 b). Purple membrane (PM) is found as large patches (µm-sized, Figure 30a) that can occupy up to 80% of the total cell surface and are made of lipids and of a unique type of protein: bacteriorhodopsin (BR)[120]. Under anaerobic conditions, bacteriorhodopsin is responsible for the conversion of light, driving ATP synthesis.

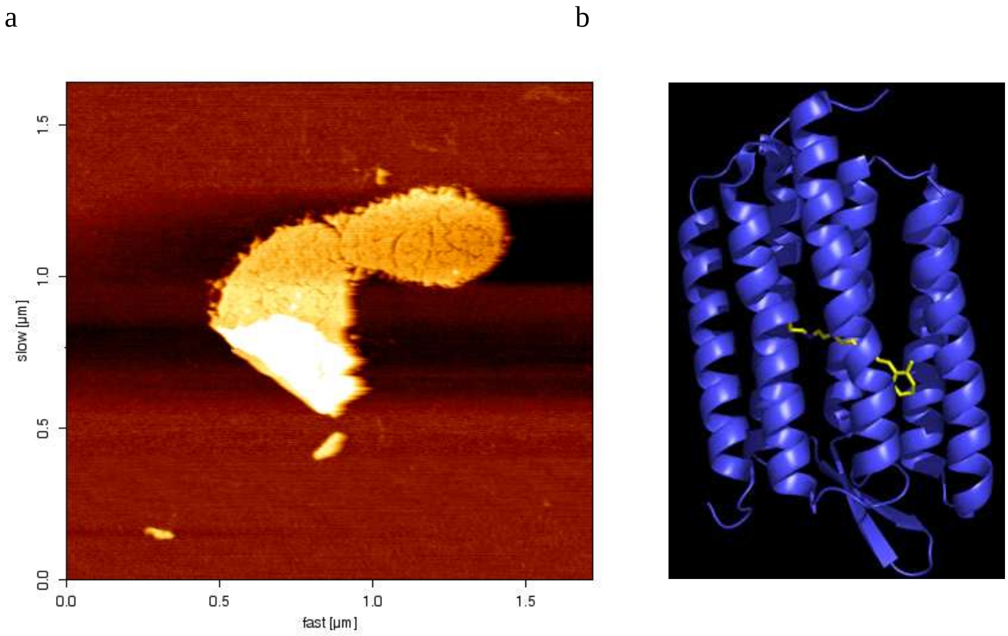

Figure 3.2: BR-containing purple membrane and overall view of BR.
a. AFM image of one patch of purple membrane. Contact mode in phosphate buffer.
b. Representation of the putative 7 TDM of bacteriorhodopsin and its retinal chromophore (cross section of the structural model PDB: 1FBB).

3.1.2 Bacteriorhodopsin

Bacteriorhodopsin (BR) is a seven transmembrane domain protein with short inter helical loops. It is made of 248 amino acids with a total molecular weight of 26 kDa[122], and functions as a light-driven proton pump[123-125]. Its purple colour is due to a chromophore, retinal, which is embedded within the protein through a covalent, protonated Schiff base linkage to the Lys-216 residue, near the middle of the seventh helix[8, 126-128]. Its composition and structure are closely related to visual pigments of higher animals[129-132]. Although bacteriorhodopsin is capable of converting sunlight into chemical energy as a monomer, it is organised within the purple membrane as a two-dimensional, hexagonal crystalline lattice of uniformly oriented trimers which are the basic functional units[8, 53, 126, 133-137]. The protein has a remarkably high level of stability towards chemical and thermal degradation: indeed, BR is stable towards temperatures over 80°C in solution or 140°C in dry state, towards pH ranging from 0 to 12, and resists high ionic strength and digestion by most proteases[121].

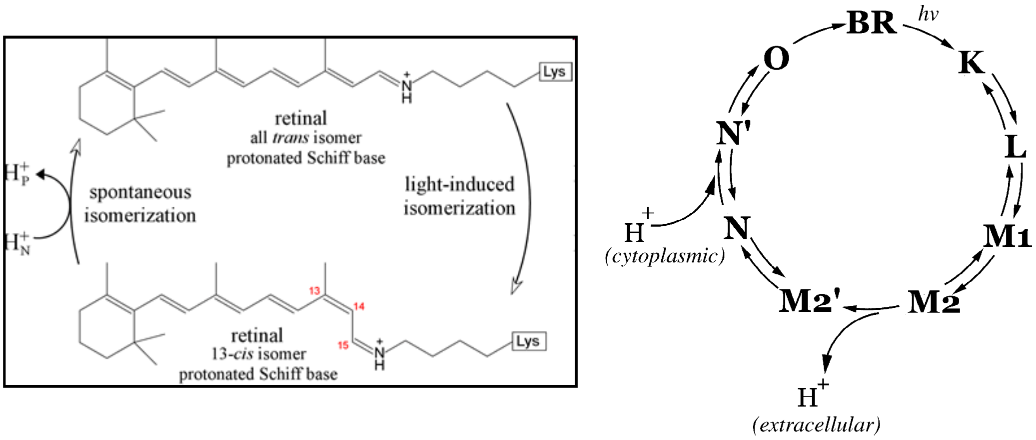

Figure 3.3: Light absorption drives the retinal isomerization from all trans to 13-cis (left), which generates the photocycle (right).

The purple membrane exists in a dark-adapted state containing both 13-*cis*- (λ_{max}= 558 nm) and all-*trans*- (λ_{max}=568 nm) retinal isomers in equimolar ratios. Illumination generates a metastable light-adapted form, BR_{568}, containing the retinal chromophore in its all-*trans*-retinal configuration[138]. While both 13-*cis* and all-*trans*-retinal-containing BRs undergo photoreaction cycles, only the cycle of the all-trans component (light-adapted) is accompanied by proton translocation (Figure 3.3). This photocycle of BR_{568} contains five main intermediates, which are designated by their visible spectral transitions as K_{600}, L_{550}, M_{412}, N_{530} and O_{640}[139]. The photocycle intermediates are formed as a function of the modulations of the electronic interactions between the retinal chromophore and the surrounding amino acids.

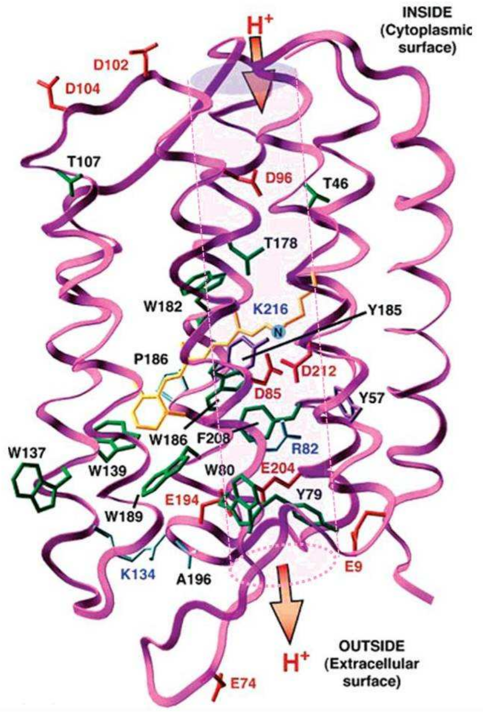

Figure 3.4: Structure of bacteriorhodopsin showing the residues involved in sequential proton transfer events coupled to conformational changes. To summarize, protonation of Asp85 from the Schiff Base results in a proton release to the extracellular side; reprotonation of the retinal Schiff base occurs from Asp96, which then uptakes of a proton from the cytoplasmic side; 5. proton transfer from Asp85 to the release group, which is believed to involve Glu194, Glu204 and a $H_5O_2^+$ cluster (adapted from[140]).

.

Absorption of a photon of light causes isomerization of retinal from the all-*trans* to the 13-*cis* retinal isomer. After photoexcitation and retinal isomerization, the pK_a of the Schiff base drops from 13 to 8.3, whereas the pK_a of Asp-85 increases from 2.2 to 6.9. These pK_a changes result in the transfer of a proton from the Schiff base to Asp-85, and a proton is released to the extracellular side of the membrane. Then, the Schiff base is reprotonated by Asp-96 when the pK_a of Asp-96, the primary proton donor to the Schiff base, drops from >12 to 7.1. After reprotonation, retinal isomerizes back to all-*trans*, and the pK_a values of the Schiff base and Asp-96 increase back to their initially very high values and Asp-96 is reprotonated from the intracellular side of the membrane. The initial or ground state is ultimately regenerated when the pK_a of Asp-85 decreases back to its initial value, causing transfer of its proton to the proton-releasing group at the extracellular side of the membrane. The cycle is achieved within 10 ms, the decay of the O state resulting in a return of the protein to its resting state[141].

The original concept of one single M intermediate was challenged by Janos Lanyi and Dieter Oesterhelt in the early 1990s. Both scientists made the hypothesis that the M stage could be split into two forms, both with similar absorbances, but with different overall conformations. This has been subsequently supported through electron crystallographic studies of various mutants trapped at different stages[142].The split has been proposed to allow the unidirectional nature of the proton transfer. A requirement for vectorial proton transport is that de- and reprotonation of the Schiff base occur from opposite sides of the membrane. Since the M-intermediate is the only state in which the Schiff base is deprotonated, it seemed logical to have at least two M substates that differ in the relative accessibility of the Schiff base to both sides of the membrane, where M_1 is extracellular accessible and M_2 is cytoplasmic accessible.

Studies have shown that there are strong similarities between the structure of the extracellular moiety of both the L and M_1 intermediates, but one main difference was observed in the protonation states of the key intermediates: in the L state, the Schiff base is protonated and Asp85 is deprotonated, whereas in the M_1 intermediate, the opposite occurs. The transferred proton (from the Schiff base to Asp85) remains on Asp85, while the proton release is generated from the interaction of the hydrogen-bonded network between the extracellular surface and Asp85. The key molecules (“proton release group”) contributing to this include water molecules and residues Arg82, Glu194 and Glu204. The change from M_1 to M_2 constitutes the main conformational change in the photocycle.

3.1.2.a Importance of the EF loop

Among functionally relevant structural changes occuring during the photocycle, one results in a variation of the solvent accessibility of the interhelical cavity, related to an outward tilt of helix F in the M intermediate[143]. Increasing hydrostatic pressure suggested that the proton transfer from Asp96 to the Schiff base can be manipulated by changing the cytoplasmic dipole environment. Placing a bulky group on helix F that blocks this putative opening would predispose the helix to tilting out and resist its return to original position. This result in a more rapid reprotonation of the Schiff base (i.e. in increase in the rate of M intermediate decay), but a slower reprotonation of the cytoplasmic region (i.e. decrease the rate of N state decay), showing the potential significance of the EF loop on regulating proton transfer[144].

The intermediates are measured through spectral changes in the retinal and its surroundings, and thus do not directly comment on protein conformational change. Such conformational changes do occur during the photocycle, however, as confirmed by numerous structural work (X-ray diffraction, NMR, EM, AFM, ESR)[127, 137, 145-159]. As an example, atomic force microscopy data have showed a clear reversible change of the surface structure of the BR lattice[146, 160, 161] upon retinal isomerisation, which also results in a succession of charges displacements within BR molecules: a photoelectric response from the protein was detected for the first time in 1978[162].

3.1.2.b Nanotechnological applications of BR

Examples of photochromic proteins are rare in nature, although they play a key role in photosynthesis and visual perception, e.g. photo reaction centres and visual pigments. Due to their enormous importance, numerous studies have been performed in order to elucidate the function of these molecules, their interaction with light, and the mechanisms of how the light energy is transformed into chemical energy or into physiological signals, for potential device use. As mentioned earlier in Chapter I, bioelectronics, which investigates the use of native and modified biological molecules in electronic or photonic devices, is a promising alternative to current lithographic manipulation. Although a number of proteins have been explored for such devices applications, BR has received the most attention[163-165]. It is a very robust protein, easily expressed and purified. It must function at high temperatures, under high light fluxes and for extended periods of time for the organism to survive, and these unique properties make it particularly attractive for nanodevice applications over other proteins and conventional inorganic or organic photochromic materials. Moreover, the photoactivity of the purple membrane remains, after water removal, for dried films of bacteriorhodopsin[162], increasing its attractiveness for developing biomolecular devices[166-170] such as optical memories[27, 121], data processing[171] or photodetectors[172, 173] (Figure 3.5).

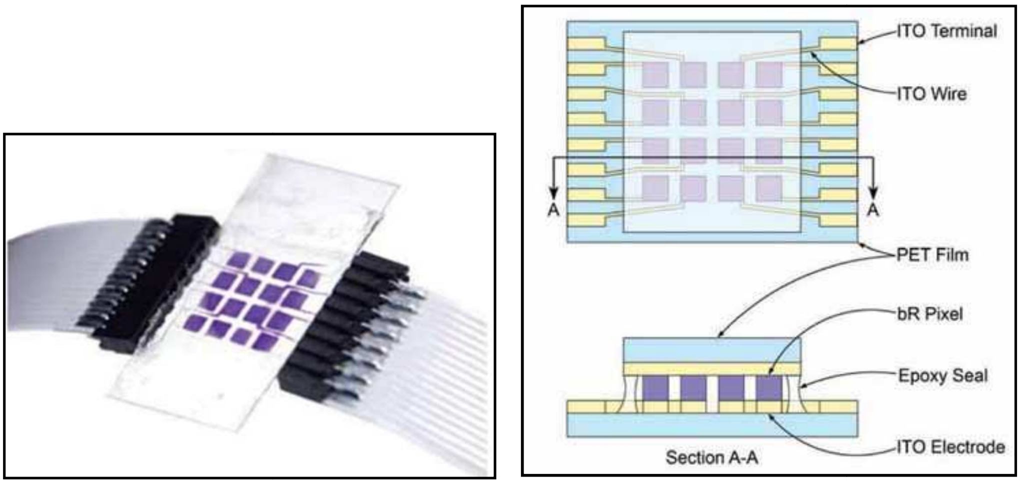

Figure 3.5: Example of technical application of BR: 16-pixel BR-based photocell array. Rudimentary imaging system with 1.3 x 1.3 mm^2 pixels based on purple membrane adsorbed on ITO and showing differential response to illumination (adapted from[174]).

Although photocurrents have been detected in BR films for thirty years, they are multicomponent in nature and have been the subject of conflicting assignments and proposed mechanistic origins. Despite the fact that initial hypothesis suggested photoinduced intramolecular charges displacements (pH independent) as the cause of photocurrent [175], it is likely that the typically measured response is associated with proton discharge from the extracellular surface as the BR photocycle evolves towards the M state[140, 176-178].

The first successful use of BR in such applications was reported as early as 1981, in the *Biochrome* project[27], and consisted in a real-time photochromic and holographic film based on chemically modified polymer films containing bacteriorhodopsin. Numerous patents for devices using BR have then been published by diverse organisations, including academic research labs and industrial groups such as Panasonic/Sanyo Electrics, Fuji, or Canon (world international property organisation, http://www.wipo.int). Patented technical applications include, for example, the use of BR as an optical recording material, the use of BR variants for data storage, imaging arrays based on BR thin films (Figure 3.5), and BR-based artificial retinas. As of July 2011, 1031 patents applications involving BR had been made. One of them, the last of a long list of patents applied for by Robert Birge, concerned the creation of photosensors using BR as a detector for chemical and environment toxins [179].

The primary photochemical event of light-adapted bacteriorhodopsin involves two subpicosecond processes. The first process is a nearly instantaneous event that has a measurable photovoltaic consequence due to the large shift in electron density that accompanies electronic excitation of the long-chain, protonated Schiff-base polyene (Figure 3.6). This large shift in electron density is equivalent to moving an electron ~2.5Å down the polyene chain toward the nitrogen atom, resulting in a more negative $C_{14}C_{15}H$=NH-Lys linkage. The interactions between the $C_{14}C_{15}H$= NH-Lys and the two nearby negative Aspartic acid residues (Asp-85 and Asp-212), which were favorable electrostatic interactions, become repulsive and help direct the photoisomerization of the 13-*cis* double bond to generate the primary photochemistry.

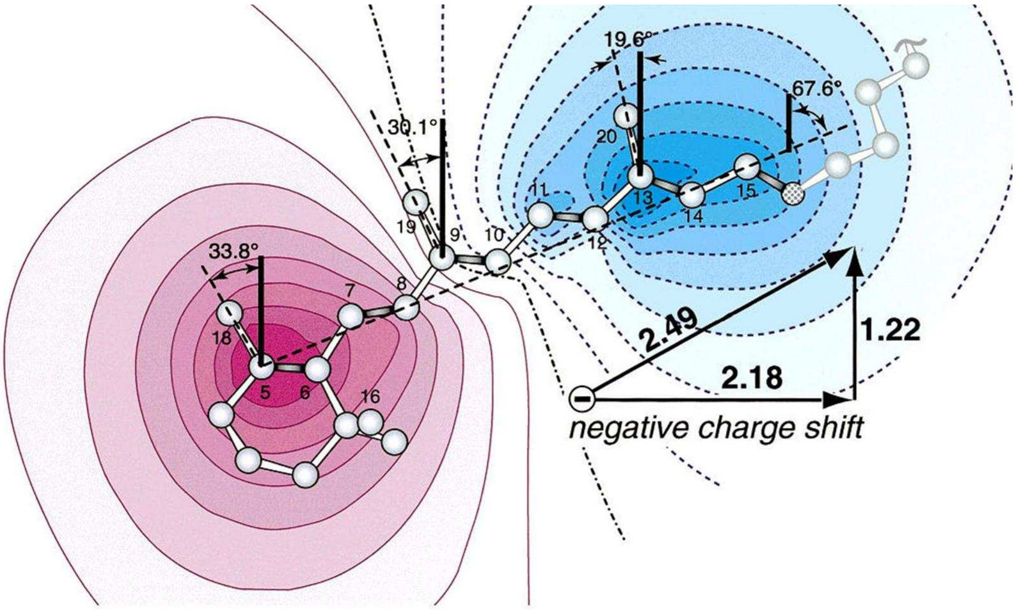

Figure 3.6: Schematic representation of the electron density of the long-chain Schiff base. Excitation of the protonated Schiff base polyene is accompanied with a large shift in electron density, resulting in a measurable photovoltaic signal. (Adapted from[27]).

This electrostatic interaction, coupled with significant bond order reversal due to the excitation process, is sufficient to generate a nearly barrier less excited state potential surface for 13-*trans* to 13-*cis* photoisomerization. The barrier to isomerization in the ground state is thus altered dramatically in the excited state and yields to the biological equivalent of a high-electron mobility transistor.

The photoisomerization process also generates a photovoltaic signal due to the motion of the protonated Schiff base away from the negative counterions (Figure 3.6). However, relaxation of both the chromophore and the protein following isomerization is complex, and deconvolution of the various components of the fast photovoltage is not yet possible. It is known that the primary photochemical event is a subpicosecond phenomenon and recent studies suggest a small barrier to isomerization. It is likely thus that the photovoltaic signal observed on the picosecond time scale from bacteriorhodopsin has contributions from both the excitation and photoisomerization process.

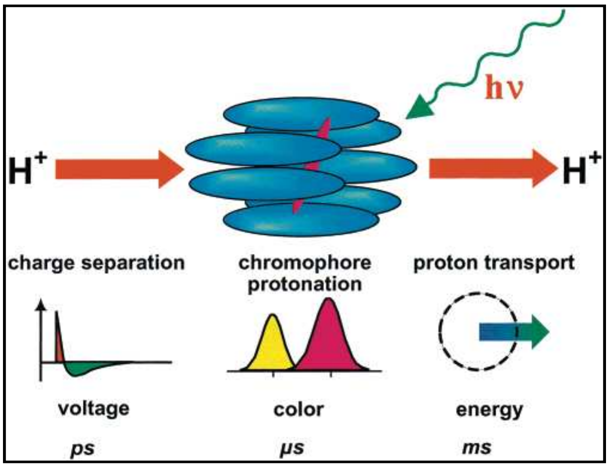

Figure 3.7: Basic molecular functions of BR. Photon absorption and a charge separation step initialise the proton transport, which is completed in about 10 ms (adapted from[121]).

3.1.2.c Genetic engineering of BR

The biological function of BR is strictly optimized for energy conversion. Turning this molecule into a material for technology applications requires the controlled modification of its molecular properties, in particular its optical properties.

Genetic engineering consists in altering target characteristics of an organism by the systematic manipulation of its genetic code. Mutagenesis is a standard method in biochemistry and pharmaceuticals for the precise understanding of gene function and for altering the properties of biological molecules, like proteins, but it has only been recently used by molecular electronics engineers as a tool for device applications[180].

Genetic mutations of BR have been extensively and successfully performed in order to better understand the different stages of the complex photocycle[181, 182]. For example, the largest variations during the photocycle occurring between the ground state and the early and late M intermediates, numerous mutations aimed at obtaining an extended lifetime of these intermediates[24]. Genetic modifications were also performed in order to study the crucial activity of the proton pump. Replacing the Schiff base counter ion (Asp-85) with a Thr or a Ser converts the proton pump into a chloride pump. In eubacterial rhodopsins, the extracellular proton release network is missing, but transport is not affected. Lanyi *et al*. suggested that the two half-channels between the active site and both membrane surfaces only existed to optimise the proton transport, but had no direct effect on it. Several mutations were performed to verify this hypothesis. One of the most commonly used mutation, D96N, is located on the cytoplasmic side and results in accumulation of the M state. D96N is deprived of internal proton donor and thus prolongs the lifetime of the deprotonated Schiff base.

Mutagenesis studies have reported a model where the Schiff base and aspartate moieties form, with a hydrogen-bonded network of water molecules, a proton channel[183, 184]. R82Q, E194Q and E204Q, are mutations located on the intracellular side of BR for which there is no proton-release group. These mutations each resulted in the proton release being delayed to the end of the photocycle, and the sequence of proton release and uptake were inversed. All these mutations showed that the proton pump activity was only due to the active site, and that the two half-channels connecting it to the membrane surfaces do not play crucial roles in the process: they optimize the proton transport but do not inactivate the pump.

Site-directed mutagenesis has also been used to design bacteriorhodopsin mutants with enhanced materials properties[25, 185-187]. The production of mutants having an M state extended lifetime, mentioned above, was used to enhance the holographic properties of the protein[188, 189] while mutants with an increased yield of the O state presented a better branched-photocycle memory[190].

3.1.3 Gold-BR-gold junction construction

The use of bacteriorhodopsin for molecular devices involves binding the protein between electrodes, in a robust and controllable manner, while maintaining the protein functionality. A wide range of methods for BR immobilisation have been explored[180, 191-198]. These include drop drying, resulting in non-orientated protein multilayers[199], Langmuir-Blodgett approaches, in which BR films are initially compressed at an air-water interface[178, 200], the use of electrophoretic sedimentation (where external electric fields act on the purple membrane dipole moments) that generates oriented mono/multilayers[196, 201, 202], antibody-mediated oriented immobilisation [175], host-guest-mediated immobilisation [203] and encapsulation in polymeric gel supports[204, 205]. Molecular junctions created via these diverse methods were have been characterised by SPM[206-208] and electron microscopy[200, 209], though often giving relatively poor results. Using a cysteine mutation to adsorb covalently BR on gold was the method of choice here.

3.1.3.a Partial delipidation of BR

Bacteriorhodopsin is the main component of the purple membrane, with a 3:1 protein/lipid molar ratio[135]. About 90% of the total lipids in *H. salinarium* are polar lipids and are derivatives of a branched glycerol diether, 1,2-di-O-phytanyl-*sn*-glycero-3-phosphoryl-3'-*sn*-glycerol-1'-phosphate (DPhPGP) and a glycolipid sulphate (DPhGLS)[153, 210] (Figure 3.8). The lipid organisation within the membrane consists of 30 lipid molecules associated with each trimer, 24 lipids surrounding the trimer, while 6 lipid molecules are inserted within the trimer[126]. Of the maximum number of ten lipid molecules per BR monomer, crystallographic studies could assign nine phytanyl moieties per BR unit: four lipids could be modeled in the cytoplasmic half, and five in the extracellular half of the membrane (Figure 3.10).

.

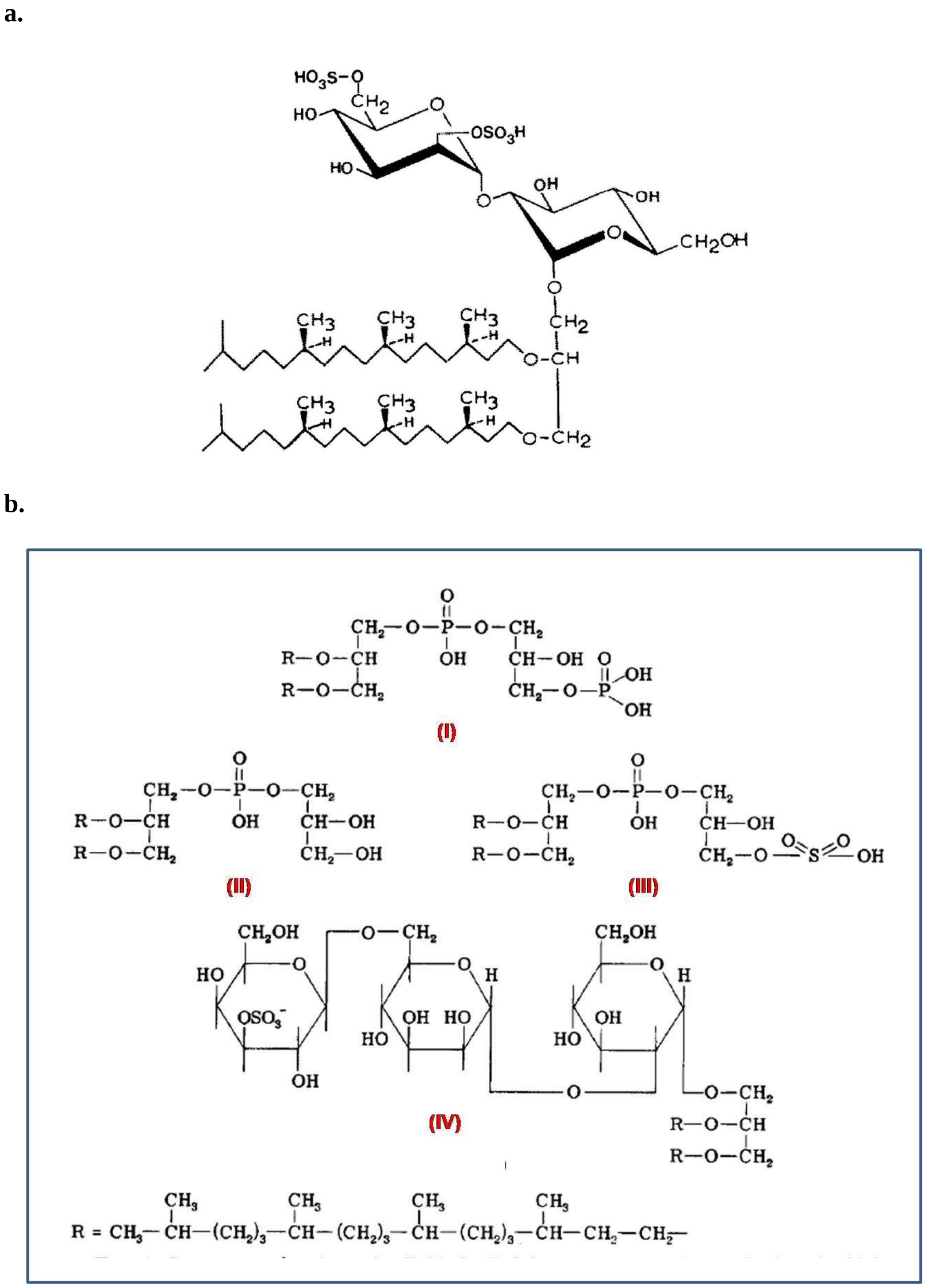

Figure 3.8: Structure of BR polar lipids, that have been found to be derivatives of a glycerol diether (a). structure of the glycolipid sulphate BR polar lipids are derivative of**.** Its complete structure is established as 2,3-di-O-phytanyl-l-O-[β-D-galactopyranosyl- 3’-sulfate-(1’->6’)-O-α-D-mannopyranosyl-(1’-> 2’)-0-α-D glucopyranosyl]sn-glycerol. **b.** structures of BR major polar lipids: I. phosphatidylglycerolphosphate; II. Phosphatidylglycerol;III. Phosphatidylglycerophosphate; IV.glycolipid sulfate (adapted from[211, 212]). Moreover, the lipid composition and density differ between the cytoplasmic side the lipid composition and density differ between the cytoplasmic side and the extracellular side of the membrane[134], both sides having different surface charges and stiffness[147].

In the absence of the endogenous lipids, BR is unable to form crystalline arrays in dimyristoylphosphatidylcholine (DMPC) bilayers. These facts as well as numerous other studies suggest that the lipid - protein interactions are indispensable for the association of BR monomers into the trimeric structure and the crystalline array[210, 213].

Most of the studies mentioned above, in particular those related to the technical applications of BR, have been performed on the protein within the membrane, on relatively large (micron-sized) surfaces. However, membrane lipids may play a restrictive role in the protein adsorption on the electrode surface, and are thought to interfere with the efficiency of the current transmission through the protein.

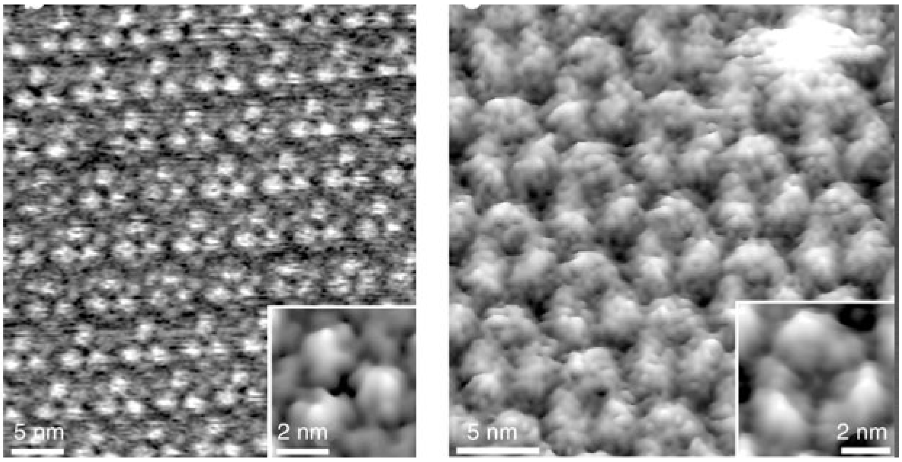

Figure 3.9: AFM high resolution pictures of the intra and extracellular side of one purple menbrane patch. The lattice of BR trimers is clearly visible on both sides, and so is the difference between both sides (adapted from[70]).

High resolution AFM imaging previously showed a clear distinction between each leaflet of the purple membrane (Figure 3.9), and also showed that wild-type bacteriorhodopsin will adsorb onto a substrate on either of the membrane side in a random manner[70] . The protein orientation on the surface may not be of primary importance for imaging experiments, but it is crucial, however, to be able to orient specifically and homogeneously the sample on the substrate in order to obtain accurate and reliable measurements of the protein electronic behaviour.

The first phase of this work consists in removing the outer lipids surroundings BR trimers while keeping the inner lipids involved in the cohesion of the native trimeric structure (Figure 3.10). The expecting result of this partial delipidation would be an increased and intimate coupling onto the surface, accompanied by a clear enhancement of the molecular electronic properties of BR.

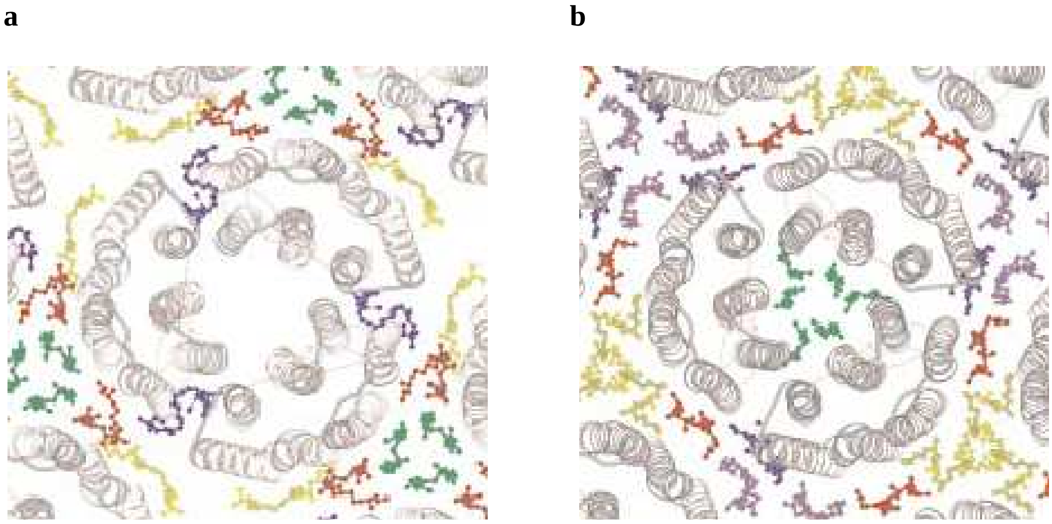

Figure 3.10: Lipids within and around the BR trimers, viewed along the *c* axis. The seven transmembrane helices are depicted in ribbon representation and colored gray, the coloured lipid molecules (green, blue, red and yellow) are shown in ball-and-stick representation. **(a)** Cytoplasmic side, showing the four lipids that surround each monomer. **(b)** Extracellular side, showing the four lipids surrounding the monomer, and the fifth located within the trimer. Adapted from[126]. The aim of this work is to remove most of the lipids surrounding BR trimers in order to lose the native lattice organisation and study the electric properties of isolated trimers.

Partial detergent-mediated delipidation of BR is a non-destructive way of depleting bacteriorhodopsin of 75% of its native highly charged lipids (mono- and di-sulfate, and phosphate analogues, with residual negative charges 1 or 3), while retaining endogenous lipids involved in the cohesion of the protein[214]. The process triggers a spectral shift of the protein λ_{max}[214], but does not significantly affect the detectable proton pumping capabilities[182, 213-215].

Regarding potential nanodevices applications, partially delipidated protein, whose size would go from the µm scale in the membrane, down to the nm as isolated trimers, would also have the huge advantage of further decreasing the size of the device, when miniaturisation has become a real technological challenge, as mentioned in Chapter I.

3.1.3.b BR cysteine mutation (M163C) for gold-BR-gold junctions construction

The photoelectric conversion efficiency of BR strongly depends upon its electrode-bound orientation[175]: it is thus crucial to obtain a strong, homogenously oriented binding of the protein on the surface prior measurement of its electronic behaviour.

A cysteine mutant, M163C (Figure 3.11) , has been used to obtain strong covalent binding on a gold surface via a thiol bond (BR naturally lacks cysteine residues), as well as enhancing the measured response through a homogeneous orientation on the surface. The mutation is located in the conformationally sensitive EF intracellular loop of the protein (which plays a key role in signal transduction in rhodopsins), it is thus expected to orient the transmembrane helices of the protein perpendicular to the conducting surface.

High speed AFM has confirmed this conformational sensitivity of the EF loop, as mentioned above, indicating that real-time light-induced conformational changes occur in BR in PM, resulting in a counter-clockwise twist outward from the protein centre upon illumination, with the loop being displaced by a greater distance (~0.8 nm) than the helices move. Such distance and conformational sensitivity makes this location of the immobilization site for switching electrical measurements more attractive than for more inert, and less conformationally sensitive locations.

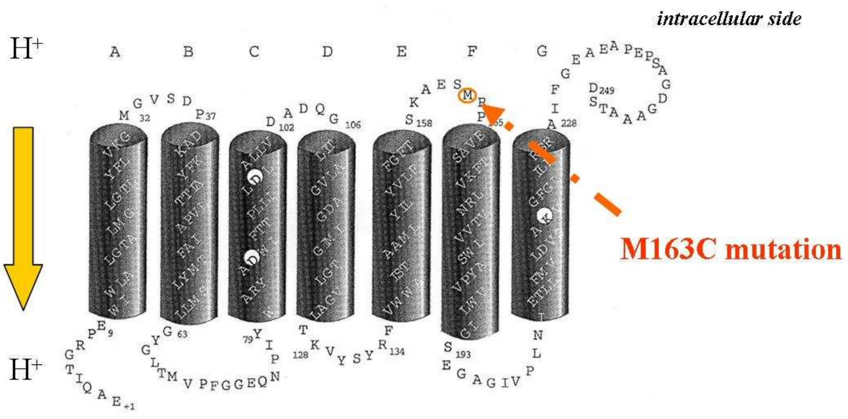

Figure 3.11 : Schematic representation of the secondary structure of BR. The methionine residue located at position 163 was replaced by a cysteine residue in the mutant used in this study. The mutation occurs on the EF loop that is the longest cytoplasmic loop of the protein and plays a key role in signal transduction in rhodopsins and GPCRs (adapted from[159]).

The aims of the work described in this chapter are to combine the genetic engineering of BR with partial delipidation of the protein in order to get a tightly and intimately-bound, homogenously-orientated protein sample. BR is maintained in its native trimeric structure and its conductivity is measured upon illumination, for the first time, on isolated protein trimers.

3.2 Material and Methods

3.2.1 Preparation of bacteriorhodopsin

High Na^+ concentrations are required for *Halobacterium* membrane stability, and the salt cannot be replaced by high concentrations of sucrose or other solutes. Peptone medium (see *Appendix 1* for composition) was used bacterial growth. The M163C mutant was originally kindly provided by Professor George Turner, University of Miami School of Medicine, USA.

3.2.1.a Culture of Halobacterium salinarium

Four BR colonies (wild-type BR or M163C mutant) from stock were placed into 2x 25 ml peptone media (see composition in *Appendix1*), to which 10 µl/ml vitamins (thiamine and biotin) were added; the cultures were incubated at 37°C and 170 rpm agitation. The growth of the culture was checked by measuring the cell density (OD measurements at $\lambda = 660$ nm) and of the amount of BR produced (OD measurements at $\lambda = 565$ nm).

3.2.1.b Purple membrane isolation

Starter cultures from a colony grow up to OD~1.2 in 5-7 days, while larger scale cultures take 7-14 days to grow up. When the OD_{660} reached 1.2, cultures were inoculated in 500 ml peptone media, and incubated at 37°C and 110 rpm agitation until OD_{660} reached 1.2 again. Cultures were centrifuged (7,000 g; 15 min; 4°C) and the pellets were resuspended in 4 M NaCl, mixed together, stirred and 15 µl of DNase was added. The preparation was dialysed overnight in 0.1 M NaCl and centrifuged (29,000 g; 45 min; 4°C). Purification of the purple membrane was performed by layering the sample on top of a sucrose gradient made of 25% (10 ml), 35% (9 ml) and 45% (9 ml) sucrose solution. An ultracentrifugation was performed at 25,000 rpm for 15h at 4°C. The supernatant was discarded, the purple band was harvested and sucrose remaining in the sample was removed by three washes in distilled water. After the last wash, the sample was resuspended in small volume of dH_2O and the amount of BR was assessed (OD reading at λ = 565 nm). Purple membrane preparation produces up to 50 mg of BR and an average of 30 mg of BR for 1 L culture. Samples to be used within a couple of months were stored at -20°C, while samples for long term storage were placed at -80°C. Sample preservation from the frost and from dimerisation of the cysteine was obtained by supplementing the samples with 20% TCEP reducing agent.

3.2.1.c Partial delipidation of BR

Partial (75%) delipidation of wild-type BR or BR_{cys} in purple membrane, which removes the outer lipids of the trimers but maintains the inner ones, was achieved by centrifuging the protein sample (20,900 rpm; 40 min; 4°C), discarding the supernatant and resolubilising the pellet in 50% (w/v) 20 mM CHAPS detergent. The preparation was kept overnight at 4°C under gentle stirring, washed in double-distilled water by centrifugation and the process was repeated twice. After the third and last incubation in detergent, the sample was centrifuged as stated earlier, resolubilised in distilled water to the desired concentration and stored at 4°C. A first test of the actual delipidation of the sample was performed by UV-vis spectrophotometry: 80µl of freshly delipidated BR was placed in a plastic cuvette and a continuous measurement of the sample absorbance was performed for wavelengths ranging from 250 nm to 650 nm. a shift in maximum absorbance of the sample from 568 nm to 560 nm was observed, as expected[214]. Samples were used within a week following delipidation.

3.2.1.d Bleaching of bacteriorhodopsin

Retinal removal was achieved by adding 0.2 M hydroxylamine (pH 7.0) to the BR samples and stirring under a halogen lamp placed at ~10 cm from the sample[216]. As the halogen lamp caused an elevation of sample temperature, the process was performed at 4°C in a cold room. Depending on the volume of BR to be bleached, samples were either placed in a small bleaker or in mini glass vials containing magnetic stirrers, then in a beaker with ice which was then placed on a stirrer. The solution was left stirring (30 min), then washed by centrifugation (15,000 rpm; 4°C; 30min) in double-distilled water in order to remove hydroxylamine and retinaloxime. The supernatant was discarded and incubated in hydroxylamine for 30 min. According to the volume of sample to be bleached, three to six incubations were required in order to see the typical colour change of the sample from purple to beige. The preparation was then centrifuged and washed several times in distilled water.

3.2.2 Gold-BR-gold junction construction

Although the first step when performing C-AFM on gold-BR-gold junctions consists in scanning the surface in order to locate the sample on the substrate, the major part of the experiments is performed in a static mode, with the conducting probe sensing the current passing through the junction. Such static spectroscopic studies were best performed on BR molecules packed on the surface, particularly in the case of the partially delipidated sample. Indeed, if the tip drifts during the experiment, it would then move to another group of trimers, continuing to record data of interest, rather than to bare gold substrate, thus stopping the measurements.

Single molecule experiments using SPM techniques are usually performed on substrates incubated with a low concentration of protein, in order to make sure that an individual molecule will be probed. AFM imaging has been successfully performed on low-concentration BR-incubated gold substrates. However, here in C-AFM, higher protein concentrations were used when performing *I-V* spectroscopy. Indeed, the probe required for such experiments has a thin gold layer that makes it conducting. The drawback of low protein coverage in this case is that probing individual mMm junctions for *I-V* measurements requires more scanning of the surface to detect the protein on the surface, thus increasing the risk of damaging or simply pulling off the probe gold layer. As a result, in this work, mMm junction construction was facilitated by using 20 µM concentration of BR_{cys}.

Modifying the conducting probe surface with BR_{cys} and engaging the ensemble on bare gold substrate has been achieved as an alternative protocol. The main issue was to adsorb the protein at the very apex of the probe, a process that cannot be controlled, and although some positive results were obtained, the sample layer was easily pulled off the probe. This had for direct consequence to cancel the experiment, while coating a gold substrate allows to move to another point of the surface, and measure the characteristics of another protein.

3.2.3 Characterisation of BR_{cys} chemical immobilization

UV-Visible spectroscopy was initially used as a quick and easy way to detect BR_{cys} adsorption onto transparent gold surface, confirmed by AFM imaging and ellipsometry. SPR was then used to assess preferential mutant protein binding to gold over the wild-type, showing that adsorption is via the cysteine mutation. Cyclic voltammetry (reductive stripping) confirmed the anchoring role of the cysteine residue and KFM then confirmed the homogeneous orientation of the protein.

Solution and solid phase UV-Vis spectroscopy were performed with a V600 Series UV-Visible spectrometer (Jasco, Japan).

3.2.3.a Solution phase UV-Vis spectroscopy

Confirmation of successful partial delipidation of BR was obtained by UV-vis spectroscopy prior construction of the gold-protein junctions.

The sample solution was placed in a 1cm quartz cuvette, which was washed thoroughly with acetone and deionized water before use. The extinction coefficient for BR has been previously measured to be 63000 $M^{-1}cm^{-1}$ at 568nm, maximum of absorbance of the protein embedded in PM. Continuous spectroscopy was ran for wavelengths ranging from 450 nm to 650 nm in order to detect the expected shift of BR peak of absorbance following delipidation. Data were processed using the Spectra Manager built-in software.

3.2.3.b Solid phase UV-Vis spectroscopy

After confirmation of the successful sample delipidation, BR_{cys} solution (25 µM) was incubated overnight at 4°C on a cleaned, transparent gold-on-glass substrate. Solid-phase UV-Vis spectroscopy was performed as an initial test for gold-protein junction formation prior starting scanning probe microscopy experiments. The protein-incubated transparent gold substrate was rinsed in phosphate buffer in order to remove any unbound material, and dried under nitrogen flow. The substrate was then placed in the thin solid sample holder of the spectrometer and a bare transparent gold substrate was used a blank. Continuous spectroscopy was performed for wavelengths ranging from 450 nm to 650 nm and data were processed using the built-in software.

3.2.3.c AFM imaging

AFM was used to image BR_{cys} before and after delipidation (mica substrate), as well as to confirm the gold-delipidated BR_{cys}-gold junction formation and estimate the surface coverage of the protein on gold (gold-on-glass substrate). AFM imaging of BR was performed with the PicoSPM and JPK Nanowizard systems and the data were processed with the systems ‘respective built-in softwares, as well as with the open source Gwyddion (http://gwyddion.net/).

The cysteine mutant was first imaged after purification. Since the purpose here is only to obtain images of the purple membrane, a mica substrate is used instead of gold. The freshly cleaved substrate is incubated in BR_{cys} solution (5μM in phosphate buffer) for 10 min, rinsed in phosphate buffer and dried under nitrogen. Imaging was performed in tapping mode in air using non-contact AFM probes (Tap300, Budget Sensors).

Imaging after BR_{cys} delipidation

The same procedure was followed after BRcys delipidation: the presence or absence, as expected, of membrane patches will confirm the efficiency of the delipidation process. Imaging was here performed in contact mode in solution (phosphate buffer) using contact mode AFM probes (Contact-G, Budget Sensors).

3.2.3.d Surface plasmon resonance

Glass substrates suitable for SPR with a 50nm coating of gold were obtained from Windsor Scientific. These substrates were cleaned by dropping hot piranha solution onto the area for 20-30 seconds before washing copiously with deionized water. Once cleaned the surfaces were used immediately to avoid contamination. An Autolab Espirit SPR system (Eco Chemie) was used for characterizing BR adsorption onto gold substrates. All measurements were performed at room temperature.

3.2.3.e Ellipsometry

The thickness of the BR sample adsorbed on gold substrates was measured by ellipsometry. Bare, un-annealed gold substrates (gold-on-glass, Arrandee, Germany) were cleaned as described in Chapter II and incubated overnight in protein solution (5 µM in phosphate buffer) at 4°C. The substrate was then rinsed in phosphate buffer and dried under nitrogen flow. The thickness of the samples adsorbed on gold was assessed using a Beaglehole Instruments (New Zealand) ellipsometer, and two sets of five measurements at different points of the surface were performed for each substrate. Since measurements were done over macroscopic distances, annealing the gold substrates was unnecessary. A non protein-modified un-annealed gold substrate was used as a blank, and results were averaged for each sample. The model used to assess the layer thickness assumed a single monolayer of refractive index 1.45 on the gold surface and 100% coverage.

3.2.3.f Cyclic voltammetry

The formation of sulphate-gold bonds between BR_{cys} and pristine gold substrates was confirmed by reductive stripping voltammetry. Gold disc electrodes were prepared following the protocol described in the Methods section, Chapter II. Electrochemical reductive desorption was performed using a μ-Autolab Type II potentiostat (Windsor Scientific UK Ltd.) controlled using GPES version 4.9 software and a home-made glass cell with a conventional three electrode-two compartment configuration. The counter electrode was a platinum wire gauze and all potentials were referred to a standard calomel electrode (SCE, Radiometer, UK). Macrodisk gold electrodes (BAS, 1.6 mm diameter) were pretreated by reductive desorption in 0.1 M NaOH in deionized water by cyclic voltammetry from -0.5 to -1.5 V at a sweep rate of 1 V/s (40 scans). Electrodes were rinsed with deionized water and mechanically cleaned by successive polishes with 1, 0.3 and 0.1 μm alumina/diamond slurry (Struers A/S) on a Buehler microcloth polishing pad. This was followed by sonication in deionized water and hot piranha solution treatment for about 15 min. The electrodes were then electrochemically polished by 25 successive cyclic voltammetry scans from -0.2 to +1.5 V in 100 mM H_2SO_4 at 100 mV/s. The gold oxide produced on the gold surface was stripped by running 10 cyclic voltammetry scans from 0.75 to 0.2 V in 100 mM H_2SO_4 and further reduced by incubation with absolute alcohol at ambient temperature for 20 min.

3.2.3.g KFM imaging and surface potential measurements

Gold substrates (Arrandee) were flame-annealed and cleaned with successive washes in piranha solution, water and ethanol before being dried under nitrogen. BR sample was pipetted on the substrate and left to incubate overnight at 4°C in a sealed humid container. After incubation, BR solution was gently washed off with de-ionised water in order to remove any non/weakly-immobilised BR molecules/patches.

The gold substrate was then analysed with KFM carried out using a Nanoscope IV multimode (Veeco/Bruker, USA) with gold coated tapping mode probes (Tap300E, Budget Sensors). Controlled environmental conditions of light were achieved by placing the microscope in a light-proof box with an optical aperture. Samples were illuminated using a M-150 fibre light source (150 W halogen lamp) passed through 495 nm long pass filter, or 550 nm used for controls.

In order to ascertain surface potential changes, BR trimers or patches were systematically scanned twice: once with the light off and once with the light on (i.e. the surface potential of the same BR patch or delipidated BR trimer was measured under both conditions). KFM topographical and surface potential data were further processed using Gwyddion (http://gwyddion.net/).

3.3 Results and Discussion

3.3.1 Preparation of bacteriorhodopsin

3.3.1.a Isolation of the purple membrane

Bacteriorhodopsin expression during bacterial cell growth can be easily followed visually, by the increasing intensity of the colour of the bacterial cultures from yellow starting cultures (Figure 41 a, left) to purple at the final stage (Figure 3.12 b).

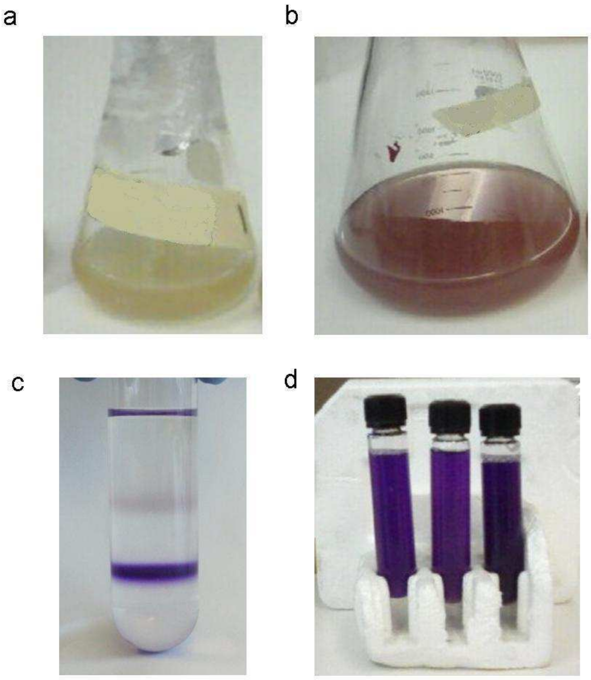

Figure 3.12: Expression and purification of the purple membrane of *H.salinarium* by sucrose gradient and ultracentrifugation. a. Starting culture of *Halobacterium salinarium*. The high level of BR expression is clearly visible by the intensity of the purple colour at the end of cell growth **b**. After dialysis and ultracentrifugation, the resuspended pellet of M163C BR mutant was layered on top of a 25% to 45% sucrose gradient; a tight band corresponding to the purified purple membrane was observed at 45% sucrose. Several washes then provided 30 mg of BR per 1L of culture on average, of a typical purple colour.

Purification of the protein resulted in typically purple suspensions containing patches of purple membrane. AFM imaging is performed after purification in order to compare the sample condition before and after its delipidation, which the next preparation step before performing the conductance measurements. As seen in Figure 3.13, isolated membrane patches are clearly visible all over the surface.

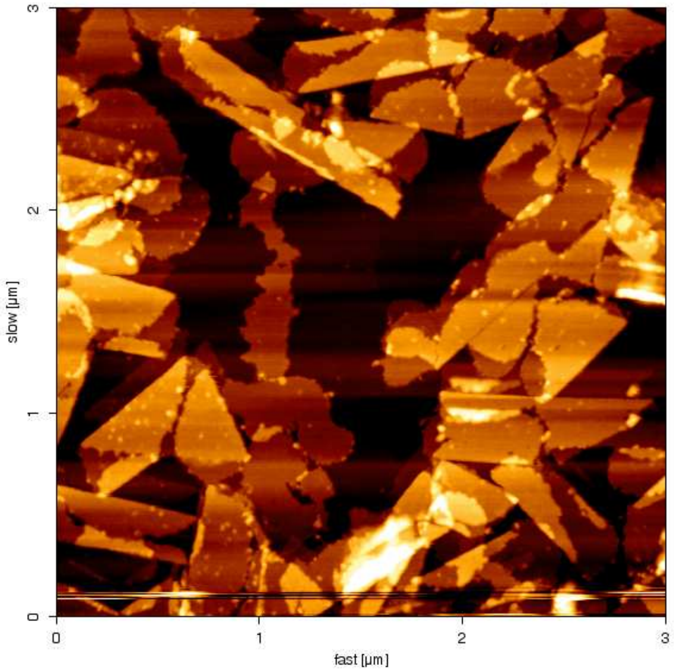

Figure 3.13: AFM picture of BR$_{cys}$ after purification. BR-containing membrane patches isolated from the bacterial cell were imaged in solution after a very short (3 min) incubation time on mica explaining why some of them are “floating” instead of being adsorbed on the surface (topographic image; contact mode; phosphate buffer; 3µm x 3µm).

3.3.1.b Partial delipidation of BR

The efficiency of the delipidation was systematically controlled by UV-vis spectroscopy. When performing the partial delipidation process for the first time, the sample was also imaged by AFM on mica in order to obtain a visual confirmation of the absence of membrane patches in the sample before incubating the sample on gold for measuring the sample electrical conductance.

3.3.1.b.i UV-vis spectroscopy

After partial delipidation in CHAPS detergent, a shift of the maximum of absorbance of BR is progressively observed over the three phases of delipidation, up to a maximum shift of absorbance from 570 nm in the purple membrane to 560 nm. Reaching this point means that the lipids surrounding the trimers have been removed, and further CHAPS incubations do not affect the sample after this stage.

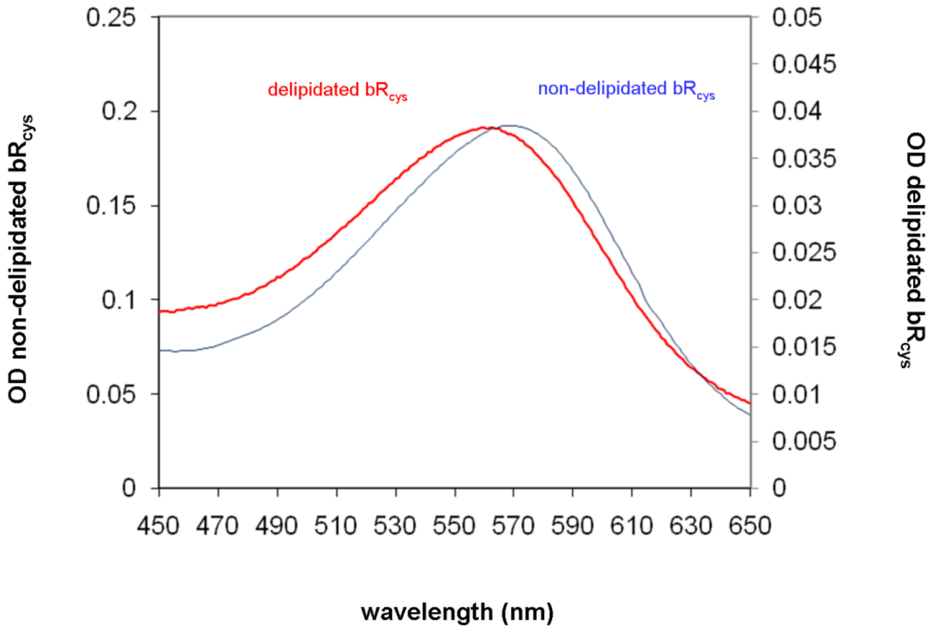

Figure 3.14: UV- visible absorption spectra of BR$_{cys}$ before and after partial delipidation. A shift of maximum absorbance from 570 nm (blue curve) to 560 nm (red curve) is observed after the 75% delipidation process, as expected [214].

Removing the remaining lipids, located within the trimers and which are involved in the cohesion of the trimeric structure would require a harsher, TritonX100-based treatment.

3.3.1.b.ii AFM imaging of delipidated sample

The efficiency of the first three partial delipidations was also tested by AFM imaging on mica, a much faster (a few minutes incubation time, *vs* overnight incubation on gold) and affordable way to visualize whether purple membrane patches are still present in the sample solution.

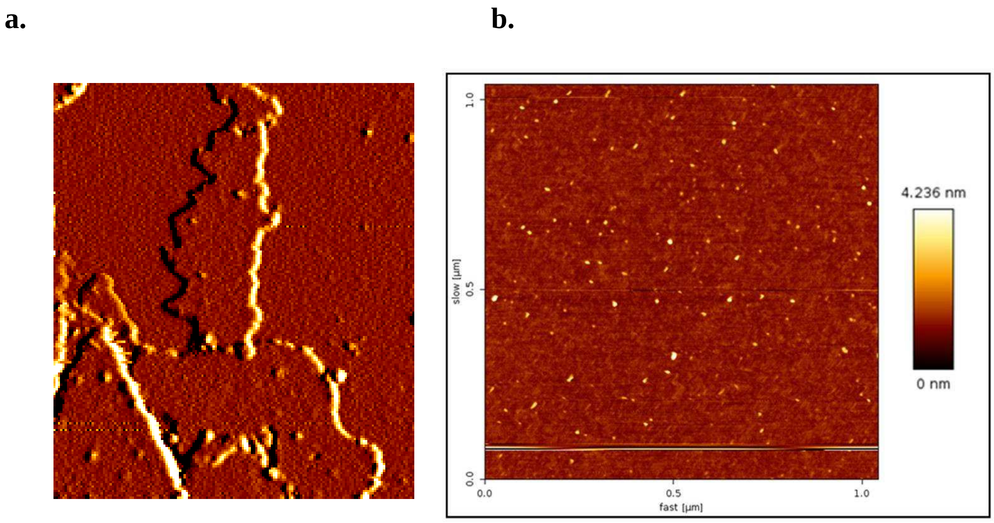

Figure 3.15: AFM imaging of the M163C mutant of bacteriorhodopsin before and after 75% delipidation. **a**. AFM picture of native BRcys on mica, before delipidation. Purple membrane patches are clearly visible (error signal; 20µM, contact mode in phosphate buffer; 1.9 µm x 2.05 µm). **b.** AFM image of 75% delipidated BR_{cys} mutant on mica. Micrometer-wide patches have disappeared to leave place to sparse BR molecules, showing a height close to the 5 nm expected from crystallography data[133, 217](contact mode, 8 µM in phosphate buffer; 1.1µm x 1.1µm)

Figure 3.15.a shows an AFM image obtained after BR purification but before delipidation: purple membrane patches are clearly visible. After delipidation (Figure 3.15.b), isolated features can be seen, sparsely adsorbed on the substrate, while no more PM patches are observed. The height of these features, close to the 5 nm expected for BR from crystallographic data[127, 133], together with the UV-vis spectra and the typical peak at 560 nm confirm that bacteriorhodopsin has been successfully isolated from its native lipid

environment. Identical results were obtained for wild-type BR and BR_{cys} after delipidation.

3.3.1.c Bleaching of bacteriorhodopsin

Removal of the retinal chromophore was performed to provide a control sample and ensure that differential responses to illumination observed in C-AFM were due to changes in BR conductance. Bleaching was obtained by stirring a hydroxylamine-containing solution of bacteriorhodopsin under illumination, resulting in the typical purple solution of retinal-bound BR to become a white solution of retinal-free BR (Figure 3.16).

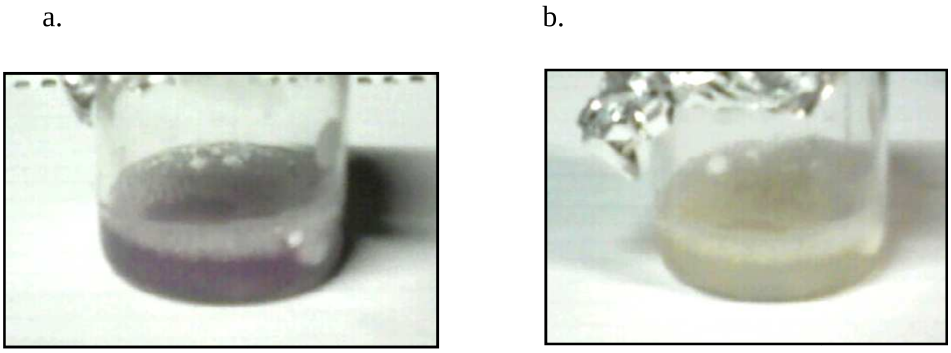

Figure 3.16: Bleaching of bacteriorhodopsin. The bleaching process uses a hydroxylamine-containing solution of bacteriorhodopsin stirred under illumination. The sample solution goes from a typical purple solution of retinal-bound BR (a) to a white solution of retinal-free BR (b).

3.3.2 Characterisation of gold-delipidated BR_{cys} -gold junctions

Characterisation of the mMm junctions is crucial before starting to measure their conductance behaviour. Numerous biophysical and electrochemical techniques have been used in order to assess the efficiency of the delipidation process (solid-phase UV-vis spectroscopy, AFM, STM and KFM imaging), the robust binding onto gold of the cysteine mutant compared to the wild-type protein (SPR and reductive cyclic voltammetry), the sample thickness on gold (ellipsometry) and the homogeneous orientation of the sample (transient photocurrent measurements).

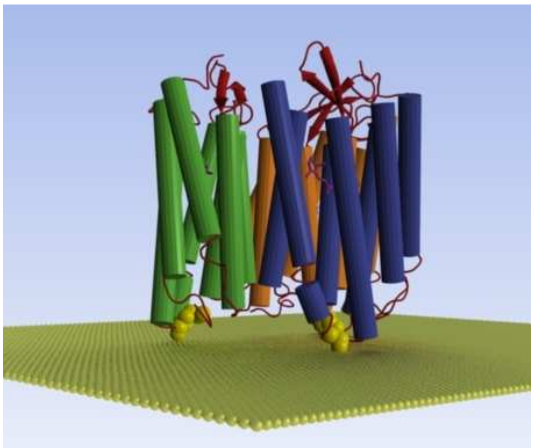

Figure 3.17. Diagrammatic representation of the mutant BR$_{cys}$ adsorbed on gold via its cysteine residue. The methionine-163 residue on the CP side of BR in the accessible helix E-F loop, has been specifically replaced with a solution exposed cysteine (shown as orange spheres), enabling orientated chemisorption. The resulting adlayers are demonstrably covalently bound, stable to washing, and fully functional. The retinal moieties (purple) are approximately orthogonal to the supporting surface (PBB: 1BRR; Thanks to Amol Patil).

3.3.2.a Solid phase UV-Vis spectroscopy

In order to ensure that the partially delipidated cysteine mutant does adsorb on gold, a first control consisted in comparing the absorbance of the sample in solution and after incubation on a gold substrate. An absorbance peak was observed at 560 nm for the delipidated sample in solution, as expected[174], and a hypsochromic shift to 500 nm occurred after binding onto gold (Figure 3.18), showing that the cysteine mutant was bound to the gold substrate and retained its absorption characteristics.

An explanation for this hypsochromic shift could be the plasmon effect due to the gold substrate: coupling of the incident wave of light of the spectrophotometer with the conduction band electrons in the metal induces a coherent electronic oscillation of the free electrons on the gold surface, which may interact with the retinal and thus alter the detected peak of absorbance.

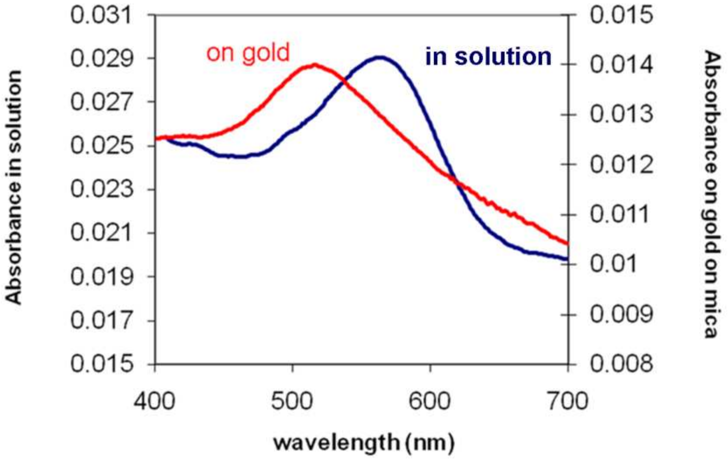

Figure 3.18: UV-Visible absorption spectra of the 75% delipidated BR$_{cys}$ mutant in solution and after adsorption onto a transparent gold surface. The expected peak of absorbance at 560nm is observed for the partially delipidated sample[214]. A shift of the maximum of absorbance to 500 nm is observed after binding onto transparent gold on mica substrate. This peak of absorbance shows that M163C binds on gold and keeps its photon absorption characteristics as a dry film.

Previous BR adsorption on gold-containing substrates reportedly resulted in a shift of the protein's absorption peak[224]. Indeed, in 2005, Horn and Steinem adsorbed purple membrane samples onto gold-coated alumina substrates and observed a 20nm hypsochromic shift of absorbance compared to values obtained in solution. BR was not directly adsorbed on the gold layer, but on an intermediate lipid monolayer. Here, not only was the protein directly adsorbed on the gold substrate without any intermediate lipid layer, but it was also partially delipidated, and thus not confined to micron-scale two- dimensional PM patches anymore. The retinal triggers BR response to light, and the protein environment drastically modulates the absorption maximum of the chromophore: in solution, BR maximum of absorbance is shifted to 600 nm at pH 3[119], while at neutral pH the value is shifted to 555nm on acetylation[193] and to 560 nm upon partial delipidation. We can conclude that the combination of a drastic change in the protein (and retinal) environment and the plasmon effect of the gold substrate causes the 60 nm shift observed upon BR_{cys} binding on gold.

UV-visible spectroscopy constitutes a quick and easy way of showing that partially delipidated BR_{cys} adsorbed onto gold, however, the technique does not provide any quantitative information. Further surface characterisation was obtained by STM, AFM and KFM imaging, as well as SPR, ellipsometry, cyclic voltammetry and photocurrent measurements.

3.3.2.b STM and AFM imaging of BR_{cys}

Imaging of non-delipidated wild-type BR showed some sample adsorption, due to the µm-wide interaction areas offered by the membrane patches, but with sparse and non-homogenous coverage. Topographical analysis of delipidated wild-type BR, where the protein-surface association lacks the stability conferred either by the cysteine-gold bond of the mutant or by the large surface area of interaction (native purple membrane), was only possible with difficulty and showed very sparse trimer coverage.

AFM imaging of annealed gold surfaces exposed to solutions of non-delipidated BR_{cys} showed numerous patches of purple membrane which ranged from a few tens to hundreds of square nanometers (Figure 3.19 a) with a coverage ranging from 8 to 40 % (20 µM solution incubations varying from an hour to overnight) of the available surface.

Analyses of delipidated BR_{cys} samples resolved fairly homogeneous adlayers of high molecular density (70 - 80% as calculated using Gwyddion SPM analysis software). Significantly, no membrane patches are observed in either of the delipidated samples, showing the efficiency of the delipidation process.

Imaging of delipidated M163C was also performed using STM. All SPM images obtained for the partially delipidated mutant showed that the isolated protein features on the gold surfaces exhibit heights around 5 nm (Figure 3.19 b), which corresponds to the crystallographic data reported in the literature[127]. It is noteworthy that features observed on STM and AFM images may consist of individual trimers of BR but are more likely to consist, since the delipidation was partial, of several trimers that remained linked to each other (around 25% of native lipids are still present if the sample[206]). Partially delipidated BR forms a relatively homogeneous sub monolayer of isolated features with diameters in the range of 20-30nm, and the average diameter, measured to be 24.8±3.9 nm over 100 features in 3 different samples, is in correlation with this assumption (the diameter of a single trimer in the purple membrane is 7.5 nm[50]).

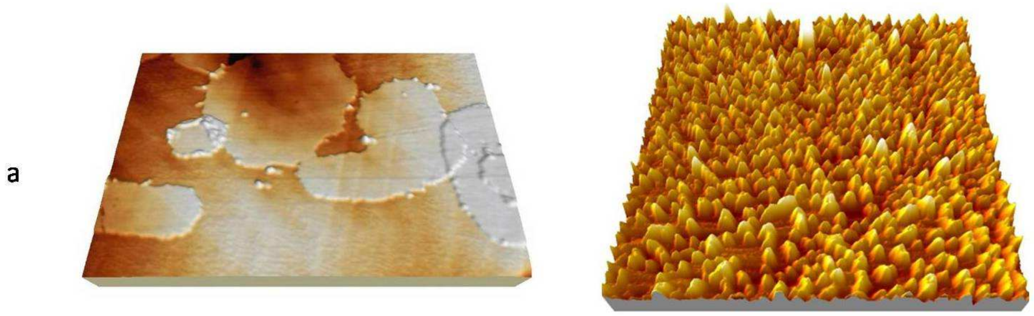

20 µM non-delipidated BR_{cys}

20 µM delipidated BR_{cys}

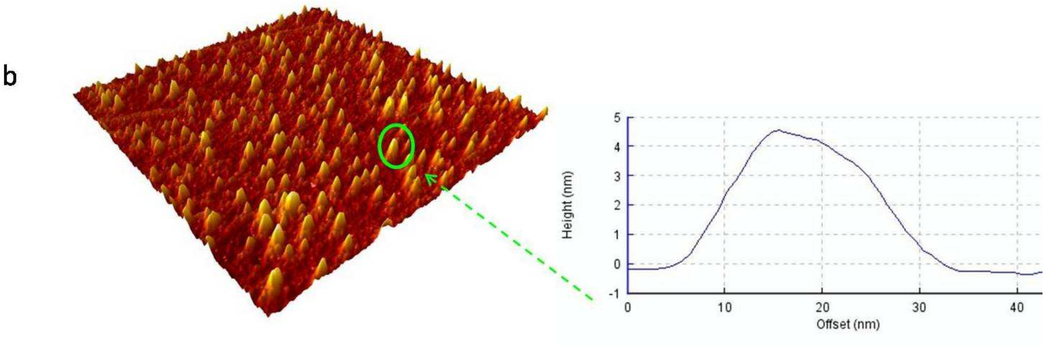

10 µM delipidated BR_{cys}

Figure 3.19: AFM and STM imaging of BR_{cys} adsorbed on gold before and after delipidation with different surface coverage densities. **a.** AFM images of gold on glass substrates incubated with 20µM non-delipidated BR_{cys} concentration, where patches of purple membrane are clearly visible (left), and incubated with 20µM of partially delipidated BR_{cys}, where no more patches are visible, and where a homogenous coverage is observed. **b.** STM image of gold on glass substrate incubated with 10µM BR_{cys}. The height of one of the sample features, around 5 nm, is shown on the right graph and is close to the height expected for BR.

Morevover, the tip-sample convolution phenomenon described in Chapter II, which provides higher values than the actual feature's measurements, is likely to occur here due the gold coating present of the C-AFM probe. The aim of this work was to study BR out the 2D crystal organisation of the purple membrane, while retaining its native trimeric structure - hence the partial, instead of total, delipidation. High resolution imaging and a more accurate determination of the number of trimers present in each feature are part of a future work.

For the rest of this work, the terms "isolated trimers" will be used to designate isolated BR_{cys} features that may consist of groups of trimers.

3.3.2.c Ellipsometry

The thickness of the BR sample adsorbed on gold substrates was measured by ellipsometry. The sample thicknesses on gold were found to be 2.67± 0.17nm for the delipidated mutant and 5.27±1.84nm for the non-delipidated M163C mutant, which is still embedded within the membrane and thus showed a thickness close to the 5nm expected from crystallographic data[127]. AFM imaging showed that this sample adsorbs on substrates as patches of membrane, each of them being up to several micrometers wide (Figure 3.19 a). This result agrees with the initial assumption of a protein monolayer and 100% coverage. The delipidated sample, however, shows a significantly smaller thickness, less than half that expected. In this case, 75% of the PM lipids were removed, and bacteriorhodopsin was expected to be found as isolated trimers, some of them being possibly still linked to each other in high oligomers of trimers, but with a definite loss of organisation into extended patches of PM. The small (2.67 nm) thickness recorded for this sample is thus due to a scatter distribution of protein molecules on the gold surface, suggesting a sub-monolayer coverage of delipidated BR on gold.

3.3.2.d SPR

Surface plasmon resonance was performed in order to assess the role of the M163C mutation by comparing the adsorption on gold of both partially-delipidated WT and mutant proteins (Figure 3.20).

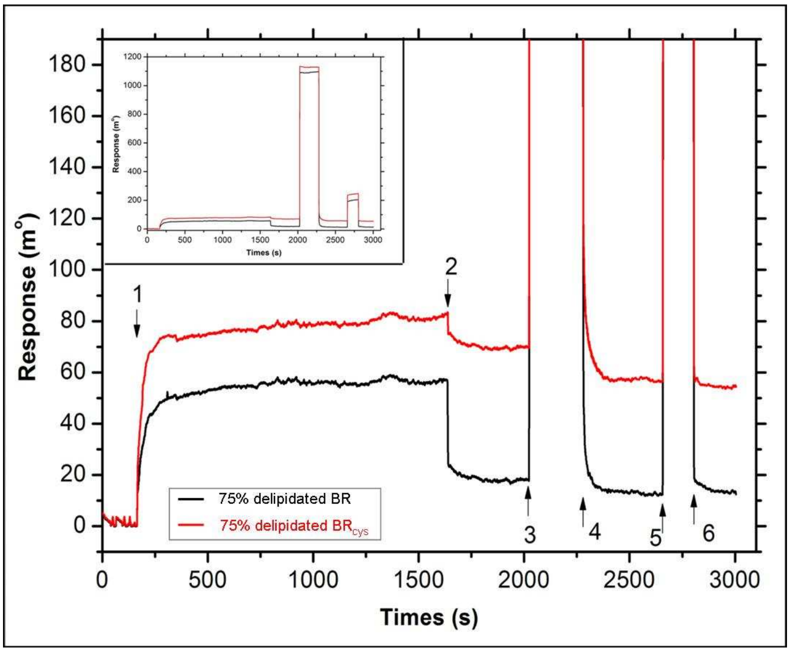

Figure 3.20 : Comparison of the immobilization of partially delipidated BR$_{cys}$ and partially delipidated wild-type BR on bare gold using SPR.1: sample injection (8 μM); 2, deionized water injection to start a dissociation phase; 3: surface regeneration by injection of 1 M KCl; 4: further draining of the cell by injection of deionized water; 5: injection of 1% v/v Tween 20 solution into the cell; 6: the surface wash with deionized water. BR$_{cys}$ and WT BR were both immobilised on the gold electrode after injection, but the amount of cysteine mutant detected after washing the gold chip was four times higher (57.13 ± 4.06 m° equivalent to a protein density on the surface of 46.83 ± 3.33 ng/cm^2 or 1.80 ± 0.13 pmol/ cm^2) than the amount of wild-type BR (13.69 ± 1.86 m° equivalent to 11.22 ± 1.52 ng/cm^2 or 0.43 ± 0.06 pmol/ cm^2). This is fully consistent with the presence of the cysteine mutation.

Although SPR binding curves showed that BR$_{cys}$ and wild-type BR were both immobilized on the sensor chips (bare gold surfaces) after injection, the amount of cysteine mutant detected after washing the gold chip with detergent buffer was four times higher (protein density on the surface of 46.83 ± 3.33 ng/cm^2) than for wild-type BR

(11.22 ± 1.52 ng/cm^2). This confirms that BR$_{cys}$ is chemisorbed via a thiolate bond rather than being physisorbed as observed for WT BR.

3.3.2.e Cyclic voltammetry

The thiolate chemisorption of the M163 mutant on gold was studied further and quantified by reductive stripping voltammetry (cyclic voltammetry). Specifically, in sweeping the surface potential of the underlying electrode cathodically in 100 mM NaOH, a reduction peak originating from the cleavage of the gold-thiolate bonds was detected at~ -1.1V *vs* SCE, while no stripping peak were observed in control experiments with the wild-type BR (Figure 3.21).

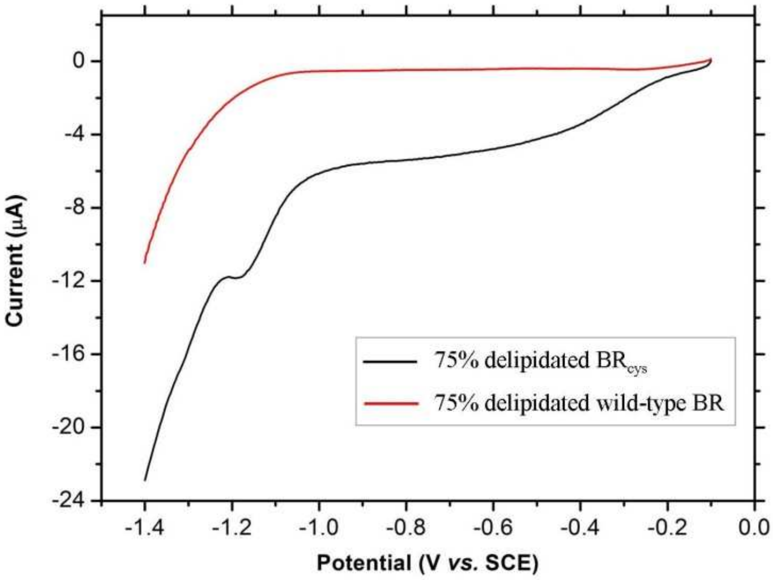

Figure 3.21: Cyclic voltammogram of 75% delipidated BR$_{cys}$. Adlayer on bare gold substrate, confirming the presence of an anchoring thiolate-gold bond (in contrast to delipidated wild type BR) and indicating a controllable assembly of BR$_{cys}$ from sub- to full- coverage on gold. This is in good agreement with the AFM and surface plasmon resonance data.

An integration of this cathodic current produces average surface coverage values of 5.3 pmols/cm^2 (approximately 80% coverage, considering a 35 nm^2 footprint for each trimer including their inner lipids[186]), which is in agreement with the AFM observations.

3.3.2.f KFM analysis of BR_{cys}

As described in Chapter II, KFM is performed by double-scanning each line of the surface, acquiring topographical data and surface potential information, with the possibility to provide an image of the sample surface potential (Figure 3.22).

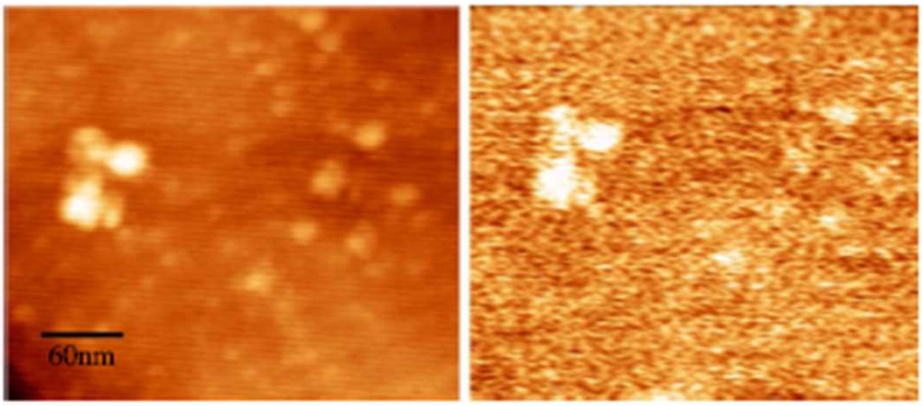

Figure 3.22: Topograph (left, z range 5nm) and surface potential (right, potential range 18mV) images of BR_{cys} on a gold surface obtained in lift mode. The driving voltage amplitude for potential imaging was 6V, during which the tip was lifted 10 nm above the surface. The protein on the left is clearly visible in the potential image while what appears to be individual protein species to the right are less well resolved (thanks to Ben Peters for this image).

Images of adsorbed delipidated BR_{cys} on gold show isolated protein trimers on both topographic and surface potential images (as discussed earlier for Figure 3.19, the observed BR features may be groups of trimers that remained attached to each other after partial delipidation), where the protein features correspond to regions of higher potential.

Further experiments focused on measuring the surface potential of partially delipidated BR_{cys} upon illumination, and in reproducing the experiments on WT BR and on partially delipidated WT BR. The aim is to try and see whether KFM can provide evidence of a homogenous orientation of the mutant sample on gold compared to the wild-type.

Surface potential values were obtained as successive measurements of the surface potential of cross sections of the samples. These data were processed and their distribution is shown on Figure 3.23.

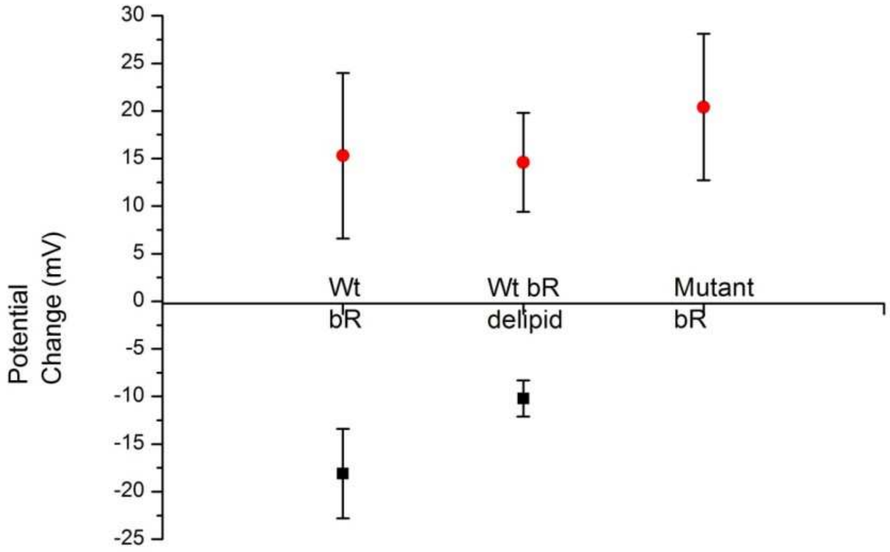

Figure 3.23. Comparative distribution of photoinduced surface potential switch for WT-BR, partially delipidated WT BR and partially delipidated BR_{cys} as measured upon illumination with a 495 nm long pass filter. Wild-type proteins (lipidated/non lipidated) lack orientational preference for surface contact and their surface potential thus switches positively or negatively on illumination depending on whether the cytoplasmic or extracellular surfaces are being sampled. Immobilized delipidated BR_{cys} displays only photoinduced increases in surface potential, confirming the molecular homogeneous orientation on gold. Data were acquired across 10 WT PM patches, 20 isolated features of delipidated WT BR and 50 isolated trimers of delipidated BR_{cys}.

Data presented on this graph only show the results obtained on illumination.

WT samples (delipidated or not) are only present on the gold surface through weak physical interactions with the surface and have no orientational preference upon adsorption on gold. Therefore, upon illumination, a positive or negative shift of surface potential will be detected, depending on whether the cytoplasmic side (proton depletion) or the extracellular side (proton accumulation) is probed.

Positive and negative values of the surface potential shift were, indeed, observed for both WT samples, confirming the random orientation of the wild-type specie. Regarding the delipidated cysteine mutant, however, shifts of surface potential upon illumination are only displaying positive values: these results confirm that isolated trimers of BR_{cys} retain their surface potential characteristics and that the M163C mutation, in addition to its anchoring role, also facilitates the homogeneous orientation of the sample on gold.

3.4 Conclusion

The unique physical and chemical properties of bacteriorhodopsin discussed in this chapter have driven a considerable interest in the incorporation of BR into electronic devices.

The hallmark of any molecular bioelectronic device is the ability for facile, reproducible, robust and controlled interfacial assembly. The work presented here explored the combined effects of a strategically located cysteine mutation (M163C) and partial delipidation of bacteriorhodopsin. The anchoring role of the cysteine residue has been demonstrated through electrochemical stripping and surface plasmon resonance analyses, which both showed a increased (approximately three-fold) and more robust association of BR_{cys} on a gold surface compared to wild-type BR under identical conditions. More importantly, this coverage was achieved in a unique orientation of the mutant, its cytoplasmic side homogeneously facing the gold surface, as confirmed by photocurrent measurements.

Chapter IV – Molecular scale conductance photoswitching in engineered bacteriorhodopsin

4.1 Introduction

The highly wavelength-selective proton pumping ability of bacteriorhodopsin, coupled with a high quantum yield efficiency (as high as 0.7)[218], thermal and pH stability, has led to the protein being largely studied for possible applications as a photoactive component in biological transistors[27], molecular sensors[166], data storage devices and artificial retinas[219], as discussed in Chapter III. Previous C-AFM studies have shown that the electrical conductance of BR within the purple membrane could be reversibly switched upon illumination[169, 194, 220, 221], while it was demonstrated in Chapter III, and for the first time, that BR could be depleted from most of its membrane lipids and adsorbed on a gold electrode in a robust, reproducible and homogeneously oriented way while remaining photoactive.

Here, C-AFM measurements are performed in an attempt to detect, for isolated trimers of BR_{cys}, the shift of conductance upon illumination that was previously reported for membrane-embedded BR. The wavelength specificity as well as the role of the retinal chromophore in BR electronic response has also been investigated by C-AFM, KFM and photocurrent measurements.

4.1.1 Preliminary C-AFM measurements on SAMs

Current-voltage spectroscopy performed on light-sensitive BR involves illuminating the sample with a light source, which will thus also illuminate the microscope and its current-sensing constituents. In order to ensure that the *I-V* curves obtained for BR will only reflect the protein's behaviour on illumination, octanethiol self-assembled monolayers were used as a control system prior BR analysis. Indeed, as described in Chapter I, alkanethiols-based SAMs are commonly used for molecular electronic measurements and are easily formed. Most importantly in this case, they are not light-sensitive, alternation of light and dark during data acquisition should thus not have any influence on the conductance results.

4.1.2 C-AFM measurements of BR electrical conductance

Conducting-probe atomic force microscopy was used to measure the electrical response of isolated trimers of BR_{cys} towards an applied bias, alternating from dark conditions to subsequent illumination at a fixed wavelength.

The CP-AFM approach provides a means of robustly engaging BR_{cys} with both electrodes (gold tip and substrate). Previous C-AFM analyses with metal coated probes have specifically resolved and modelled protein conductance under a wide range of experimental conditions. Attempts to engage monolayers of BR in the native PM for electronic measurements, through the use of either lithographically fabricated contacts or C-AFM probes, have lead to reported junction resistances in the TΩ[191] range and low (pA range) currents per trimer[169, 191, 193].

4.1.3 KFM measurements of BR surface potential

KFM is used here to provide alternative measures of BR electronic properties, by studying the surface potential of the protein adsorbed on gold.

While there has been much work reporting AFM imaging of BR[222, 223], surface potential analysis of the protein has not been as widely researched; in general, there is very little literature on the surface potential analysis of biomolecules. So far, all KFM analysis performed on BR have been carried out on highly ordered pyrolytic graphite (HOPG) substrates, with the protein embedded within the purple membrane. HOPG is a conductive mineral with a lamellar structure, atomically flat, which facilitates the resolution of BR patches. KFM has been used to measure a shift in potential of purple membrane on illumination[224] . The surface potential work carried out by Knapp *et al.* of BR deposited on HOPG showed a potential switching of 3-5 mV of BR upon illumination[206]. However, similar work carried out by Lee *et al.* reported a potential switching of 37mV upon illumination, measured by Scanning Surface Potential Microscopy (SSPM)[225]. It is possible that the lift heights used by the two groups differed largely, hence the variance in the reported surface potential switching. By using a higher lift height for the second pass the interaction between the tip and the sample will be weaker, thus giving a smaller potential difference.

Bacteriorhodopsin in the membrane has a permanent dipole moment which has been measured to range from ~98D[226] to ~1000D[227] per monomer, oriented perpendicularly to the plane of the membrane (i.e. parallel to the proton transport channel). On illumination with light of a suitable wavelength a shift in the dipole moment has been observed, falling in the 10-30D range[226] . It is likely that interaction of native BR with the lipid bilayer and with adjacent proteins in the tightly packed crystal structure will affect this shift, with Kestheyli[227] observing a complete disappearance of a permanent dipole moment on solubilization, and Otomo *et al.* measuring a strong pH dependence on the magnitude and direction of the shift. Despite these variations in the measured size of the effect, a shift in the dipole moment should lead to a shift in the measured surface potential relative to the gold substrate.

To the best of our knowledge, no studies have been performed on an isolated, oriented molecular species such as the isolated trimers of BR_{cys} studied in this work.

KFM was used here as a control of the C-AFM experiments : the surface potential of the M163C mutant was measured on gold under light and dark conditions and compared to that of WT-BR under same conditions.

4.1.4 Photocurrent measurements of BR

The photon-generated currents of BR and BR_{cys} during their photocycle were measured using chrono-amperometric methods. Experiments were performed in the dark and under illumination using varied wavelengths and light intensities, in order to determine whether variation of BR photocurrent is wavelength-specific, and in particular, whether the cysteine residue involves any enhancement in the photocurrent detected for BR_{cys}, compared to the photocurrent measured for wild-type BR.

Photocurrent analysis of BR and different mutant variants of the protein has been extensively studied under various experimental conditions, however, there has not been any conclusive results so far deciphering the mechanism by which illumination induces the current variation detected in the supporting electrode.

The vast majority of interfacial photocurrent analyses have employed an optically transparent indium tin oxide (ITO) surface[177, 200, 228], with, additionally, some precedence for immobilisation on metallic films[199, 229, 230 231]and model membranes[232]. Attempts to enhance BR photocurrent by co-deposition of quantum dots (activated by the same optical wavelength as BR)[233] or silver nanoparticles (to increase the photoinduced current by forcing BR molecules to follow a shorter photocycle and, thus, increase the rate of proton release) have also been reported[234]. All prior research does agree, though, on the fact that the current transients observed when BR is subjected to yellow light are a result of the molecule photocycle and the changes in local pH associated with it[177]. Significantly, under conditions of moderate (<1V) bias, current densities per BR monolayer are typically in the pA order[169].

4.2 Material et Methods

4.2.1 C-AFM conductance measurements of mMm junctions

4.2.1.a Octanethiol SAMs formation

A freshly annealed gold substrate (protocol described in Chapter III) was incubated in a 5mM ethanolic solution of octanethiol for at least 8 hours at room temperature. The substrate was then washed with ethanol in order to discard any unbound material, and dried under nitrogen flow. It is crucial to avoid any contamination of the gold surface, all preparation steps were thus performed with absolute ethanol.

4.2.1.b I-V spectroscopy parameters

4.2.1.b.i Initial checks

In order to ensure that the microscope is ready to measure the sample electrical characteristics, the elements involved in current transmission between the module holding the conducting probe and the plate carrying the sample were tested with an ampmeter. Current testing was performed after the initial experimental set up, as well as each time a new probe or substrate was used. Indeed, all CP-AFM systems are made of small units that require being in contact for sensing current during I-V scans. It may happen that one item (such as the spring connecting the sample to the sample stage) is slightly misplaced: this may not be visible when setting up the experiment, but then results in no current or abnormal *I-V* curves being detected.

On the PicoSPM microscope (Agilent), electrical cables are connected from the microscope head (holding the conducting probe) to a current sensing circuit on the sample plate (Figure xx in chapter II). Current transmission between both units was tested between the gold sample and the current sensing circuit.

On the JPK microscope, current transmission was tested between the probe and the conducting module on the head of the microscope (chapter II), as well as between the gold substrate and the sample plate.

4.2.1.ii Probes

Conducting probes used for current-voltage spectroscopy experiments are soft contact-mode silicon probes with an overall gold coating and a spring constant of 0.2 N/m (ContGB, Budget Sensors, Bulgaria). In order to limit as much as possible the risk of gold substrate contamination, the probes were cleaned in a benchtop UV-ozone cleaner (Bioforce UV/Ozone ProCleaner, USA) for 30 minutes before use.

4.2.1.iii I-V spectroscopy

Current-voltage spectroscopy was performed on gold-partially delipidated BR_{cys}-gold junctions prepared according to the procedure described in Chapter III. Molecular Imaging Pico STM instrument (Agilent Technologies) using a 1196 AFMS scanner, and on a NanoWizard AFM fitted with the C-AFM module (JPK, Germany) at different times. Illumination was performed with a light source (KL 1500 halogen cold light source,150 W, Schott) whose light guide was fitted onto the microscope, at the substrate level for direct illumination of the sample. Experiments were performed in a dark room. Gold-on-glass substrates (Arrandee, Germany) were cleaned in the UV/ozone box for 30 minutes, washed with ethanol followed by deionised water and were then annealed to obtain atomically flat gold terraces. Annealing was performed by passing a flame for a few seconds over the substrate, gold face up, repeated 2-3 times. Successful annealing was detected by the change in appearance of the gold layer, from a shiny to a cloudy aspect. The substrate was then allowed to cool down for a few minutes and was incubated overnight at 4°C in 120 µl of 10 µM protein solution in a Petri dish. A layer of parafilm was placed between the dish and its lid in order to avoid sample evaporation overnight.

The substrate was then thoroughly washed with distilled water to ensure removal of any unbound protein, dried under nitrogen and glued onto a metallic disk. Nitrogen was flowed in the microscope chamber before starting the experiment to reduce the level of humidity. The conducting tip was then brought into contact at low force (1 nN) and surface characterisation was performed in contact mode C-AFM: the substrate was partially scanned at constant voltage (limited scanning is required due to the fragility of the probe's gold coating) in order to obtain height and current images and thus localise the delipidated proteins on the surface. Between 5 and 45 BR_{cys} junctions were probed for each substrate. Coating the gold substrate, rather than the gold AFM probe, with the protein provides the possibility to see the gold-BR junctions and, with the JPK microscope, to choose which junctions to study. The small size of the probe would result in less protein being adsorbed, and this, added to the fragility of the probe thin gold coating, increases the risk of damaging the sample and cancelling the experiment soon after beginning the measurements. Electrical characteristics were recorded independently of force feedback. Preliminary I-V curves were obtained in order to determine the minimum range of forces that could be applied to the sample to detect a current flow through the molecules without damaging the protein. The minimum force to apply was 6 nN, results becoming more stable and reproducible at 10nN, while the maximum force to be applied before exerting a too high pressure to the sample was 45 nN. A force of 15 nN was then systematically applied during the experiments, unless stated otherwise. A voltage bias ranging from -1.5V to +1.5V was applied to the sample and the sweep duration was set up at 0.5s.

4.2.1.d Illumination cycles

All *I-V* spectroscopy experiments were started in the dark. A Schott KL1500 light box was used as a light source, located on a separate table in order to avoid causing vibrations to the C-AFM each time the light was switched on and off. A fibre-optic cable was used to deliver illumination to the sample under investigation. Illumination cycles were started after a few minutes of data acquisition in the dark, by turning on the light source fitted with a filter of the required wavelength (GG495 and OG550 long-pass filters, or 325 nm short-pass filter, SCHOTT). Illuminations of 5sec were alternated with dark periods. “On/off” illumination cycles were performed manually, explaining the slight difference in cycles duration that can be observed on real-time diagrams.

4.2. 1.e I-V data analysis

The simplest measure of the properties of the CP-AFM BR junctions is the low-bias resistance calculated from the *I-V* curves, since the current at $V \approx 0$ is linear with voltage. The inverse of the gradient of this line then gives a measure of junction ‘resistance’, although it should be stressed that this is not the same as the concept of resistance in a bulk conductor, but is similarly derived from the slope of the *I-V* curve.

In order to ensure the reliability and reproducibility of the results, several hundreds of *I-V* curves (between 200 and 500) are obtained for each molecular junction, in each (dark or light) condition. Considering the fact that tens of mMm junctions are assessed per experimental day, a tremendous amount of data then needs to be processed. Although conclusive results were observed with both the Agilent and JPK systems, overall, most of the results presented in this thesis, and in particular most of the controls, have been obtained on the JPK machine. This equipment is brand new on the market and no data analysis software is available for the moment for processing I-V spectroscopy results. Raw data are thus analysed with a home-written MatLab routine (R2008b, MathWorks). The first step consists in manually selecting, among all recorded curves, those to be discarded from further analysis (such as, for example, noisy curves). Then, the MatLab routine selects the predominantly linear IV response regime (between -0.2 to 0.2 Volts for backward and forward sweeps) and computes a linear fit, thus enabling the calculation of the ohmic resistance for each IV curve. The results of the IV analysis are then collated and further statistically analysed using the OriginLab software. Despite the Matlab routine, there is not an automated process yet for determining whether to accept or not an I-V curve for further analysis: this -long- part of the data analysis process still needs to be performed manually.

4.2.2 KFM Surface potential measurements

The experimental set up and sample preparation followed the same protocol as described in Chapter III.

4.2.3 Photocurrent measurements

Photocurrent measurements were carried out using an Autolab Potentiostat in chrono-amperometry mode, while data analysis was done using GPES (AUTOLAB) and Origin (OriginLab©) softwares. The light source used to illuminate the photocell was an M-150 FibreLite with a 150W halogen bulb, as for SPM experiments. The two filters used were a 495nm long pass filter (yellow light) and a 325nm short pass filter (blue light), the latter of which was used for control purposes. Measurements of the photocell were carried out in a Faraday cage in order to reduce the amount of electrical noise and to block out any external light. The beam of light was chopped using a home assembled compact optical shutter, consisting of a rotating disk driven by a battery powered motor. The frequency and time period of illumination were controlled by altering the speed at which the disc rotated. The photocell itself was held 2 cm above the optical cable, with the perspex filter and a glass petri dish separating the two electrodes.

Transparent electrodes

Thin gold films (2 nm of Chromium as adhesion layer, 10 nm of gold), to be used as working electrodes, were prepared by evaporating on glass coverslips (0.08-0.11 mm thick, Menzel Glasser). ITO coated glass (0.14 mm thick, 100 Ω/cm^2, Diamond Coatings

Ltd) was used as a counter electrode. Electrodes (Gold & ITO), prior to use, were cleaned in freshly prepared piranha solution.

BR layer formation

Within the assembly of the photocell, 50µL of 10-20 µM BR (wild-type/ delipidated wild-type/delipidated BRcys) solution was pipetted on to the working gold electrode surface. Controlled submonolayer of BR was generated by placing the photocell, overnight, in a humid light proof box at 4°C. Before use, the remnant BR solution was removed and the working electrode rinsed with deionized water (in order to remove any weakly bound protein). This protocol (termed “solution deposition”) was used also used in multiple iterative manner (i.e. solution deposition, surface washing, solution deposition...) to investigate the possibility of incremental coverage increase.

Cell Setup

In order to maximise the surface coverage of BR on the gold, various deposition techniques were used. In all cases the cell used consisted of two optically transparent gold slides, one acting as the working and the other as a counter/reference electrode, between which the BR film and electrolyte solution were sandwiched. The two gold slides required used for the cell were first cleaned in concentrated piranha solution for 10 seconds. Piranha solution, made up by mixing conc. H_2SO_4 and H_2O_2 in a ratio of 3:1, is a very strong oxidising agent and is used to remove most organic contaminates. Once cleaned with the piranha solution the slides were then washed with ethanol followed by DI water, before being dried under nitrogen. A silicon o-ring of 4mm radius and 1mm thickness was then placed onto the working slide and the desired bR solution was then pipetted into the o-ring. After the required deposition time period the o-ring was then backfilled with an electrolyte solution of 100mM Na_2SO_4 in 10mM PBS, and the cell sealed with the second gold slide. For all the photocells used aluminium foil was attached to both slides using silver conductive paint to create electrical contacts.

4.3 Results and Discussion

4.3.1 Preliminary C-AFM conductance experiments on octanethiol SAMS

Initial I-V spectroscopy measurements were performed on octanethiol-based self-assembled monolayers, which are non-sensitive to light, on gold substrates. Conductance measurements were performed in the dark and under illumination, under similar conditions (light filter, illumination time) to those that will later be applied to the bacteriorhodopsin molecular junctions.

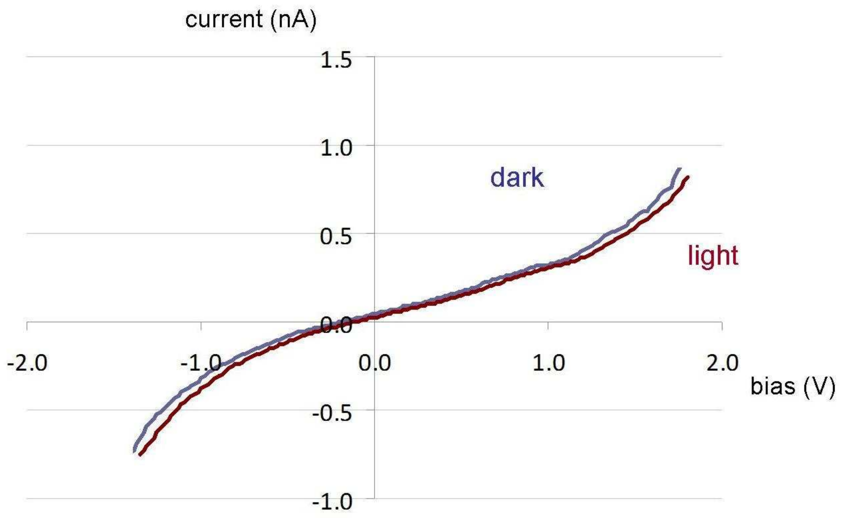

Figure 4.1: Averaged I-V curves obtained for octanethiol SAMs on gold in dark conditions (blue) and under illumination (red; λ>495 nm). No variation of conductance can be seen upon illumination. Moreover, resistances calculation shows a value of 10.9 GΩ in the dark and 10.1 GΩ on illumination. Average of 318 curves in the dark and 225 on illumination. Force applied: 20 nN. Data obtained on a PicoSPM system (Agilent).

Over 300 *I-V* curves were recorded in the dark and over 200 under illumination (averaged results on Figure 4.1): no difference could be seen between both conditions. Control *I-V* spectra taken on an octanethiol monolayer show resistances of 10.9 GΩ and 10.1GΩ in the dark and illuminated states respectively, an insignificant shift. While this control system differs somewhat from the protein system, it is a reliable, well defined measure of a photo-inert junction that shows that the tip-molecule-substrate system is not prone to switching due to some spurious process.

4.3.2 C-AFM conductance measurements of BR molecular junctions

The aim of these experiments is to try and detect, for isolated trimers of BR_{cys} on gold, a photoswitch of conductance similar to that observed for membrane-embedded wild-type BR. *I-V* spectroscopy is performed by C-AFM on junctions made of partially-delipidated BR_{cys} adsorbed on a gold substrate and probed by the gold tip of the C-AFM. Measurements of the conductance of WT-BR or non-delipidated BR_{cys} have been briefly performed initially but the focus of these experiments is the electrical behaviour of partially delipidated BR_{cys}. Before measuring the electronic response of the delipidated protein towards an applied bias upon illumination, crucial experimental set up points, such as the minimum and maximum forces or the voltage bias range to be applied to the sample, need to be determined.

4.3.2.a I-V spectroscopy in the dark

In conducting-AFM, a voltage is applied to the probe while the substrate is held at ground potential, and the current passing from the tip to the substrate, through the sample, is measured. Applying too low a contact force to the sample will result in an unstable detected current. Conversely, a too high applied load would compress the sample and results would show the probe-substrate interactions rather that the characteristics of the molecule of interest.

Extensive *I-V* spectroscopy was first performed in the dark only, on isolated trimers of BR_{cys} on gold. Force loads in the range of 5-40nN (± 2nN) have been applied to 5 to 10 molecular junctions for each force, and an average of 250 *I-V* curves were recorded for each molecular junction, at each applied force. At loads below 10nN intermittent conduction was observed, indicative of poor electrical contact between tip and the protein. Reliable electrical contact was established at 10-15 nN of contact force in engaging delipidated BR_{cys} with a metal coated AFM probe. The current flowing through delipidated molecular BR_{cys} studied here reached +10 nA and -10 nA at +1V and -1 V bias, respectively (Figure 4.2).

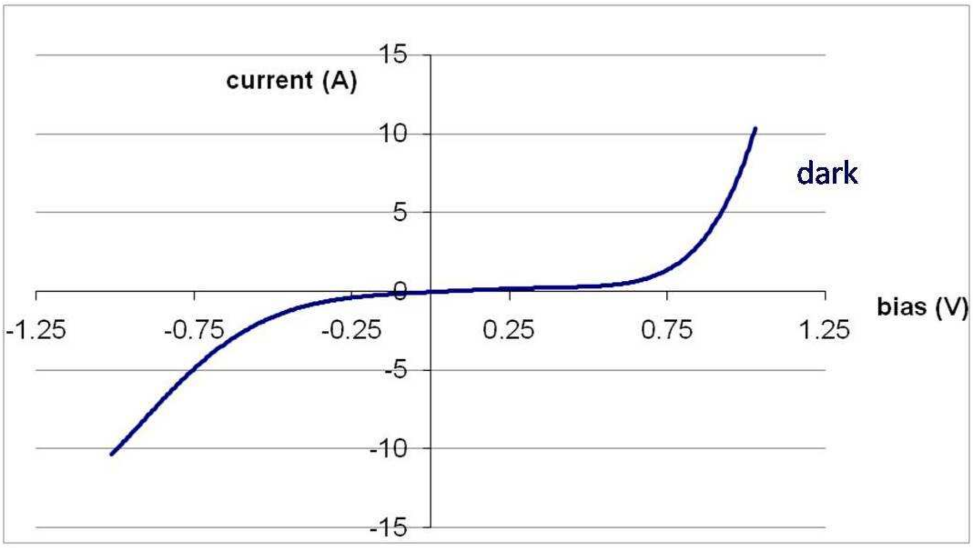

Figure 4.2: Average of 214 *I-V* curves obtained in the dark for one gold-partially delipidated BR_{cys}-gold molecular junction. Reproducible, stable current was observed at an applied force of 15nN. The calculated junction resistance was 142 ± 26MΩ.

At applied loads higher than 25 nN, the level of compression exerted by the C-AFM tip on BR is such that the protein is physically distorted and does not exhibit its conductance behaviour anymore: a straight conductance is then observed on the I-V curve, representing the direct gold probe-gold substrate interaction (Figure 4.3). Unless stated otherwise, *I-V* spectroscopy of partially delipidated BR_{cys} was performed at 15nN applied load, towards an applied bias ranging from -1.25 / +1.25V.

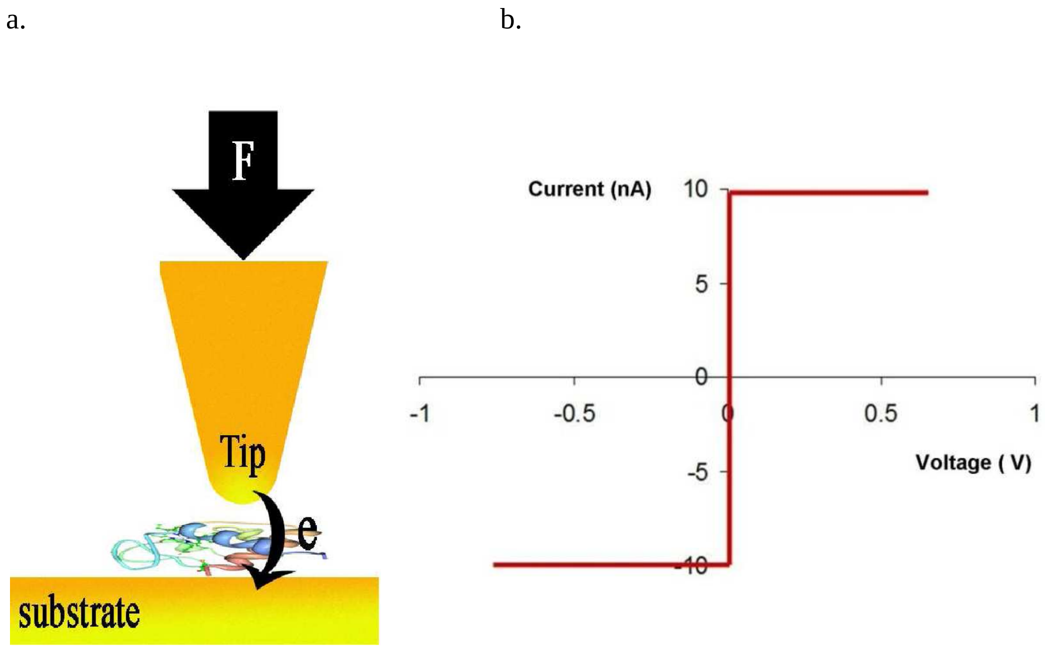

Figure 4.3: Determination of the optimal experimental conditions in C-AFM: case of a too high force load applied to the sample. When too high forces are applied (**a**), the compression exerted by the C-AFM tip on the sample is such, that the protein is physically distorted and does not exhibit its conductance behaviour (**b**): a straight conductance is observed on the I-V curve, representing the direct gold probe-gold substrate interaction. In the case of isolated trimers of BR_{cys}, this phenomenon is observed for applied loads higher than 25 nN.

4.3.2.b I-V spectroscopy on illumination (λ> 495 nm)

After setting up optimal experimental conditions, studies of the conductance on illumination of isolated trimers of BR_{cys} could be performed. Chapter III was focused on the gold-partially delipidated BR_{cys} junction characterisation, and UV-visible spectroscopy showed that binding of delipidated BR_{cys} onto transparent gold on glass resulted in a shift of its peak of absorbance from 560nm to 500nm . The light source used for illumination cycles was thus fitted with a 495 nm long pass filter for illuminating the sample. As mentioned in Chapter III, the number of BR_{cys} trimers assayed in such gold-protein-gold junctions is hard to determine precisely, as partial delipidation does not necessarily lead to isolated individual BR_{cys} trimers; indeed, although the purple membrane environment and the 2D lattice organization of the protein are disrupted, bulk structures comprising several protein trimers can be formed. The molecular junctions probed may thus not be all identical. However, AFM imaging showed homogenous protein coverage on the gold surface, with no major size difference among protein features adsorbed on the surface (Figure 3.19): although molecular junctions may not be made of strictly identical number of trimers, there are no big variations among them.

Experiments were started in the dark, then the light source was turned on for 5 seconds before being switched off: current passing through the molecular junctions as a function of the applied bias was measured while “on/off” illumination cycles were alternated.
Illumination induced a distinct conductance increase (Figure 4.4 c, red *I-V* curve) which decayed back to its initial value when the light was switched off. This phenomenon was reproducibly observed over an average of five “on/off” cycles for one metal-molecule-metal junction, before the amplitude of the shift of conductance upon illumination started to decrease over the following cycles and reached the point where no more shift was detected. However, moving the C-AFM probe to another molecular junction immediately reinstated conductance photoswitching. In order to ensure the reliability of the results, extensive measurements were performed. Several hundreds *I-V* curves were obtained in dark and on illumination, at one applied force and for each probed mMm junction: between 5 and 45 junctions were tested per experiment, over a range of 3 to 5 applied forces, although 15 nN was the most commonly applied contact force.

The amplitude of the photo-induced increase in conductance could be explained by the plasmon effect of the gold substrate mentioned in Chapter III (Figure 3.18). However, although this effect may occur, it cannot be the main reason for the particularly high current increase observed here. Indeed, previous conductance measurements have been performed on BR on gold[192, 193] in buffer and in air[232], and have thus experienced thus plasmon effect, but none of these works displayed such a photo-induced increase.

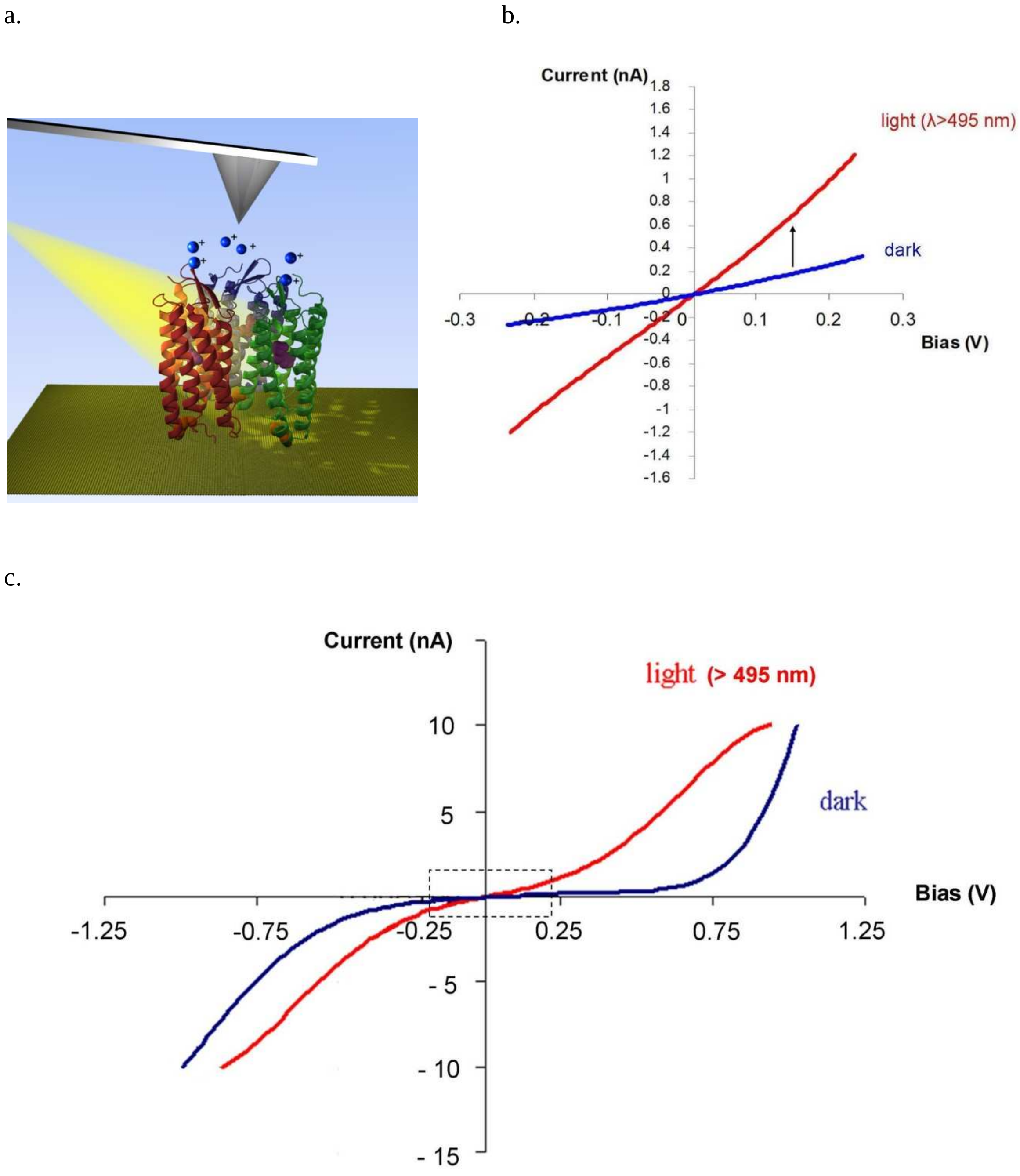

Figure 4.4 : *I-V* spectroscopy of partially delipidated M163C bacteriorhodopsin in dark and illumination (λ>495 nm). a. Schematic representation of the experimental set-up: an isolated trimer of BR_{cys}, adsorbed on gold, is probed by the C-AFM tip under illumination. **b**. Magnification of the linear part of the *I-V* curves (±0.2 V bias section, represented by the "boxed" region in c.) obtained in the dark (blue) and on illumination (red): an increase of conductance is clearly visible on illumination (black arrow). Data analysis showed that the molecular junction switched from 137 ±28MΩ in the dark, to 39 ±12MΩ when illuminated. **c.** Averaged *I-V* curves obtained during successive illumination cycles of 5s each. Data shown here from an average of 240 "light" and 260 "dark" curves at a junction force of 15 nN ± 1.3 nN over 42 gold-BR-gold junctions; bias range ±1V, sweep rate = 0.5s.

The major difference between this work and previous related studies is the isolation of BR from the purple membrane environment. The protein can thus form electrode-molecule-electrode junctions in a closer and more robust way than achieved before.

Several thousands of raw data in total were then processed and provided valuable information about the molecular junction behaviour upon illumination.

As mentioned earlier, junction resistances are calculated from the linear part of *I-V* curves. Although it is already clear from the main graph on Figure 4.4 that illumination triggers a shift to a higher BR_{cys} trimers conductance, Figure 4.4 b emphasises the very linear part of both dark and light averaged *I-V* curves: the increase of conductance is even more visible here, and can be estimated as being around a three-fold increase of conductance. Statistical analysis of these results has then provided precise values of the evolution of the molecular junction resistances upon illumination.

4.3.2.c Statistical analysis

Several thousands of *I-V* curves were recorded in each condition and were first discriminated according to the general aspect of the curve (noisy or occasionally unstable signals, for example, were discarded). Then, a home-written MatLab routine was used to determine BR molecular junction resistance from the low bias regions of each *I-V* curve. The drop of resistance (and thus, the shift to a higher resistance) upon illumination is clearly visible on the resistance distribution (Figure 4.5).

Resistances calculation shows that molecular junction resistances, specifically, drop by approximately three fold from 137 ± 28 MΩ pre-excitation to 39 ± 12 MΩ on illumination. The statistical distribution of the “dark” and “light” resistances showed that light-induced fluctuation was reproducible over some 42 BR_{cys} junctions.

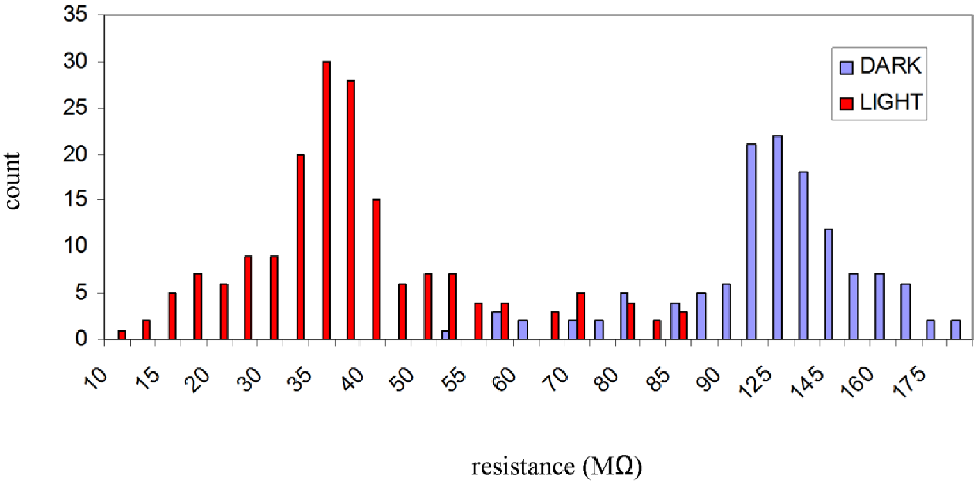

Figure 4.5: Resistance distribution of partially delipidated BR_{cys} on gold, in dark and light conditions (>495nm), obtained for 42 molecular junctions. Only I-V curves presenting a symmetrical shape toward positive and negative bias were retained for data processing. These curves were analysed by a computed fit enabling the calculation of individual resistances. This distribution confirms the over three-fold drop of resistance, from 137 ± 28 MΩ to 39 ± 12MΩ, observed for trimers of BR_{cys} on illumination (long pass filter cut off at 495 nm, results obtained from 42 BR_{cys} junctions for an applied force of 15 ± 1.3 nN

Considering the fact that molecular junctions studied here are likely to be made of a few BR trimers isolated from the purple membrane but remaining linked to each other, a general assessment of the average number of trimers per junction has been performed. As mentioned in Chapter III (figure 3.18), the average diameter of one single feature, observed over 100 junctions and in 3 different samples, is 24.8±3.9 nm, while an individual BR trimer reportedly shows a diameter of 7.5 nm[50]. It can thus be assumed that the BR features observed after partial delipidation are made of an average of 3 individual trimers. Upon illumination, one metal-BR_{cys}-metal junction displays a resistance of 39± 12MΩ, i.e. an averaged 13 MΩ resistance per individual BR trimer in the + 0.2V region of the I-V curve. Results obtained here thus show an average current of 17nA per BR_{cys} trimer upon illumination, which is far higher than previous results obtained so far for membrane-embedded BR.

Indeed, in 2006, Jin *et al.*[186] used the C-AFM technique to measure the conductance of monolayers of bacteriorhodopsin reconstituted into lipid vesicles fused on a solid substrate and covered by gold pads. These experimental settings provided resistances over the GΩ range, and estimated current values of 3.10^{-19}A/trimer. The following year, Casuso *et al*[191], performed C-AFM measurements of the conductance of purple membrane patches and obtained a current of 50 pA/trimer, eight orders of magnitude higher than previously reported. Such a difference was explained by a better protein-electrode contact resulting in a homogeneous current flow obtained for the whole BR monolayer.

Conductance measurements results obtained here for partially delipidated BR_{cys} (17 nA/trimer) are also of interest when compared to the expected conductance of water-free peptides. Indeed, direct tunnelling through a water-free, 1nm-long, peptide has been measured to be 12 nA at a 0.5V applied bias[186]. Assuming an exponential decrease in tunnel current with increasing molecular length leaded to an expected current value of 10^{-23}A for a 35 nm^2 area (area of a BR trimer), using the Simmons model for direct tunnelling[186]. Here, protein samples are depleted from most of their environmental lipids: molecular junctions are thus established in closer proximity of the protein and show an unprecedented average conductance for individual BR trimers.

These results show that conductance mechanisms through BR are more complex than direct tunnelling through a single barrier, which will be discussed further in section 4.3.2.g with the use of retinal-free BR_{cys}.

4.3.2.d Investigating BR_{cys} conductance photoswitching reproducibility

Average results obtained so far have demonstrated a three-fold photoswitching of the molecular conductance of isolated trimers of BR_{cys} on illumination. In order to better visualise the reproducibility of this behaviour, real-time *I-V* spectroscopy has been performed: the conductance of one single BR_{cys} molecular junction was recorded, over time, towards a fixed applied bias. The entire photocycle takes place within 10ms when the protein is embedded in its native membrane environment; it is thus unlikely that, on the timescale of a current-voltage sweep, the natural individual cycle will be reflected in the *I-V* spectra. However, these measurements will provide insight towards the average behaviour of the delipidated protein over such a timescale, when trapped between two electrodes.

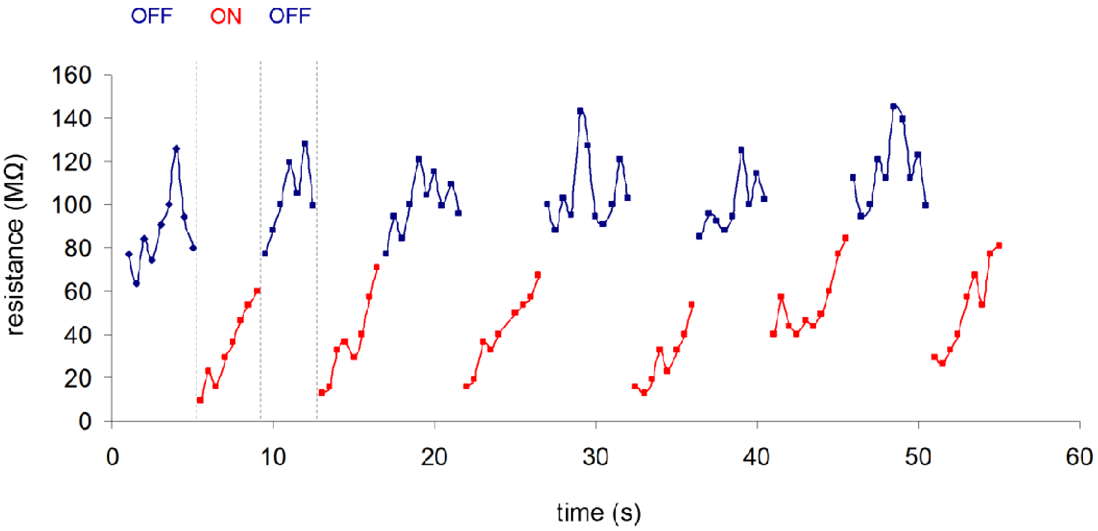

Figure 4.6: Demonstration of the reproducibility of delipidated BR$_{cys}$ conductance photoswitching: real-time *I-V* spectroscopy of one single BR$_{cys}$ junction upon successive illuminations (>495nm). The graph shows the evolution of BR junction resistances under dark & light conditions measured over time by CP-AFM. Each point corresponds to the resistance of one single *I-V* curve recorded every 0.5s. At 7.5 seconds (after 15 consecutive *I-V* sweeps), a light source is switched on for a few (~4 – 5) seconds and then turned off A drop of resistance is clearly visible on illumination, and is reproducibly observed for an average of ten cycles of interspersed illuminations. Following cycles showed an attenuation of the shifts to the point where no shift occurs at the same junction, probably due to current saturation (data not shown). Repeating the experiment on another point of the sample restored the photoswitching behaviour. Applied force: 9 ±1.2 nN; voltage bias ranging from ± 1V. Illumination times were of slightly variable duration as switching of the light source was performed manually.

Processed data show the evolution of the junction resistance over time: multiple successive measurements over illumination cycles of ~ 5 s interspersed with measurements in the dark, on a same BR$_{cys}$ junction without withdrawing the tip, lead to a reproducible series of shifts in conductance observable for typically 5 full cycles (Figure 4.6) and confirming retention of molecular photoactivity through the process.

In most cases, a gradual decrease in conductance was observed for junctions following 5 to 10 dark-light switching cycles, an observation independent of illumination time. Conductance and its photomodulation, however, were robustly reinstated on moving the probe to a different part of the BR modified surface. This observation suggests that the progressive conductance decrease was due to a local current saturation of the protein under the C-AFM probe, rather than being illumination-induced since the whole sample was illuminated. Changing the illumination times did not affect this phenomenon. However, moving to another point of the sample reinstated photoswitching, indicating that current saturation is a local current phenomenon, rather than an illumination-induced saturation since the whole sample was illuminated

4.3.2.f Investigating the photoswitching wavelength specificity

Partially delipidated BR_{cys} has been shown to exhibit a three-fold increase of its molecular conductance upon illumination (> 495nm), in a reproducible way, for individual gold-BR-gold junctions. A control experiment consisted of investigating the wavelength-specificity of this unique behaviour, by reproducing the same experiments at a different wavelength.

As shown in Chapter III, partially delipidated BR_{cys} adsorbed on gold has a peak of absorbance of 500nm, hence the choice λ>495nm longpass filter for the previous experiments. When delipidated M163C is in solution, its peak of absorbance is at λ= 560nm. A 550nm long-pass filter has thus been used for control experiments assessing the wavelength- specificity of the photowitching.

Engaging the CAFM probe with partially delipidated BR_{cys} immobilized on gold using a 550 nm long pass filter for illumination resulted in current-voltage curves showing no significant shift of conductance over 200 curves (Figure 4.7) between dark and light conditions, with a mean resistance of 213 ±29MΩ in the dark and of 207 ± 15MΩ upon illumination, thus confirming the wavelength specificity of the BR conductance photoswitching.

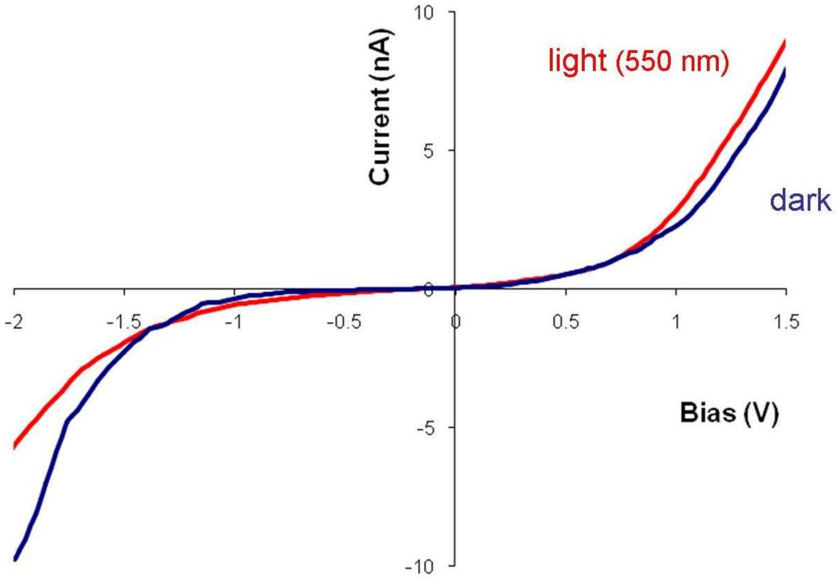

Figure 4.7. Assessing the wavelength-specificity of BR junction conductance photoswitching: I-V spectroscopy of partially delipidated BR$_{cys}$ in dark and light (> 550 nm) conditions. Average of 210 “dark” and 200 “light” I-V curves obtained for 35 mMm junctions. The linear part of the curves show no significant shift of conductance after several alternations of dark and light. Applied force: 20 ± 1.3nN. Mean resistance in the dark: 213 ± 29MΩ, upon illumination: 207 ± 15MΩ.

4.3.2.g Investigating the role of the retinal chromophore in BR$_{cys}$ conductance photoswitching: I-V spectroscopy on retinal-free BR$_{cys}$.

Bacteriorhodopsin entire biological function relies on the photocycle, triggered by the photoisomerisation of the retinal chromophore. Final C-AFM-based control experiments consist in confirming the crucial role of the chromophore in the electric conductance behaviour of BR.

4.3.2.g.i Comparative C-AFM study of BR_{cys} and bleached BR_{cys}

The first control experiment consisted in performing *I-V* spectroscopy on a bleached (retinal-depleted) BR_{cys}, and in comparing it with the results obtained for retinal-bound BR_{cys}. Fitted on the same axis scale, the conductance of partially delipidated bleached BR_{cys} looks close to 0 nA compared to delipidated retinal-bound BR_{cys} (Figure 4.8). When fitting results of the bleached protein on a different scale (figure 4.8, inset), its *I-V* curve displays the common sinusoidal shape, with the major difference that the current detected for bleached BR is comprised within the pA range, while BR $_{cys}$ displays 10 nA at a same applied bias.

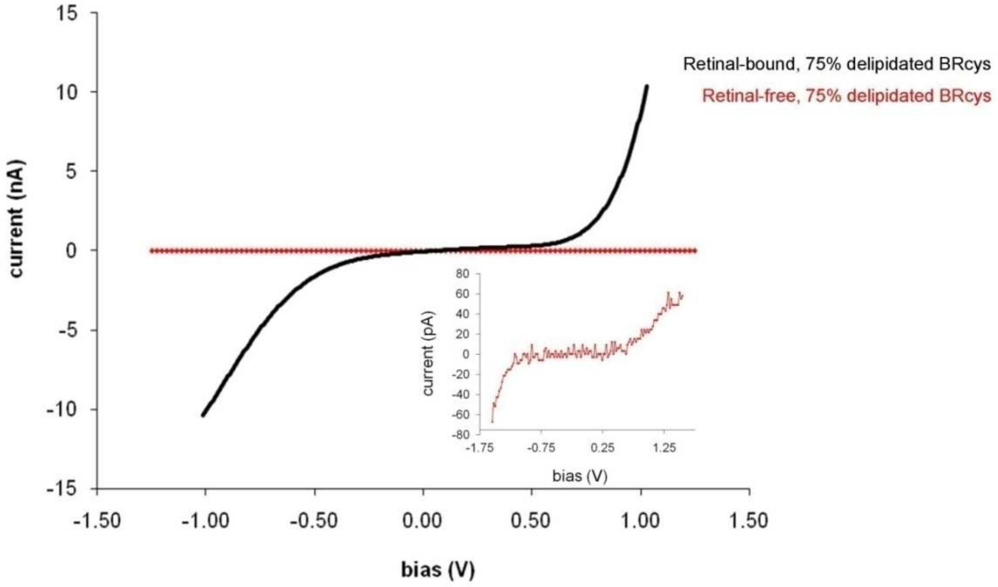

Figure 4.8 : Conductance measurements of bleached (retinal-free), partially delipidated BR_{cys} compared with retinal-bound protein. Averaged *I-V* curves obtained in the dark for partially delipidated BR_{cys} (black) and bleached partially delipidated BR_{cys} (red). Curves obtained for the bleached protein were much noisier than those obtained for the retinal-bound protein. Applied force = 10 ±1.3nN. Average of 50 curves in each condition.

The presence of the retinal is thus not only responsible for BR electronic behaviour upon illumination, but also affects the protein conductance in the dark. Indeed, measurements of BR_{cys} "single channel conductance" (the protein depleted from its core chromophore can be assimilated to a single channel path for electrons) show an average current of 26.6 ± 2.4pA/molecular junction, and thus an average current of 8 pA/trimer passing through retinal-free BR_{cys} upon illumination: a result that is four orders of magnitude lower than what was obtained for the retinal-bound protein. The chromophore thus serves as a current transport mediator.

4.3.2.g.ii I-V spectroscopy of bleached BR_{cys} in the dark and on illumination (λ> 495 nm)

A last control consisted in assessing the capability of bleached BR to undergo a photoswitch of its electrical properties while deprived from its chromophore. Figure 4.9 shows *I-V* curves in dark and in light of isolated trimers of BR_{cys}. The current detected dropped from the nA range for BR_{cys} to the pA range in the absence of retinal. Then, detection of a photoswitch has been tested on bleached delipidated BR_{cys}, alternating periods of darkness and illumination at the >495 nm working wavelength. Not only the detected currents were in the pA range, but also no switch of conductance could be observed over successive illuminations.

Resistance calculations showed a 38.6± 2.6 GΩ resistance in the dark (measured over 147 *I-V* curves) and a 37.5± 3.4 GΩ resistance upon illumination (calculated from 132 *I-V* curve). Figure 4.9 shows that partially-delipidated retinal-free BR_{cys} under illumination has a resistance dropped by three orders of magnitude compared to retinal-bound BR_{cys} under the same conditions. As seen earlier, current passing through BR_{cys} is much higher than originally expected for direct tunnelling through a 5 nm-long, water-free peptide. In the case of proteins naturally involving electron transports over long distances, cofactors such as redox centers are required. Here, the retinal chromophore and its π-electron system present in the core of BR can be considered as the intermediate on the electron path through the protein. Indeed, the electrode-BR$_{cys}$-electrode junctions show conductivity as long as retinal is present and can isomerise upon illumination.

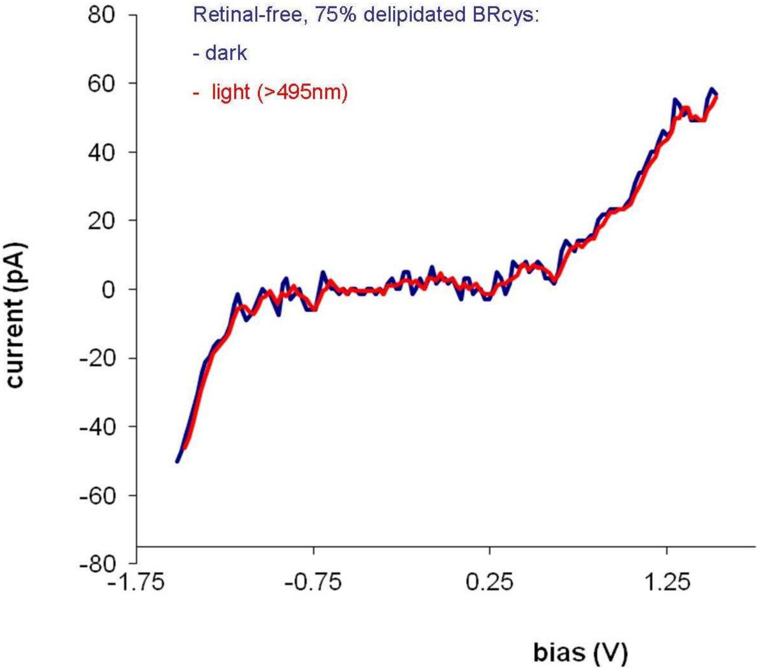

Figure 4.9: **Conductance measurements of bleached, partially delipidated BR$_{cys}$ in dark and light conditions (>495 nm)**. Experiments were performed at the wavelength showing a conductance photoswitch in retinal-bound BR$_{cys}$. No significant shift of conductance was observed here for bleached BR$_{cys}$ after several dark and light alternations, as expected. Average of 147 *I*-*V* curves obtained in the dark and 132 *I*-*V* curves obtained during illumination. The force applied was 10 ±1.3nN. Note that currents observed here are in the pA range, instead of nA obtained for retinal-bound BR$_{cys}$.

Experiments were performed out of the purple membrane and in absence of buffer, the effect of light-induced proton ejection is thus considered negligible here. Indeed, the proton channel in the core of BR becomes an open path in absence of retinal: an ionic conductance mechanism would then lead to a several orders of magnitude increase of conductance in retinal-free BR$_{cys}$, but the opposite phenomenon is observed. These results confirm that BR can be used as a biological material to explore electronic transport.

4.3.3 KFM surface potential analysis of BR_{cys} on gold

Any detected shift in protein surface potential on illumination would imply a retention of BR photoactivity and confirm the usability of the isolated protein in molecular electronic applications.

4.3.3.a KFM measurements of membrane-embedded BR_{cys} on gold

KFM is not commonly used for measuring surface potential of biomolecules, in particular for species such isolated protein trimers, like here for partially delipidated BR_{cys}. First KFM studies were thus on BR_{cys} purple membrane patches.

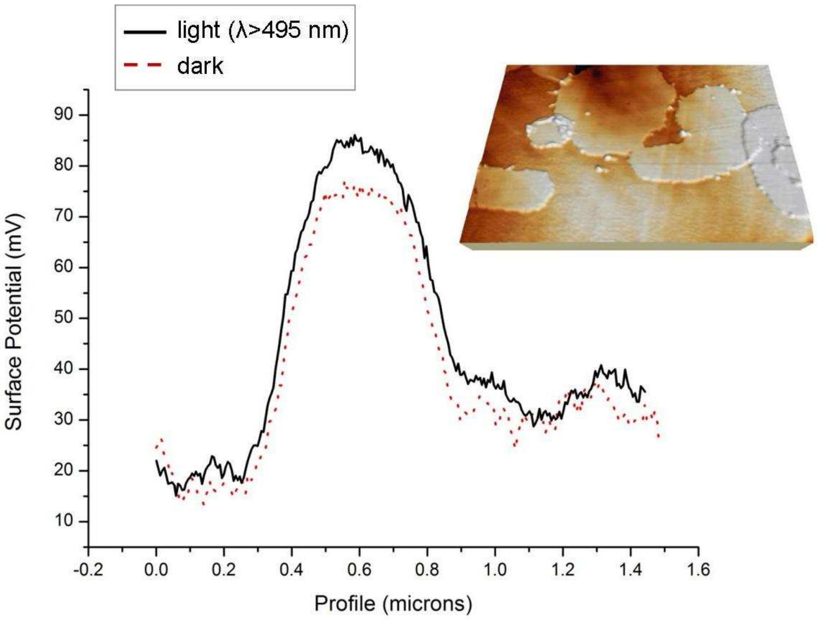

Figure 4.10. Surface potential cross-section of one patch of cysteine mutant purple membrane immobilized on flame annealed gold as mapped by KFM in the absence (dotted red line) and presence (black line) of 495 nm long pass filtered 150 watt light excitation. The potential switch here is approximately 10 mV. Inset: Tapping mode topographical image (1.1µm×1µm) of typical native wild type PM patches on gold. The surface potential of such patches can be reversibly switched through a number of cycles (typically 7 to 10)

Experiments were started in the dark (red dotted line). Upon illumination of the mutant, a potential switch to higher value (typically 10 mV, Figure 4.10) was reproducibly observed across several membrane patches, as expected for membrane-embedded BR. These cycles were reproducibly observed for one same membrane patch for around 7 to 10 cycles before attenuation of the phenomenon.

4.3.3.b KFM measurements of partially delipidated BR_{cys} on gold

After observing a photoswitch of the surface potential of membrane-embedded BR_{cys}, the experiment was reproduced on delipidated BR_{cys} (Figure 4.11).
Experiments were started in the dark and recorded continuously from the first illumination (blue line), then after switching off the light (red dotted line) and switched on again (dark line): the surface potential drops when the sample returns to dark conditions, and increases again upon illumination: the shift of conductance observed with C-AFM is confirmed here with a shift of surface potential.

The cross section mapped here in potential measurement (a), is larger - 100 nm - than topographical cross sections obtained previously in C-AFM, since the probe does not map topographical data but long range electrostatic interactional force.

A statistical analysis (counts vs. surface potential) of switching characteristics of approximately 20 trimers, (c) indicates a consistent switch direction (black: no light, red: incident light) to higher surface potential upon illumination, but a switching magnitude that varies from 15 to 30 mV, a dispersion likely to be reflective of differences within the complex convolution of parameters that contribute to the electrostatic force imparted on the sampling probe. Some of these may be environmental, though it is also likely that a contribution from dispersion in, for example, protein charge and hydration state across the surface contributes to the differences observed.

Although KFM results do show a switch of surface potential upon illumination for isolated trimers of BR_{cys}, the magnitude of the shift is not constant compared to the 3 fold increase of conductance repeatedly observed across numerous isolated trimers with AFM. Here the surface potential systematically increases for each sample, but according to the feature probed, the increase will range from 15 mV to 30 mV.

KFM experiments so far have only focused on detecting the photoswitch of surface potential for isolated trimer of BR_{cys}. Further control experiments remain to perform, regarding the wavenlength-specificity of the shift, and the surface potential of bleached BR_{cys}, where the absence of retinal chromophore has been ascertained by C-AFM to be the reason for the shift.

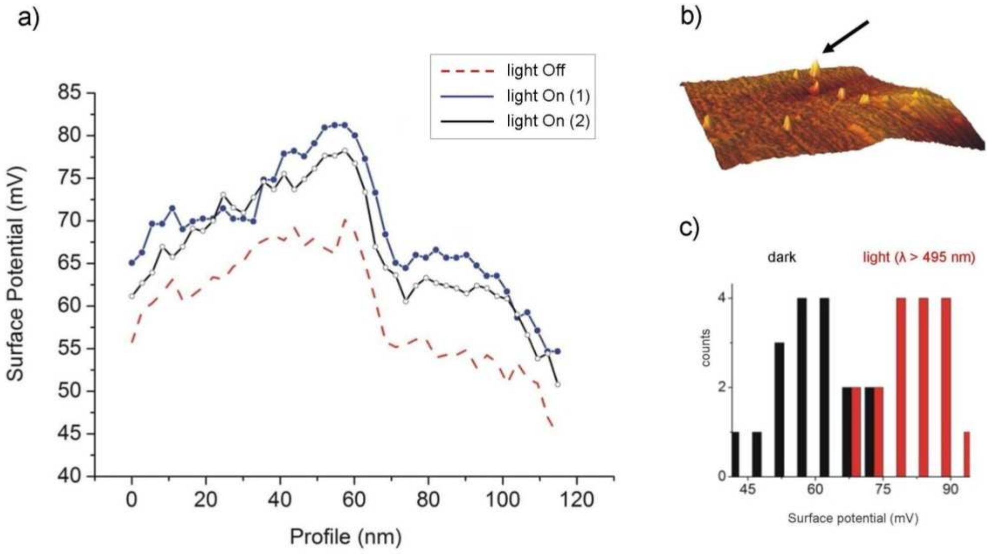

Figure 4.11. KFM measurements of the shift in the surface potential of a delipidated M163 mutant trimer on flame annealed gold as incident light is turned “On” (blue line), “Off” (red line) and then “On”(black line). The x axis (a) shows the surface cross section. A 495 nm long pass filter was used on the incident light. b) Topographical KFM image showing the BR isolated trimers (arrow) probed during the experiment. A statistical analysis of approximately 20 trimers (c) indicates a consistent switch direction (black: no light, red: incident light) but a switching magnitude that varies from 15 to 30 mV.

4.3.4 Photocurrent measurements of gold-BR$_{cys}$-gold junctions

As an alternative to scanning probe techniques, the electrical properties of BR upon illumination were assessed by measuring its photon-generated current by chronoamperometry. To do so, the protein was trapped with an electrolyte solution between two electrodes in a photocell, as described in Chapter II.

4.3.4.a Photocurrent responses of membrane-embedded BR and partially delipidated BR$_{cys}$

First measurements were performed on membrane-embedded WT-BR on gold during successive illumination cycles, where the protein is adsorbed by weak physisorption onto substrate.

Indeed, there is not chemical interaction like the one happening with BR$_{cys}$, so it is assumed that adsorption on gold will not alter tthe maximum of absorbance of the protein: WT BR was illuminated with a 550 nm long pass filter.

Illumination triggers WT BR photocycle in the photocell, causing local pH variations in contact with the working electrode, which results in the polarisation of the electrode. (Figure 4.12 “Light on”). Indeed, at the onset of light irradiation, the first stages of the photocycle (up to the formation of the M intermediate) result in a net proton release from the EC side of the BR molecules. This large increase in the proton concentration will lead to a drop in the local pH within the monolayer region, resulting in the anodic polarisation of the working electrode which under potentiostatic conditions will drive a transient cathodic capacitive current[235], seen at “Light on” in Figure 4.12 b. During constant illumination this build up of positive charge no longer exists as the uptake of protons at the CP side occurs at the same rate as the proton release from the EC side, thus returning the current to its stationary value.

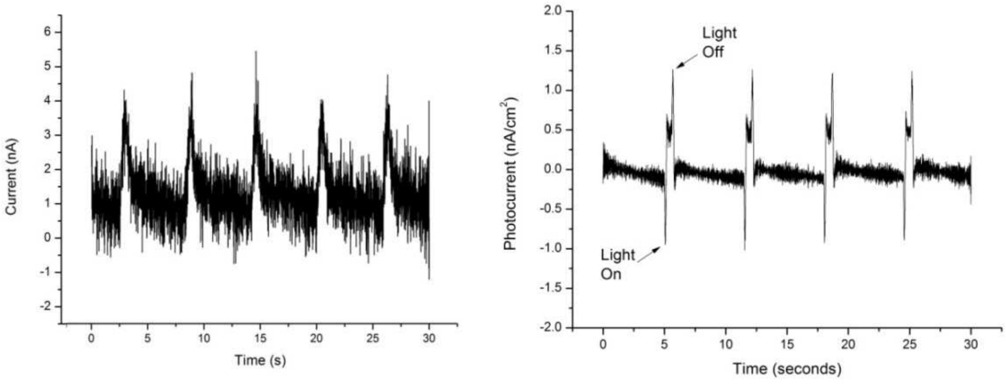

a. bare gold

b. wild-type BR

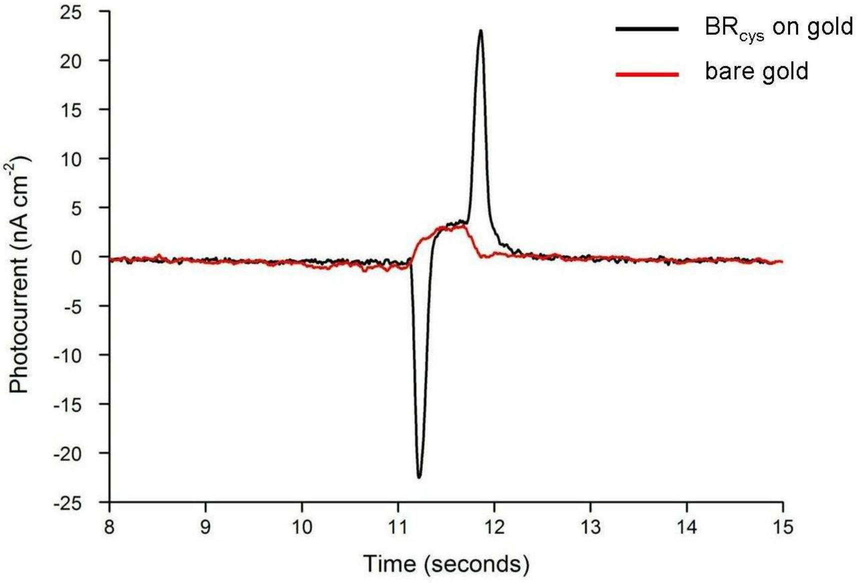

c. delipidated BR$_{cys}$ *vs* bare gold

Figure 4.12: Photocurrent responses of WT-BR and BR$_{cys}$ upon illumination.
a.Typical anodic stationary current response of a cleaned transparent gold electrode. **b.** Transient photocurrent responses, coincident with illumination (λ>550nm) frequency, observed for a typical, randomly orientated wild-type BR sample (overnight solution deposition from 20 µM stock) on a optically transparent gold electrode (0.5 cm^2) at 100 mV bias, under 150 W/cm^2. **c** Overlay of bare gold stationary response with the transient photoresponse obtained for delipidated BR$_{cys}$.

Finally when the light is turned off the photocycle ceases and the BR molecules stop releasing protons, however the final step of the cycle is the reprotonation of the CP side, thus the molecules will continue to uptake protons for a ms period.

This results in a net decrease in the proton concentration at the electrode interface and thus an increase in the local pH, which is seen as a second transient capacitive current but of opposite polarity to that seen at the onset of illumination (seen at “Light off”, Figure 4.12 c).

Variation of WT BR behaviour upon illumination detected by chronoaperometry, showed transient photocurrent values ranging from -1 to +1 nA/cm^2. However, as discussed in Chapter III, membrane-embedded protein will randomly orient on the gold electrode, resulting in part of the protein response not being detected. Results obtained for partially delipidated BR$_{cys}$ also show a change of the protein response upon illumination ($\lambda >$ 495 nm) but provides strikingly higher photocurrent values, ranging from -20 to +20 nA/cm^2: this confirms that the M163C mutation provides robust and homogeneously oriented coupling to the gold electrode.

4.3.4.b Wavelength specificity of BR$_{cys}$ photoresponse: comparative analysis at $\lambda >$ 495 nm and λ 325 nm

The wavelength-specificity of BR$_{cys}$ conductance photoswitch observed by C-AFM was controlled by measuring the photocurrent response of partially-delipidated BR$_{cys}$ at 495nm and at 325 nm.

A small anodic stationary currents attributed to a photoelectrochemical response of gold oxide[236] is detected for partially delipidated BR$_{cys}$ upon illumination with a 325 nm short pass filter. This current scales with light intensity and applied bias with typical maximal values (~5 nA/cm^2 at 500 mV bias and light intensity of 150 watts/cm^{2,}, Figure 4.13).

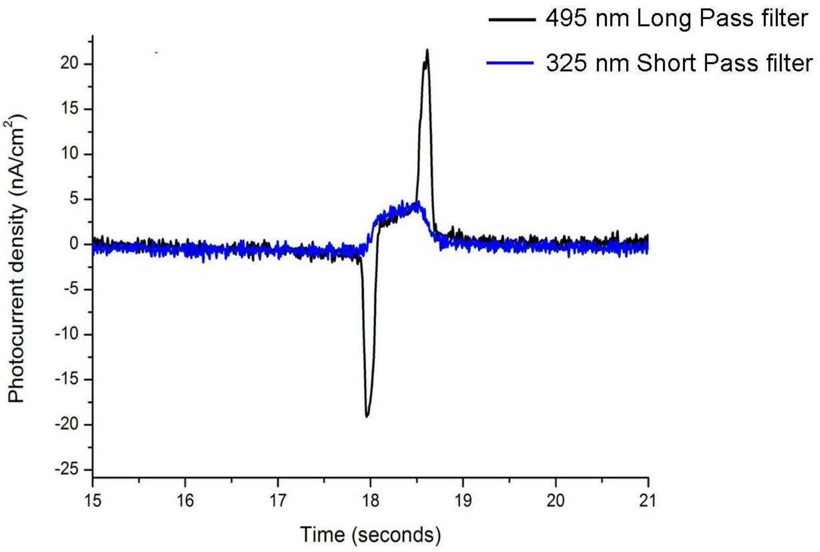

Figure 4.13 : Photocurrent response of BR$_{cys}$ film illuminated through a 325 nm short pass filter. The graph is overlaid with the transient photoresponse of delipidated BR$_{cys}$ illuminated with a 495 nm long pass filter.

Compared to the transient photoresponse obtained with the 495 nm long pass filter (~ 20 nA/cm^2) under similar conditions, these results clearly confirm the wavelength specificity of BR photoresponse demonstrated with C-AFM.

4.3.4.c Photocurrent measurements of bleached BR$_{cys}$

In order to confirm that the observed photocurrents were due to the retinal chromophore within the BR molecules, photocurrent analysis was carried out on retinal-free samples of mutant BR.

When the retinal chromophore is removed from the BR sample the cathodic current transient upon illumination and the subsequent anodic transient when the light is turned off cannot be detected anymore (Figure 4.14). Indeed, in the absence of retinal, BR is unable to accomplish its photocycle, resulting in no proton pumping activity: there is thus no pH variation occuring at the onset and termination of illumination in the vicinity of the working electrode, which is thus not polarised.

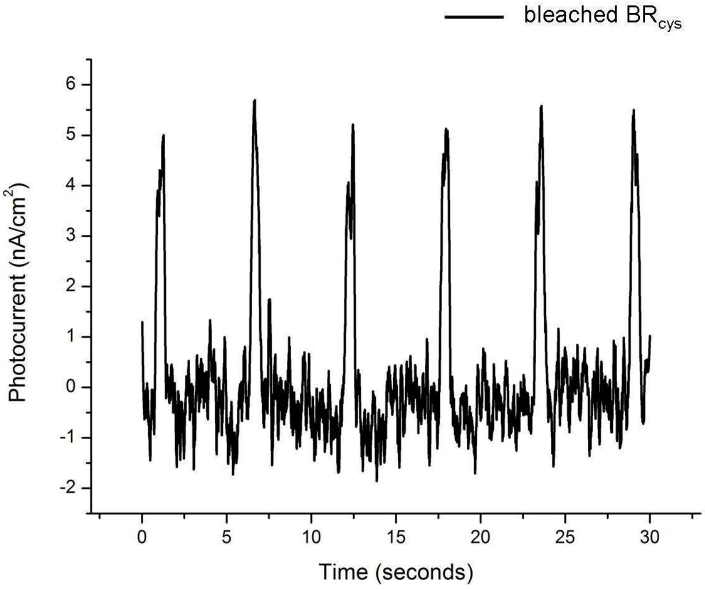

Figure 4.14: Temporal current plots of bleached mutant BR with +500mV bias and 100% light intensity. The anodic current transients that are observed in the plots are a result of the photo-assisted oxidation of water molecules on areas of Au_2O_3.

The figure does however reveal similar anodic current transients to those that were observed with the blank gold cell, indicating the presence of areas of gold oxide which are absorbing photons.

The absence of transient photocurrent for bleached delipidated BR_{cys} confirms the crucial role of retinal in BR response to illumination.

4.4 Conclusion

While all previously reported studies of the electrical conductance of BR were performed within the purple membrane, here, for the first time, extensive C-AFM measurements of the electrical response of delipidated BR_{cys} towards an applied bias have demonstrated that BR photoswitching of conductance upon illumination could be detected out of the purple membrane, for isolated protein trimers. An averaged three-fold increase of conductance (detected as a three-fold drop of the molecular junction resistance) was reproducibly observed.

In summary, the following has been demonstrated for the gold-BR_{cys}-gold junction:

- partially delipidated BR_{cys} can be covalently bound onto gold with a surface coverage suitable for SPM studies and with a homogenous orientation.
- C-AFM can reliably measure the *I-V* characteristics of BR_{cys} in a mMm junction, demonstrating MΩ resistances and currents of up to 10nA through the junction.
- On applying high loads the protein is systematically compressed, and shows direct tunnelling behaviour.
- At loads between 6nN and 15nN, a photoswitch is observed for isolated trimers of BR_{cys}, showing 3 fold decrease of the mMm junction resistance.
- A shift of to a higher surface potential upon illumination has been reproducibly probed by KFM for isolated trimers of BR_{cys}, though the magnitude of the shift is not constant depending of the probed molecular junction.

Numerous controls, presented in Chapter III, were performed in order to ensure the role of cysteine mutant in the covalent binding and homogenous orientation of the sample on the surface, and additional experiments were carried on to confirm the role of the retinal chromophore in the photoswitching of conductance, and the wavelength specificity of the reaction. All controls are summarised in Table 2.

Control	**Techniques**	**Results**
Partial delipidation of BR_{cys}	UV - vis spectroscopy	λmax shifted from 570 nm to 560 nm
	AFM imaging *(mica)*	absence of membrane patches
	KFM imaging *(gold)*	absence of membrane patches
Adsorption on gold / Role of Cys residue *(BR_{cys} vs wild-type BR)*	UV-vis spectroscopy	λmax shifted from 560 nm to 500 nm
	AFM, STM and KFM imaging	homogenous surface coverage of BR_{cys}, very sparse for WT
	SPR	3 times more BR_{cys} on gold than wild-type
	Reductrive stripping voltammetry	peak observed for BR_{cys}, not for WT
Sample homogeneous orientation	Photocurrent (electrochemistry)	Potentiated transient photoresponse
	KFM (surface potential)	increased, positive-only surface potential for BR_{cys} *vs* WT
Wavelength Specifity (light source λ≠ 495 nm)	CP-AFM	no photoswitch on *I-V* curves
	Photocurrent	no transient photocurrent
Role of retinal (bleached BR_{cys})	CP-AFM	low (pA) current, no switch
	photocurrent	lower current, no transient photoresponse

Table 4.1: Summary of all tested parameters and techniques used to confirm the reliability of the results obtained for BR_{cys}.

The ability of surface-confined organic chromophores to present a means of photoswitching conductance has generated a great interest in recent years. We have shown here, not only that a biologically and technologically important biomolecule can be anchored in an orientated and functionally competent form to man-made electrodes, but also that the molecular conductance of BR can be both measured and reversibly photoswitched with predictable wavelength sensitivity. This is the first time this has been reported, and constitutes a major change in the way BR can be used in nanodevices.

Chapter V – Reconstitution of the Neurotensin Receptor type 1 into liposomes for single molecule studies of ligand-receptor interactions

5.1 Introduction

After studying the electronic properties of light-sensitive bacteriorhodopsin for potential nanotechnological use (Chapter III and Chapter IV), the work presented here focuses on the study of a potential drug target: the neurotensin receptor type 1, NTS1. The aim of this project is to reconstitute NTS1 into liposomes in order to perform biophysical studies (using AFM and other techniques such as solid state NMR) and improve the knowledge about structural and functional properties of this receptor.

5.1.1 Neurotensin

Neurotensin is a brain and gastrointestinal 13 amino acid peptide (N-Glu-Leu-Tyr-Glu-Asn-Lys-Pro-Arg-Arg-Pro-Tyr-Ile-Leu-C) discovered by Carraway and Leeman in 1973[237]. Like many others neuropeptides, it fulfils a dual action of neurotransmitter in the central nervous system, and of local hormone in the periphery. Neurotensin possesses a wide spectrum of biological activities[238]: it is a modulator of anterior pituitary hormone secretion and of dopamine transmission (and thus is involved in Parkinson’s disease), and exerts hypothermic and analgesic effects in the brain. In the periphery, NT is a paracrine and endocrine modulator of the digestive tract, and acts as a growth factor on a variety of normal and cancer cells. Consequently, NT agonists or antagonists are suggested to be of potential use in the treatment of pain, eating disorders, psychiatrics disorders, and NT-related ligands are proposed to represent valuable tools for tumour targeting.

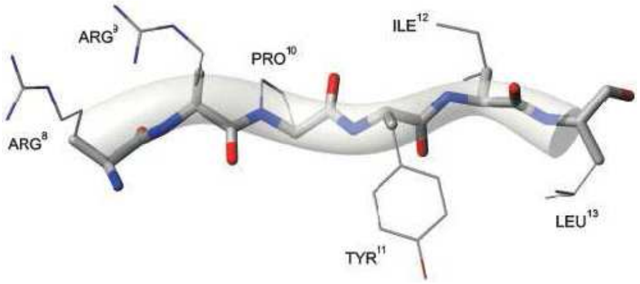

Figure 5.1: Representative backbone conformation of $NT_{8\text{-}13}$ bound to its G-protein coupled receptor, NTS1. All side-chains are indicated for reference only, but with no refined conformation[239].

5.1.2 Neurotensin receptors

Neurotensin acts through its binding to specific receptors. Binding and pharmacological experiments have shown the existence of three different subtypes of these receptors to date: NTS1, NTS2 and NTS3 (previously named NTR1, NTR2 and NTR3).

NTS1 and NTS2 share 60% homology (Figure 5.2). They have seven transmembrane domains and belong to the family of G protein-coupled receptors (GPCRs), whereas NTS3 is identical to gp95/sortilin, a 100kDa protein with a single transmembrane domain. NTS1 and NTS2 activate multiple signal transduction pathways, involving several G proteins. NT acts as an agonist towards all NTS1-mediated pathways, and may exert either agonist or antagonist activities, depending on the NTS2-mediated pathway in question. Despite the differences of structure, all three receptors bind to the C-terminal sequence of neurotensin[240], and all have similar structure-function relationships towards this peptide.

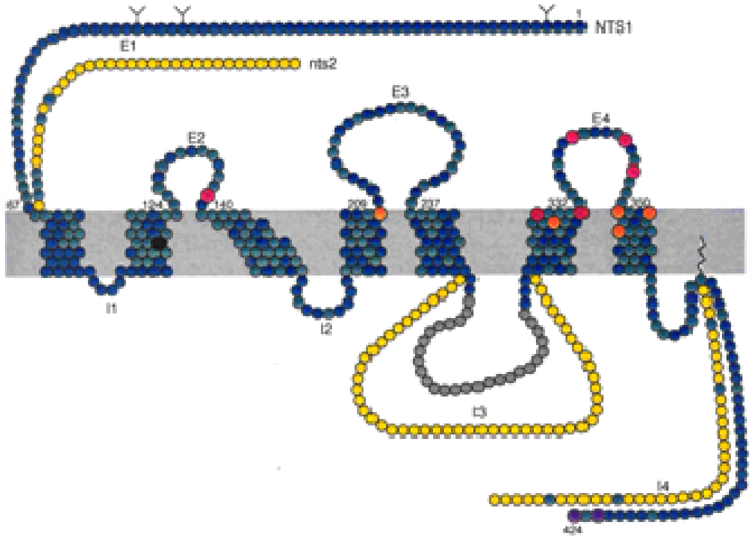

Figure 5.2: The rat neurotensin receptor NTS1 (blue). Green: invariant residues between NTS1and NTS2. Yellow: regions of NTS2 that strongly differ from NTS1. Black: Na^+ binding site. Residues involved in the binding of NTS1 (pink), of its non-peptidic antagonist SR48692 (orange) or both (red) are indicated. Violet: residues crucial for NTS1 internalisation. Grey: region of the third intracellular loop that is essential for coupling to phospholipase C (adapted from[241]).

5.1.2.a NTS1

Experiments performed with two non-peptide antagonist ligands, SR 48692, an antagonist of NTS1 with a higher affinity for this receptor than for NTS2, and SR 142948A, an analogue which does not discriminate between both receptors, suggested that most of the physiologic and pharmacologic effects of NT could be attributed to NTS1 stimulation[240]. Moreover, NTS1 has a higher affinity (nM) for neurotensin than NTS2. The signalling pathway of NTS1 is promiscuous and involves several G proteins.

NTS1 functional activation occurs by NT ligand binding into a “binding pocket” located between the transmembrane domains TM4 and TM6 (Figure 5.3). Only the last six C-terminal amino-acids of the peptide, NT $_{(8\text{-}13)}$, are required for its biological activity.

Competition binding experiments with ^{125}I-NT $_{(8\text{-}13)}$ and different NT $_{(8\text{-}13)}$ derivatives indicate that Tyr11 likely makes π-π contacts with Trp339, Phe344, and Tyr347 located in the third EC loop. Other similar studies elucidated further interactions, in addition to implicating an ionic interaction between Arg327 and the carboxyl-terminus of NT $_{(8\text{-}13)}$. These were supported by Williamson *et al.* in 2002, using solid-state NMR with fully ^{13}C- and ^{15}N-labelled NT $_{(8\text{-}13)}$ bound to receptor[242]. However, all data are not in agreement, as different residues are implicated; the EC loop 1, for example, has been shown to be involved in earlier computer homology modelling between EC loop 3 and NT $_{(8\text{-}13)}$[243].

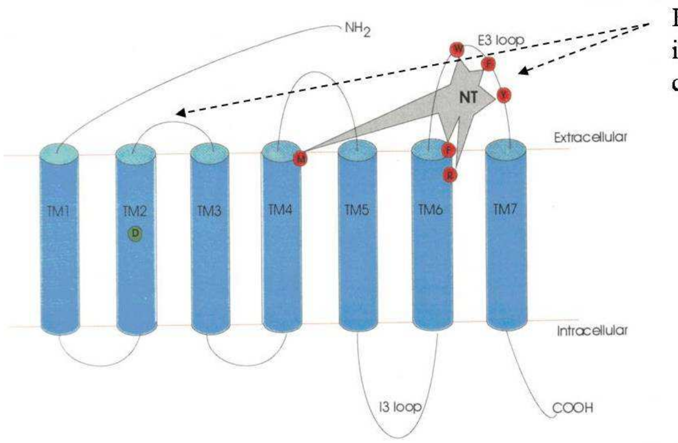

Homologous sequence comparisons identify two evolutionarily-conserved regions

Figure 5.3: NTS1 binding pocket. Schematic depicting some of the residues proposed to form the NT-binding pocket of rat NTS-1. The Na+ binding site is shown in green on TM2, with NT-binding residues shown in red. Note: charged and hydrophobic residues in EC loop 3 are not shown, nor are residues in the other evolutionary-conserved region encompassing EC loop 1 and adjacent TM-spanning domains. I3 is essential for coupling to phospholipase C, whilst the carboxy-terminus domain is involved in receptor internalisation in a cell-type specific manner (Adapted from[244]).

A particularly challenging aspect of NTS1 relies on its oligomerisation state. Opposite theories have been formulated, as to whether the receptor is present as a dimer within the membrane, or as a monomer with ligand binding triggering the receptor oligomerisation.

5.3.2.b Neurotensin Receptor 2 (NTS2)

NTS2 was first identified by radioactive ligand binding studies which suggested the presence of two separate binding sites in isolated brain or gastrointestinal membranes[245].

The high affinity, sodium sensitive sites (0.1 – 1 nM) were attributed to NTS1, while the lower affinity sites (3 – 5 nM), which were insensitive to sodium, but sensitive to the anti-histamine drug levocabastine, were attributed to a distinct NT receptor. Subsequent cloning of NTS2 showed it to be a 416 amino acid protein of the GPCR family, which shares 43 % amino acid identity and 64 % amino acid homology with NTS1[246] (Chalon *et al.*, 1996).

Pharmacological evidence suggests that, whilst the majority of NT functions are mediated by NTS1, two of the most prominent effects of centrally-administered NT, analgesia and hypothermia, are mediated by NTS2, since the NT-selective antagonist, SR 48692, did not antagonise these effects (Dubuc *et al.*, 1994; Mazella and Vincent,2006).

5.3.2.c Neurotensin Receptor 3 (NTS3)

The third neurotensin receptor, NTS3, was first identified as an NT-binding protein in detergent-solubilised brain membrane preparations and subsequent cloning revealed that it is not a member of the GPCR superfamily, but shares 100 % sequence identity with the previously identified sorting protein, sortillin[247]. It belongs to a new receptor family characterised by the presence of a luminal / extracellular region containing a cysteine-rich domain homologous to that found in the yeast protein Vsp10p. The physiological function of NTS3 remains unclear, not because it has been shown to bind several ligands in addition to NT[248] but it has been suggested that it is involved in receptor internalisation and ligand degradation[249].

5.1.3 Purification of NTS1

Neurotensin receptor 1 (NTS1) from rat is one of the few GPCRs which has been successfully overexpressed in a functional form capable of binding ligand at the *E.coli* plasma membrane. Functional expression was achieved by expressing the receptor as a fusion protein with N- and C-terminal fusion partners which aid targeting, membrane insertion, protein stability and purification. A fusion protein, termed NTS1A (Figure 5.4), was found to yield the highest expression level of functional receptor.

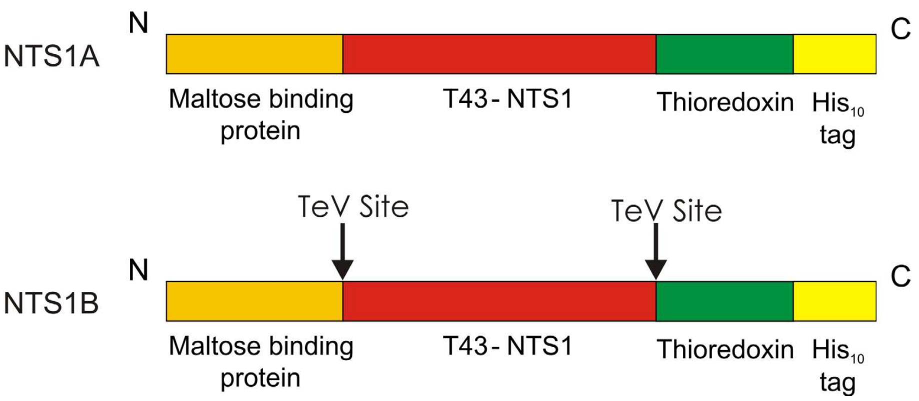

Figure 5.4: Schematic representation of the rat NTS1 constructs. NTS1A consists of maltose binding protein (MBP), an N-terminally truncated form of NTS1 (T43NTS1), thioredoxin and a deca-histidine tag (His10 tag). The NTS1B was constructed by including tobacco etch virus (TEV) protease cleavage sites into the NTS1A construct between the MBP and T43NTS1 moieties and the T43NTS1 and thioredoxin moieties to facilitate proteolytic removal of the fusion tags.

This consisted of T43NTS1 (NTS1 with the 43 N-terminal residues truncated) with the *E.coli* maltose binding protein (MBP), including its periplasmic targeting sequence, attached to the N-terminus, plus *E.coli* thioredoxin (TrxA) and a deca-His tag attached to the C-terminus.

The NTS1A construct was later modified to include tobacco etch virus (TeV) protease recognition sites between the MBP and T43NTS1 moieties and the T43NTS1 and TrxA moieties. This construct, termed NTS1B allows the removal of the N- and C-terminal fusions after expression and purification, yielding the NTS1 receptor alone[250].

Purification of the receptor expressed in E.Coli combines nickel affinity chromatography, followed by gel filtration and sucrose gradient.

5.1.4 Manual Peptide Synthesis

Purified NTS1 will then be reconstituted into liposomes with the aim of the receptor to retain its ligand-binding activity. The receptor purification and reconstitution steps are thus followed by a competitive ligand-binding assay, using a full-length radiolabelled peptide: tritiated neurotensin (^{3}H-NT) and native neurotensin peptide.

Unlabelled neurotensin was synthesised manually by solid phase peptide synthesis (SPPS). In SPPS, the peptide is synthesised with the C-terminus of the first amino-acid covalently bound to an insoluble support (resin) via an acid-labile linker, which allows easy separation of the growing peptide from unreacted precipitants and by-products. The other amino-acids are then added following protecting-deprotecting cycles. At last, the full peptide is cleaved from the resin.

5.1.5 Reconstitution of NTS1

5.1.5. a Liposomes

Liposomes are vesicles (40-1000nm in diameter) formed by hydrated phospholipids. They are composed of one or several self-closed bilayers and contain an aqueous core, unlike micelles, which are composed of a single lipid monolayer, and have no aqueous core (Figure 5.5). When proteins are inserted, these structures are called proteoliposomes.

Lipid bilayers are frequently used as membrane models and liposomes, due to their similarity but greater simplicity, are considered as a good tool for studying biological membranes.

In addition to their role as model-membrane systems, liposomes can also be used on a biomedical purpose. Indeed, a great variety of molecules can be loaded on the surface or inserted inside liposomes through the destabilisation of their bilayer[251]. In this case, liposomes can play the role of transfer vectors, allowing a targeted delivery of drug via the binding of specific antibodies at their surface, thus increasing the efficiency of the treatment and limiting secondary effects due to the systemic delivery of the drug.

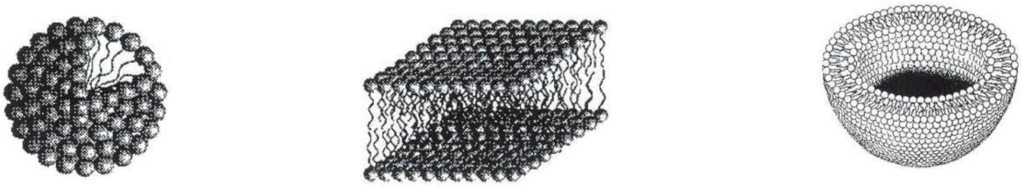

Figure 5.5: Examples of structural organisations of lipids. Left: single, self-closed lipid monolayer: micelle._Center: lamellar structure, lipid bilayer. Right: several lipids bilayers (one is shown here) self-closed on an aqueous core: structure of a liposome (cross-cut) (adapted from[251]).

5.1.5.b Receptor insertion into liposomes

Four basic strategies have been described for the insertion of membrane proteins into liposomes: mechanical means, freeze-thaw, organic solvent and detergents. However, the destabilisation of lipid membrane structure required for the protein insertion, and the need to keep the protein in a non-denaturing environment during further purification, requires the use of detergent. The addition of detergent disrupts lipid-lipid interactions, which results in a more permeable bilayer. These structures are more receptive to protein uptake, and after protein is introduced, excess of detergent is removed.

Three stages during detergent-mediated lipid solubilisation have been described (Figure 5.6). As the turbidity of the solution decreases as the lipid solubilisation increases, the evolution of the solubilisation can be assessed by measuring the OD. The best stage for protein insertion is between the onset of solubilisation, R_{sat}, and the complete solubilisation of liposomes, R_{sol}.

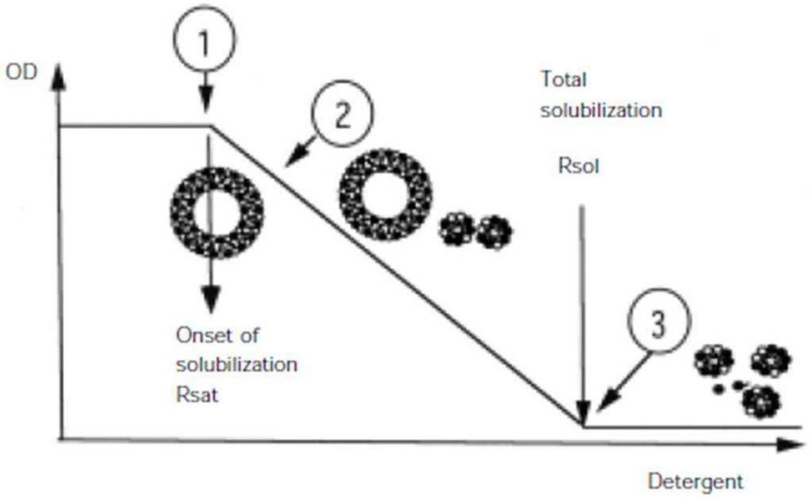

Figure 5.6: Schematic diagram showing the polymorphic changes from liposome to micelle caused by detergent partitioning into bilayers. The solubilisation of lipids can be divided into three stages. Prior to point 1, detergent begins to partition into bilayer. From point 1, the detergent:lipid ratio of greatest saturation is reached (onset of solubilisation). The further increase of detergent concentration induces the liposomes solubilisation and a mix of liposomes and micelles is found in the solution (point 2 to 3). When OD has reached its minimal value (Rsol, point 3), the solubilisation is complete and the mixture consists of micelles at varying detergent:lipid ratios (adapted from[252]).

5.1.5.c Detergent removal

After lipid and proteins co-solubilization, it is thus necessary to remove the detergent, which could impair the functions of the receptor. Different methods exist to remove detergent, such as dialysis, dilution, gel chromatography, ion-exchange chromatography, or nickel columns, but these methods are not suitable for detergent with low cmc[253] (such as DDM, used in this study) and large micelle size. The technique used here is based on the adsorption of detergent to insoluble hydrophobic resins or “beads”. Due to their amphiphillic nature, detergents bind to the biobeads through the interaction of their hydrophobic tail with the hydrophobic surface of the beads.

Neurotensin is involved in numerous biological functions as well as in diverse pathologies: studying NT signalling may therefore provide useful insight into treatments for conditions such as Parkinson’s disease, schizophrenia and obesity.

The aim of this project was to prepare the neurotensin receptor type 1 NTS1 for biophysical studies of its structure (in particular its oligomerisation state) and its ligand-receptor interactions, using solid state NMR and AFM force spectroscopy. This work focused on purifying the receptor and performing the functional reconstitution of this membrane protein into liposomes. Electron microscopy and the AFM proximal probe technique were used to control the size homogeneity of the liposomes preparations prior protein insertion, while the retained functionality of the reconstituted receptor was confirmed by competitive radioligand binding assay.

5.2 Materials and Methods

5.2.1 Purification of NTS1

NTS1 was expressed as a fusion protein (Figure 5.4) in *E.coli* BL21 cells from the pRG-hs-MBPP-T43NTR-TrxA-H10 plasmid. NTS1 is expressed with a maltose binding protein at the N-terminus, allowing targeting to the periplasm. Thioredoxin, helping for stability, and a deca-his tag, used for nickel column purification, are attached to the C terminus.

Once expressed in *E.coli*, the fusion protein is purified by using a Nickel affinity column (His-Trap column) followed by a gel filtration chromatography.

Detergents used during purification can strip phospholipids that are needed for folding and functions of the receptor. In order to prevent delipidation of the receptor, buffers used during purification were supplemented by a mix of three lipids, POPC, POPG and POPE which have acyl chains similar to the major lipids naturally present in biological membranes of mammals. This supplementation improves the yields for the purification, by aiding stability of the protein compared to a 100% detergent solution.

In order to stabilise NTS1 and thus, to improve purification, buffers are supplemented with some of the major lipids found in mammalian cell membranes (Table 5). All steps were performed in a cold room (4°C), where possible.

About 20g pellets were thawed by stirring in 2X solubilisation buffer (2x vol/g pellet). Protease inhibitors were then added : 1/500 dilute leupeptin, 1/1000 dilute pepstatin A, 1/5000 dilute aprotinin, followed by $MgCl_2$ to a final concentration of 5mM, DNase (10µl/10g) and lysozyme (0.5 mg/ml from a 10 mg/ml stock). The solution is then topped up with dH_2O, so that the buffer concentration is 1X, and resuspended using a hand-held homogeniser. Each detergent stock was added to a 10% of the total volume: 5%CHAPS-

1%CHS first, then 10% DDM, drop-wise, stirring. The next step consists in adding the phospholipids mix POPC:POPG:POPE, 3:1:1 at 0.1 mg/ml final concentration and stirring during one hour. The pellets are then centrifuged 60 min at 75,000g. The supernatant is removed and filtered through a stericup.

5.2.1.a Nickel affinity chromatography

A 5 ml His-Trap column is washed with 5 CV dH_2O and 5 CV NiA, before loading the sample at 2.5 ml/min onto the nickel column. A 30-40 CV wash is done until $OD_{\lambda=280}$ drops and stabilises at baseline, NiA. At last, elution is performed with NiB. 20µl of each fraction are collected before the fractions are pooled.

Another 20µl sample is collected after the pool, and the sample is concentrated to 2.5 ml by several centrifugation cycles (6,000g, 10 min, 100,000 MWCO membrane (Vivaspin 20, Vivascience/Sartorius)). Care is taken to gently stir the sample between each cycle so that it does not precipitate on the membrane. 20 µl aliquots are taken after concentration for a future SDS-PAGE.

5.2.1.b Gel Filtration Chromatography

Once concentrated, the sample is centrifuged (3 min, 10,000g) and loaded onto a 190 ml Superdex column (XK 16/100). The run is set at 0.25 ml/min, overnight. The day after, 20 µl aliquots are taken from eluted fractions corresponding to the peak on the chromatograph. Those fractions are kept on ice while running the SDS-PAGE and then pooled depending on the results of their migration on the gel.

At last, the sample is concentrated till 1ml as before, aliquoted in 50µl aliquots and stored at - 80°C.

5.2.2 Solid Phase Peptide Synthesis of the NT ligand

Full length unlabelled NT $_{(1-13)}$ was synthesised using the solid phase peptide synthesis. In SPPS, the first amino-acid is bound to a resin via an acid-labile linker, the other amino-acids being added following protecting-deprotecting cycles. At last, the full peptide is cleaved from the resin. Synthesis is made more efficient by protecting the N-terminal of amino acid that have been added to the growing deprotected polypeptide. Two main protecting groups exist, Boc and Fmoc. The Fmoc (9-fluoenylmethoxycarbonyl), strategy, more expensive but requiring softer deprotecting conditions (piperidine in DMF, instead of TFA for Boc protections), is used in this study (Figure 5.7). Moreover, some amino acids side chains have functional groups which can interfere with the formation of the amide bond: these are masked using chemical groups that are removed during cleavage. This synthesis is usually done using an automated process, however, due to technical issues, the peptide has been prepared manually. Some hydrophobic amino acid (Leu, Ile, Tyr, Pro) do not couple as efficiently as others, a double-coupling is therefore required for them.

5.2.2.a Swell resin

Novasyn TGR resin (0.4g) was used for the synthesis of NT (1-13) (loading 0.25mmol/g). Resin was swelled in excess DCM for 20 minutes, washed with DMF and swelled for a further 20 minutes in excess DMF, followed by drainage.

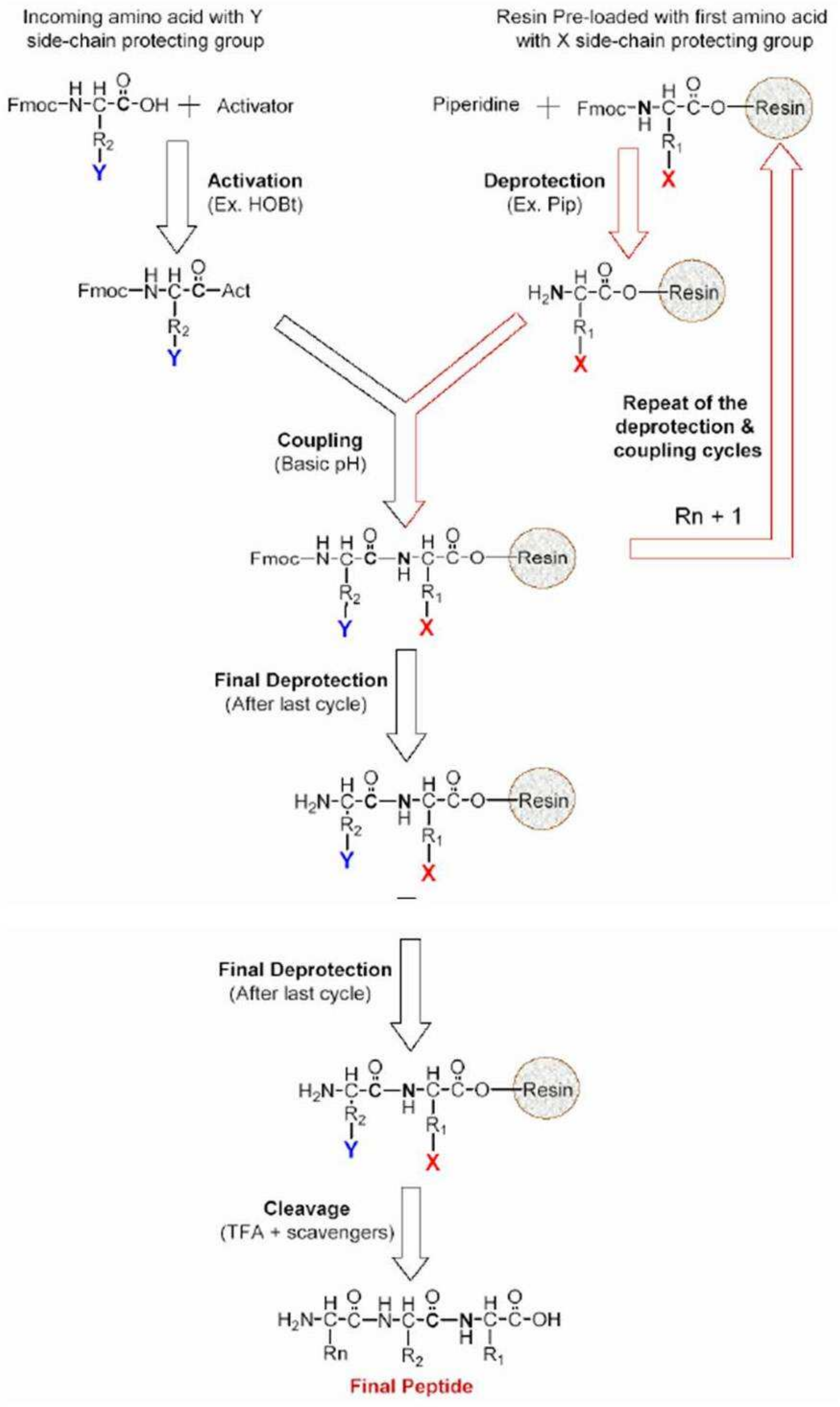

Figure 5.7: General scheme for SPPS using Fmoc chemistry. The first Fmoc-protected amino acid is linked to an insoluble support resin via an acid labile linker. Piperidine in solution in DMF is used here for deprotecting the Fmoc protecting group. The second protected amino acid is added using a preactivated specie. After coupling, excess reagents are removed by washing the resin. The process is repeated until the desired peptide sequence is assembled. The last step consists in deprotecting the resin bound-peptide and cleaving it from the resin via TFA (the activator of incoming amino-acid is HOBt/HBtu,or HOBt/PyBOP in this study). Adapted from Sigma Genosys technical bulletin).

5.2.2.b Coupling

All coupling reagents and Fmoc-protected amino acids were supplied by CN Biosciences. Coupling was carried out using a three times excess of the coupling reagents N-Hydroxybenzotriazole (HOBt), 2-(H-Benzotriazole-1-yl)-1,1,3,3-tetramethyluronium hexafluorophosphate (HBTU) and Benzotriazol-1-yl-oxytripyrrolidinophosphonium hexafluorophosphate (PyBOP) and a two times excess of Fmoc-protected amino acids. HOBt/HBTU were used for single couplings, while HOBt/PyBOP were used for double-couplings.

Coupling reagents and amino acids were dissolved in a minimal amount of DMF and 200µl DIPEA were added to start the reaction. This was left for 2 minutes before the addition of the resin. The coupling reaction mixture was agitated for ~1 hour, drained, washed 3 times with excess DMF and tested with ninhydrin for the presence of primary amine groups. If a positive result was obtained (blue colour), further coupling was carried out.

5.2.2.c Deprotection

Fmoc deprotection was carried out using 5ml 20% piperidine in DMF under agitation for 30 minutes, followed by 3 times washing with DMF. A positive ninhydrin test indicated deprotection had been carried out successfully.

5.2.2.d Cleavage

The resin was washed 3 times with DCM and 3 times with methanol in order to collapse the beads, followed by a single wash with diethylether wash. The resin was then dried for 24h in a dessicator under vacuum. The resin was then separated in two columns, and two cleavage protocols were used.

First cleavage protocol consisted in adding 5ml of the TFA (95%), triethylsilane (2.5%) and water (2.5%) solution (v/v), and agitating for 3 hours. Second cleavage was achieved by agitating overnight in 5ml of cleavage solution TFA (82.5%), thioanisole (5%), water (5%), phenol (5%), and EDT (2.5%). For each cleavage protocol, the resultant liquid was drained off under vacuum and the resin washed two times with TFA. Excess TFA was then evaporated off using nitrogen until ~1ml remained. 50 ml of ice cold diethyl ether was added followed by centrifugation (6000 rpm, 4°C, 15 minutes). The ether extraction process was repeated twice on the peptide pellet and the resulting pellet suspended in minimal water and lyophilised until dry.

5.2.2.e High Performance Liquid Chromatography (HPLC)

New synthesised peptide was purified using a C18 Dynamics 83-213-C 20 ml semi-preparative column with a flow rate of 3 ml/min. De-gassed acetonitrile and water solvents containing 0.1% TFA were used, ramping from 80% water, 20% acetonitrile, to 74% water, 26% acetonitrile in 14 minutes.

Absorption of eluant was tested at 220nm and 280nm and the major fractions were collected and analysed by ESI mass spectrometry.

5.2.3 Reconstitution of NTS1 into liposomes

5.2.3.a Formation of 100 nm lipid vesicles

Previous work using POPC-only bilayers for reconstitution showed that NTS1 insertion was successfull[254], as confirmed by incorporation of fluorescent receptor into the liposomes, but the receptor showed no ligand binding activity. Here, reconstiution was performed using Porcine Brain Polar Lipids (BPL).

BPL (Avanti Polar Lipids) were dissolved in a 50:50 v/v methanol: chloroform mix to reach a final lipid concentration of 5 mg/ml. The solution was dried down to a lipid film under nitrogen, and then further dried in a dessicator under vacuum ($<10^{-5}$ torr) for several hours. The lipid film is suspended in buffer A (*Appendix 2*, saturated under nitrogen prior to use) at 5 mg/ml by pipetting, forming a milky suspension. Resuspension is completed by a 1-2 min sonication bath, followed by 10 freeze-thaw cycles in liquid nitrogen. This step allows the formation of large multilamellar liposomes.

Homogenous-sized unilamellar vesicles were formed by extrusion (filtration under high pressure) through 0.4µm and 0.1µm polycarbonate membranes (11 passes for each, Figure 74), and stored at 4°C after saturation under nitrogen.

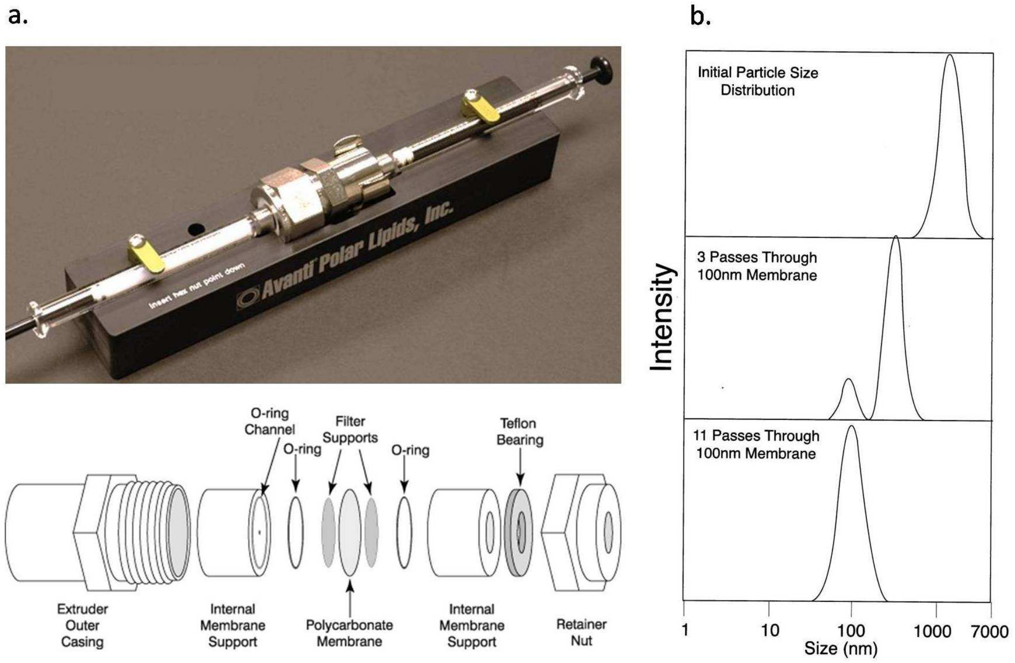

Figure 5.8: Extrusion process. **a.** picture of an extruder (top) and detailed representation of its inner parts (bottom). **b.** Evolution of the liposomes size distribution according to the number of passes through the extruder, using a 100 nm membrane: 11 passes are required to produce a unimodal, normal size-distribution centred about the mean, expected value. Adapted from Avanti Polar Lipid.

5.2.3.b Liposome disruption with DDM: determining Rsat and Rsol

Solubilisation of liposomes is carried out by adding increasing amounts of detergent to aliquoted vesicle suspensions. The detergent used in this study, DDM, is a non-ionic detergent with a low critical micellar concentration (cmc) and is characterised by an intermediated length of the hydrophobic moiety and a bulky hydrophilic sugar group. Optimal insertion of membrane proteins into liposomes occurs at DDM:lipid ratios between the onset of solubilisation, R_{sat} and the total solubilisation of the lipids, R_{sol}.
One of the first steps of this study consisted of determining R_{sat} and R_{sol}.

Detergent was added to preformed liposomes using a range of detergent concentrations that cause the transformation of lamellar structures to mixed micelles. Since the turbidity of lipids increases as they become more saturated with detergent, the different steps of solubilisation were followed by measuring the sample absorbance.
The extruded lipid solutions (5 mg/ml) were diluted to concentrations ranging from 1.5 to 3.9 mg/ml in buffer A (pre-saturated with nitrogen) and aliquoted as 200 µl per tube. For each lipid dilution, volumes of DDM were added to reach detergent concentrations ranging from 0 to 10 mM. Preparations were left at RT for 6 h, and the OD was read at 500nm using a buffer blank. Once R_{sat} and R_{sol} were determined, lipid disruptions of all experiments were performed by treating 200 µl liposomes aliquots with different amounts of 10% DDM, using detergent:lipid ratios between Rsat and Rsol, and the preparation was incubated 3 h at RT.

5.2.3.c Protein insertion

The equilibrated detergent-phospholipid mixtures were added to 50µl of purified receptor (the concentration of which was 0.1 mg/ml), using a 2000:1 lipid-protein molar ratio. Samples are incubated for 1h after gentle agitation. These steps were performed at 4°C.

5.2.3.d Detergent removal

DDM was removed by adsorption on hydrophobic beads (SM2 Biobeads, BioRad). The biobeads were prepared according to the manufacturer's instructions and added to each DDM-lipid-receptor to a final concentration of 120 mg/ml. Preparations were left on a rotating wheel overnight at 4°C.

5.2.3.e Isolation of the proteoliposomes

5.2.3.e.i Centrifugation and resuspension of pellet

Two different ways to isolate proteoliposomes were used.

The first method consisted of diluting the biobead supernatant into 750 µl buffer, and ultracentrifugating (100,000g, 1h, 4°C). The proteoliposomes were isolated by resuspending the pellets in 200 µl buffer A, aliquoted in 50 µL aliquots and stored at -80°C.

5.2.3.e.ii Sucrose gradient, ultracentrifugation and SDS-PAGE

A second technique of proteoliposomes purification consisted of layering the biobeads supernatant on top of a sucrose gradient is preferred for isolating the proteoliposomes.

A 5% to 35% sucrose gradient was made with 5% increments from a 70% sucrose solution diluted in buffer B (see composition in Appendix 2). Each sucrose solution (1.5 ml) was layered in ultracentrifuge tubes.

Reconstituted samples (200µl) were layered on top of the gradients. An ultracentrifugation was then performed (100,000 g, 15h, 4°C) using an SW41 swingout rotor. Proteoliposomes migrate in the gradient depending on their density, which depends on their protein:lipid ratio. Bands were seen where the proteoliposomes stopped their migration in the gradient. Fractions (500µl) surrounding the bands were collected, and

20µl of each were used for SDS-PAGE. Fractions containing the proteoliposomes were pooled.

5.2.3.f SDS-PAGE

Pre-poured 4%-12% Tris-Glycine gels (Invitrogen Novex) were used in the 1x Tris-Glycine SDS-PAGE running buffer (25 mM Tris Base, 192 mM Glycine, 0.1 % SDS) with a voltage of 150 V during 1.30 h. Protein bands were visualised by Coomassie brilliant blue staining and compared to the bands obtained with prestained protein markers (ranging from 6.5 to 175kDa, BioLabs), during NTS1 purification. However, in the case of reconstitution, where small amounts of inserted receptor were present, Coomassie blue staining was replaced by silver staining (Silver Stain Plus, BioRad).

5.2.3.g Ligand-binding Assay

After NTS1 purification, and for each reconstitution, the amount of available receptor is assessed by measuring its ligand- binding activity using a full length radiolabelled ^{3}H-NT peptide ([3,11-tyrosyl-3,5-^{3}H(N)] with specific activity 92.5 Ci/mmol (3.7 TBq/mmol) and total activity 0.025 mCi (0.925MBq), Perkin Elmer). Competition with the unlabelled peptide is used to determine non- specific binding.

Two samples were used for each ligand binding assay: one sample for measuring the specific binding, in which diluted receptor is supplemented with assay buffer and labelled peptide, while the other sample was used for measuring the non-specific binding and had the same composition, with addition of an excess of unlabelled peptide (Table 1). Specific and non specific samples were done in triplicate and left one hour at 4°C. Receptor dilution in the assay preparation was usually 1/1000 for activity assay after purification, 1/10 after reconstitution, and 1/2 after resolubilisation.

The ligand binding activity of purified receptor was assessed by filtering 50µl of the preparations through gel filtration spin columns by centrifugation (1,000g, 3min). Columns (Micro Bio Spin-30 chromatography columns, Bio Rad) were previously pre-equilibrated with 500 µl assay buffer and centrifuged just before use (2min, 1,000g). Samples were flowed through columns and added to 3ml of scintillation cocktail (Optiphase Hisafe 3, Perkin Elmer), vortexed, and analysed.

---

a. Ligand binding assay performed on proteoliposomes (membrane filtration)

	3H NT 1/100 dilution	Assay Buffer	Protein : dilute 1/10	Unlabelled (2mM)
specific	10 µl	165 µl	25 µl	0
non specific	10 µl	155 µl	25 µl	10 µl

b. Ligand binding assay performed on purified receptor and resolubilised proteoliposomes (gel filtration column)

	3H NT 1/100 dilution	Assay Buffer	Protein : dilute 1/x	Unlabelled (2mM)
specific	5 µl	30 µl	25 µl	0
non specific	5 µl	28 µl	25 µl	2 µl

Table 5.1: Sample preparations for ligand-binding assays. The amount of active receptor is assessed by measuring its binding to labelled NT in competition with the unlabelled peptide. Two types of preparations, specific and non specific, were done in triplicate. Receptor dilution was usually 1/1000 for activity assay after purification, 1/10 after reconstitution, and 1/2 after resolubilisation. The amount of active receptor was obtained by subtracting the non specific activity to the specific activity, and by converting the results given in cpm (count per minute) into pmol (60,000 cpm/pmol).

The ligand binding activity of the reconstituted receptor, was assayed by filtering 190µl of the preparations through a membrane under vacuum and washing them in 190µl assay buffer (different buffers were used depending on the type of sample assayed, see Appendix 2). Then 6ml of scintillation cocktail were added to the membranes in scintillation vials, vortexed and left for at least 2 hours at RT. Preparations were vortexed again before the assay.

Ligand binding assays were performed using a scintillation counter (Beckman-Coulter Bioresearch) taking the average counts per minute in a five minute period. The amount of active receptor was obtained by subtracting the non specific activity to the specific activity, and by converting the results given in cpm (count per minute) into pmol (60,000 cpm/pmol).

The radiolabelled peptide, ^{3}H-NT, used in the activity assay was supplied (Perkin Elmer), but the full length unlabelled peptide needed to be synthesised in the laboratory. Manual SPPS was performed to produce $NT_{(1-13)}$, followed by a reversed phase HPLC for purifying the new-synthesised peptide.

5.2.3.h AFM high resolution imaging of liposomes

Imaging of liposomes has been performed with AFM before and after protein insertion in order to control, first that the extrusion process did produce homogeneously-sized 100 nm liposomes, and then, that the liposomes retained their vesicular structure and average dimension following NTS1 insertion. Imaging was performed on mica, using a Veeco (Bruker) Multimode AFM, in tapping mode in air.

AFM imaging has also been performed in order to follow the behaviour of adsorbed liposomes on the substrate over time. All liposomes images were obtained using high-resolution AFM probe, exhibiting a low (< 5 nm) radius of curvature.

5.3 Results and Discussion

5.3.1 Purification of NTS1

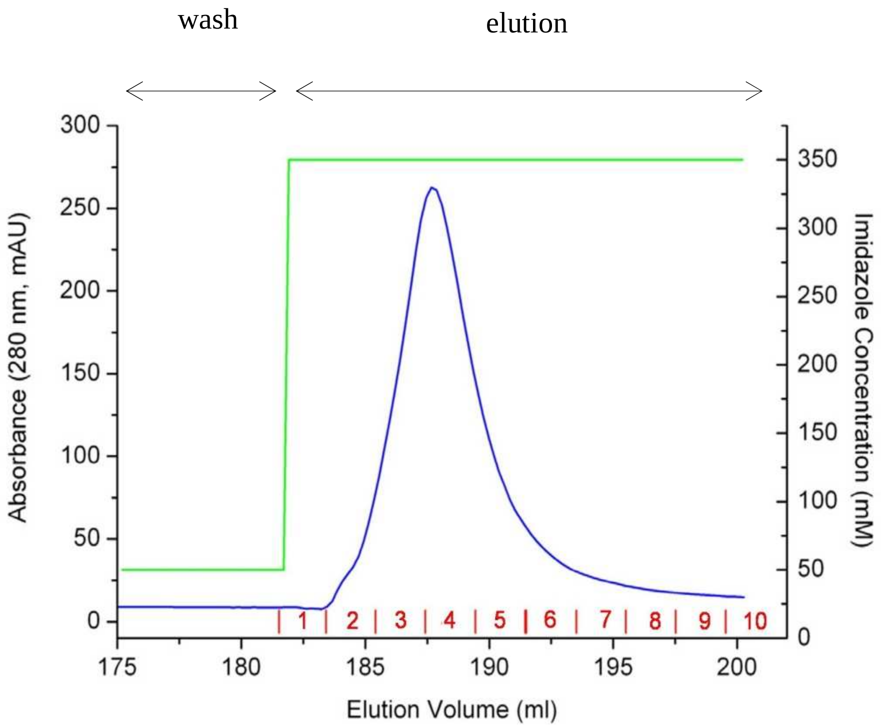

<u>Figure 5.9</u>: His-Trap elution profile of NTS1B fusion protein. Absorbance at 280 nm is shown in blue. The peak at ~188 ml corresponds to eluted receptor. The step gradient from NiA wash buffer (50 mM imidazole) to elution buffer (350 mM imidazole) is shown in green.

NTS1 purification was first carried out on a His-Trap column (nickel affinity chromatography). The non-specifically bound protein was eluted during the washing step in 50 mM imidazole (NiA buffer). Washing was continued until OD_{280} dropped and stabilised at baseline NiA, before eluting NTS1 in a higher concentration of imidazole (350 mM). Figure 5.9 shows the receptor elution profile (absorbance at 280 nm is shown in blue). Eluted fractions 1 to 6 were collected and concentrated.

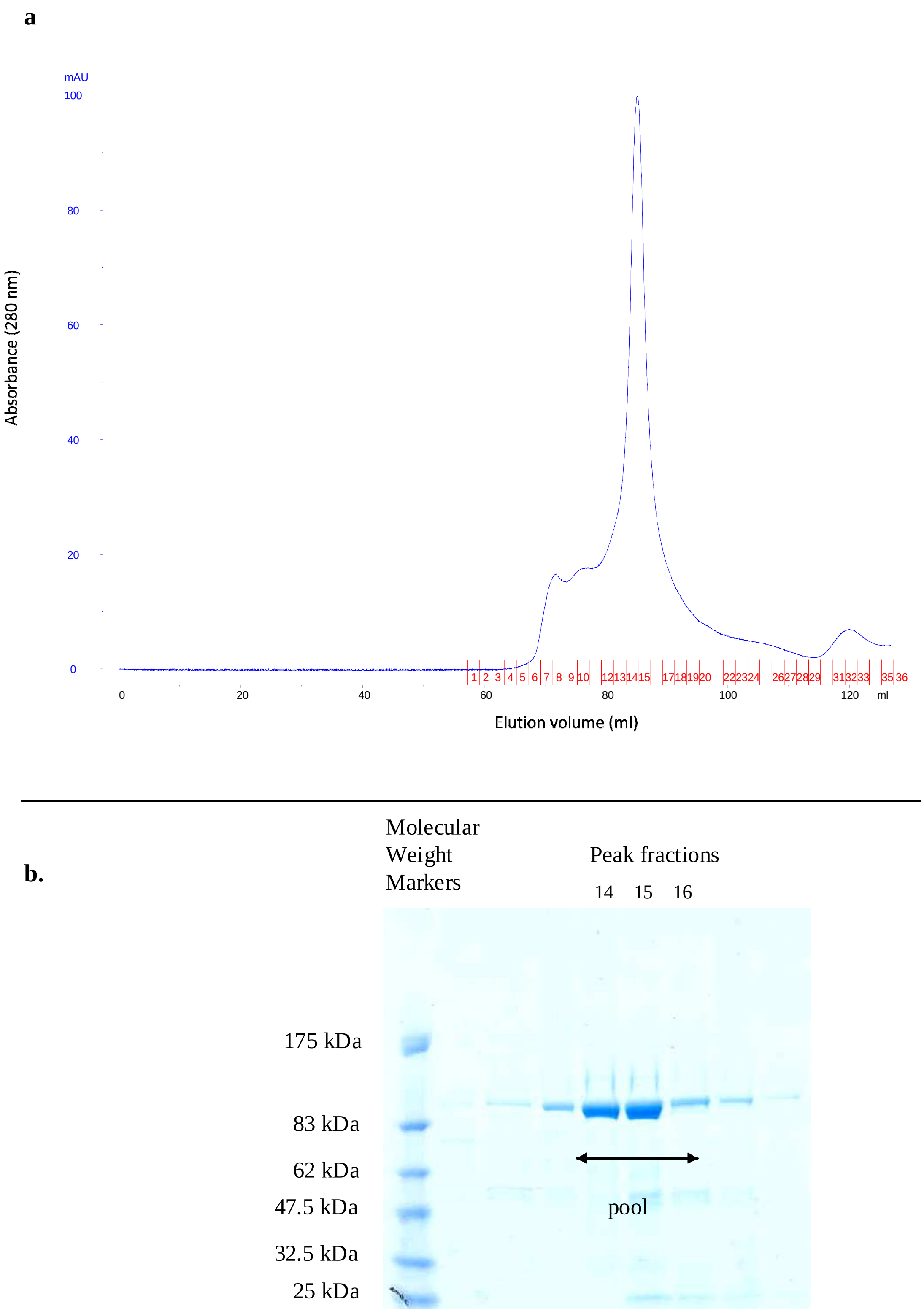

Figure 5.10: Purification of NTS1B by gel-filtration chromatography. a. Superdex 200 gel filtration elution profile, showing a large peak corresponding to eluted NTS1 (fractions 6-18). The absorbance at 280 nm (blue) and the fraction number (red) are shown**. b.** Coomassie-stained SDS-PAGE of gel filtration peak fractions**.** Fractions 8, 10,12, 14,15,16,17,and 19 were loaded on the gel. After migration, fractions 14 to 16 were pooled.

The concentrated sample was then loaded on a Superdex 200 column (size-exclusion gel-filtration) and the run was monitored at 280nm (Figure 5.10). Fractions were collected overnight: a large peak was obtained corresponding to eluted NTS1. A SDS-PAGE was run on different peak fractions, which were pooled depending on the gel results.

Active receptor was obtained from a 20 g pellet at an average concentration of 0.15 mg/ml when purified with only POPC, and at an average concentration of 0.25 mg/ml when the 3 lipids were used. POPE and POPG were omitted from future preparations because of the complications they caused in the reconstitution (see below).

5.3.2 Solid Phase Peptide Synthesis-HPLC

The neurotensin NT (1-13) ligand used for ligand-binding assays was synthesised manually using the SPPS technique. After cleavage from resin and lyophilisation, new-synthesised peptide was purified using reverse phase HPLC column and the major peaks were collected and analysed by ESI mass spectrometry.

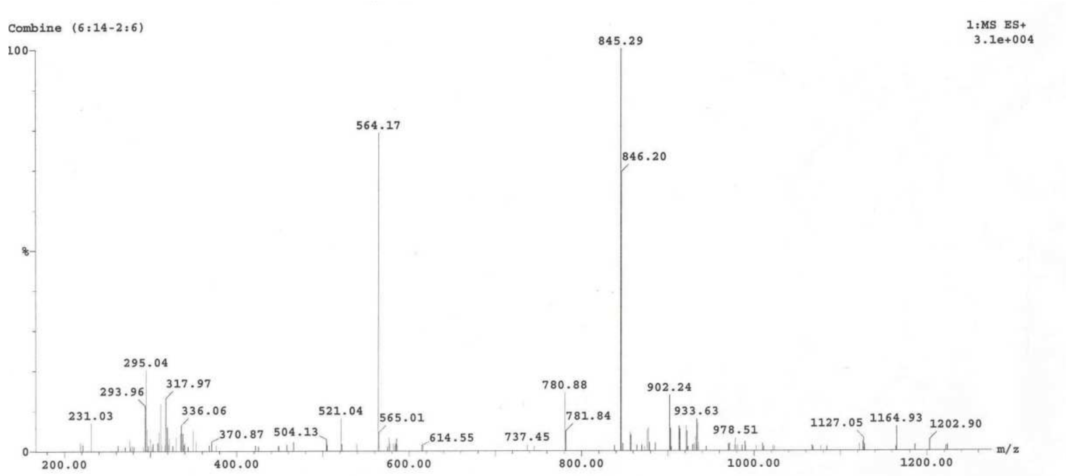

Figure 5.11: ESI mass spectrum of full NT$_{(1-13)}$. The peaks at 564.17 and 845.29 correspond to the full neurotensin peptide. m/z = 3 for the peak 564.17, and m/z = 2 for the peak 845.29.

This analysis gave a mass spectrum containing one major peak with an m/z ratio of 845.29 Da (Figure 5.11) and another one at 564, corresponding to doubly and triply charged peptide (the weight of the parent ion is 1690 Da).

5.3.3 Reconstitution of NTS1 in liposomes

5.3.3.a EM /AFM imaging of 100 nm lipid vesicles

Purified NTS1 will be inserted during the reconstitution process into 100 nm BPL lipid vesicles formed by extrusion through two sizes of polycarbonate membrane. Liposomes ready for reconstitution were studied with transmission electron microscopy (TEM) and AFM, providing images of the preparations and confirming that the lipid vesicles were in the expected range of sizes. Figure 5.12 shows micrographs obtained from liposomes formed after extrusion through 400nm (left) and 100nm (right) polycarbonate membranes; samples studied with TEM were stained prior to imaging. TEM experiments were performed after the first liposomes preparation; further liposomes size assessments were then performed using AFM, which is a much faster process for sample preparation (direct deposition onto imaging substrate) that does not require any sample treatment.

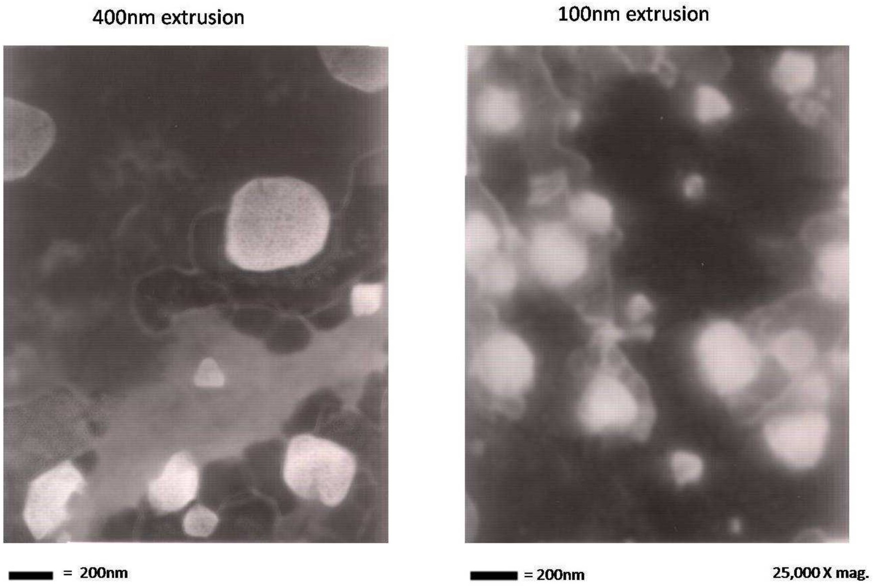

Figure 5.12: TEM micrographs of liposomes before protein reconstitution. a: TEM micrograph of negatively-stained 0.4µm liposome sample at 25,000x magnification. The liposomes appear lighter than the background since they are negatively stained. The scale bar (200nm) indicates that the majority of liposomes are in the 300-400nm size range. Light-grey material is an artefact of the uranyl- acetate staining method used. **b**. **TEM micrograph of negatively-stained 0.1µm liposome sample at 25,000 x magnification**. The scale bar (200nm), indicates that the majority of liposomes are in the 100-200nm size-range, although larger liposomes are also visible. (Thanks to Daniele Selmi for these micrographs).

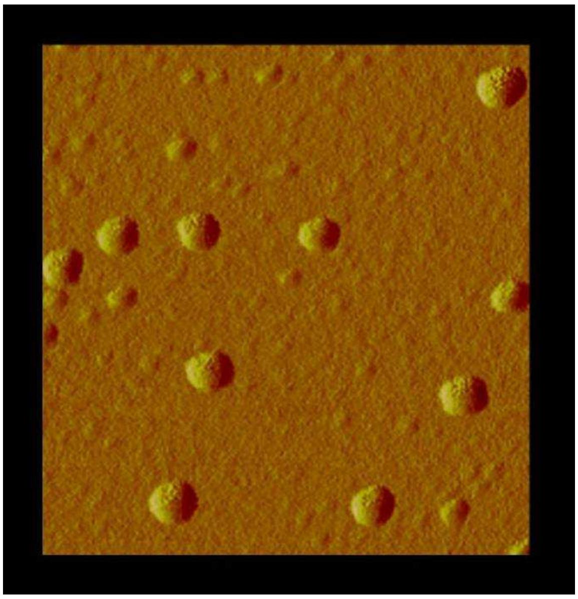

Figure 5.13: AFM images of 100 nm BPL lipid vesicles after 5 min incubation on mica. Sample (10µM) adsorbed on mica straight after extrusion. Tapping mode imaging in buffer; scan size 1 µm.

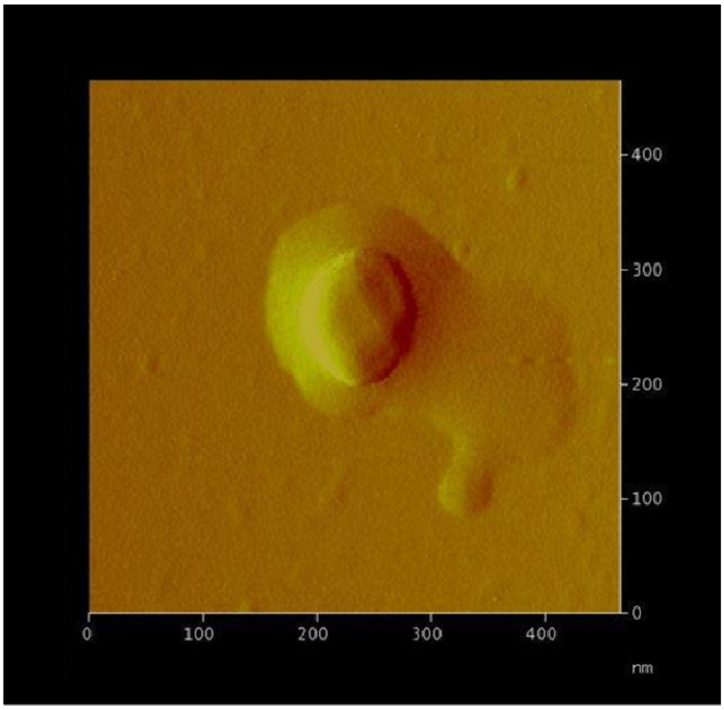

Figure 5.14: AFM image of one liposome adsorbed on mica (10 minutes incubation time) prior protein insertion. This confirms that the vesicles are in the expected range size of ~100 µm after extrusion; scan size 460 nm, tapping mode in air, amplitude image; Veeco instruments.

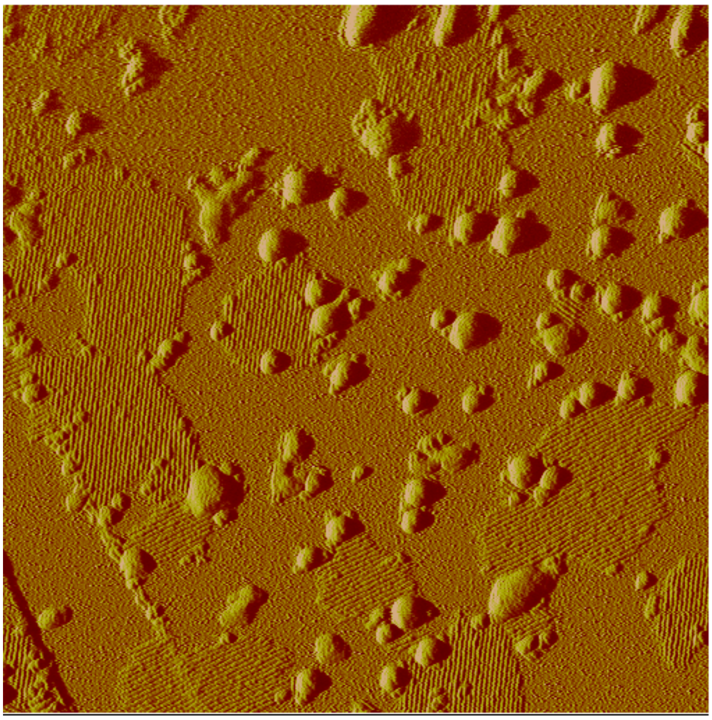

Figure 5.15:. Evolution of the liposomes adsorption following a 15-min incubation on mica Half of the vesicles have fused into lipid bilayers on the surface. Amplitude image; scan size 1 µm.

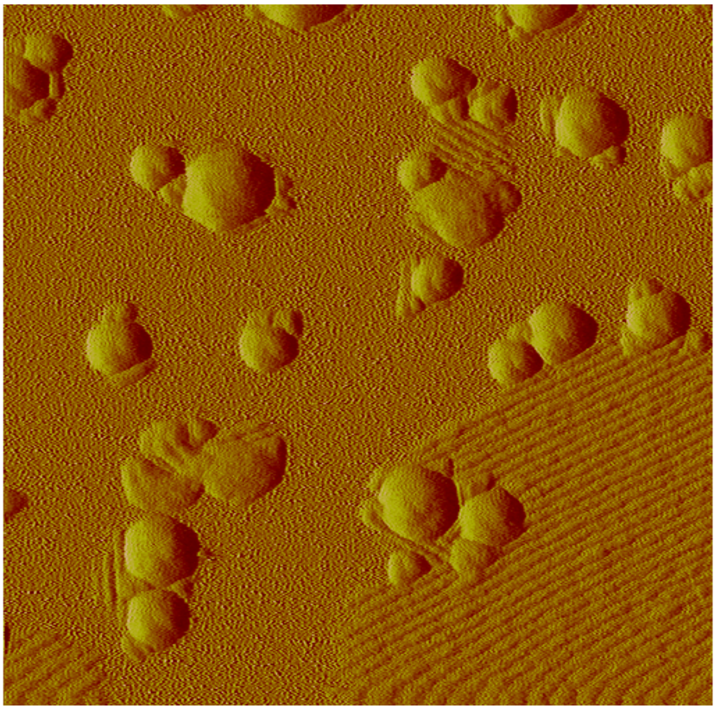

Figure 5.16. **AFM image of liposomes on mica after 15 minutes incubation**.Same sample as on the previous AFM picture, imaged at a smaller, 400 nm, scan size; amplitude image.

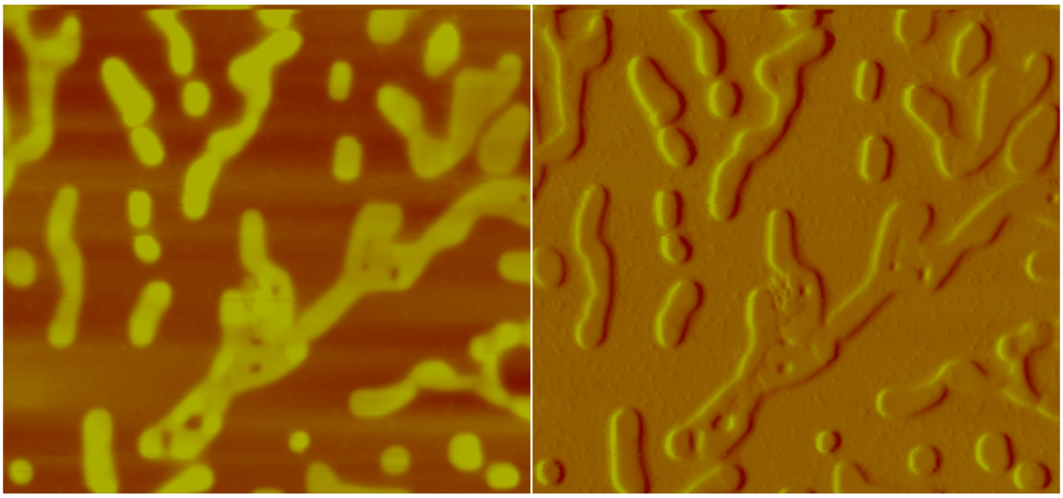

Figure 5.17 After 20 min of incubation, no lipid vesicles are visible anymore, they have all merged into bilayers (topographic, left, and amplitude, right, images; scan size: 2 µm for each picture; Veeco instrument).

Assessment of the actual size of newly-formed liposomes was performed after extrusion by TEM and AFM, and confirmed that the lipid vesicles exhibited the expected dimensions. AFM imaging was then used to look at the evolution of the liposomes adsorbed on the non polar mineral mica substrate over time: the images clearly show a progressive fusion of the lipids onto the surface to the point where all vesicles have fusent into bilayers (Figures 5.13 to 5.17).

5.3.3.b Lipids disruption - Determination of R_{sat} and R_{sol}

Lipid vesicles (100nm) at concentrations ranging from 1.5 mg/ml to 3.9 mg/ml (2 to 5 mM) were disrupted by addition of increasing concentrations of detergent. For each lipid concentration, the highest OD value was considered as R_{sat}, and the lowest OD value before stabilisation at baseline was corresponding to R_{sol}. The global values of R_{sat} and R_{sol} used as references for all the following experiments were obtained by the derivation of these results as a function of the lipid concentration, and by drawing the linear equation:

[detergent] = Reff . [lipids] + cmc

where Reff is the effective detergent:lipid ratio, ie Rsat or Rsol here.

The OD measurements and their derivation showed that the DDM : lipid ratio corresponding to the onset of solubilisation was Rsat = 1, while the ratio corresponding to the total solubilisation of liposomes into mixted micelles was Rsol = 1.3 (Figure 5.18).

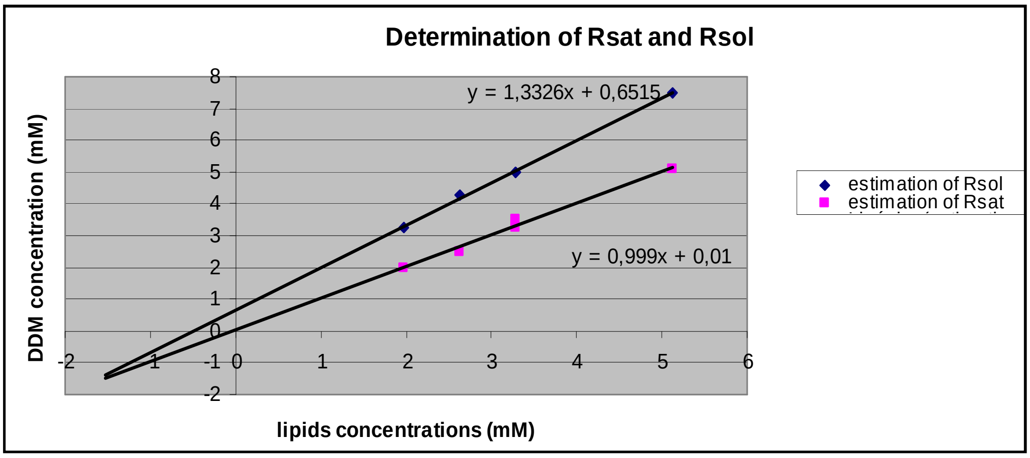

Figure 5.18: Determination of Rsat and Rsol. OD measurements were performed at 500 nm on lipids vesicles disrupted with a 0 to 10 mM range of DDM concentrations. The derivation of the highest (estimation of Rsat) and lowest (estimation of Rsol) OD values for each lipids concentration allowed to obtain an estimation of Rsat = 1 and Rsol = 1.3

5.3.3.c Isolation of the proteoliposomes (sucrose gradient)

It was found that proteoliposome isolation by pelleting using ultracentrifugation was not reliable, especially for small amounts of reconstituted receptor (in this case, pellets may be so small that they cannot be seen and thus isolation of the proteoliposomes cannot be done efficiently). The other method used therefore was the isolation on a sucrose gradient. Sucrose gradient has the added advantage of removing any aggregated/uninserted protein: this is another purification step that separates by density.

Before using this technique to isolate proteoliposomes, one sucrose gradient was first performed with a 5 mg/ml lipid vesicles solution. A tight band was clearly distinct on top of the gradients (Figure 5.19). These encouraging results lead us to try this technique with proteoliposomes.

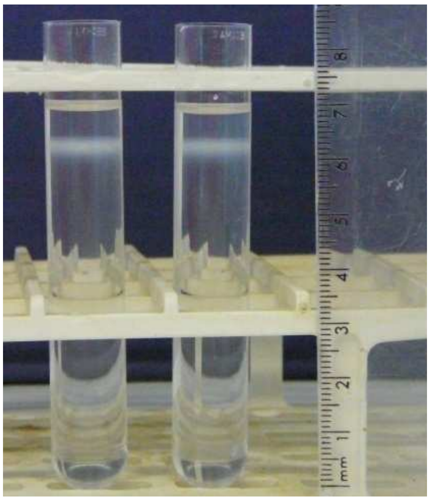

Figure 5.19 Sucrose gradient performed on 100nm liposomes.
An aliquot of 5 mg/ml solution of 100 nm liposomes was layered on top of 0-30% sucrose gradients. The migration of the liposomes during the 15h-long ultracentrifugation is clearly shown by two tight bands, at 5% sucrose, for each sample.

When carried out on proteoliposomes, the migration on the sucrose gradient is followed by the collection of fractions (500 µl) surrounding the bands and the run of a SDS-PAGE. Tight and distinct band on the gradient, represented by a few bands on the gel, indicates that most of the proteoliposomes moved at the same point of the gradient. Thus, reconstitution lead to the formation of homogenous proteoliposomes, all having quite similar lipid: protein ratios. The results presented here (Figure 5.20) show a tight band at 30% sucrose after migration of proteoliposomes, corresponding to a lipid protein ratio weight of 400:1, which is a good receptor density for biophysical studies, including solid state NMR and AFM structural work.

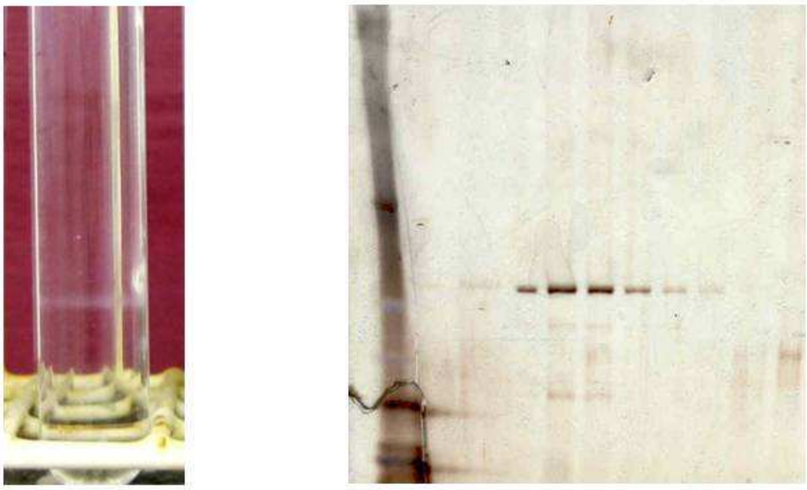

Figure 5.20: Isolation of homogeneous NTS1: POPC proteoliposomes using a sucrose gradient and SDS-PAGE (silver staining). A tight band can be observed at 30% sucrose after migration of proteoliposomes, corresponding to a lipid protein ratio of 400:1. Fractions (500µl) were collected from the gradient and loaded on a gel. After migration, fractions containing the reconstituted receptor are clearly localised, indicating that all proteoliposomes moved at the same point in the gradient, and thus, are all with similar lipid:protein molar ratios. Those fractions are pooled. (this experiment was performed on proteoliposomes formed with a DDM:lipid ratio = 1 and a receptor purified using buffers only supplemented by POPC)

However, these encouraging results have shown not to be reproducible. Indeed, in numerous experiments, diffused bands were observed on the gradient, although the same protocol was used each time. In these cases, diffused bands observed on the gradient were confirmed by the run of an SDS-PAGE detecting receptor all over the gel (Figure 5.21). This indicates that heterogenous proteoliposomes were formed, containing disimilar lipid: protein ratios.

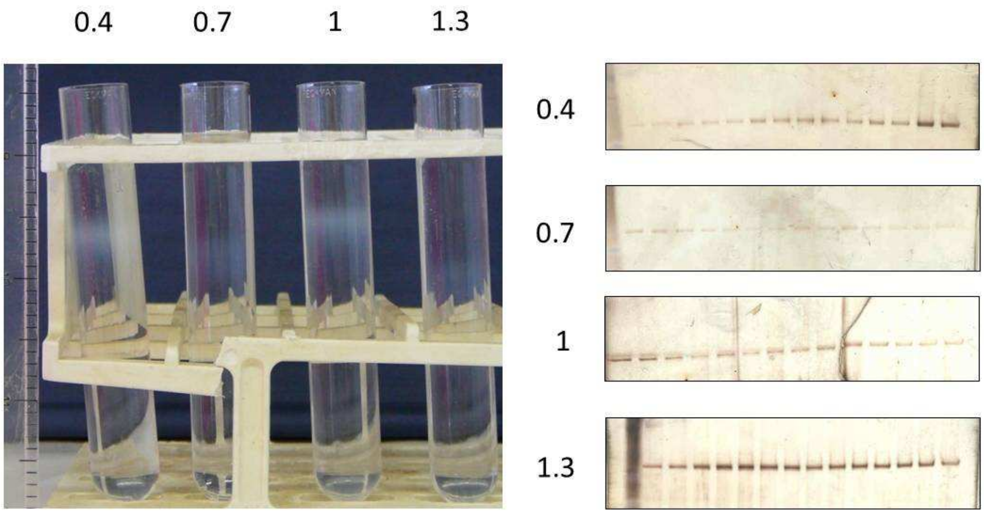

Figure 5.21: Isolation of heterogeneous-sized proteoliposomes using a sucrose gradient and SDS-PAGE. Sepration of proteoliposomes formed with DDM:lipid ratios = 0.4, 0.7, 1 and 1.3, and a receptor purified using buffers only supplemented by POPC, POPE and POPG. Migration in the sucrose gradient leads to diffused bands, and migrations on SDS-PAGE show that receptor is widely distributed across the sucrose gradients. This indicates that the samples tested here were made of proteoliposomes with heterogeneous sizes, and heterogeneous lipid:protein molar ratios. Consequently, they had different densities and migrated at different levels of the gradient, explaining the diffused band (the reconstitutions have been loaded on different gels, with slightly different conditions of staining, so no comparison can be made in terms of intensity).

5.3.3.c Ligand binding Assay

After isolating the proteoliposomes, the next step consists of measuring the amount of active reconstituted receptor. Different purifications of NTS1 have been performed, the products of which have then been reconstituted into liposomes. Activity assays have been performed at each of these steps. A wide range of irreproducible results were obtained, although the same protocol of reconstitution was followed each time. Two examples are shown on Table 5.2.

When comparing the amount of purified receptor added to the liposomes to the amount of active NTS1 after reconstitution, we can see that a loss of more than 80% of receptor seems to have occurred. During reconstitution a 50% loss of receptor is expected (in particular because of the half-life of the receptor in detergent, approximatively 50h), but that does not explain such a great loss of ligand-binding activity. Ligand-binding assays were performed on fractions pooled from a sucrose gradient and SDS-PAGE results, in which the presence of proteoliposomes is certain. Consequently, the lowest results (<5%) cannot be due to an absence of insertion in the liposomes. This does not necessarily mean that only a small amount of receptor have been reconstituted: indeed, the assay gives an idea of the amount of active receptor from the binding of the peptide-ligand. More receptor could be inserted into the membrane than detected, but in the wrong orientation, with the binding site facing the interior of the vesicle. In this case, the receptor would be unable to bind the neurotensin peptide, and thus, would not be detected during the assay.

A. Purification		B. Reconstitution (filter assay)			C. Resolubilisaton		D. Site occlusion
a.total amount (pmol)	b. added to reconstitution (pmol)	DDM:lipid ratio	pmol of active receptor	% yield	pmol of active receptor	% yield	% occluded
452.64	22.6	0.4	2.9	12.9	13.9	61.4	78.8
		0.8	1.7	7.7	5.3	23.2	66.8
		1	2.1	9.2	7.6	33.8	72.9
		2	2.6	11.3	16.9	74.6	84.8
		0.4	1.1	4.7			n/a
		0.8	1.1	5.01	n/a		
		1	1.7	7.7	2.3	10.4	26.2
		2	1.3	5.7	n/a	n/a	n/a
967.1226	73.9	0.4	8.8	11.9	37.03	50.1	76.2
		0.7	6.3	8.5	8.1	10.9	22.2
		1	6.5	8.7			n/a
		1.3	13.1	17.8	n/a		n/a

Table 5.2: Ligand binding assay performed on purified NTS1, reconstituted NTS1 and resolubilised proteoliposomes. This table shows the amounts of active NTS1 at each step of its study: just after purification (Aa); in the volume of receptor added to reconstitution (Ab); once reconstitution is done (B) (quantity of correctly inserted receptor); and after Resolubilisation (C). The percentage of yield compares the amount of receptor after reconstitution or resolubilisation with the amount of pure receptor initially added to reconstitution. The percentage of sites occluded (D) is obtained by comparing the amount of receptor before and after resolubilisation. The first purification has been performed with buffers supplemented with a mix of POPC, POPE and POPG, whereas only POPC was added during the second purification presented here.

To verify this suggestion, reconstituted receptor was resolubilised in DDM, CHAPS-CHS and 2X solubilisation buffer. This should give a measure of the total amount of inserted receptor, whether toward the inner or outer side of the liposome, provided the receptor is resolubilised with high efficiency. The first data (Table 5.2) seem to show that in every reconstitution experiment, higher amounts of receptor are detected after resolubilisation, confirming that significant proportion of receptor does not insert properly. These experiments were started later than the others, and not enough results are available yet to draw more quantitative conclusions.

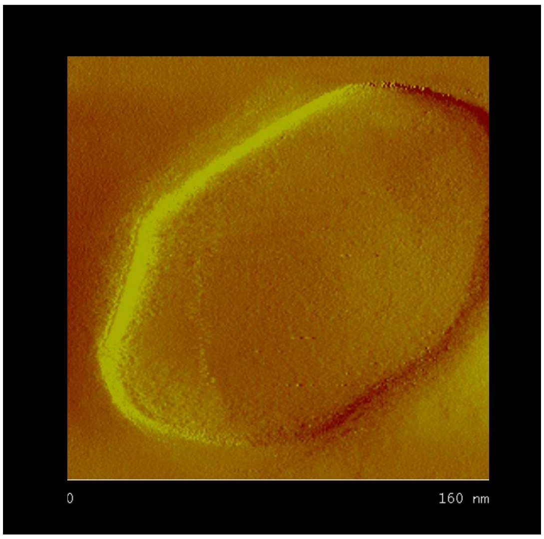

Figure 5.22. Close up AFM image of a NTS1-containing liposome on mica 48h following reconstitution; 160 nm scan size; Veeco instrument. This figure shows that the liposome still displays a 100nm size two days following reconstitution; the reconstitution process, thus, does not affect the final size or shape of the liposome obtained after extrusion.

Although preparation of specific-sized lipid vesicles can be easily performed, the subsequent insertion of membrane proteins during the reconstitution process requires numerous criteria to be considered, such as the final orientation of the protein or the homogeneity of the receptor insertion among all liposomes, and leads to the loss of an important amount of receptor. Regarding this protein loss over reconstitution, one could suggest that protein insertion might lead to leaking liposomes that might loose their closed, vesicular structure. Here, this hypothesis has been refuted by AFM imaging performed on NTS1-containing liposomes, two days following reconstitution (proteoliposomes were stored at -80°C between the end of the reconstitution and the imaging experiment). As shown on Figure 5.22, proteoliposomes purified from sucrose gradient do maintain their vesicular structure, and in particular, they retain their 100 nm diameter. Moreover, varying the ddm: lipid ratio did not have much effect on the reconstitution, unlike previously stated in the litterature. These experiments have shown the difficulty to produce unified proteoliposomes. One reason of these results may be the composition of BPL used for the formation of liposomes. Indeed, as shown on table 5.3, BPL contain three times more POPE than POPC. The structure of POPE is made of a small hydrophilic head with a big hydrophobic tail, leading to the formation of big vesicles. Preparing liposomes with a 50:50 mix of BPL-PC would lead to a lipid composition of the vesicles similar to the one of cell membrane (Table 5.3) and should improve the reconstitution.

Mammalian cell membrane	45-55% PC	15-25% PE
BPL	12% PC	33% PE
50:50 BPL – PC	56% PC	16% PE

Table 5.3: Composition in major lipids of mammalian cell membranes, BPL and a 50:50 mix of BPL and POPC. POPC and POPE are present with a 3:1 ratio in mammalian cell membrane and BPL, but in opposite proportions. Moreover, BPL used for reconstitution have thrice more PE, the structure of which leading to the formation of big vesicles, than PC. Preparing liposomes with a 50:50 mix of BPL-PC would lead to a lipid composition of the vesicles similar to the one of cell membrane and should improve the reconstitution.

Even though purification buffers were supplemented with a mix of lipids to help stability and give a better yield for the purification. However, it seems that the presence of these lipids interferes with the reconstitution. Indeed, the structure of POPE, and the negatively charged POPG seem to disrupt the liposomes when the receptor is added for reconstitution.

To verify this suggestion, an experiment was carried out on a receptor purified with buffers only supplemented by POPC, and the first results seem to show an improvement of the reconstitution (represented by a tight band on the sucrose gradient and few focused bands on the gel). However, insufficient number of data is available for the results to be reliable.

5.4 Conclusion

NTS1 has been successfully reconstituted in an active form into liposomes and is ready to be used for biophysical studies of its structure and functions. The TEM and AFM imaging of pre-formed liposomes, prior the protein insertion, showed that the lipid vesicles are in a range of sizes close to the 100nm that were expected after extrusion, and AFM imaging showed that the liposomes sizes remain in the same range following protein insertion. The purification of NTS1 and the synthesis of its full length ligand, neurotensin receptor, have also been successfully performed.

Future work will consist in producing proteoliposomes with a constant amount of inserted receptor, and in improving the reliability and reproducibility of the results. A first improvement could be done during the purification step. Indeed, major lipids found in mammalian biological membranes (POPC, POPE, and charged lipids such as POPS) have been supplemented in buffers during the receptor purification, so that NTS1 is purified and reconstituted in conditions as close as possible to a native environment. This method has revealed been successful concerning the stability of the protein during the process, improving the results of NTS1 purification. However, the structure of POPE and the charge of POPG seem to interfere with the insertion of receptor into lipid vesicles, leading to heterogeneous-sized proteoliposomes. A solution would be to supplement purification buffers with POPC only, since it presents no structural properties that could disrupt the reconstitution and does not decrease the yield of purification (Table 5.2). The first experiment carried out in this new condition gave an encouraging results. However it needs to be repeated to ensure its reliability.

Succeeding in getting a higher amount of reconstituted NTS1 would allow different biophysical studies to be performed, such as solid state NMR. Indeed, the lipid protein ratio of 400:1 determined after migration of proteoliposomes in sucrose gradient (Figure 5.20) is a good receptor density for ssNMR structural work. Moreover, efforts can be made to form 2D crystals for structural studies by decreasing the lipid: protein ration further. This would improve the knowledge about structural and functional properties of this receptor. This improvement could be extended to the study of other membrane proteins which have not been asymmetrically reconstituted and could be used as a basis for future activity measurements and structure-based drug design or screening.

Preliminary results obtained in the Watts group by solid state NMR suggest that the protein might be aggregating during experiments performed at room temperature. Therefore, probing the NTS1-NT interactions by AFM force spectroscopy may require to work on a thermostable receptor mutant (thermostable in the presence and absence of agonist NT peptide) such as that used by Grisshammer and co-workers[255]. Indeed, while AFM imaging can be performed after a few minutes-incubation time on mica, and provide images within a few hours by scanning the whole sample surface, interaction force measurements require much longer time for setting up the experiment and acquire reliable data at numerous individual locations of the surface in order to detect ligand-receptor interactions, thus increasing the risk of receptor precipitation or degradation.

Chapter VI – Conclusion and future work

The work presented in this thesis has investigated the use of scanning probe microscopy techniques, together with numerous biophysical and electrochemical methods, to study two seven transmembrane domain proteins - one with potential use in nanodevice, the other being a potential drug target - at the single molecule scale.

For the first time, photoswitching of the electrical conductance of a light-sensitive protein could be seen on isolated protein trimers, after partial removal of the membrane lipids. This work, based on the molecular electronic properties of light-driven archea proton pump bacteriorhodopsin, has also demonstrated that controlled molecule-electrode coupling could be obtained through the use of a strategically-engineered cysteine mutant - M163C - providing improved protein conductance in comparison to membrane-embedded conditions.

The neurotensin receptor type 1, NTS1, is the initial component of the neurotensin signalling pathway, and is involved in numerous physiological and pathological conditions. Here, the receptor was reconstituted into liposomes for future ligand-receptor interactions studies.

Bacteriorhodopsin

Evidence of partially-delipidated BR molecular conductance photoswitching upon illumination was obtained by current-voltage spectroscopy, using conducting-probe AFM. A distinct switch to a 3-fold higher conductance state was reproducibly observed upon illumination (>495 nm), for repeated dark-illumination cycles of gold-BR$_{cys}$ junctions over time, proving that partially delipidated BR$_{cys}$ trimers exhibit a controllable electronic behaviour. These results have been obtained using two different C-AFM systems (Agilent and JPK), thus further confirming the reliabilty of the observations. The prospect of a highly efficient, robust, photoswitchable molecular electronic system is appealing, particularly from a photonic device perspective. Characterization of the gold-BR$_{cys}$-gold junctions and further refinement of the conductance switching process have been performed using various biophysical and electrochemistry methods.

Operating under controlled load, C-AFM showed that at low probe-sample contact forces, 6-15nN, switching of conductance is present in the vast majority of individual junctions under illumination (λ>495 nm). On increasing the load, distorting the protein by applying excessive force annihilates the photoswitching. No variation of conductance was observed upon illumination with other wavelengths, nor in bleached (retinal-free) controls, confirming that photoswitching is a wavelength-specific phenomenon due to the retinal chromophore.

Although conductance photoswitching is reproducibly observed on one single protein-electrode junction over time, the amplitude of the shift tends to progressively decrease after an average of five illumination cycles, and reaches the point where no shift can be detected anymore. The exact reason for this phenomenon remains to be elucidated: moving the C-AFM probe to another molecular junction instantly reinstates photoswitching, the attenuation is thus not due to the sample illumination. Indeed, while one metal-molecule-metal junction is probed, the whole sample surface is illuminated. If light was the cause of the attenuation, the whole sample surface would be affected and photoswitching would not be observed when probing another junction. A potential explanation could be that of a current saturation of the protein under the probe. Another explanation could be that sample illumination of BR sandwiched within the mMm junction results in an accumulation of the O state ("shunt" intermediate of the photocycle). Studying the cause of the photoswitching attenuation constitutes one aspect of the future work related to this project.

Control experiments

Physical and electrochemical techniques were used in order to characterise the gold surface after protein adsorption, and to confirm or complement the C-AFM data. SPR showed that BR cysteine mutant, M163C, provides a ~ 3 time-stronger binding on the surface than wild-type BR. Reductive stripping voltammetry confirmed the role of the cysteine residue in the stronger adsorption of the mutant. STM, AFM and KFM imaging showed the delipidation efficiency by the absence of purple membrane patches on the surface, and that lipid-depleted BR_{cys} was homogeneously adsorbed all over the gold surface. Ellipsometry showed a sub-monolayer coverage of the surface and confirmed the sample thickness of 5 nm, corresponding to the height of BR molecules obtained from crystallographic data.

Photocurrent experiments were used to demonstrate the homogenous orientation of BR_{cys} on gold, and as a control of the molecular conductance photoswitching of BR_{cys}. BR trimers behaviour on illumination was also confirmed by KFM surface potential measurements. These KFM results are preliminary results, comparing the surface potential of WT BR in the membrane and that of partially delipidated BR_{cys} upon illumination at >495nm. Next experiments will consist in testing the wavelength specificity by using a different light filter, and confirming the role of retinal by using a bleached protein.

Study of the long-term stability of gold-BR$_{cys}$ trimers-gold junctions

The unique aim of the BR work presented here was to manage to detect a conductance photoswitching for delipidated BR similar to that reported for BR in the purple membrane[169]. Fresh samples were used for each experiment in order to work with the best possible samples. Further study will consist in studying the delipidated BR-based mMm junction stability and activity over time and in various environmental conditions. Storing delipidated BR$_{cys}$ solution and measuring the evolution of its conductance over time could be used as a control, but technological applications will require the sample to remain fixed on a circuit and to maintain its efficiency over long periods of time. Practically, this would consist in re-using a sample adsorbed on gold and monitor the evolution of its electrical properties. While such experiments can be easily performed for photocurrent measurements, the test is more challenging as far as scanning probe techniques are concerned. Indeed, great care must always be taken not to have any contamination of the gold substrate that could then be detected by the microscope probe and provide unreliable results. Re-using a gold substrate with adsorbed protein will greatly increase the risk of contamination, especially after multiple re-uses. Such control could be performed using SPM techniques, but would require strict environmental and sample handling conditions.

Effect of the gold-BR-gold junction on BR photocycle

Attenuation of BR conductance photoswitching observed after several illumination cycles might be due to current saturation of BR under the C-AFM probe, but it might also be due to the protein photocycle being affected by the combination of the solubilisation, gold binding and drying of the protein. As seen chapter III, numerous site-directed mutagenesis experiments have been performed in order to both understand and alter the protein characteristics. Several of these have a direct impact on BR photocycle, such as

D96N, which results in an extended lifetime of the M photocycle intermediate. Combining the M163C mutation used in this work, which provides controlled electrode adsorption and enhanced electronics responses, with D96N, might improve our knowledge of the effects of mMm junction construction on the photocycle of delipidated BR, and may lead to more readily detectable molecular conductance changes within BR trimers.

Scanning probe techniques and molecular junctions

Despite not forming molecular junctions that are practical from a nanodevice perspective, SPM techniques will continue to play a crucial role in bioelectronics research. Indeed, they are currently the only high-throughput methods for mMm junction formation. Moreover, given the flexibility of local environmental controls (temperature, force, ambient/fluidic atmosphere, potential control etc.) and range of possible imaging modes (topographic, current, surface potential, magnetic/ electric force, electrochemical), they remain a method of choice for the assessment of molecular conductance characteristics and electronic transport mechanisms.

Studying the conductance of BR monomers

Considering the encouraging results presented here for isolated trimers of BR, future work could consist in going further down the size of the molecular junction by adsorbing isolated BR monomers between the electrodes.

Total delipidation of BR has been successfully and routinely performed, monomer isolation would thus not be a limiting step in such a project. However, CP-AFM / *I-V* spectroscopy and KFM / surface potential measurements, which rely on placing an nm-wide conducting tip in contact with the sample in order to probe its electrical properties, would be hard to perform on such small and soft sample. Indeed, crystallographic data have assessed the dimension of one BR monomer to be 2.5 x 3.5 x 4.5 nm. The sharpest commercially available SPM probes present a radius of curvature of up to 5 nm, and these are not conducting. It would then be extremely challenging to detect the sample properties as the probe would likely also be in contact with the gold substrate, thus providing unreliable results.

One solution could be to try and perform STM measurements, as the tips used for this technique are often made manually, by the user: one could design an extremely sharp conducting element that would be part of the apex of the probe, allowing the detection of BR monomer electrical behaviour. Another experiment that could be tested, although there again the extremely small size of the sample may well reach the technical limits of the method, is the measurement of photocurrent, as this technique only requires the sample to be adsorbed between gold electrodes, with no local surface probing.

Another point to consider is that, although BR has been shown to be active as a monomer, its binding between electrodes may destabilise the protein.

Applications in bioelectronics

Numerous technological applications of BR have been presented in Chapter III, for membrane-embedded protein. Similar applications (optical memory, data storage, image detection, wavelength-sensitive photodetector…) could use BR trimers, resulting in a further decrease of the device size, provided that the protein in this condition retains its photoswitching properties over long period of time. Directed evolution could also be used in order to modulate wavelength sensitivity.

NTS1

The neurotensin receptor type 1 (NTS1) is of particular interest as NT signalling networks have been identified as a potential drug target with critical roles in medical conditions such as pain, eating behaviour, Schizophrenia, Parkinson's disease or colon cancer[256, 257 258]. The ultimate goal of this project is to investigate the NTS1-NT interactions at the single molecule scale.

NTS1 expressed in *E.coli* was purified and inserted into 100 nm brain polar lipid (BPL) liposomes in a conformation which retained its ligand-binding capabilities, as described in Chapter V. Although it has been shown that only the six C-terminal amino acids of NT (NT_{8-13}) are sufficient for ligand binding[259], the native full-length peptide was synthesised by SPPS for assessing the capability of the reconstituted receptor to bind its ligand. The receptor used for reconstitution into liposomes was the whole NTS1B fusion protein. Future experiments could reconstitute NTS1B after TEV cleavage, separated from the fusion tags, leading to NTS1 only being incorporated.

Another project will consist in inserting NTS1 into planar lipid bilayers and imaging the receptor before and after ligand binding, as a control experiment, before performing ligand-receptor interaction measurements that would be compared to the results obtained for NTS1 in liposomes.

Initial AFM imaging characterisation of liposomes was performed as a prelude for biophysical studies, including AFM high resolution imaging of the membrane receptor, solid state NMR approaches and AFM force spectroscopy in order to probe the ligand-receptor interactions. The information gained from these studies could then potentially lead to novel antagonist design, since only two known agonists are currently available and more will be required if NTS1 is to become a drug target.

Final remarks

Switchable molecular electronic species hold much promise in an array of technological applications and fundamental investigations. This thesis has shown, for the first time, that it is possible to probe the electronic properties of isolated trimers of BR in a manner that is akin to existing semiconductor devices.

Neurotensin is involved in numerous biological functions as well as in diverse pathologies: probing NT's interactions with its main receptor, NTS1, may therefore provide useful insight into treatments for major conditions such as Parkinson's disease, schizophrenia and obesity through drug design based on its characterisation.

Appendix 1: Culture Media and buffers used for bacteriorhodopsin

Peptone Media

To prepare one litre of media: 250 g NaCl, 10g oxoid bacteriological peptone, 20g $MgSO_4 \cdot 7H_20$), 3g Na_3Citrate, and 2g KCl was dissolved. Trace metals were added ($MnSO_4$ (0.3μg/l), $FeCl_2 \cdot 4H_2O$ (3.6 μg/l), $ZnSO_4 \cdot 7H_2O$ (0.44 μg/l), and $CuSO_4 \cdot 5H_2O$ (0.05 μg/l), and the pH was adjusted to 7.4

Agar Plates

Add 3.75 g agar to 250 mL peptone media and adjust pH to 7.4.

AFM imaging

- Adsorption buffer : 300 mM KCl, 10 mM Tris/HCl (pH 7.8)
- imaging buffer **:** 150 mM KCl, 10 mM Tris/HCl (pH 7.8)

Photocurrent measurements:

electrolyte solution of 100mM Na_2SO_4 in 10mM PBS, pH 7.1

Phosphate buffer

3:1 mixture of NaH_2PO_4 and Na_2HPO_4.

Phosphate buffer used for cleaning material before sample incubation, and for diluting BR depending on the experiment :
60mM PB, 150mM NaCl, pH 7.0

Appendix 2: Buffers used in NTS1 reconstitution

NTS1 purification

Detergent stocks : 10% DDM, 5% CHAPS/ 1%CHS, 10% DDM / 1% CHS

Protease inhibitors: Aprotinin (2µg/ml), Leupeptins (2µg/ml), Pepstatin A (1µg/ml).

Phospholipid stock (PPP): POPC:POPG:POPE, 3:1:1 in 1%DDM (5mg/ml).

2x solubilization buffer

100mM Tris/HCl, pH 7.4, 400mM NaCl, 60% glycerol.

NiA

50mM Tris-HCl, pH 7.4, 200mM NaCl, 30% glycerol, 0.5% CHAPS/0.1% CHS, 0.1% DDM, 50mM imidazole. 1/50 dilute PPP, 1/500 dilute leupeptin, 1/1000 dilute pepstatin A, and 1/5000 dilute aprotinin added just before use.

NiB

NiA plus 350mMimidazole.

GF200

50mM Tris-HCl, pH 7.5, 200mM NaCl, 15% glycerol, 1mM EDTA, 0.1% DDM / 0.1%CHS, 1/50 dilute PPP added just before use

NiA, NiB and GF200 were filtered and de-gassed prior to use.

Lipid preparation (“buffer A”)

50mM Tris-HCl, pH 7.4, 200mM NaCl, 1mM EDTA, filtered.

Sucrose Gradient (“buffer B”)

20mM Tris-HCl, pH 7.4, 200mM NaCl, 2mM EDTA (2x solution stock)

Ligand binding assay

- Assay on purified receptor and resolubilised proteoliposomes:

50mM Tris, pH 7.4, 0.5%CHAPS-0.1%CHS, 0.1% DDM, 1mM EDTA, 0.1 mg/ml BSA

- Assay on reconstituted proteoliposomes:

50mM Tris, pH 7.4, 1mM EDTA, 0.1 mg/ml BSA

Bibliography

1. Jain, M., *Introduction to biological membranes, Second Edition*. Wiley: 1988.

2. Singer, S. J.; Nicholson, G. L., The fluid mosaic model of the structure of cell membranes. *Science* **1972,** 175, (23), 720-31.

3. Jacobson, K.; Sheets, E. D.; Simson, R., Revisiting the fluid mosaic model of membranes. *Science* **1995,** 268, (5216), 1441-2.

4. everydayscience, http://2.bp.blogspot.com/_bAYLalavZ6w/TQIUBaPXroI/AAAAAAAAAEA/LOBlAOfYy4A/s1600/cell-membrane.gif

5. Nelson, D. L.; Cox, M. M., *Lehninger Principles of Biochemistry*. W.H. Freeman, New York: 2004; p 1100 pp.

6. Yeagle, P. L., *The Membrane of Cells*. Academic Press: 1993; p 349 pp.

7. Dube, D. H.; Bertozzi, C. R., Glycans in cancer and inflammation potential for therapeutics and diagnostics. *Nature Reviews Drug Discovery* **2005,** 4, (6), 477-88.

8. Henderson, R.; Baldwin, J. M.; Ceska, T. A.; Zemlin, F.; Beckmann, E.; Downing, K. H., Model for the Structure of Bacteriorhodopsin Based on High-Resolution Electron Cryomicroscopy. *Journal of Molecular Biology* **1990,** 213, (4), 899-929.

9. Wallin, E.; von Heijne, G., Genome-wide analysis of integral membrane proteins from eubacterial, archaean, and eukaryotic organisms. *Protein Science* **1998,** 7, (4), 1029-38.

10. Lundstrom, K., Structural genomics and drug discovery. *Journal of Cellular and Molecular Medecine* **2007,** 11, (2), 224-38.

11. Terstappen, G. C.; Reggiani, A., In silico research in drug discovery. *Trends in Pharmacological Sciences* **2001,** 22, (1), 23-26.

12. RCSB, Protein Data Bank (http://www.rcsb.org/pdb/home/home.do). **2011**.

13. Rajagopal, K.; Lefkowitz, R. J.; Rockman, H. A., When 7 transmembrane receptors are not G protein-coupled receptors. *Journal of Clinical Investigation* **2005,** 115, (11), 2971-4.

14. Rockman, H. A.; Koch, W. J.; Lefkowitz, R. J., Seven-transmembrane-spanning receptors and heart function. *Nature* **2002,** 415, (6868), 206-212.

15. Lowes, V. L.; Ip, N. Y.; Wong, Y. H., Integration of signals from receptor tyrosine kinases and g protein-coupled receptors. *Neurosignals* **2002,** 11, (1), 5-19.

16. Miller, K. J.; Murphy, B. J.; Pelleymounter, M. A., Central G-Protein Coupled Receptors (GPCR)s as molecular targets for the treatment of obesity: assets, liabilities and development status. *Current Drug Targets-CNS and Neurological Disorders* **2004,** 3, (5), 357-77.

17. Parker, S. L.; Parker, M. S.; Sah, R.; Sallee, F., Angiogenesis and rhodopsin-like receptors: a role for N-terminal acidic residues? *Biochemical and Biophyicals Research Communications* **2005,** 335, (4), 983-92.

18. Rayasam, G. V.; Tulasi, V. K.; Davis, J. A.; Bansal, V. S., Fatty acid receptors as new therapeutic targets for diabetes. *Expert Opinion on Therapeutic Targets* **2007,** 11, (5), 661-71.

19. Blakeney, J. S.; Fairlie, D. P., Nonpeptide ligands that target peptide-activated GPCRs in inflammation. *Current Medicinal Chemistry* **2005,** 12, (25), 3027-42.

20. Kroeze, W. K.; Sheffler, D. J.; Roth, B. L., G-protein-coupled receptors at a glance. *Journal of Cell Science* **2003,** 116, (Pt 24), 4867-9.

21. Hall, R. A.; Premont, R. T.; Lefkowitz, R. J., Heptahelical receptor signaling: beyond the G protein paradigm. *Journal of Cell Biology* **1999,** 145, (5), 927-32.

22. Bockaert, J.; Pin, J. P., Molecular tinkering of G protein-coupled receptors: an evolutionary success. *Embo Journal* **1999,** 18, (7), 1723-1729.

23. Schulz, M., The end of the road for silicon? *Nature* **1999,** 399, 729.

24. Birge R., R., *Molecular and Biomolecular Electronics*. American Chemical Society: Washington, D.C, 1994; p 595.

25. Sienko, T.; Birge, R. R.; Conrad, M.; Rambidi, N. G.; Adamatzky, A., *Molecular computing*. The MIT Press: 2003; p xvii, 257.

26. Martin, A. S.; Sambles, J. R.; Ashwell, G. J., Molecular rectifier. *Physical Review Letters* **1993,** 70, (2), 218-221.

27. Birge, R. R.; Gillespie, N. B.; Izaguirre, E. W.; Kusnetzow, A.; Lawrence, A. F.; Singh, D.; Song, Q. W.; Schmidt, E.; Stuart, J. A.; Seetharaman, S.; Wise, K. J., Biomolecular electronics: Protein-based associative processors

and volumetric memories. *Journal of Physical Chemistry B* **1999,** 103, (49), 10746-10766.

28. Moore, R.; Vodopich, D., *Botany*. William C. Brown publishing: 1995.

29. Davis, J. J.; Wrathmell, C. L.; Zhao, J.; Fletcher, J., The tunnelling conductance of molecularly ordered metalloprotein arrays. *Journal of Molecular Recognition* **2004,** 17, (3), 167-73.

30. Bernasek, S. L.; Lavrich, D. J.; Wetterer, S. M.; Scoles, G., Physisorption and chemisorption of alkanethiols and alkyl sulfides on Au(111). *Journal of Physical Chemistry B* **1998,** 102, (18), 3456-3465.

31. Davis, J. J.; Bruce, D.; Canters, G. W.; Crozier, J.; Hill, H. A. O., Genetic modulation of metalloprotein electron transfer at bare gold. *Chemical Communications* **2003**, (5), 576-577.

32. Nuzzo, R. G.; Allara, D. L., Adsorption of bifunctional organic disulfides on gold surfaces. *Journal of the American Chemical Society* **1983,** 105, (13), 4481-83.

33. Song, S.; Clark, R. A.; Bowden, E. F.; Tarlov, M. J., Characterization of Cytochrome-C Alkanethiolate Structures Prepared by Self-Assembly on Gold. *Journal of Physical Chemistry* **1993,** 97, (24), 6564-6572.

34. Ulman, A., *An Introduction to Ultrathin Organic Films: from Langmuir-Blodgett to Self-Assembly*. Academic Press, Boston: 1991.

35. Ulman, A., Formation and structure of self-assembled monolayers. *Chemical Reviews* **1996,** 96, (4), 1533-1554.

36. Elghanian, R.; Storhoff, J. J.; Mucic, R. C.; Letsinger, R. L.; Mirkin, C. A., Selective colorimetric detection of polynucleotides based on the distance-dependent optical properties of gold nanoparticles. *Science* **1997,** 277, (5329), 1078-1081.

37. Katz, H. E.; Wilson, W. L.; Scheller, G., Chromophore Structure, 2nd-Harmonic Generation, and Orientational Order in Zirconium Phosphonate/Phosphate Self-Assembled Multilayers. *Journal of the American Chemical Society* **1994,** 116, (15), 6636-6640.

38. Berggren, K. K.; Bard, A.; Wilbur, J. L.; Gillaspy, J. D.; Helg, A. G.; Mcclelland, J. J.; Rolston, S. L.; Phillips, W. D.; Prentiss, M.; Whitesides, G. M., Microlithography by Using Neutral Metastable Atoms and Self-Assembled Monolayers. *Science* **1995,** 269, (5228), 1255-1257.

39. Porter, M. D.; Bright, T. B.; Allara, D. L.; Chidsey, C. E. D., Spontaneously Organized Molecular Assemblies .4. Structural Characterization of Normal-Alkyl Thiol Monolayers on Gold by Optical

Ellipsometry, Infrared-Spectroscopy, and Electrochemistry. *Journal of the American Chemical Society* **1987,** 109, (12), 3559-3568.

40. Bain, C. D.; Troughton, E. B.; Tao, Y. T.; Evall, J.; Whitesides, G. M.; Nuzzo, R. G., Formation of Monolayer Films by the Spontaneous Assembly of Organic Thiols from Solution onto Gold. *Journal of the American Chemical Society* **1989,** 111, (1), 321-335.

41. Troughton, E. B.; Bain, C. D.; Whitesides, G. M.; Nuzzo, R. G.; Allara, D. L.; Porter, M. D., Monolayer Films Prepared by the Spontaneous Self-Assembly of Symmetrical and Unsymmetrical Dialkyl Sulfides from Solution onto Gold Substrates - Structure, Properties, and Reactivity of Constituent Functional-Groups. *Langmuir* **1988,** 4, (2), 365-385.

42. Camillone, N.; Chidsey, C. E. D.; Liu, G. Y.; Putvinski, T. M.; Scoles, G., Surface-Structure and Thermal Motion of Normal-Alkane Thiols Self-Assembled on Au(111) Studied by Low-Energy Helium Diffraction. *Journal of Chemical Physics* **1991,** 94, (12), 8493-8502.

43. Biebuyck, H. A.; Whitesides, G. M., Interchange between Monolayers on Gold Formed from Unsymmetrical Disulfides and Solutions of Thiols - Evidence for Sulfur Sulfur Bond-Cleavage by Gold Metal. *Langmuir* **1993,** 9, (7), 1766-1770.

44. Rodriguez, J. A.; Liu, G.; Dvorak, J.; Hrbek, J.; Jirsak, T., Chemistry of sulfur-containing molecules on Au(111): thiophene, sulfur dioxide, and methanethiol adsorption. *Surface Science* **2002,** 505, (1-3), 295-307.

45. Park, J.; Pasupathy, A. N.; Goldsmith, J. I.; Chang, C.; Yaish, Y.; Petta, J. R.; Rinkoski, M.; Sethna, J. P.; Abruna, H. D.; McEuen, P. L.; Ralph, D. C., Coulomb blockade and the Kondo effect in single-atom transistors. *Nature* **2002,** 417, (6890), 722-725.

46. Simmons, J. G., Generalized Formula for Electric Tunnel Effect between Similar Electrodes Separated by a Thin Insulating Film. *Journal of Applied Physics* **1963,** 34, (6), 1793-1803.

47. Simmons, J. G., Conduction in Thin Dielectric Films. *Journal of Physics D-Applied Physics* **1971,** 4, (5), 613-657.

48. Hill, H. A. O.; Davis, J. J.; Bond, A. M., The application of electrochemical scanning probe microscopy to the interpretation of metalloprotein voltammetry. *Coordination Chemistry Reviews* **2000,** 200, 411-442.

49. Hill, A., Scanning probe microscopy and the electrochemistry of metalloproteins and metalloenzymes: Seeing is believing? *Journal of Inorganic Biochemistry* **2003,** 96, (1), 7-7.

50. Zhao, J.; Davis, J. J.; Sansom, M. S.; Hung, A., Exploring the electronic and mechanical properties of protein using conducting atomic force microscopy. *Journal of the American Chemical Society* **2004,** 126, (17), 5601-9.

51. Muller, D. J.; Engel, A.; Amrein, M., Preparation techniques for the observation of native biological systems with the atomic force microscope. *biosensors and bioelectronics* **1997**.

52. Muller, D. J.; Sapra, K. T.; Scheuring, S.; Kedrov, A.; Frederix, P. L.; Fotiadis, D.; Engel, A., Single-molecule studies of membrane proteins. *Current Opinion in Structural Biology* **2006,** 16, (4), 489-95.

53. Engel, A.; Gaub, H. E., Structure and mechanics of membrane proteins *Annual Reviews of Biochemistry* **2008,** 77, 127-48.

54. Engel, A.; Muller, D. J.; Fotiadis, D., Mapping flexible protein domains at subnanometer resolution with the atomic force microscope. *Febs Letters* **1998,** 430, (1-2), 105-111.

55. Contera, S. A.; Lemaitre, V.; de Planque, M. R. R.; Watts, A.; Ryan, J. F., Unfolding and extraction of a transmembrane alpha-helical peptide: Dynamic force spectroscopy and molecular dynamics simulations. *Biophysical Journal* **2005,** 89, (5), 3129-3140.

56. Milhiet, P. E.; Yamamoto, D.; Berthoumieu, O.; Dosset, P.; Le Grimellec, C.; Verdier, J. M.; Marchal, S.; Ando, T., Deciphering the Structure, Growth and Assembly of Amyloid-Like Fibrils Using High-Speed Atomic Force Microscopy. *Plos One* **2010,** 5, (10).

57. Brasseur, R.; Deuleu, M.; Mingeot Leclercq, M. P.; Francius, G.; Dufrene, Y. F., Probing peptide–membrane interactions using AFM. *Surface and Interface Analysis* **2008,** 40, 151-156.

58. Taranta, M.; Bizzarri, A. R.; Cannistraro, S., Probing the interaction between p53 and the bacterial protein azurin by single molecule force spectroscopy. *Journal of Molecular Recognition* **2008,** 21, (1), 63-70.

59. Drew, M. E.; Chworos, A.; Oroudjev, E.; Hansma, H.; Yamakoshi, Y., A Tripod Molecular Tip for Single Molecule Ligand-Receptor Force Spectroscopy by AFM. *Langmuir* **2010,** 26, (10), 7117-7125.

60. Pellequer, J. L.; Odorico, M.; Teulon, J. M.; Berthoumieu, O.; Chen, S. W. W.; Parot, P., An integrated methodology for data processing in dynamic force spectroscopy of ligand-receptor binding. *Ultramicroscopy* **2007,** 107, (10-11), 887-894.

61. Taninaka, A.; Takeuchi, O.; Shigekawa, H., Hidden variety of biotin-streptavidin/avidin local interactions revealed by site-selective dynamic

force spectroscopy. *Physical Chemistry Chemical Physics* **2010,** 12, (39), 12578-83.

62. Allison, D. P.; Mortensen, N. P.; Sullivan, C. J.; Doktycz, M. J., Atomic force microscopy of biological samples. *Wiley Interdisciplinary Reviews-Nanomedicine and Nanobiotechnology* **2010,** 2, (6), 618-634.

63. Binnig, G.; Quate, C. F.; Gerber, C., Atomic force microscope. *Physical Review Letters* **1986,** 56, (9), 930-933.

64. Ros, R.; Fuhrmann, A.; Staunton, J. R.; Nandakumar, V.; Banyai, N.; Davies, P. C. W., AFM stiffness nanotomography of normal, metaplastic and dysplastic human esophageal cells. *Physical Biology* **2011,** 8, (1).

65. Brucker, *technical note: http://www.bruker-axs.com/uploads/tx_linkselectorforpdfpool/BioScope_Catalyst_Atomic_Force_Microscope_brochure.pdf.*

66. Suzuki, Y.; Yoshikawa, Y.; Yoshimura, S. H.; Yoshikawa, K.; Takeyasu, K., Unraveling DNA dynamics using atomic force microscopy. *Wiley Interdisciplinary Reviews-Nanomedicine and Nanobiotechnology* **2011,** 3, (6), 574-588.

67. Scheuring, S. Atomic force and electron microscopic analysis of membrane chanels and transporters. Basel, 2000.

68. Giocondi, M. C.; Milhiet, P. E.; Lesniewska, E.; Le Grimellec, C., From cell imaging to molecular manipulation: biological applications of atomic force microscopy *M S-Medecine Sciences* **2003,** 19, (1), 92-99.

69. Ron, A.; Singh, R. R.; Fishelson, N.; Socher, R.; Benayahu, D.; Shacharn-Diamand, Y., Site localization of membrane-bound proteins on whole cell level using atomic force microscopy. *Biophysical Chemistry* **2008,** 132, (2-3), 127-138.

70. Muller, D. J.; Engel, A., Atomic force microscopy and spectroscopy of native membrane proteins. *Nature Protocols* **2007,** 2, (9), 2191-7.

71. Milhiet, P. E.; Gubellini, F.; Berquand, A.; Dosset, P.; Rigaud, J. L.; Le Grimellec, C.; Levy, D., High-resolution AFM of membrane proteins directly incorporated at high density in planar lipid bilayer. *Biophysical Journal* **2006,** 91, (9), 3268-3275.

72. Scheuring, S.; Seguin, J.; Marco, S.; Levy, D.; Breyton, C.; Robert, B.; Rigaud, J. L., AFM characterization of tilt and intrinsic flexibility of Rhodobacter sphaeroides light harvesting complex 2 (LH2). *Journal of Molecular Biology* **2003,** 325, (3), 569-80.

73. Kasai, N.; Ramanujan, C. S.; Fujimoto, I.; Shimada, A.; Ryan, J. F.; Torimitsu, K., AFM observation of single, functioning ionotropic glutamate receptors reconstituted in lipid bilayers. *Biochimica et Biophysica Acta* **2010,** 1800, (7), 655-61.

74. Hughes, T.; Strongin, B.; Gao, F. P.; Vijayvergiya, V.; Busath, D. D.; Davis, R. C., AFM visualization of mobile influenza A M2 molecules in planar bilayers. *Biophysical Journal* **2004,** 87, (1), 311-322.

75. Wang, H.; Bash, R.; Lohr, D., Two-component atomic force microscopy recognition imaging of complex samples. *Analytical Biochemistry* **2007,** 361, (2), 273-9.

76. Thormann, E.; Simonsen, A. C.; Nielsen, L. K.; Mouritsen, O. G., Ligand-receptor interactions and membrane structure investigated by AFM and time-resolved fluorescence microscopy - drug-ligand interaction. *Journal of Molecular Recognition* **2007,** 20, (6), 554-60.

77. Martin, Y.; Williams, C. C.; Wickramasinghe, H. K., Atomic Force Microscope Force Mapping and Profiling on a Sub 100-Å Scale. *Journal of Applied Physics* **1987,** 61, (10), 4723-4729.

78. Dai, H. J.; Hafner, J. H.; Rinzler, A. G.; Colbert, D. T.; Smalley, R. E., Nanotubes as nanoprobes in scanning probe microscopy. *Nature* **1996,** 384, (6605), 147-150.

79. Bunch, J. S.; Rhodin, T. N.; McEuen, P. L., Noncontact-AFM imaging of molecular surfaces using single-wall carbon nanotube technology. *Nanotechnology* **2004,** 15, (2), S76-S78.

80. Borgia, A.; Williams, P. M.; Clarke, J., Single-molecule studies of protein folding. *Annual Review of Biochemistry* **2008,** 77, 101-125.

81. Clarke, J.; Forman, J. R., Mechanical unfolding of proteins: insights into biology, structure and folding. *Current Opinion in Structural Biology* **2007,** 17, (1), 58-66.

82. Ng, S. P.; Rounsevell, R.; Randles, L. G.; Steward, A.; Clarke, J., Single molecule studies of protein folding by atomic force microscopy(AFM). *Biophysical Journal* **2005,** 88, (1), 184a-184a.

83. Voyer, N.; Barattin, R., Chemical modifications of AFM tips for the study of molecular recognition events. *Chemical Communications* **2008**, (13), 1513-1532.

84. Kedrov, A.; Janovjak, H.; Sapra, K. T.; Muller, D. J., Deciphering molecular interactions of native membrane proteins by single-molecule force spectroscopy. *Annual Review of Biophysics and Biomolecular Structure* **2007,** 36, 233-260.

85. Muller, D. J.; Buldt, G.; Engel, A., Force-induced conformational change of bacteriorhodopsin. *Journal of Molecular Biology* **1995,** 249, (2), 239-43.

86. Muller, D. J.; Engel, A., Conformational changes, flexibilities and intramolecular forces observed on individual proteins using AFM *RIKEN Review No. 36 (June, 2001): Focused on Science and Technology in Micro/Nano Scale* **2001,** 36.

87. Engel, A.; Muller, D. J., Observing single biomolecules at work with the atomic force microscope. *Nature Structural Biology* **2000,** 7, (9), 715-718.

88. Li, Z.; Liu, Z. G.; Zhou, H. L.; Wei, G.; Song, Y. H.; Wang, L., Observation of the mica surface by atomic force microscopy. *Micron* **2005,** 36, (6), 525-531.

89. Berthoumieu, O. Antobody-antigen interactions measurements by dynamic force spectroscopy. Master's Degree Thesis.2006.

90. Veeco, A practical guide to scanning probe microscopy (user's manual).

91. Stemmer, A.; Jacobs, H. O.; Leuchtmann, P.; Homan, O. J., Resolution and contrast in Kelvin probe force microscopy. *Journal of Applied Physics* **1998,** 84, (3), 1168-1173.

92. Palermo, V.; Liscio, A.; Samori, P., Nanoscale Quantitative Measurement of the Potential of Charged Nanostructures by Electrostatic and Kelvin Probe Force Microscopy: Unraveling Electronic Processes in Complex Materials. *Accounts of Chemical Research* **2010,** 43, (4), 541-550.

93. Henning, A. K.; Hochwitz, T.; Slinkman, J.; Never, J.; Hoffmann, S.; Kaszuba, P.; Daghlian, C., 2-Dimensional Surface Dopant Profiling in Silicon Using Scanning Kelvin Probe Microscopy. *Journal of Applied Physics* **1995,** 77, (5), 1888-1896.

94. Meoded, T.; Shikler, R.; Fried, N.; Rosenwaks, Y., Direct measurement of minority carriers diffusion length using Kelvin probe force microscopy *Applied Physics Letters* **1999,** 75, (16), 2435-2437.

95. Burgi, L.; Sirringhaus, H.; Friend, R. H., Noncontact potentiometry of polymer field-effect transistors. *Applied Physics Letters* **2002,** 80, (16), 2913-2915.

96. Frisbie, C. D.; Puntambekar, K. P.; Pesavento, P. V., Surface potential profiling and contact resistance measurements on operating pentacene thin-film transistors by Kelvin probe force microscopy. *Applied Physics Letters* **2003,** 83, (26), 5539-5541.

97. Gil, A.; de Pablo, P. J.; Colchero, J.; Gomez-Herrero, J.; Baro, A. M., Electrostatic scanning force microscopy images of long molecules: single-walled carbon nanotubes and DNA *Nanotechnology* **2002,** 13, (3), 309-313.

98. Kwak, K. J.; Yoda, S.; Fujihira, M., Observation of stretched single DNA molecules by Kelvin probe force microscopy. *Applied Surface Science* **2003,** 210, (1-2), 73-78.

99. Leung, C.; Kinns, H.; Hoogenboom, B. W.; Howorka, S.; Mesquida, P., Imaging Surface Charges of Individual Biomolecules. *Nano Letters* **2009,** 9, (7), 2769-2773.

100. Nonnenmacher, M.; Oboyle, M. P.; Wickramasinghe, H. K., Kelvin Probe Force Microscopy. *Applied Physics Letters* **1991,** 58, (25), 2921-2923.

101. Meoded, T.; Shikler, R.; Fried, N.; Rosenwaks, Y., Direct measurement of minority carriers diffusion length using Kelvin probe force microscopy. *Applied Physics Letters* **1999,** 75, (16), 2435-2437.

102. Vincenzo, P.; Matteo, P.; Zcaron; eljko, T.; cacute; Mark, D. W.; Rainer, F.; Klaus, M.; Paolo, S., Influence of Molecular Order on the Local Work Function of Nanographene Architectures: A Kelvin-Probe Force Microscopy Study. *ChemPhysChem* **2005,** 6, (11), 2371-2375.

103. Sinensky, A. K.; Belcher, A. M., Label-free and high-resolution protein/DNA nanoarray analysis using Kelvin probe force microscopy. *Nature Nanotechnology* **2007,** 2, (10), 653-659.

104. Chiesa, M.; BÃ¼rgi, L.; Kim, J.-S.; Shikler, R.; Friend, R. H.; Sirringhaus, H., Correlation between Surface Photovoltage and Blend Morphology in Polyfluorene-Based Photodiodes. *Nano Letters* **2005,** 5, (4), 559-563.

105. Palermo, V.; Ridolfi, G.; Talarico, A. M.; Favaretto, L.; Barbarella, G.; Camaioni, N.; Samorì, P., A Kelvin Probe Force Microscopy Study of the Photogeneration of Surface Charges in All-Thiophene Photovoltaic Blends. *Advanced Functional Materials* **2007,** 17, (3), 472-478.

106. Kanan, P. P.; Paul, V. P.; Frisbie, C. D., Surface potential profiling and contact resistance measurements on operating pentacene thin-film transistors by Kelvin probe force microscopy. *Applied Physics Letters* **2003,** 83, (26), 5539-5541.

107. Salomon, A.; Cahen, D.; Lindsay, S.; Tomfohr, J.; Engelkes, V. B.; Frisbie, C. D., Comparison of electronic transport measurements on organic molecules. *Advanced Materials* **2003,** 15, (22), 1881-1890.

108. Davis, J. J.; Peters, B.; Xi, W.; Axford, D., Molecularly-resolved bioelectronics. *Current Nanoscience* **2008,** 4, (1), 62-70.

109. Facci, P.; Alessandrini, A.; Salerno, M.; Frabboni, S., Single-metalloprotein wet biotransistor. *Applied Physics Letters* **2005,** 86, (13).

110. Debe, M. K., Optical Probes of Organic Thin-Films - Photons-in and Photons-Out. *Progress in Surface Science* **1987,** 24, (1-4), 1-282.

111. Chang, M. J.; Pang, C. R.; Liu, J.; Bai, H.; Deng, J.; Xu, Z. G.; Zhang, H. L., High spatial resolution label-free detection of antigen-antibody binding on patterned surface by imaging ellipsometry. *Journal of Colloid and Interface Science* **2011,** 360, (2), 826-833.

112. Madeira, A.; Ohman, E.; Nilsson, A.; Sjogren, B.; Andren, P. E.; Svenningsson, P., Coupling surface plasmon resonance to mass spectrometry to discover novel protein-protein interactions. *Nature Protocols* **2009,** 4, (7), 1023-37.

113. Homola, J.; Yee, S. S.; Gauglitz, G., Surface plasmon resonance sensors: review. *Sensors and Actuators B-Chemical* **1999,** 54, (1-2), 3-15.

114. Su, X. D.; Wu, Y. J.; Knoll, W., Comparison of surface plasmon resonance spectroscopy and quartz crystal microbalance techniques for studying DNA assembly and hybridization. *Biosensors & Bioelectronics* **2005,** 21, (5), 719-726.

115. Bard, A. J.; Faulkner, L. R., *Electrochemical methods: fundamentals and applications*. Wiley: 2001.

116. Forster, R. J., Microelectrodes - New Dimensions in Electrochemistry. *Chemical Society Reviews* **1994,** 23, (4), 289-297.

117. Forster, R. J.; Campagnoli, E.; Hjelm, J.; Milios, C. J.; Sjodin, M.; Pikramenou, Z., Adsorption dynamics and interfacial properties of thiol-based cobalt terpyridine monolayers. *Electrochimica Acta* **2007,** 52, (24), 6692-6699.

118. Levy, R.; Maaloum, M., Measuring the spring constant of atomic force microscope cantilevers: thermal fluctuations and other methods. *Nanotechnology* **2002,** 13, (1), 33-37.

119. Oesterhelt, D.; Stoeckenius, W., Rhodopsin-like protein from the purple membrane of Halobacterium halobium. *Nature - New Biology* **1971,** 233, (39), 149-52.

120. Oesterhelt, D.; Stoeckenius, W., Isolation of the cell membrane of Halobacterium halobium and its fractionation into red and purple membrane. *Methods in Enzymology* **1974,** 31, (Pt A), 667-78.

121. Hampp, N., Bacteriorhodopsin as a photochromic retinal protein for optical memories. *Chemical Reviews* **2000,** 100, (5), 1755-1776.

122. Khorana, H. G.; Gerber, G. E.; Herlihy, W. C.; Gray, C. P.; Anderegg, R. J.; Nihei, K.; Biemann, K., Amino acid sequence of bacteriorhodopsin. *Proceedings of the National Academy of Sciences of the United States of America-Biological Sciences* **1979,** 76, (10), 5046-50.

123. Lanyi, J. K., Bacteriorhodopsin. *Annual Review of Physiology* **2004,** 66, 665-688.

124. Mowery, P. C.; Stoeckenius, W., Photoisomerization of the Chromophore in Bacteriorhodopsin during the Proton Pumping Photocycle. *Biochemistry* **1981,** 20, (8), 2302-2306.

125. Khorana, H. G., Bacteriorhodopsin, a Membrane-Protein That Uses Light to Translocate Protons. *Journal of Biological Chemistry* **1988,** 263, (16), 7439-7442.

126. Belrhali, H.; Nollert, P.; Royant, A.; Menzel, C.; Rosenbusch, J. P.; Landau, E. M.; Pebay-Peyroula, E., Protein, lipid and water organization in bacteriorhodopsin crystals: a molecular view of the purple membrane at 1.9 angstrom resolution. *Structure* **1999,** 7, (8), 909-917.

127. Luecke, H.; Schobert, B.; Richter, H. T.; Cartailler, J. P.; Lanyi, J. K., Structure of bacteriorhodopsin at 1.55 angstrom resolution *Journal of Molecular Biology* **1999,** 291, (4), 899-911.

128. King, G. I.; Mowery, P. C.; Stoeckenius, W.; Crespi, H. L.; Schoenborn, B. P., Location of the Chromophore in Bacteriorhodopsin *Proceedings of the National Academy of Sciences of the United States of America-Biological Sciences* **1980,** 77, (8), 4726-4730.

129. Palczewski, K.; Kumasaka, T.; Hori, T.; Behnke, C., A.; Motoshima, H.; Fox, B., A.; Le Trong, I.; Teller, D. C.; Okada, T.; Stenkamp, R.; Yamamoto, M.; Miyano, M., Crystal Structure of Rhodopsin: A G Protein-Coupled Receptor. *Science* **2000,** 289, 739.

130. Essen, L. O.; Mailliet, J.; Hughes, J., The structure of a complete phytochrome sensory module in the Pr ground state. *Proc Natl Acad Sci U S A* **2008,** 105, (38), 14709-14.

131. Essen, L. O.; Siegert, R.; Lehmann, W. D.; Oesterhelt, D., Lipid patches in membrane protein oligomers: Crystal structure of the bacteriorhodopsin-lipid complex. *Proceedings of the National Academy of Sciences of the United States of America* **1998,** 95, (20), 11673-11678.

132. Henderson, R.; Schertler, G. F. X., The Structure of Bacteriorhodopsin and Its Relevance to the Visual Opsins and Other Seven-Helix G-Protein Coupled Receptors *Philosophical Transactions of the Royal Society of London Series B-Biological Sciences* **1990,** 326, (1236), 379-389.

133. Brouillette, C. G.; Mcmichens, R. B.; Stern, L. J.; Khorana, H. G., Structure and Thermal-Stability of Monomeric Bacteriorhodopsin in Mixed Phospholipid Detergent Micelles. *Proteins-Structure Function and Genetics* **1989,** 5, (1), 38-46.

134. Hayward, S. B.; Grano, D. A.; Glaeser, R. M.; Fisher, K. A., Molecular orientation of bacteriorhodopsin within the purple membrane of Halobacterium halobium. *Proceedings of the National Academy of Sciences of the United States of America* **1978,** 75, (9), 4320-4.

135. Henderson, R.; Unwin, P. N., Three-dimensional model of purple membrane obtained by electron microscopy. *Nature* **1975,** 257, (5521), 28-32.

136. Kimura, Y.; Vassylyev, D. G.; Miyazawa, A.; Kidera, A.; Matsushima, M.; Mitsuoka, K.; Murata, K.; Hirai, T.; Fujiyoshi, Y., High resolution structure of bacteriorhodopsin determined by electron crystallography. *Photochemistry and Photobiology* **1997,** 66, (6), 764-767.

137. Watts, A., Bacteriorhodopsin - the Mechanism of 2d-Array Formation and the Structure of Retinal in the Protein. *Biophysical Chemistry* **1995,** 55, (1-2), 137-151.

138. Schreckenbach, T.; Walckhoff, B.; Oesterhelt, D., Specificity of the retinal binding site of bacteriorhodopsin: chemical and stereochemical requirements for the binding of retinol and retinal. *Biochemistry* **1978,** 17, (25), 5353-9.

139. Mowery, P. C.; Lozier, R. H.; Chae, Q.; Tseng, Y. W.; Taylor, M.; Stoeckenius, W., Effect of Acid pH on the Absorption Spectra and Photoreactions of Bacteriorhodopsin. *Biochemistry* **1979,** 18, (19), 4100-4107.

140. Lee, I.; Greenbaum, E.; Budy, S.; Hillebrecht, J. R.; Birge, R. R.; Stuart, J. A., Photoinduced surface potential change of bacteriorhodopsin mutant D96N measured by scanning surface potential microscopy. *Journal of Physical Chemistry B* **2006,** 110, (22), 10982-90.

141. Chu, L. K.; El-Sayed. M., Bacteriorhodopsin O-state Photocycle Kinetics: A Surfactant Study. *Photochemistry and Photobiology* **2010,** 86, (70-76).

142. Subramaniam, S.; Lindahl, I.; Bullough, P.; Faruqi, A. R.; Tittor, J.; Oesterhelt, D.; Brown, L.; Lanyi, J.; Henderson, R., Protein conformational changes in the bacteriorhodopsin photocycle. *Journal of Molecular Biology* **1999,** 287, (1), 145-161.

143. Brown, L. S.; Varo, G.; Needleman, R.; Lanyi, J. K., Functional significance of a protein conformation change at the cytoplasmic end of

helix F during the bacteriorhodopsin photocycle. *Biophysical Journal* **1995,** 69, (5), 2103-2111.

144. Heymann, J. B.; Pfeiffer, M.; Hildebrandt, V.; Kaback, H. R.; Fotiadis, D.; de Groot, B.; Engel, A.; Oesterhelt, D.; Muller, D. J., Conformations of the rhodopsin third cytoplasmic loop grafted onto bacteriorhodopsin. *Structure* **2000,** 8, (6), 643-653.

145. Brown, L. S.; Needleman, R.; Lanyi, J. K., Conformational change of the E-F interhelical loop in the M photointermediate of bacteriorhodopsin. *Journal of Molecular Biology* **2002,** 317, (3), 471-8.

146. Shibata, M.; Uchihashi, T.; Yamashita, H.; Kandori, H.; Ando, T., Structural changes in bacteriorhodopsin in response to alternate illumination observed by high-speed atomic force microscopy. *Angewandte Chemie International Edition* **2011,** 50, (19), 4410-3.

147. Voitchovsky, K.; Antoranz Contera, S.; Kamihira, M.; Watts, A.; Ryan, J. F., Differential stiffness and lipid mobility in the leaflets of purple membranes. *Biophysical Journal* **2006,** 90, (6), 2075-85.

148. Thorgeirsson, T. E.; Xiao, W.; Brown, L. S.; Needleman, R.; Lanyi, J. K.; Shin, Y. K., Transient channel-opening in bacteriorhodopsin: an EPR study. *Journal of Molecular Biology* **1997,** 273, (5), 951-7.

149. Balint, Z.; Vegh, G. A.; Popescu, A.; Dima, M.; Ganea, C.; Varo, G., Direct observation of protein motion during the photochemical reaction cycle of bacteriorhodopsin *Langmuir* **2007,** 23, (13), 7225-8.

150. Cartailler, J. P.; Luecke, H., X-ray crystallographic analysis of lipid-protein interactions in the bacteriorhodopsin purple membrane. *Annual Reviews of Biophysics and Biomolecular Structure* **2003,** 32, 285-310.

151. Luecke, H., Atomic resolution structures of bacteriorhodopsin photocycle intermediates: the role of discrete water molecules in the function of this light-driven ion pump. *Biochimica et Biophysica Acta* **2000,** 1460, (1), 133-56.

152. Pfeiffer, M.; Rink, T.; Gerwert, K.; Oesterhelt, D.; Steinhoff, H. J., Site-directed spin-labeling reveals the orientation of the amino acid side-chains in the E-F loop of bacteriorhodopsin. *Journal of Molecular Biology* **1999,** 287, (1), 163-171.

153. Gale, P.; Watts, A., Effect of bacteriorhodopsin on the orientation of the headgroup of 1,2-dimyristoyl-sn-glycero-3-phosphocholine in bilayers: a 31P- and 2H-NMR study. *Biochimica et Biophysica Acta* **1992,** 1106, (2), 317-24.

154. Watts, A.; Sternberg, B.; Ulrich, A. S.; Whiteway, C. A.; Seifert, G.; Sami, M.; Fisher, P.; Heyn, M. P.; Wallat, I., Bacteriorhodopsin - the Effect of Bilayer Thickness on 2d-Array Formation, and the Structural Re-Alignment of Retinal through the Photocycle. *Biophysical Chemistry* **1995,** 56, (1-2), 41-46.

155. Andersson, M.; Malmerberg, E.; Westenhoff, S.; Katona, G.; Cammarata, M.; Wohri, A. B.; Johansson, L. C.; Ewald, F.; Eklund, M.; Wulff, M.; Davidsson, J.; Neutze, R., Structural Dynamics of Light-Driven Proton Pumps *Structure* **2009,** 17, (9), 1265-1275.

156. Casuso, I.; Kodera, N.; Le Grimellec, C.; Ando, T.; Scheuring, S., Contact-Mode High-Resolution High-Speed Atomic Force Microscopy Movies of the Purple Membrane. *Biophysical Journal* **2009,** 97, (5), 1354-1361.

157. Muller, D. J.; Heymann, J. B.; Oesterhelt, F.; Moller, C.; Gaub, H.; Buldt, G.; Engel, A., Atomic force microscopy of native purple membrane. *Biochimica et Biophysica Acta* **2000,** 1460, (1), 27-38.

158. PebayPeyroula, E.; Rummel, G.; Rosenbusch, J. P.; Landau, E. M., X-ray structure of bacteriorhodopsin at 2.5 angstroms from microcrystals grown in lipidic cubic phases. *Science* **1997,** 277, (5332), 1676-1681.

159. Persike, N.; Pfeiffer, M.; Guckenberger, R.; Fritz, M., Changes in the surface structure of purple membrane upon illumination measured by atomic force microscopy. *Colloids and Surfaces B-Biointerfaces* **2000,** 19, (4), 325-332.

160. Yamamoto, D.; Uchihashi, T.; Kodera, N.; Yamashita, H.; Nishikori, S.; Ogura, T.; Shibata, M.; Ando, T., High-Speed Atomic Force Microscopy Techniques for Observing Dynamic Biomolecular Processes. *Methods in Enzymology, Vol 475: Single Molecule Tools, Pt B* **2010,** 474, 541-564.

161. Butt, H. J.; Downing, K. H.; Hansma, P. K., Imaging the membrane protein bacteriorhodopsin with the atomic force microscope. *Biophysical Journal* **1990,** 58, (6), 1473-80.

162. Nagy, K., Photoelectric activity of dried, oriented layers of purple membrane from Halobacterium halobium *Biochemical and Biophysical Research Communication* **1978,** 85, (1), 383-90.

163. Greenbaum, E., Vectorial Photocurrents and Photoconductivity in Metallized Chloroplasts. *Journal of Physical Chemistry* **1990,** 94, (16), 6151-6153.

164. Birge, R. R., Photophysics and Molecular Electronic Applications of the Rhodopsins. *Annual Review of Physical Chemistry* **1990,** 41, 683-733.

165. Lee, I.; Lee, J. W.; Greenbaum, E., Biomolecular electronics: Vectorial arrays of photosynthetic reaction centers. *Physical Review Letters* **1997,** 79, (17), 3294-3297.

166. Pandey, P. C., Bacteriorhodopsin - Novel biomolecule for nano devices. *Analytica Chimica Acta* **2006,** 568, (1-2), 47-56.

167. Wang, W. W.; Knopf, G. K.; Bassi, A. S., Biological transducers based on bacteriorhodopsin for smart biosensor applications. *2004 International Conference on Mems, Nano and Smart Systems, Proceedings* **2004**, 274-279.

168. Chu, L. K.; Yen, C. W.; El-Sayed, M. A., Bacteriorhodopsin-based photo-electrochemical cell. *Biosensors & Bioelectronics* **2010,** 26, (2), 620-6.

169. Jin, Y.; Honig, T.; Ron, I.; Friedman, N.; Sheves, M.; Cahen, D., Bacteriorhodopsin as an electronic conduction medium for biomolecular electronics. *Chemical Society Reviews* **2008,** 37, (11), 2422-32.

170. Ron, I.; Pecht, I.; Sheves, M.; Cahen, D., Proteins as Solid-State Electronic Conductors. *Accounts of Chemical Research* **2010,** 43, (7), 945-953.

171. Hampp, N.; Thoma, R.; Popp, A.; Zeisel, D.; Renner, T.; Brauchle, C.; Oesterhelt, D., Bacteriorhodopsin Variants for Optical Information-Processing. *Biosensors : Fundamentals, Technologies and Applications* **1992,** 17, 146-151.

172. Miyasaka, T.; Koyama, K., Image Sensing and Processing by a Bacteriorhodopsin-Based Artificial Photoreceptor. *Applied Optics* **1993,** 32, (31), 6371-6379.

173. Choi, H. G.; Jung, W. C.; Min, J. H.; Lee, W. H.; Choi, J. W., Color image detection by biomolecular photoreceptor using bacteriorhodopsin-based complex LB films. *Biosensors & Bioelectronics* **2001,** 16, (9-12), 925-935.

174. Wang, W., W.; Knopf, G. K.; Bassi, A. S., Toward mimicking biological vision with protein-based flexible imaging arrays. *Proceedings of SPIE* **2007,** 8527.

175. Koyama, K.; Yamaguchi, N.; Miyasaka, T., Antibody-Mediated Bacteriorhodopsin Orientation for Molecular Device Architectures. *Science* **1994,** 265, (5173), 762-765.

176. Watanabe, T.; Saga, Y.; Koyama, K.; Miyasaka, T., pH-dependent photocurrent response from bacteriorhodopsin at electrode-electrolyte interfaces. *Chemistry Letters* **1998**, (9), 961-962.

177. Robertson, B.; Lukashev, E. P., Rapid pH change due to bacteriorhodopsin measured with a tin-oxide electrode. *Biophysical Journal* **1995,** 68, (4), 1507-1517.

178. Weetall, H. H.; Samuelson, L. A., Optical and electrical properties of bacteriorhodopsin Langmuir-Blodgett films. *Thin Solid Films* **1998,** 312, (1-2), 306-312.

179. STUART, J. A.; MARCY, D.; BIRGE, R. R. Bacteriorhodopsin-based photochromic sensor for detection of chemical and environmental toxins 2010.

180. Brizzolara, R., A.; Boyd, J., L.; Tate, A., E., Evidence for covalent attachment of purple membrane to a gold surface via genetic modification of bacteriorhodopsin. *Journal of Vacuum Science and Technology A* **1997,** 15, (3), 773.

181. Balashov, S. P.; Govindjee, R.; Kono, M.; Imasheva, E.; Lukashev, E.; Ebrey, T. G.; Crouch, R. K.; Menick, D. R.; Feng, Y., Effect of the arginine-82 to alanine mutation in bacteriorhodopsin on dark adaptation, proton release, and the photochemical cycle. *Biochemistry* **1993,** 32, (39), 10331-43.

182. Heyes, C. D.; El-Sayed, M. A., Proton transfer reactions in native and delonized bacteriorhodopsin upon delipidation and monomerization. *Biophysical Journal* **2003,** 85, (1), 426-434.

183. Lanyi, J. K., Proton Translocation Mechanism and Energetics in the Light-Driven Pump Bacteriorhodopsin. *Biochimica Et Biophysica Acta* **1993,** 1183, (2), 241-261.

184. Khorana, H. G., 2 Light-Transducing Membrane-Proteins - Bacteriorhodopsin and the Mammalian Rhodopsin. *Proceedings of the National Academy of Sciences of the United States of America* **1993,** 90, (4), 1166-1171.

185. Miercke, L. J. W.; Betlach, M. C.; Mitra, A. K.; Shand, R. F.; Fong, S. K.; Stroud, R. M., Wild-Type and Mutant Bacteriorhodopsins D85n, D96n, and R82q - Purification to Homogeneity, Ph-Dependence of Pumping, and Electron-Diffraction. *Biochemistry* **1991,** 30, (12), 3088-3098.

186. Hampp, N.; Thoma, R.; Brauchle, C.; Kreuzer, F. H.; Maurer, R.; Oesterhelt, D., Bacteriorhodopsin Variants for Optical Information-Processing - a New Approach in Material Science. *Molecular Electronics - Science and Technology* **1992,** 262, 181-190.

187. Hampp, N.; Thoma, R.; Oesterhelt, D.; Brauchle, C., Biological Photochrome Bacteriorhodopsin and Its Genetic Variant Asp96 -] Asn as

Media for Optical-Pattern Recognition. *Applied Optics* **1992,** 31, (11), 1834-1841.

188. Gergely, C.; Ganea, C.; Groma, G.; Varo, G., Study of the Photocycle and Charge Motions of the Bacteriorhodopsin Mutant D96n. *Biophysical Journal* **1993,** 65, (6), 2478-2483.

189. Zeisel, D.; Hampp, N., Spectral Relationship of Light-Induced Refractive-Index and Absorption Changes in Bacteriorhodopsin Films Containing Wildtype Brwt and the Variant Brd96n. *Journal of Physical Chemistry* **1992,** 96, (19), 7788-7792.

190. Misra, S.; Govindjee, R.; Ebrey, T. G.; Chen, N.; Ma, J. X.; Crouch, R. K., Proton uptake and release are rate-limiting steps in the photocycle of the bacteriorhodopsin mutant E204Q. *Biochemistry* **1997,** 36, (16), 4875-4883.

191. Casuso, I.; Fumagalli, L.; Samitier, J.; Padrós, E.; Reggiani, L.; Akimov, V.; Gomila, G.; , Electron transport through supported biomembranes at the nanoscale by conductive atomic force microscopy *Nanotechnology* **2007,** 18, (46).

192. He, J. A.; Samuelson, L.; Li, L.; Kumar, J.; Tripathy, S. K., Photoelectric properties of oriented bacteriorhodopsin/polycation multilayers by electrostatic layer-by-layer assembly. *Journal of Physical Chemistry B* **1998,** 102, (36), 7067-7072.

193. Jin, Y.; Friedman, N.; Cahen, D.; Sheves, M., Chemically induced enhancement of the opto-electronic response of Halobacterium purple membrane monolayer. *Chemical Communications (Camb)* **2006**, (12), 1310-2.

194. Jin, Y. D.; Friedman, N.; Sheves, M.; He, T.; Cahen, D., Bacteriorhodopsin (bR) as an electronic conduction medium: Current transport through bR-containing monolayers. *Proceedings of the National Academy of Sciences of the United States of America* **2006,** 103, (23), 8601-8606.

195. Li, R.; Cui, X. Q.; Hu, W. H.; Lu, Z. S.; Li, C. M., Fabrication of oriented poly-L-lysine/bacteriorhodopsin-embedded purple membrane multilayer structure for enhanced photoelectric response. *Journal of Colloid and Interface Science* **2010,** 344, (1), 150-157.

196. Ron, I.; Sepunaru, L.; Itzhakov, S.; Belenkova, T.; Friedman, N.; Pecht, I.; Sheves, M.; Cahen, D., Proteins as Electronic Materials: Electron Transport through Solid-State Protein Monolayer Junctions. *Journal of the American Chemical Society* **2010,** 132, (12), 4131-4140.

197. Singh, K.; Korenstein, R.; Lebedeva, H.; Caplan, S. R., Photoelectric conversion by bacteriorhodopsin in charged synthetic membranes. *Biophysical Journal* **1980,** 31, (3), 393-401.

198. Lee, I.; Lee, J. W.; Stubna, A.; Greenbaum, E., Measurement of electrostatic potentials above oriented single photosynthetic reaction centers. *Journal of Physical Chemistry B* **2000,** 104, (11), 2439-2443.

199. Watanabe, T.; Saga, Y.; Koyama, K.; Miyasaka, T., Mechanism of photocurrent generation from bacteriorhodopsin on gold electrodes. *Journal of Physical Chemistry B* **1999,** 103, (1), 234-238.

200. Miyasaka, T.; Koyama, K., Photoelectrochemical Behavior of Purple Membrane Langmuir-Blodgett-Films at the Electrode-Electrolyte Interface. *Chemistry Letters* **1991**, (9), 1645-1648.

201. Maximychev, A. V.; Chamorovsky, S. K.; Panov, V. I.; Fedorov, E. A.; Rambidi, N. G., Purple membrane multilayers: detailed structure and photoelectric characteristics of bacteriorhodopsin. *Biosystems* **1992,** 27, (4), 195-9.

202. Choi, J. W.; Min, J. H.; Choi, H. G.; Lee, W. H.; Kim, U. R., Photocurrent of bacteriorhodopsin films deposited by electrophoretic method. *Thin Solid Films* **1998,** 327, 698-702.

203. Hu, K. S.; Chen, D. L.; Lu, Y. J.; Sui, S. F.; Xu, B., Oriented assembly of purple membrane on solid support, mediated by molecular recognition. *Journal of Physical Chemistry B* **2003,** 107, (15), 3598-3605.

204. Chen, Z. P.; Lewis, A.; Takei, H. Y.; Nebenzahl, I., Bacteriorhodopsin Oriented in Polyvinyl-Alcohol Films as an Erasable Optical Storage Medium. *Applied Optics* **1991,** 30, (35), 5188-5196.

205. Weetall, H. H., Retention of bacteriorhodopsin activity in dried sol-gel glass. *Biosensors & Bioelectronics* **1996,** 11, (3), 327-333.

206. Knapp, H. F.; Mesquida, P.; Stemmer, A., Imaging the surface potential of active purple membrane. *Surface and Interface Analysis* **2002,** 33, (2), 108-112.

207. Choi, J. W.; Min, J. H.; Choi, H. G.; Lee, W. H.; Kim, U. R., Optimal fabrication condition of bacteriorhodopsin films by electrophoretic sedimentation technique. *Supramolecular Science* **1998,** 5, (5-6), 687-690.

208. Moller, C.; Allen, M.; V, E.; Engel, A.; Muller, D. J., Tapping-mode atomic force microscopy produces faithful high-resolution images of protein surfaces. *Biophysical Journal* **1999,** 77, (2), 1150-1158.

209. Furuno, T.; Takimoto, K.; Kouyama, T.; Ikegami, A.; Sasabe, H., Photovoltaic Properties of Purple Membrane Langmuir-Blodgett Films. *Thin Solid Films* **1988,** 160, (1-2), 145-151.

210. Grigorieff, N.; Beckmann, E.; Zemlin, F., Lipid Location in Deoxycholate-Treated Purple Membrane at 2.6 Angstrom. *Journal of Molecular Biology* **1995,** 254, (3), 404-415.

211. Kates, M.; Kushwaha, S. C.; Sprott, G. D., Lipids of Purple Membrane from Extreme Halophiles and of Methanogenic Bacteria. *Methods in Enzymology* **1982,** 88, 98-111.

212. Kates, M., The phytanyl ether-linked polar lipids and isoprenoid neutral lipids of extremely halophilic bacteria. *Prog Chem Fats Other Lipids* **1978,** 15, (4), 301-42.

213. Heyes, C. D.; El-Sayed, M. A., The role of the native lipids and lattice structure in bacteriorhodopsin protein conformation and stability as studied by temperature-dependent Fourier transform-infrared spectroscopy. *Journal of Biological Chemistry* **2002,** 277, (33), 29437-43.

214. Szundi, I.; Steckenius, W., Effect of Lipid Surface-Charges on the Purple-to-Blue Transition of Bacteriorhodopsin. *Proceedings of the National Academy of Sciences of the United States of America* **1987,** 84, (11), 3681-3684.

215. Huang, K. S.; Bayley, H.; Khorana, H. G., Delipidation of Bacteriorhodopsin and Reconstitution with Exogenous Phospholipid. *Proceedings of the National Academy of Sciences of the United States of America-Biological Sciences* **1980,** 77, (1), 323-327.

216. Moller, C.; Buldt, G.; Dencher, N. A.; Engel, A.; Muller, D. J., Reversible loss of crystallinity on photobleaching purple membrane in the presence of hydroxylamine. *Journal of Molecular Biology* **2000,** 301, (4), 869-879.

217. Gulikkrzywicki, T.; Seigneuret, M.; Rigaud, J. L., Monomer-Oligomer Equilibrium of Bacteriorhodopsin in Reconstituted Proteoliposomes - a Freeze-Fracture Electron-Microscope Study. *Journal of Biological Chemistry* **1987,** 262, (32), 15580-15588.

218. Govindjee, R.; Ebrey, T. G.; Crofts, A. R., The Quantum Efficiency of Proton Pumping by the Purple Membrane of Halobacterium-Halobium. *Biophysical Journal* **1980,** 30, (2), 231-242.

219. Chen, Z. P.; Birge, R. R., Protein-Based Artificial Retinas. *Trends in Biotechnology* **1993,** 11, (7), 292-300.

220. Shinwari, M. W.; Deen, M. J.; Starikov, E. B.; Cuniberti, G., Electrical Conductance in Biological Molecules. *Advanced Functional Materials* **2010,** 20, (12), 1865-1883.

221. Zhao, J.; Davis, J. J.; Sansom, M. S.; Hung, A., Exploring the electronic and mechanical properties of protein using conducting atomic force microscopy. *Journal of the Americal Chemical Society* **2004,** 126, (17), 5601-9.

222. Muller, D. J.; Heymann, J. B.; Oesterhelt, F.; Moller, C.; Gaub, H.; Buldt, G.; Engel, A., Atomic force microscopy of native purple membrane. *Biochimica Et Biophysica Acta-Bioenergetics* **2000,** 1460, (1), 27-38.

223. Kienberger, F.; Stroh, C.; Kada, G.; Moser, R.; Baumgartner, W.; Pastushenko, V.; Rankl, C.; Schmidt, U.; Müller, H.; Orlova, E.; LeGrimellec, C.; Drenckhahn, D.; Blaas, D.; Hinterdorfer, P., Dynamic force microscopy imaging of native membranes. *Ultramicroscopy* 97, (1-4), 229-237.

224. Lee, I.; Stuart, J. A.; Budy, S.; Hillebrecht, J. R.; Birge R., R.; Greenbaum, E., Scanning Surface Potential Microscopy of Bacteriorhodopsin Mutant D96N. *Microscopy and Microanalysis* **2005,** 11, (2), 356.

225. Ida Lee, † Elias Greenbaum,‡ Stephen Budy,§ Jason R. Hillebrecht,| Robert R. Birge,| and; Jeffrey A. Stuart*, Photoinduced Surface Potential Change of Bacteriorhodopsin Mutant D96N Measured by Scanning Surface Potential Microscopy. *Journal of Physical Chemistry* **2006,** 110, 10982-10990.

226. Kimura, Y.; Fujiwara, M.; Ikegami, A., Anisotropic Electric Properties of Purple Membrane and Their Change during the Photoreaction Cycle. *Biophysical Journal* **1984,** 45, (3), 615-625.

227. Keszthelyi, L., Orientation of Membrane-Fragments by Electric-Field. *Biochimica Et Biophysica Acta* **1980,** 598, (3), 429-436.

228. Miyasaka, T.; Koyama, K.; Itoh, I., Quantum Conversion and Image Detection by a Bacteriorhodopsin-Based Artificial Photoreceptor. *Science* **1992,** 255, (5042), 342-344.

229. Hampp, N.; Schranz, M.; Noll, F., Oriented purple membrane monolayers covalently attached to gold by multiple thiole linkages analyzed by single molecule force spectroscopy. *Langmuir* **2007,** 23, (22), 11134-11138.

230. Choi, H. G.; Min, J. H.; Lee, W. H.; Choi, J. W., Adsorption behavior and photoelectric response characteristics of bacteriorhodopsin thin films fabricated by self-assembly technique. *Colloids and Surfaces B-Biointerfaces* **2002,** 23, (4), 327-337.

231. Griep, M. H.; Walczak, K. A.; Winder, E. M.; Lueking, D. R.; Friedrich, C. R., Quantum dot enhancement of bacteriorhodopsin-based electrodes *Biosensors & Bioelectronics* **2010,** 25, (6), 1493-1497.

232. Horn, C.; Steinem, C., Photocurrents generated by bacteriorhodopsin adsorbed on nano-black lipid membranes. *Biophysical Journal* **2005,** 89, (2), 1046-1054.

233. Li, C. M.; Li, R.; Bao, H. F.; Bao, Q. L.; Lee, V. S., Stationary current generated from photocycle of a hybrid bacteriorhodopsin/quantum dot bionanosystem. *Applied Physics Letters* **2007,** 91, (22).

234. El-Sayed, M. A.; Yen, C. W.; Chu, L. K., Plasmonic Field Enhancement of the Bacteriorhodopsin Photocurrent during Its Proton Pump Photocycle. *Journal of the American Chemical Society* **2010,** 132, (21), 7250-7251.

235. Saga, Y.; Ishikawa, T.; Watanabe, T., Effect of metal ion exchange on the photocurrent response from bacteriorhodopsin on tin oxide electrodes. *Bioelectrochemistry* **2002,** 57, (1), 17-22.

236. Watanabe, T.; Gerischer, H., Photoelectrochemical Studies on Gold Electrodes with Surface Oxide Layers .1. Photocurrent Measurement in the Visible Region. *Journal of Electroanalytical Chemistry* **1981,** 117, (2), 185-200.

237. Carraway, R. E.; Leeman, S. E., The isolation of a new hypotensive peptide, Neurotensin, from hypothalami. *Journal of Biological Chemistry* **1973,** 248, 6854.

238. Brown, D. R.; Miller, R. J., Neurotensin. *British Medical Bulletin* **1982,** 38, (3), 239-45.

239. Luca, S.; White, J. F.; Sohal, A. K.; Filippov, D. V.; van Boom, J. H.; Grisshammer, R.; Baldus, M., The conformation of neurotensin bound to its G protein-coupled receptor. *Proceedings of the National Academy of Sciences of the United States of America* **2003,** 100, (19), 10706-10711.

240. Pelaprat, D., Interactions between neurotensin receptors and G proteins. *Peptides* **2006,** 27, (10), 2476-87.

241. Vincent, J. P.; Mazella, J.; Kitabgi, P., Neurotensin and neurotensin receptors. *Trends in Pharmacological Sciences* **1999,** 20, (7), 302-9.

242. Watts, A.; Williamson, P. T. F.; Bains, S.; Chung, C.; Cooke, R., Probing the environment of neurotensin whilst bound to the neurotensin receptor by solid state NMR. *Febs Letters* **2002,** 518, (1-3), 111-115.

243. Pang, Y. P.; Cusack, B.; Groshan, K.; Richelson, E., Proposed ligand binding site of the transmembrane receptor for neurotensin(8-13). *Journal of Biological Chemistry* **1996,** 271, (25), 15060-15068.

244. Kitabgi, P., Inverse agonism at neurotensin receptors NTS1 and NTS2. *Inverse Agonism* **2003,** 1249, 207-216.

245. Kitabgi, P.; Checler, F.; Mazella, J.; Vincent, J. P., Pharmacology and biochemistry of neurotensin receptors. *Reviews in Clinical and Basic Pharmacology* **1985,** 5, (3-4), 397-486.

246. Chalon, P.; Vita, N.; Kaghad, M.; Guillemot, M.; Bonnin, J.; Delpech, B.; Le Fur, G.; Ferrara, P.; Caput, D., Molecular cloning of a levocabastine-sensitive neurotensin binding site. *FEBS Letters* **1996,** 386, (2-3), 91-4.

247. Mazella, J.; Zsurger, N.; Navarro, V.; Chabry, J.; Kaghad, M.; Caput, D.; Ferrara, P.; Vita, N.; Gully, D.; Maffrand, J. P.; Vincent, J. P., The 100-kDa neurotensin receptor is gp95/sortilin, a non-G-protein-coupled receptor. *Journal of Biological Chemistry* **1998,** 273, (41), 26273-6.

248. Mazella, J.; Vincent, J. P., Functional roles of the NTS2 and NTS3 receptors. *Peptides* **2006,** 27, (10), 2469-2475.

249. Mazella, J.; Martin, S.; Navarro, V.; Vincent, J. P., Neurotensin receptor-1 and-3 complex modulates the cellular signaling of neurotensin in the HT29 cell line. *Gastroenterology* **2002,** 123, (4), 1135-1143.

250. Grisshammer, R.; White, J. F.; Trinh, L. B.; Shiloach, J., Automated large-scale purification of a G protein-coupled receptor for neurotensin. *Febs Letters* **2004,** 564, (3), 289-293.

251. Paquot, M., Nanostructures et fonctionnalités des tensioactifs naturels *ProBio Revue* **2004,** 12, 31-50.

252. Rigaud, J. L., Membrane proteins: functional and structural studies using reconstituted proteoliposomes and 2-D crystals. *Brazilian Journal of Medical and Biological Research* **2002,** 35, (7), 753-66.

253. Seddon, A. M.; Curnow, P.; Booth, P. J., Membrane proteins, lipids and detergents: not just a soap opera. *Biochimica Et Biophysica Acta* **2004,** 1666, (1-2), 105-17.

254. Harding, P. J.; Hadingham, T. C.; McDonnell, J. M.; Watts, A., Direct analysis of a GPCR-agonist interaction by surface plasmon resonance. *Eur Biophysical Journal* **2006,** 35, (8), 709-12.

255. Grisshammer, R.; Shibata, Y.; White, J. F.; Serrano-Vega, M. J.; Magnani, F.; Aloia, A. L.; Tate, C. G., Thermostabilization of the Neurotensin Receptor NTS1. *Journal of Molecular Biology* **2009,** 390, (2), 262-277.

256. Cusack, B.; Richelson, E.; Pang, Y. P.; Zaidi, J.; Kozikowski, A. P., Pharmacological Studies on Novel Neurotensin Mimetics - Discovery of a Pharmacologically Unique Agent Exhibiting Concentration-Dependent Dual Effects as Antagonist and Agonist. *Molecular Pharmacology* **1993,** 44, (5), 1036-1040.

257. Kitabgi, P., Neurotensin Modulates Dopamine Neurotransmission at Levels Along Brain Dopaminergic Pathways. *Neurochemistry International* **1989,** 14, (2), 111-119.

258. Tanaka, K.; Masu, M.; Nakanishi, S., Structure and Functional Expression of the Cloned Rat Neurotensin Receptor. *Neuron* **1990,** 4, (6), 847-854.

259. Kitabgi, P.; Carraway, R.; Vanrietschoten, J.; Granier, C.; Morgat, J. L.; Menez, A.; Leeman, S.; Freychet, P., Neurotensin - Specific Binding to Synaptic-Membranes from Rat-Brain. *Proceedings of the National Academy of Sciences of the United States of America* **1977,** 74, (5), 1846-1850.